Anchorage and Bond Behaviour of Near Surface Mounted Fibre Reinforced Polymer Bars

Kalupahana, Kalpana

Award date:
2009

Awarding institution:
University of Bath

Anchorage and Bond Behaviour of Near Surface Mounted Fibre Reinforced Polymer Bars

W. K. Kalpana G. Kalupahana

A Thesis Submitted for the Degree of Doctor of Philosophy

University of Bath

Department of Architecture and Civil Engineering

December 2009

TABLE OF CONTENTS

LIST OF FIGURES

LIST OF TABLES

LIST OF NOTATIONS

A	Empirical bond parameter of Malvar model
A_c	Cross-sectional area of the concrete prism
A_f	Cross-sectional area of the FRP bar
B	Empirical bond parameter of Malvar model
C	Empirical bond parameter of Malvar model
D	Diameter of an FRP bar, empirical bond parameter of Malvar model
E	Empirical bond parameter of Malvar model
E	Young's modulus
E'	Stiffened Young's modulus in plane strain conditions
E_c	Young's modulus of the concrete prism
E_f	Young's modulus of the FRP bar
ED	Internal energy dissipation
F	Empirical bond parameter Malvar of model
G	Empirical bond parameter Malvar of model
G_f	Interfacial fracture energy
L	Distance from the edge of the concrete specimen to the free end
L	Bond length of the joint
L_{peri}	Perimeter of the failure interface of a NSM FRP bonded joint
P	Applied load
P_{exp}	Actual failure load
P_{ult}	Ultimate load
P_1	Load at which the elastic stage ends
P_2	Load at which the elastic - softening stage ends
P_3	Load at which the elastic - softening - frictional resistance stage ends
P_4	Load at which the elastic - softening - frictional resistance - frictional softening stage ends
P_5	Load at which the elastic - softening - frictional resistance - frictional softening - debonding stage ends
P_6	Load at which the softening - frictional resistance - frictional softening - debonding stage ends
P_7	Load at which the frictional resistance - frictional softening - debonding stage ends
$\overline{P}$	Non-dimensional parameter in the analytical solution presented in Chapter 6
W_l	Dissipation per unit length of the yield line
W_E	External work
X_1	Normal stress between concrete and groove filling material along the vertical sides
X_2	Normal stress between concrete and groove filling material along the horizontal side
a	Portion of the bond length which is at softening state
a_2	Value of 'a' when the elastic - softening stage ends

a_3 Value of '*a*' when the elastic - softening - frictional resistance stage ends

a_4 Value of '*a*' when the elastic - softening - frictional resistance - frictional softening stage ends

a_5 Value of '*a*' when the elastic - softening - frictional resistance - frictional softening - debonding stage ends

b Thickness of the concrete body

b Portion of the bond length which is at frictional (residual) stress state

b_c Width of the concrete prism

b_g Width of the groove

b_3 Value of '*b*' when the elastic - softening - frictional resistance stage ends

b_4 Value of '*b*' when the elastic - softening - frictional resistance - frictional softening stage ends

b_5 Value of '*b*' when the elastic - softening - frictional resistance - frictional softening - debonding stage ends

b_6 Value of '*b*' when the softening - frictional resistance - frictional softening - debonding stage ends

c Portion of the bond length which is at frictional (residual) softening state

c_4 Value of '*c*' when the elastic - softening - frictional resistance - frictional softening stage ends

c_5 Value of '*c*' when the elastic - softening - frictional resistance - frictional softening - debonding stage ends

c_6 Value of '*c*' when the softening - frictional resistance - frictional softening - debonding stage ends

c_7 Value of '*c*' when the frictional resistance - frictional softening - debonding stage ends

d Portion of the bond length which is at debonding state

d_b Bar diameter

d_g Groove depth/width for square grooves

d_5 Value of '*d*' when the elastic - softening - frictional resistance - frictional softening - debonding stage ends

d_6 Value of '*d*' when the softening - frictional resistance - frictional softening - debonding stage ends

d_7 Value of '*d*' when the frictional resistance - frictional softening - debonding stage ends

f_c Effective compressive strength of concrete

f'_c Cylinder compressive strength of concrete

f_{cu} Peak cube compressive strength of concrete

f_{pt} Tensile strength of the resin

f_{tsplit} Splitting tensile strength of concrete

f_t Effective tensile strength of concrete

f_t' Tensile strength of concrete

$f(\delta)$ Function of slip

h Concrete cover

h_c Depth of the concrete prism

h_f Width of the NSM FRP rectangular bar
h_g Depth of the groove
k Ratio of groove size to bar diameter
k_1 Coefficient in the model of De Lorenzis for the transverse plane
k_2 Coefficient in the model of De Lorenzis for the transverse plane
k' Slope of the linear softening branch of the MBEP model
l_{dev} Development length
l_{eff} Effective bond length
n Number of specimens
p Inner pressure in the thick cylinder model
p Transverse pressure at the bar-resin interface
p' Transverse pressure at the resin-concrete interface
p_{cr} Cracking radial pressure
p_f Bar perimeter
p_1 Perimeter of the bar
p_2 Perimeter of the groove
r Geometric parameter of the plasticity model
r Radial coordinate
r_i Internal radius in the thick cylinder model
r_e External radius in the thick cylinder model
s Slip
s_f Value of slip when bond stress reaches the frictional bond stress level in the MBEP model
s_{fe} Free end slip
s_m Parameter of the uni-linear, bi-linear and MBEP models
s_m Slip at peak bond stress
s_r Parameter of the CMR model
s_u Parameter of the MBEP model
s_1 Parameter of the bi-linear and BEP models
s_2 Parameter of the BEP model
s_3 Parameter of the BEP model
t_f Thickness of the NSM FRP rectangular bar
u_c Displacement of the concrete
u_f Displacement of the FRP bar
u_r Radial displacement
u_x Displacement along x direction
u_y Displacement along y direction
x Coordinate along the bond length starting from the free end
x Horizontal coordinate
y Vertical coordinate
Δ Slip at the loaded end
$\overline{\Delta}$ Non-dimensional parameter in the analytical solution presented in Chapter 6
Φ Angle of friction of concrete
α Angle between the principal compressive stress and the bar axis

α Parameter of the BEP, MBEP and CMR models

α Angle between the direction of the relative displacement vector and the yield line

α' Parameter of the softening branch of De Lorenzis model

β Non-dimensional bond parameter

β Geometric parameter of the plasticity model

δ Interfacial slip between the FRP bar and the concrete

δ Magnitude of the relative displacement vector

δ_{f} Bond parameter of the four-branched bond stress-slip model in Chapter 6

δ_{re} Bond parameter of the four-branched bond stress-slip model in Chapter 6

δ_{rs} Bond parameter of the four-branched bond stress-slip model in Chapter 6

δ_1 Bond parameter of the four-branched bond stress-slip model in Chapter 6

γ Angle formed between the splitting plane in the concrete and the horizontal direction

γ_{xy} Shear strain in the $x-y$ plane

ε_{f} Axial strain of the bar

ε_x Normal strain along x direction

ε_y Normal strain along y direction

λ Coefficient in the governing differential equation of the bonded joint

λ_1 Coefficient in the governing differential equation of the bonded joint

λ_2 Coefficient in the governing differential equation of the bonded joint

λ_3 Constant in the governing differential equation of the bonded joint

λ_4 Coefficient in the governing differential equation of the bonded joint

ν Poisson's ratio

ν' Stiffened Poisson's ratio in plane strain conditions

ν_{c} Effectiveness factor on cube compressive strength of concrete

ν_{t} Effectiveness factor on tensile strength of concrete

ϕ Nominal bar diameter

ρ Parameter of the MBEP model

σ Axial stress

σ Confining axisymmetric radial pressure

σ_{c} Normal stress of the concrete

σ_{f} Normal stress of the FRP bar

$\sigma_{\max}$ Maximum reinforcement stress resisted by an NSM bonded joint of De Lorenzis *et al.*2002

σ_r Normal stress in the radial direction

σ_x Normal stress along x direction

σ_y Normal stress along y direction

σ_θ Normal stress in the circumferential direction

θ Angle between the yield line AB and the horizontal direction in the plasticity model

τ Bond stress

τ Tangential bond stress at the bar-resin interface

τ' Tangential bond stress at the resin-concrete interface

τ_f Frictional bond stress

τ_f Bond parameter of the four-branched bond stress-slip model in Chapter 6

τ_r Bond parameter of the four-branched bond stress-slip model in Chapter 6

τ_m Parameter of the uni-linear, bi-linear and MBEP models

τ_m Local bond strength at the bar-resin interface

τ'_m Local bond strength at the resin-concrete interface

τ_{xy} Tangential stress in the $x-y$ plane

τ_1 Parameter of the BEP model

τ_2 Parameter of the BEP model

LIST OF PUBLICATIONS

PERERA, W. K. K. G., IBELL, T. J., DARBY, A. P. & DENTON, S. R., (2008). Anchorage and bond behaviour of near surface mounted carbon fibre reinforced polymer bars. *5th International conference on Advanced Composite Materials in Bridges and Structures (ACMBS-V).* Winnipeg, Canada.

PERERA, W. K. K. G., IBELL, T. J. & DARBY, A. P., (2009). Bond behaviour of various shapes of NSM CFRP bars and concrete. *9th International symposium on Fibre Reinforced Polymer Reinforcement for Concrete Structures (FRPRCS-9).* Sydney, Australia.

PERERA, W. K. K. G., IBELL, T. J., DARBY, A. P. & DENTON, S. R., (2009). Bond mechanisms of various shapes of NSM CFRP bars. *Advanced Composites In Construction 2009 (ACIC 2009).* Edinburgh, Scotland.

KALUPAHANA, W. K. K. G., IBELL, T. J. & DARBY, A. P., Bond characteristics of near surface mounted CFRP bars. To be submitted to *ACI Structural Journal* (publications arising from this thesis).

KALUPAHANA, W. K. K. G., IBELL, T. J., DARBY, A. P. & TENG, J.G., Full range load-slip behaviour of near surface mounted FRP bars. To be submitted to *ASCE Journal of Engineering Mechanics* (publications arising from this thesis).

ACKNOWLEDGEMENT

I gratefully acknowledge the Departmental Scholarship awarded for the research, by Department of Architecture & Civil Engineering, University of Bath. I would also like to forward my sincere thanks to everyone who has given me a helping hand and contributed in many ways to make the four years of my research project a success. First of all, I sincerely thank my supervisors, Prof. Tim Ibell and Dr. Antony Darby, for their expert guidance and motivation throughout the research. I am also very grateful to my former research supervisor, Dr. Paolo Casadei, for his direction and encouragement. Finally, I thank the technical staff who assisted me for my experimental work, especially Brian Purnell and Neil Price for their hard work.

This thesis is dedicated to my husband, Ranga Kalupahana and my parents, Premasiri Perera and Irangani Perera, for their great support and love.

ABSTRACT

The Near Surface Mounted (NSM) strengthening is an emerging retrofitting technique, which involves bonding Fibre Reinforced Polymer (FRP) reinforcement into grooves cut along the surface of a concrete member to be strengthened. This technique offers many advantages over external bonding of FRP reinforcement, for example, an increased bond capacity, protection from external damage and the possibility of anchoring into adjacent concrete members. To date, significant research has been conducted into the NSM FRP strengthening technique. However, there are still some areas which need further research in order to fully characterise bond and anchorage of NSM FRP bars. Lack of experimental data, design tools and analytical models addressing these areas create obstacles for the efficient use of these advanced polymer materials.

The particular objectives of the research are; to investigate bond behaviour between NSM FRP bars and concrete, to understand the critical failure modes involved and their mechanics, and to develop a rational analytical model to predict bond strength and anchorage length requirements for NSM FRP bars. Several significant variables affecting bond, such as bond length, size, shape and type of bar, resin type, groove dimensions and concrete strength, have been considered. In particular, attention has been focussed on the effect of bar shape on bond behaviour.

A comprehensive set of laboratory testing and their results, including the effect of the investigated parameters are presented. Various modes of anchorage failure of NSM FRP bars are identified and the underlying mechanics are investigated. Analytical models are developed to predict bond capacity and anchorage length requirements of NSM FRP bars, and are verified with experimental results.

CHAPTER 1 – INTRODUCTION

1.1 Fibre Reinforced Polymer (FRP) in general

At present, the use of FRP in the construction industry is a well known technology and FRP is becoming an effective alternative to traditional materials like steel, mainly due to its superior properties such as high strength to weight ratio, non-corrosive properties, durability and versatility. FRP can be defined as a composite formed by fibres within a resin matrix where the fibres provide the tensile strength of the composite while the resin impregnates, bonds and protects the fibres. The common types of FRPs are Carbon FRPs (CFRPs), Aramid FRPs (AFRPs) and Glass FRPs (GFRPs). There are two types of resins namely, thermosetting and thermoplastic. The most common thermosetting resins are epoxies, polyesters, vinylesters and phenolics. Epoxy is the predominant resin used in civil engineering applications due to its high strength, excellent adhesion to the substrate, good chemical resistance and lower shrinkage.

FRPs are anisotropic and linear elastic up to failure. Therefore, care should be taken in design to avoid brittle catastrophic failure. Some disadvantages of using FRPs are lack of experience in design and application, no availability of codes of practice for FRP applications, high cost of materials compared to conventional materials, low transverse strength and susceptibility to damage by fire and vandalism. Some commonly available FRP products are bars, sheets, plates, shells and grids. Different types of FRP bars are commercially available and they are categorized according to the surface finish, for example, ribbed, sand coated, and spiral wrapped. A detailed review of FRP properties can be found in Nanni (1993).

1.2 Strengthening of concrete structures using FRP

When a structure is required to withstand loads higher than those which it was originally designed for, it has to be either reconstructed after demolition or strengthened. There are several reasons for structures to be strengthened rather than demolished. For example, reconstruction is usually more expensive than a

strengthening process, it may take more time than a strengthening process and it may create congestion, sound pollution, etc. Therefore, in many instances, the strengthening is preferred over demolition and reconstruction.

In the past, the common strengthening methods for reinforced concrete structures involved casting additional concrete, dowelling additional steel reinforcement (Concrete Society, 2004), column jacketing and bonding steel plates to the tension face of the member. With the rapid development of FRP composites and due to their above-mentioned advantages over traditional methods, bonding of FRP reinforcement with an adhesive has become a popular method for strengthening of concrete structures. Due to the lightness of FRP, there is no need for temporary support until the adhesive is hardened. Further, it makes the application process easier and quicker unlike the case of steel plate bonding. Because of the flexibility of FRP reinforcement, in the form of sheets, it can easily achieve the curvature of the profile without any pre-bending, unlike steel. With those advantages FRP has become a predominant option for strengthening of existing concrete structures all over the world.

Generally, FRP strengthening involves either increasing flexural strength of structural members like beams and slabs by adding longitudinal reinforcement or increasing shear capacity of beams, slabs, and columns by transverse reinforcement or increasing confinement and strain capacity of columns by wrapping FRP sheets. There are several possible ways of applying FRP materials for strengthening;

- Unidirectional plates bonded to the concrete
- Uni-directional or bi-directional sheets bonded to the concrete
- Pre-impregnated sheets
- Preformed shells to fit concrete columns
- Near surface mounted bars
- Deep embedment of FRP bars

Externally Bonded Reinforcement (EBR) systems have been successfully applied for strengthening of existing concrete structures since mid 1980s (ACI, 2002). It has been developed as an effective alternative to the traditional techniques, for instance, steel plate bonding and column jacketing. The EBR technique can not only be used for concrete structures, but can also be applied for strengthening of timber, masonry and

steel structures. Basically, it involves bonding FRP reinforcement, sheets, plates or shells, to the substrate with an adhesive.

The most outstanding characteristic of the EBR technique is the ease and speed of installation compared to steel plate bonding. One of the drawbacks of EBR systems is the susceptibility to mechanical damages as well as to damage from environmental effects such as freeze-thaw cycles due to direct exposure. Further, EBR systems are easily susceptible to damage by fire and vandalism. Although this technique is well established among the practitioners around the world, still there are some major concerns about some issues associated with this technique, for instance, premature debonding failures causing delamination of FRP reinforcement from the substrate at relatively low loads.

The Near Surface Mounted (NSM) FRP technique has emerged as a more effective strengthening technique than the EBR technique in many instances because of its ability to gain higher bond strengths and the possibility of precluding or delaying premature debonding failures, which are often observed in the EBR technique (Hassan and Rizkalla, 2003).

1.3 Near surface mounted FRP technique

The NSM FRP technique involves bonding FRP bars into pre-cut grooves in the concrete cover of a structural member to be strengthened, using an adhesive (Figure 1.1). The application of NSM technique covers both reinforced and prestressed concrete structures as well as structures made of other materials, such as timber and masonry. Although only a limited number of research studies on NSM systems are currently available, the research carried out so far indicates that the NSM technique is a promising and effective technique in increasing both flexural and shear capacities of structural members such as beams (De Lorenzis and Nanni, 2001a;2001b; Hassan and Rizkalla, 2004; Nanni *et al.*, 2004).

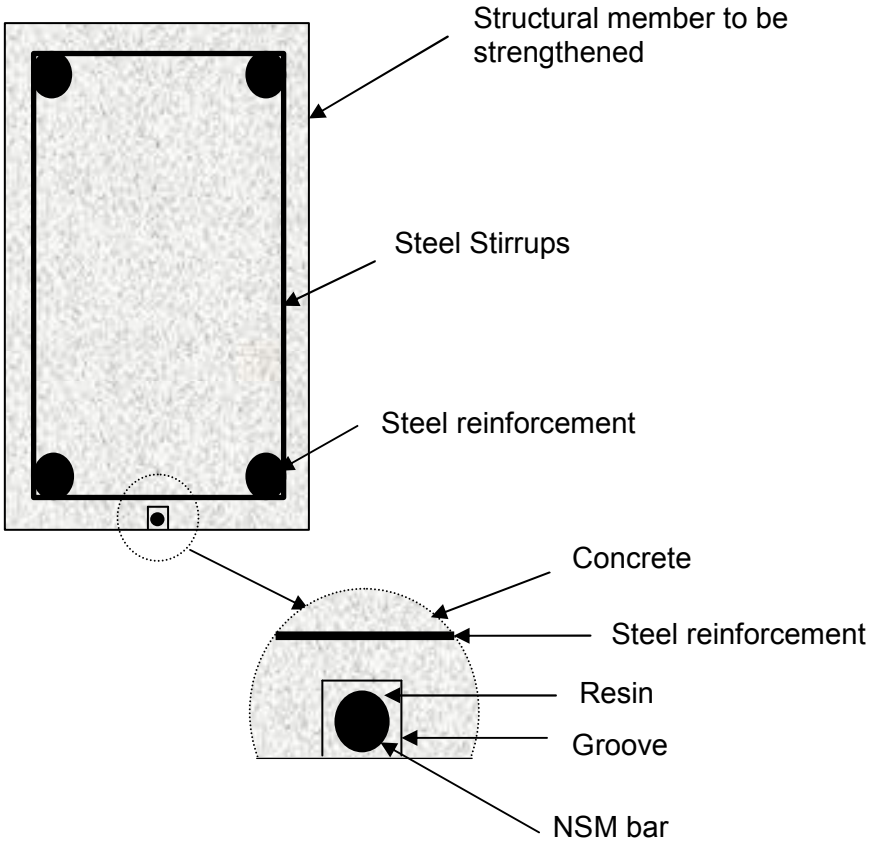

Figure 1.1 - Arrangement of an NSM FRP bar within the concrete cover

The NSM technology offers many advantages over EBR technique, for instance, the NSM technique creates a larger bonded surface area because it is in contact with the resin all round the bar perimeter thereby increasing the bond strength. As the FRP reinforcement is embedded in the concrete cover, it is not susceptible to damages from external sources such as mechanical and environmental impacts. Therefore, this technology becomes particularly important for strengthening of negative moment regions (De Lorenzis and Nanni, 2002) where additional tensile reinforcement should be added to the top side of the concrete member. Unlike in the EBR technique, there is a possibility of anchoring the NSM reinforcement into adjacent concrete members (De Lorenzis and Nanni, 2002). For example, the horizontal NSM rods used for a strengthening application of two reinforced concrete silos have been anchored in to a common wall between the two RC silos (Prota *et al.*, 2003). Since the bond area is much larger than that of EBR systems, there is a possibility of achieving higher strengths or even the ultimate tensile strength of the FRP reinforcement before debonding type failures occur (Hassan *et al.*, 2001).

However, this technique can only be used for structures with a sufficient concrete cover. A major drawback of this technique is the consumption of more time and labour for groove cutting. For example, when strengthening soffits of slabs and beams, it is more difficult and time consuming compared to EBR technology. Moreover, lack of experience and guidelines and the need for further research in certain areas such as bond and anchorage requirements are some other obstacles for the efficient use of this technique.

1.3.1 Experimental investigations of NSM FRP technique

Many researchers have been interested in characterising bond behaviour between NSM FRP rods and concrete and they have performed various bond tests investigating the effect of various bond parameters (Barros *et al.*, 2004; Blaschko and Zilch, 1999; De Lorenzis, 2002; De Lorenzis and Nanni, 2001b; Pickles, 2004; Yan *et al.*, 1999). A detailed review of previous experimental work on NSM FRP technique can be found in Chapter 2.

1.3.2 Applications of NSM FRP technique

Although the near surface mounting of FRP bars is a relatively new technique, the first practical use of near surface mounted steel bars was reported in the late 1940s (Asplund, 1949). The deformed steel bars were mounted and grouted in grooves cut with the aid of a diamond saw, on the concrete cover of a bridge deck (as a remedial action for the settlement of negative moment reinforcement of a bridge in Sweden). First NSM FRP application was reported in 1998 which involved strengthening of Pier 12 of the Naval Station San Diego, CA (USA) (Warren,1998 cited by De Lorenzis (2002)), where NSM CFRP rods were used to increase the capacity of the deck slab in the negative moment regions.

Six cement silos, a cluster of four and a cluster of two, with concrete spalls and radial and circumferential cracking, built over 30 years ago and situated in the Boston area have been repaired with NSM FRP bars (ICRI, 2001). The repair was needed to cater for over 30% of the required steel missing due to design and construction oversights

which limited the full loading of the silos. Another application of the NSM FRP technique is the strengthening of the street level floor of Myriad Convention Centre, Oklahoma City, USA (Hogue *et al.*, 1999), where NSM FRP bars were used for shear strengthening of one of the reinforced concrete joists. Figure 1.2 shows some examples of practical implementation of the NSM technique. Examples of strengthening applications in the UK include use of NSM FRP bars to strengthen top surfaces of slabs at two car parks in Bristol and Liverpool (Farmer, 2003a,b cited by Concrete Society (2004)).

Strengthening of negative moment regions of a bridge deck with NSM FRP bars (Parretti and Nanni, 2004)

Vertically placed NSM bars for shear strengthening (Hogue *et al.*, 1999)

Strengthening of a column with NSM FRP rods (Alkhrdaji *et al.* 1999, cited by De Lorenzis (2002))

Strengthening of a silo using NSM CFRP bars (ICRI, 2001)

Figure 1.2 - Practical uses of NSM FRP technique

1.4 Motivation

As further discussed in Chapter 2, there are still some areas of research needing further investigation such as bond behaviour of various shapes of FRP bars (especially square bars), the effect of internal reinforcement and anchorage length requirements. Furthermore, most of the existing bond models for NSM FRP bars are based on limited test data and are dependent on the type, size and shape of the reinforcement used, and the test conditions of the particular research study. In other words, they are empirical/semi-empirical and can only be applied to specific situations. Therefore, it is required that a generalised model which captures the mechanics of bond behaviour be developed for the design of NSM FRP bars.

1.5 Objectives

The particular objectives of this research project were to;

- carry out small scale pull-out tests to investigate bond behaviour between various shapes of NSM FRP bars and concrete
- Identify the critical failure modes and their underlying mechanics
- develop a rational analytical model to predict bond strength and anchorage length requirements for NSM FRP bars

With the above-mentioned aims, a comprehensive experimental study was undertaken investigating the effect of several bond parameters; bond length, bar shape, bar size, surface texture, groove size, resin type and concrete strength. The results were analysed and analytical models were developed capturing the underlying mechanics and all the details are presented in the following chapters.

1.6 Outline of the contents

The next chapter, Chapter 2, presents a detailed review of literature on bond behaviour between NSM FRP bars and concrete. Chapter 3 consists of the details of the experimental program while Chapter 4 presents and discusses the results of the bond

tests. Chapter 5 presents an analysis of the results and analytical methods to predict the local bond strength. Chapter 6 comprises an analytical solution to the differential equation of bond, employing different bond stress-slip models allowing prediction of the load capacity and the anchorage length requirements. Finally, Chapter 7 presents conclusions and recommendations for further research.

CHAPTER 2 – BOND AND ANCHORAGE BETWEEN CONCRETE AND NSM FPR BARS

Initial attempts of bond analysis of FRP bars were to extend the theories of steel-to-concrete bond with modifications. However, the behaviour of FRP bars is much different to that of steel bars and is controlled by mechanical and geometrical properties of FRP bars. Therefore, when extending the theories and design rules of steel-to-concrete, a critical review is needed to assess the suitability of them for the FRP case. This chapter presents a critical review of the existing literature on bond behaviour between FRP bars and concrete, along with a comparison of the behaviour with bond of steel-to-concrete where appropriate. The bond aspects of both FRP bonded to concrete by the EBR FRP technique and FRP embedded in concrete (bond of FRP reinforced concrete) are discussed where appropriate, while the major emphasis is on bond of NSM FRP bars-to-concrete.

2.1 Introduction to bond behaviour

Bond is the key parameter to ensure composite action between reinforcement and concrete. To secure the bond, avoiding any premature debonding failure, a sufficient anchorage should be provided. The success of a strengthening system is highly dependent on the interfacial bond properties between the reinforcement and the concrete. Therefore, it is of prime importance to investigate the bond between NSM FRP bars and concrete, as the preliminary study in developing rational anchorage models for the NSM FRP technique. To date several experimental studies can be found in the literature on bond behaviour between NSM FRP rods and concrete, which investigate the effect of various parameters such as bond length, surface texture of the bar, type of FRP material, groove properties and type of the groove filling material (Blaschko and Zilch, 1999; Carolin *et al.*, 2001; De Lorenzis, 2002; Perera *et al.*, 2009a; Perera *et al.*, 2008;2009b; Pickles, 2004; Sena Cruz, 2004; Seracino *et al.*, 2007a; Shield *et al.*, 2005; Yan *et al.*, 1999).

2.1.1 Bond action

The bond behaviour of FRP embedded in concrete is supposed to be relevant to that of NSM FRP bars because of the following similarities, even though there are differences in behaviour as the NSM technique involves two interfaces, namely bar-resin interface and resin-concrete interface. The first similarity is that also in the NSM technique, the bar is embedded (in the resin rather than in the concrete). The FRP-to-concrete bond behaviour differs from that of steel-to-concrete, primarily due to the FRP mechanical and geometrical properties. Secondly, in both the FRP reinforced concrete case and the NSM FRP technique case, the reinforcement is of FRP material, causing a similar influence on bond. Therefore, bond of FRP reinforced concrete is reviewed here too.

The basic mechanisms of transfer of stresses through a bonded joint of FRP-to-concrete follow that of steel-to-concrete. As the structure is loaded, the tensile stresses developed in the reinforcement are transferred to the concrete by means of longitudinal shear stresses (bond stresses) developed along the interface between the bar and concrete. Generally, bond stresses along the interface between the reinforcement and the concrete are balanced by three resisting mechanisms, namely the adhesion, the mechanical interlocking, and the friction (Cosenza *et al.*, 1997). The adhesion is the chemical bond between the concrete and the reinforcement and the mechanical interlocking is the resistance caused by the surface deformations of the bar when they interlock with the concrete. During the initial stages of loading the adhesion is the only resistance which exists and as soon as the adhesion fails, either the mechanical interlock or the friction becomes the predominant resisting mechanism. The presence of these mechanisms depends on the surface configuration of the bar. For example, for smooth bars, only two mechanisms, the adhesion and the friction, are present whereas for deformed rods all three mechanisms resist the bond stresses. In deformed steel bars the governing mechanism is the mechanical interlock since the chemical bond is very weak and the ribs are comparatively stiffer than the ribs of FRP bars. For FRP bars with surface deformations, the mechanical interlock and the friction become the primary bond mechanisms and for smooth FRP bars the friction is the primary mechanism, since the chemical bond between concrete and FRP is also very low.

The bond strength of plain bars is generally low as the bond action is primarily dependent on the chemical adhesion and no tensile cracking is likely to occur along the bar so that no radial bond stresses are likely to develop. If the reinforcement includes any surface deformation, for example ribs, then these deformations create radial bond stresses in addition to the longitudinal bond stresses. Initially, the main resisting mechanism is the chemical adhesion and, as soon as it breaks, the resisting mechanism changes to mechanical interlocking and slip increases gradually with the loading. Surface deformations develop bearing stresses and once the principal tensile stress caused by the bearing stresses reach the tensile strength of the concrete, micro cracking takes place and allows the bar to slip. At this moment, radial bond stresses develop and the angle α, between the principal compressive stress and the bar axis changes (initially 45º before the micro-cracking) (Figure 2.1), yielding a relationship of radial bond stress = tangential bond stress x *tan* α. The value of angle α is dependent on the surface texture of the bar (Tepfers, 1973). These radial stresses induce tensile hoop stresses in the surrounding concrete and, if the concrete is not sufficiently confined, splitting cracks will develop longitudinally as they exceed the tensile strength of concrete. The confinement by the surrounding concrete mass, transverse reinforcement and external pressure influence the splitting resistance (fib, 2000). For example, Malvar (1994) stated that bond strength of FRP bars can usually be increased threefold by increasing the confining pressure. However, for a given confinement the bond strength developed by a steel bar was between 1.2 to 1.5 times higher than that of the equivalent FRP bar.

Goto (1971) investigated the cracking characteristics of deformed steel bars and clarified the formation of different kinds of cracks, primary, internal, secondary and longitudinal cracks (Figure 2.2). Goto found that the slope of the internal cracks, the angle at which compressive forces leave the ribs of the deformed bar and spread in to the concrete, were generally within 45º to 80º to the bar axis. Many of the angles were roughly about 60º. Further, Goto observed that the cracking characteristics observed with a deformed steel bar are very different to those observed for a smooth bar. The primary crack spacing of deformed bars was lower than that of smooth bars. However, deformed bars resulted in narrower crack widths than those of smooth bars as the width of a primary crack was roughly proportional to the sum of the adjacent crack spacings on the two sides of the crack.

For a reinforcing bar with a sufficiently strong surface deformation, such as deformed steel bars, and strong confinement, splitting failure can be prevented and the concrete in front of the ribs can crack due to high shear stress concentrations, allowing the reinforcement to pull out. However, this failure mode is less likely to occur in FRP-concrete bond, as surface deformations on FRP bars are less stiff than those on steel bars. Therefore, it is more likely that FRP bars will be pulled out by complete/partial shearing off of bar deformations/successive layers of fibres, as discussed in Section 2.3.1.1. As the surface deformations of FRP bars are generally formed of a resin, the FRP-concrete bond is also dependent on the resin strength. Generally, FRP bars can develop comparable bond strength values to steel bars, being either similar or greater in value (Cosenza *et al.*, 1995; Greco *et al.*, 1998; Malvar, 1994).

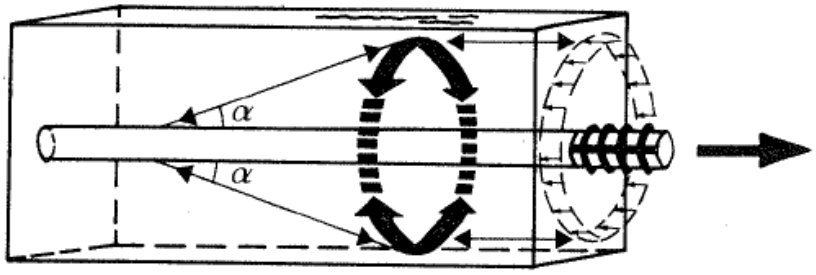

Figure 2.1 - Schematic representation of how the radial bond force components are balanced by hoop tensile stresses in the concrete in the anchorage zone (Tepfers, 1973)

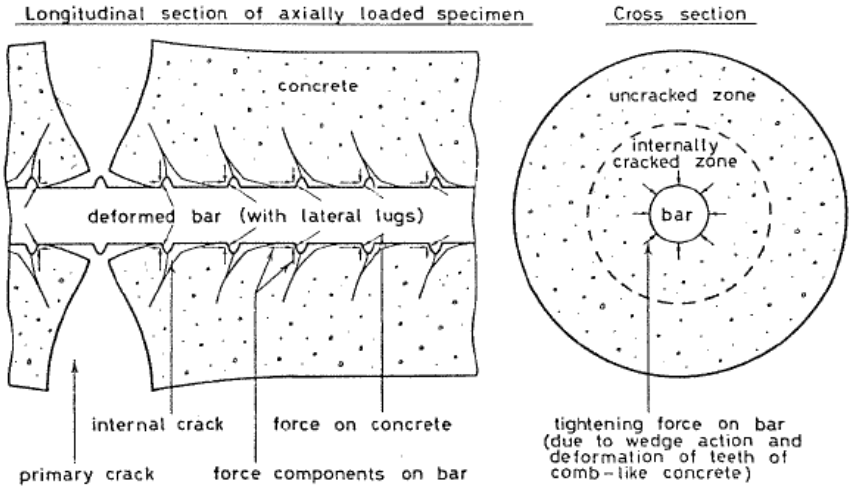

Figure 2.2 - Cracking characteristics of concrete surrounding a deformed steel bar (Goto, 1971)

Tepfers (1998) described the failure modes of bond between FRP and concrete as follows. Firstly, for plain bars, the bond fails along the perimeter of the bar and the bar is pulled out from the concrete and the adhesion between the bar and the concrete or the inter-laminar shear strength of the bar is an important factor in determining the failure. Secondly, it is splitting failure for bars with surface deformations which occurs when the radial component of the bond stress exceeds the tensile strength of concrete. The confinement by the surrounding concrete, the transverse reinforcement and the external pressure are the governing factors in this type of failure. Finally, it is pull-out failure for bars with ribs and strong confinement which has the highest possible bond resistance and the shear strength of the concrete is the important factor in this case. FRP bars can be pulled out by complete/partial shearing off of bar deformations/successive layers of fibres, if the shear strength of the bar deformations/bar layers is lower than the concrete shear strength, as discussed in Section 2.3.1.1.

2.1.2 Bond tests

In general, there are different kinds of bond test such as direct pull-out tests and beam tests which are originally developed for the investigation of bond of steel embedded in concrete. A comprehensive review of test methods used to study bond of FRP embedded in concrete can be found in Nanni *et al.* (1995) comparing FRP-to-concrete bond with steel-to-concrete bond. The list of reviewed test methods includes, concentric pull-out, axial tension, cantilever beam, spliced-reinforcement beam, notched beam, hinged beam and trussed beam. Generally, in direct pull-out tests, the bar is placed concentrically in the concrete block. However, direct pull-out tests with eccentric placement of the bar are used for the estimation of concrete splitting resistance and the cover thickness is usually 1.5 bar diameters (fib, 2000). In general, the results of direct pull-out tests give an upper-bound for the bond stress-slip behaviour as splitting of the concrete is avoided by the thicker concrete cover and confining action of the reaction plate, whereas beam tests show a lower-bound performance caused by possible longitudinal splitting cracks in the concrete in the anchorage zone (Focacci *et al.*, 2000).

Moreover, in a direct pull-out test, the concrete surrounding the bar experiences compressive stresses from the loading face as opposed to the reality where the concrete around the bar would be subject to tensile stresses. Therefore, beam tests are preferred since they give a better indication of the role of the concrete (Yan *et al.*, 1999). However, direct pull-out tests offer some other advantages over beam tests such as an easily manageable size and simplicity. In the existing literature, bond of NSM FRP-to-concrete has been studied using both direct pull-out tests (Blaschko, 2003; De Lorenzis *et al.*, 2002; Pickles, 2004; Seracino *et al.*, 2007b; Shield *et al.*, 2005; Yan *et al.*, 1999) and beam tests (De Lorenzis and Nanni, 2002; Sena Cruz, 2004). A typical direct pull-out and a beam test set-up for NSM FRP bars can be seen in Figure 2.3.

Bond stresses and the slip along a short bond length specimen can be considered to be uniform over the bond length, whereas in a long bond length specimen, there is a significant variation of bond stresses and slip along the reinforcement (Stratford, 2001).

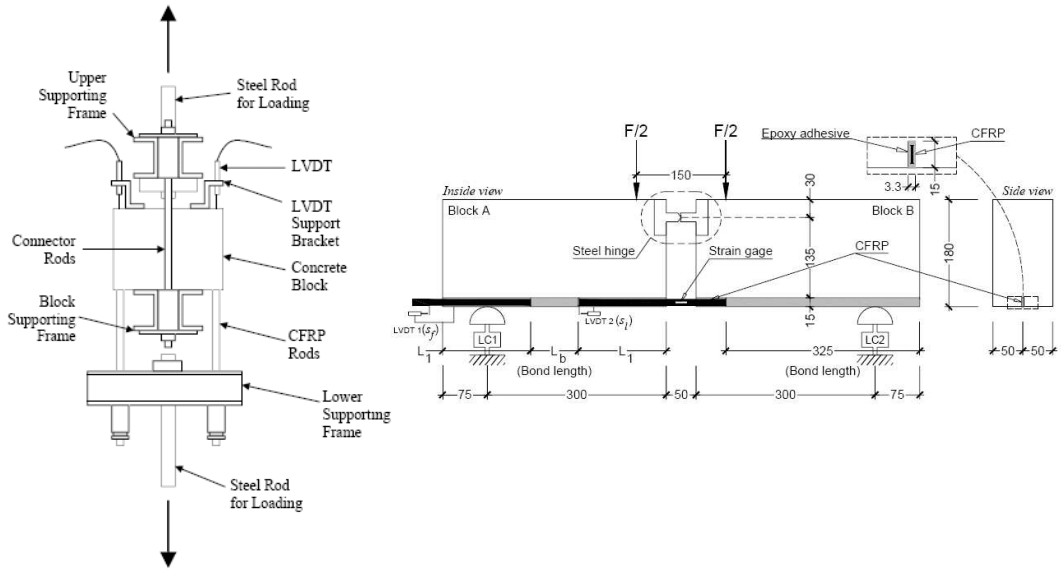

Figure 2.3 - Bond tests for NSM FRP bars: (a) a direct pull-out bond test (Yan *et al.*, 1999) and (b) a beam-type bond test (Sena Cruz, 2004a)

2.1.3 Factors affecting bond between FRP bars and concrete

The bond behaviour of FRP bars to concrete is expected to vary from that of steel-to-concrete, as the key parameters such as mechanical properties of FRP bars and

surface deformations affecting the bond are different. The anisotropic properties as well as a huge variety of FRP bars result in significant variation in bond behaviour of FRP bars to concrete, unlike steel. Several influencing factors such as bar shape, bar deformations, bar diameter, low axial elastic modulus, transverse modulus, transverse pressure and concrete strength exist and the effect of these factors can be found in detail in fib (2000) and Tepfers (1998). Surface deformations on FRP bars are less stiff than those on steel bars so that they do not produce as high stress concentrations in concrete as steel bars do. Consequently, FRP bars induce reduced micro-cracking in the concrete and a reduced tendency to split the concrete cover, unlike steel bars. However, FRP bars may have a splitting tendency superior to steel bars due to slip promoted by glossy surface deformations (Tepfers, 1998). When the bar slips, the abrasion of the concrete surface results in a reduction in the radial stresses, and thereby reduces the bond stresses too. As the bar goes in to tension, the lateral contraction (due to Poisson's effect) also reduces the bond stresses. In the case of steel bars at yield, the radial contraction occurs significantly, resulting in a reduction of the transverse stresses and thereby transferring only low bond (Lundgren, 2005).

Various parameters such as bond length, bar texture, fibre type, concrete strength, resin type, groove size, surface condition of the groove and load history have been investigated under the research studies on NSM FRP-to-concrete bond behaviour, and are listed in Table 2.1.

2.2 Previous research on bond behaviour between NSM FRP and concrete

2.2.1 Previous experimental work

Table 2.1 summarizes the previous work on bond, anchorage, shear and flexural behaviour of NSM FRP bars, from small scale bond tests to large scale beam tests. In most of those studies, Carbon was selected as the fibre material due to its superior material properties, such as high ultimate strength and high stiffness. Epoxy resin was the adhesive used in many cases, except in two cases (Carolin *et al.*, 2001; De Lorenzis, 2002), where cement grout was used as a bonding agent. Carolin *et al.*

(2001) found that cement grout performed well as an adhesive, and obtained comparable bond values with epoxy resin, in contrast to the findings of De Lorenzis (2002) where cement grout was weak as a structural bonding agent. Therefore, it seems that further research in this area would be very helpful in determining cheaper alternatives to epoxy resins.

So far, a reasonable amount of experimental study has been reported on bond behaviour between NSM FRP rods and concrete. Limited information is available on anchoring methods for NSM rods in both flexural/shear strengthening cases. De Lorenzis and Nanni (2001b) proposed that in shear strengthening, the anchoring of NSM rods in the beam flange as a continuation of the vertical NSM bars placed on the sides of the web is an effective way of anchoring, and would potentially be capable of precluding debonding of FRP rods due to the splitting of epoxy cover. Further, they revealed that sufficiently spaced 45º inclined rods also contribute in preventing debonding failures in shear strengthening. Also, it is of interest to examine the possible ways of anchoring NSM FRP shear reinforcement in rectangular beams because this method (anchoring the bars in the flange), is only applicable to T-shaped cross-sections.

De Lorenzis (2002)'s experimental series of tests on bond behaviour act as a sound foundation for the investigation of bond and anchorage of NSM FRP bars, providing valuable information of bond behaviour and effectiveness of NSM FRP bars. The effect of many important parameters such as bond length, groove size, surface configuration of the bars and groove filling material were examined. Another major experimental investigation on bond of NSM FRP bars is the study of Sena Cruz (2004) which investigated variables such as bond length, concrete strength and loading history. However, in both studies beam type bond tests were carried out ensuring that no flexural cracking occurred (therefore omitting internal steel reinforcement) before the bond failure so that pure bond behaviour could be investigated. Consequently, the observed failure modes in these studies were different to those observed for flexurally strengthened beams with NSM FRP bars (refer to Sections 2.2.2 and 2.2.3). Therefore, results such as bond stress-slip curves of NSM FRP bond tests carried out in these investigations cannot be directly transferred into predictive models for actual beams where presence of flexural/shear cracks alters the pure bond stress-slip distribution significantly.

A limited amount of research studies have been reported investigating the effect of internal reinforcement (De Lorenzis, 2002; De Lorenzis and Nanni, 2001b; Hassan *et al.*, 2001). According to the results of these studies, it seems that there is a considerable effect due to the internal reinforcement on bond behaviour which could even change the mode of failure. However, a clear relationship between the internal reinforcement and bond behaviour has not yet been developed.

Both bond test set-ups used by De Lorenzis (2002) were capable of producing reliable data and the new test set-up overcame the limitations of the previous set-up. For instance, the new test set-up had the ability to monitor the loaded end slip, an easily manageable size and the possibility of visual inspection of the bonded joint during loading.

In most of the studies listed in Table 2.1, the bond failed prior to tensile failure of the bar, leading to the inefficient use of the FRP bar. In the experiments of De Lorenzis and Nanni (2002) the ultimate loads of only up to 33% of the full strength of CFRP bars and only up to 60% of the ultimate tensile strength of GFRP bars could be utilized. The experiments of Hassan *et al.* (2001) recorded about 40-45% of the ultimate strength of the bars, whereas in their second series of tests on CFRP rectangular bars (strips), FRP rupture occurred, indicating 100% usage of the tensile capacity of the strips. De Lorenzis (2002) observed bond capacities up to 60% of the tensile strength using CFRP bars, and up to 64% using GFRP bars. Blaschko (2003) also reported tensile failure of NSM CFRP strips. The achievement of different percentages of the tensile capacity of NSM FRP reinforcement, up to 100%, implies that debonding can be completely avoided if a sufficient anchorage is facilitated.

Reference	Blaschko and Zilch (1999)		Blaschko (2003)	Yan *et al.* (1999)	Carolin *et al.* (2001)	Hassan *et al.* (2001)	
	Series 1	**Series 2**				**Series 1**	**Series 2**
Type of FRP	CFRP	CFRP	CFRP	CFRP	CFRP	CFRP	CFRP
Type of test/type of strengthening	Bond tests	Flexural strengthening	Bond tests	Bond tests	Flexural strengthening	Flexural strengthening	Flexural strengthening
Shape of bar	Rectangular	Rectangular	Rectangular	Circular	Square	Circular	Rectangular
Diameter of bar (mm)	N/A	N/A	N/A	11	N/A	10	N/A
Depth of bar (mm)	25	25	20	N/A	10	N/A	25
Width of bar (mm)	1.2	1.2	1-2	N/A	10	N/A	1.2
Depth of groove (mm)	N/A	26	N/A	19	N/A	16	25
Width of groove (mm)	N/A	3	N/A	14	N/A	30	5
Surface configuration of bar	N/A	N/A	N/A	Sand blasted	N/A	Deformed	N/A
Variables Examined	Strengthening technique	Strengthening technique	Bond length, size and material properties of the strip, concrete strength, surface texture, type of loading, edge distance	Bond length, concrete strength	Type of adhesive (epoxy and cement grout), bond length, no. of bars, high strength and high modulus CFRP bars	Type of epoxy, bond length	Bond length
Modes of failure	N/A	Rupture of FRP, shear failure in concrete	Tensile rupture, edge concrete splitting, cohesive shear failure in the adhesive	Concrete fracture, bar-resin interface failure	Fibre failure, combinded fibre failure and concrete crushing, Bond-slip failure	Splitting of concrete cover followed by complete debonding of the bars	Splitting of concrete cover, rupture of FRP
Groove filling material	Epoxy	Epoxy	Epoxy	Epoxy	Epoxy, cement grout	Epoxy	Epoxy
Loading	Double-shear	3-point bending	Direct pull-out	Direct pull-out	4-point bending	3-point bending	3-point bending
Presence of steel reinforcement	N/A	N/A	N/A	N/A	Flexural/shear reinforcement	Flexural/shear reinforcement	Flexural/shear reinforcement
Comments on findings	Good evidence for greater anchoring capacity and increased ductility in the NSM technique compared to the EBR technique	Evidence for possibility of full bond development for CFRP strips, increased strength and ductility in beams strengthened using NSM technique compared to that strengthened using the EBR technique	Shows the full development of bond is possible for CFRP strips, evidence of edge concrete splitting when the edge distance is insufficient	A preliminary study which provides minor results	Evidence of all beams failed in FRP rupture showing a ductile response, first record of using NSM square bars, positive results on using cement grout as a bonding agent	Provides evidence of minor effect of type of epoxy adhesive on ultimate capacity	Shows the possibility of full bond development for CFRP strips for bond lengths ranging from 850mm to 1200mm

Reference	De Lorenzis and Nanni (2001b)	De Lorenzis and Nanni (2002)	De Lorenzis (2002)			Sena Cruz (2004)	Pickles (2004)
			Bond tests	Flexural tests			
Type of FRP	CFRP	CFRP/GFRP	CFRP/GFRP	CFRP/GFRP	CFRP/GFRP	CFRP	CFRP
Type of test	Shear strengthening	Bond tests	Bond tests	Flexural strengthening	Flexural strengthening	Bond tests	Bond tests
Shape of bar	Circular	Circular	Circular	Circular	Circular	Rectangular	Circular
Diameter of bar (mm)	9.8	9.5/13	7.5/9.5	9.5/13	8	N/A	8
Depth of bar (mm)	N/A	N/A	N/A	N/A	N/A	10	N/A
Width of bar (mm)	N/A	N/A	N/A	N/A	N/A	1.4	N/A
Depth of groove (mm)	19	13,16,19,25	10,12,14,15,16,18,20,24	19,25.4	16	15	12,13,16,18.5,20,30
Width of groove (mm)	19	13,16,19,25	10,12,14,15,16,18,20,24	19,25.4	16	3.3	12,13,20
Surface configuration of bar	Deformed	Deformed/sand blasted	Spirally wound, ribbed	Sand blasted, deformed	Spirally Wound, sand blasted	N/A	Spirally wound and sand coated
Variables Examined	Spacing of bars, inclination of rods, anchorage in flange, presence of internal steel stirrups	Bonded length, size of groove, type of FRP material, surface configuration of bar, diameter of rod	Bonded length, size of groove, surface configuration of bar, groove filling material, surface condition of groove	Type of FRP material, amount of FRP	Internal steel reinforcement ratio, FRP reinforcement ratio	Bond length, concrete strength, load history	Bonded length, groove size, shape of the groove
Modes of failure	Splitting of epoxy cover, splitting of concrete cover	Splitting of epoxy cover, concrete cracking, pull-out failure	Splitting of epoxy cover, failure at epoxy-concrete interface, failure at mortar-concrete interface, failure at rod-mortar interface	Debonding after steel yielding	Concrete crushing after steel yielding, debonding after yielding, concrete crushing after steel yielding followed by secondary debonding	Bar-resin , resin-concrete interface failures	Splitting of epoxy cover and surrounding concrete, pull-out failure
Groove filling material	Epoxy	Epoxy	Epoxy, cement mortar	Epoxy	Epoxy	Epoxy	Epoxy
Loading	4-point bending	4-point bending	Direct pull-out	4-point bending	4-point bending	4-point bending	Direct pull-out
Presence of steel reinforcement	Flexural/shear reinforcement	N/A	N/A	Flexural/shear reinforcement	Flexural/shear reinforcement	N/A	N/A
Comments on findings	A good initial study showing the effectiveness of NSM technique in shear strengthening, investigating the effect of different reinforcement orientations	A comprehensive study investigating several bond parameters	The first foremost laboratory investigation of NSM technique involving wide range of critical bond parameters, revealing important results on bond behaviour of NSM FRP bars, as well as laboratory tests on flexural and shear strengthening using NSM technique, evidence of CCSF in flexural tests			Another major investigation of bond of NSM CFPR strips	First record of investigating different groove shapes apart from square or rectangular shape such as trapezoidal grooves

Reference	Shield *et al.* (2005)		Teng *et al.* (2006)		Seracino *et al.* (2007b)
	Series 1	**Series 2**	**Bond tests**	**Flexural tests**	
Type of FRP	CFRP	CFRP	CFRP	CFRP	CFRP
Type of test	Small scale bond tests	Large scale bond tests	Bond tests	Flexural tests	Bond tests
Shape of bar	Rectangular	Rectangular	Rectangular	Rectangular	Rectangular
Diameter of bar (mm)	N/A	N/A	N/A	N/A	N/A
Depth of bar (mm)	16	16	16	16	12-30
Width of bar (mm)	2	2	4	4	2-101
Depth of groove (mm)	19	19	22	22	N/A
Width of groove (mm)	6.4	6.4	8	8	N/A
Surface configuration of bar	N/A	N/A	Peel-ply treatment	Peel-ply treatment	N/A
Variables Examined	Type of adhesive	Type of adhesive, tape orientation, vibration during cure of the adhesive	Bond length	Bond length	Aspect ratio of the strip
Modes of failure	Failure in adhesive, failure in concrete, FRP rupture, failure at interfaces	Failure in adhesive, failure in concrete, FRP rupture, failure at interfaces	Bar-resin interface failure, shear-tension fracture within the concrete prism	Concrete cover separation failure, localized splitting of the epoxy cover, debonding at the resin-concrete interface	Resin-concrete interface failure
Groove filling material	Epoxy	Epoxy	Epoxy	Epoxy	Epoxy
Loading	Direct pull-out	Double shear	Single shear push-pull	4-point bending	Single shear push-pull
Presence of steel reinforcement	N/A	N/A	N/A	Flexural/shear reinforcement	N/A
Comments on findings	Extensive study on effect of adhesive type considering seven different adhesives, revealing that even for adhesives with similar shear strengths, bond behaviour differs significantly		Important results showing a variation between failure modes observed in bond tests to that observed in beams strengthened using NSM technique, evidence of CCSF in flexural tests		Evidence of cohesive shear failure within the concrete substrate

Table 2.1 - Summary of previous research work on NSM FRP reinforcement

(Note: N/A- Non Applicable or Not Available and CCSF-Concrete Cover Separation Failure)

However, tensile rupture is mostly achievable so far for rectangular strips, which has an increased bonded surface area compared to other shapes of bars, for a given cross-sectional area. Also, rectangular strips are less likely to induce splitting of the resin cover as the majority of the transverse bond stresses are resisted by the thicker lateral sides of the groove (De Lorenzis and Teng, 2007). Limited research has been reported on use of square NSM FRP bars (Carolin *et al.*, 2001), however, tensile rupture of square bars has been reported in that particular study, where the beam tests with full anchorage were quite ductile with large deformations before the ultimate failure, even though a linear elastic material has been used for strengthening.

2.2.2 Debonding mechanisms of NSM FRP systems - bond tests

Several debonding mechanisms have been reported from bond tests carried out on NSM FRP bars (Blaschko, 2003; De Lorenzis, 2002; Sena Cruz, 2004; Seracino *et al.*, 2007b). They include failure at the bar-resin interface, resin-concrete interface failure, resin splitting and edge concrete splitting.

2.2.2.1 Bar - resin interface failure

Bar-resin interface failure can occur as one of two modes, either pure interfacial failure or cohesive shear failure in the resin. Generally, pure interfacial failure occurs when the surface texture of the bar is not able to provide sufficient mechanical interlocking so that the bond mechanism relies only on the chemical adhesion initially and on friction after the onset of slip. This type of failure can be identified by observing the absence of resin attached to the bar surface, whereas the cohesive shear failure in the resin can be identified by the presence of resin attached on both the bar and concrete. This cohesive shear failure occurs when the shear strength of the resin is exceeded, and has been observed for NSM CFRP strips (Blaschko, 2003).

2.2.2.2 Resin - concrete interface failure

Resin-concrete interface failure can also occur in two ways, namely pure interfacial failure or cohesive shear failure in the concrete. Pure interfacial failure occurs when the

interface is weak, for example, due to the smooth surface of pre-formed grooves, or due to impurities remaining on the interface, so that the resin-concrete interface becomes the weakest or critical element amongst the possible failure planes/surfaces. However, it is possible that failure may take another form even with the pre-formed grooves, because the failure depends on other properties, such as bar surface deformations and groove dimensions. For spirally-wound bars or ribbed bars with low rib protrusions, pure resin-concrete interfacial failure has been found to be the critical failure mode independent of the groove size, whereas for bars with high rib protrusions, this mode has been found to be critical only for grooves larger than a minimum size. For low groove sizes, splitting of resin cover has been shown to occur (De Lorenzis and Teng, 2007). Cohesive shear failure in the concrete has been observed in bond tests on NSM FRP strips by (Seracino *et al.*, 2007b). This failure occurs when the shear strength of the concrete is exceeded.

2.2.2.3 Resin splitting

Longitudinal resin splitting can occur for deformed (ribbed and spirally wound) round bars (De Lorenzis and Teng, 2007). It can involve pure resin splitting or be accompanied by fracture in the concrete along inclined planes. This form of failure is induced by the radial component of the bond stresses. These stresses are balanced by the hoop tensile stresses in the resin cover so that splitting occurs once the tensile strength of the resin is exceeded. The mechanics of cover splitting failure in NSM systems are similar to that of steel deformed bars embedded in concrete. The concrete surrounding the groove is also subject to tensile stresses and will eventually fail when the tensile strength of the concrete is exceeded.

2.2.2.4 Edge concrete splitting

Splitting of the edge concrete occurs when a NSM bar is close to the edge of the concrete specimen (Blaschko, 2003) and it can be avoided by the provision of a minimum edge distance.

2.2.3 Debonding mechanisms of NSM FRP systems - flexurally strengthened beams

Although NSM FRP systems are less susceptible to debonding than externally bonded FRP systems, reinforced concrete beams strengthened with NSM FRP systems may still fail by various debonding mechanisms. It has been shown that debonding mechanisms of beams strengthened with externally bonded plates, such as intermediate crack debonding due to flexure, plate-end debonding due to curvature and critical diagonal crack induced debonding are also applicable to beams strengthened with NSM FRP bars (Oehlers *et al.*, 2004).

Concrete cover separation failure is one of the most common failure modes observed in EBR systems (Smith and Teng, 2002). This failure mode was also observed in beams strengthened with NSM systems (Corden *et al.*, 2008; De Lorenzis, 2002; Soliman, 2008; Teng *et al.*, 2006). The fundamental difference is that this failure mode is not just a local failure of the bonded joint, but it is a structural failure involving interaction between both the NSM FRP-concrete interface and the steel-concrete interface through flexural/shear cracking (De Lorenzis, 2002). Debonding failures observed in beam tests differ greatly from those observed in bond tests due to concrete cracking in the cover region, i.e. the presence of flexural and flexural-shear cracks altering the bond stress distribution. Therefore, analytical models obtained from bond tests cannot be directly transferred to predictive models for the beam tests (Teng *et al.*, 2006). There is still limited understanding of the mechanics of debonding in beams strengthened with NSM FRP systems and the interaction of bond stresses with flexural/shear cracks is yet to be fully investigated.

2.3 Bond analysis

The bond analysis of FRP bars-to-concrete has been approached through the methods of analysing steel-to-concrete bond. The three-dimensional problem of reinforcement-to-concrete bond is usually solved analytically by decomposing the problem into the bond in the longitudinal plane and the bond in the transverse plane, or just focusing on

the longitudinal plane problem. Various finite element bond models for FRP bars are also available to-date and can be found in fib (2000).

2.3.1 Bond modelling in the longitudinal plane

The distribution of bond stresses along steel reinforcement has been modelled by Tepfers (1973) using slip-modulus theory. In the slip-modulus theory, a linear relationship between the local bond stress and the local slip is assumed. In recent years, simple linear models and non-linear bond stress-slip relationships have been employed in bond modelling to solve the differential equation of bond (Figure 2.4), considering equilibrium of an infinitesimal element of length *dx*. Several empirical non-linear bond stress-slip relationships are available in the literature and some of the most relevant analytical expressions for FRP bars are discussed here.

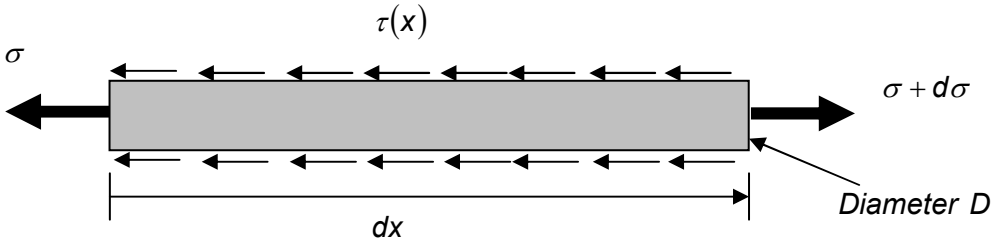

$$\tau(x) = \frac{D}{4}\frac{d\sigma(x)}{dx}$$

Figure 2.4 - Differential equation of bond

2.3.1.1 Local bond stress - slip relationships

The most important outcome of a bond test is the local bond stress-slip (τ - s) relationship. Generally, the local bond stress-slip curves are determined from strain gauge measurements along the FRP reinforcement and measured slip values. For short bonded lengths (usually up to five times the diameter), the local bond stress and the local slip can be approximated by the average bond stress and the average slip between the loaded end and the free end slips. Once the experimental τ - s relationship is obtained, it is then modelled using an analytical expression. Several researchers have come up with various equations for analysing the bond of steel-to-concrete and FRP-to-concrete (Cosenza *et al.*, 1997; Eligehausen *et al.*, 1983; Malvar,

1994). Some of the expressions for FRP-to-concrete bond have been derived by modifying the existing models for steel-to-concrete bond, for example, the modified BEP model (Cosenza *et al.*, 1997).

Stratford (2001) identified three zones in a general τ - s relationship, namely a primary zone with an ascending branch where the primary bond mechanism exists, a degradation zone (degradation of the primary bond mechanism) with a descending branch and a secondary zone with the residual bond stresses acting as the secondary bond mechanism. Degradation of the primary bond mechanism is generally brittle for FRP bars so that the degradation zone is generally short. The bond stress-slip relationships available for bond between steel and concrete provide a foundation for the modelling of bond between FRP and concrete. However, the use of available bond models developed for steel bars cannot offer the optimal solution as FRP and steel have different material properties and bond failure modes. A general theoretical bond stress vs. loaded end slip curve, as shown in Figure 2.5, can be used to describe the interaction between the FRP bar and the surrounding concrete and the resulting bond mechanisms (Achillides *et al.*, 1997).

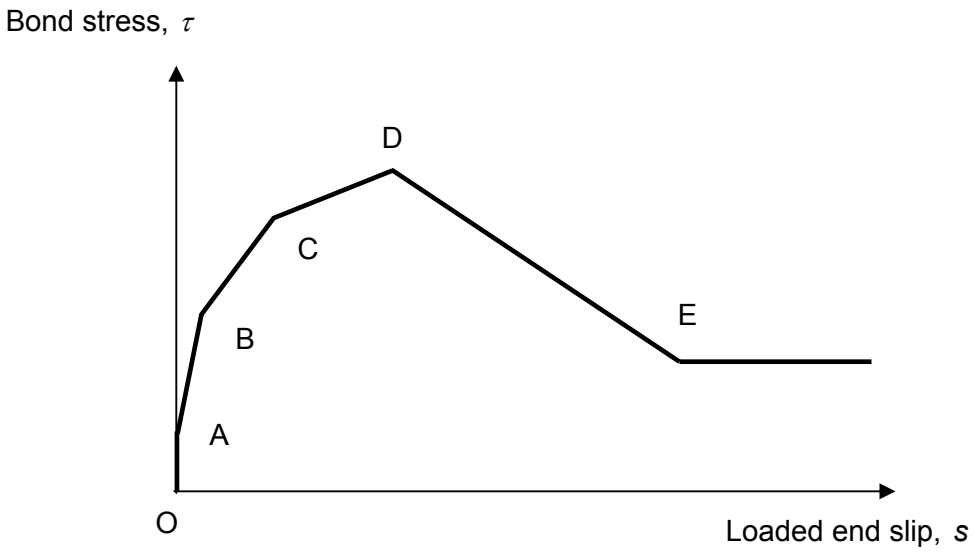

Figure 2.5 - A general bond stress vs. loaded end slip curve for FRP bars (Achillides *et al.*, 1997)

- **Segment OA** - During the early stages of loading, the main bond resisting mechanism is the chemical adhesion and there is no measurable slip.

- **Segment AB** - At point A, the chemical adhesion breaks down and the resisting mechanism changes to mechanical interlocking between bar deformations and the surrounding concrete. There are stress concentrations near the tips of the bar deformations and once the principal tensile stresses caused by the bond stresses reach the tensile strength of concrete, micro-cracks initiate at the tips of the bar deformations and these allow the loaded end of the bar to slip (point B). As the bar deformations of the FRP bars are softer than those of steel bars, initiation of these micro-cracks is delayed relative to the steel case (fib, 2000).

- **Segment BC** - At this stage, the bearing stresses from the bar deformations to the concrete increase considerably as the slip increases, and the radial component of these bond stresses are balanced by tensile stress rings in the concrete. Factors such as splitting resistance from the surrounding concrete mass, transverse reinforcement and external pressure are decisive at this stage. If there is inadequate concrete confinement when the principal tensile stress equals the tensile strength of the concrete, splitting cracks will develop parallel with the bar (point C).

- **Segment CD** - If there is sufficient splitting resistance from the surrounding concrete, the splitting mode of failure is prevented and the bond strength can be further increased up to the maximum achievable bond strength (point D). At this point, both the loaded end and the free end of the bar are slipping and bond stiffness is significantly decreased. Depending on the relative magnitude of concrete strength compared with the shear strength of bar deformations, four modes of bond failure are identified (fib, 2000) as:

    1. Concrete shear failure - The concrete in front of the bar deformations is crushed when the shear strength of concrete is exceeded and this mode is similar to that observed for deformed steel bars.

    2. Shearing off of part or all of the bar deformations on the bar surface - The failure is determined either by the inter-laminar shear strength between the

successive layers of fibres or by the shear strength of the bar deformations, which is more likely to be controlled by the resin shear strength as the bar deformations are mainly formed by resin. This type of bond failure cannot happen in the case of bond of steel-to-concrete due to the high stiffness of steel, and constitutes the highest possible bond resistance of a FRP bar.

3. Combined mode - A combined mode of failure of the above two is likely to happen for intermediate levels of concrete strength.

4. Squeeze through - Due to the low transverse stiffness, the bar can squeeze through the concrete and the ultimate bond resistance is provided by the friction through the wedging of the bar deformations and the concrete, and the bond is much more ductile in this case.

- **Segment DE** - After the ultimate bond resisting mechanism breaks (point D), the bond stress decreases as the slip increases progressively, and it reaches the residual bond resistance level (point E). The residual bond strength depends on the frictional action of the failure interface.

2.3.1.2 Bond models for the longitudinal plane

The simplest form of bond model used to simulate the actual bond stress-slip behaviour of FRP bars is the bi-linear relationship shown in Figure 2.6(a) (Neubauer and Rostasy, 1997; Yuan *et al.*, 2004). However, a linear relationship for the ascending branch cannot be that accurate for modeling of long bond lengths as there is a significant variation in bond stresses along the bond length (Stratford, 2001). Some later studies have simplified it further into a uni-linear model (shown dashed in Figure 2.5(a)) based on the observation that the slip at the maximum bond stress (s_1) is much smaller than the ultimate slip (s_m) so that the idealization has little effect and will give a slightly conservative value of the debonding resistance (Chen *et al.*, 2007; Mohamed Ali *et al.*, 2006). Further, the area under both curves, which is the fracture energy, is the same and hence, has no effect on the predicted debonding resistance (Seracino *et al.*, 2007b).

One of the most commonly used empirical bond stress-slip relationships to model the steel-to-concrete bond is Bertero-Eligehausen-Popov (BEP) model (Eligehausen *et al.*, 1983) (Figure 2.6(b)). The ascending branch of the BEP model is given by,

$$\left(\frac{\tau}{\tau_1}\right)=\left(\frac{s}{s_1}\right)^{\alpha} \tag{2.1}$$

where τ_1, s_1 and α are curve-fitting parameters. Then there is a constant bond value up to a slip value of s_2 and then the bond stress linearly decreases to the bond value corresponding to s_3. After this, the bond stresses due to friction remain constant for slip values over s_3.

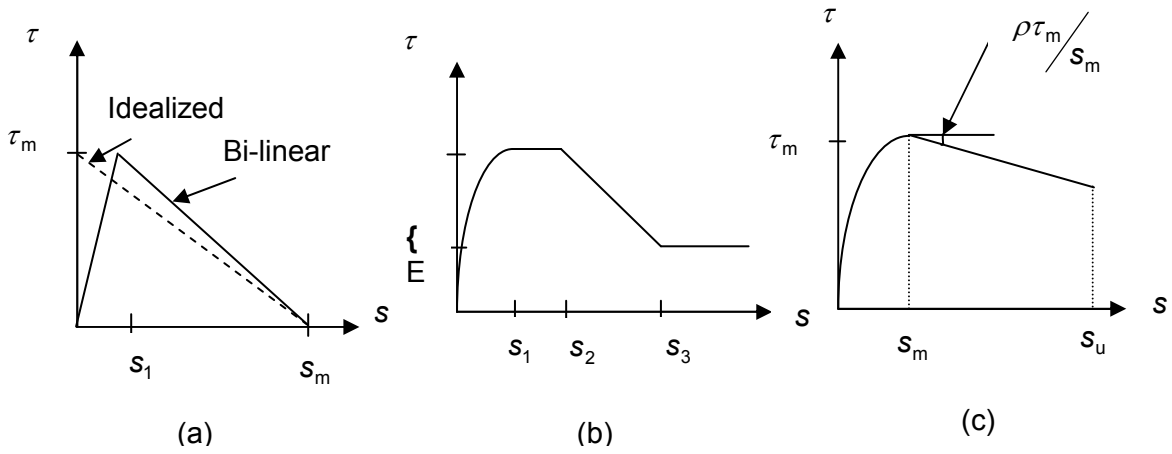

Figure 2.6 - Bond models: (a) bi-linear model, (b) BEP model and (c) MBEP model

Malvar (1994) proposed a single equation to reproduce the entire bond-slip behaviour by,

$$\left(\frac{\tau}{\tau_m}\right)=\frac{\left[F\left(\frac{s}{s_m}\right)+(G-1)\left(\frac{s}{s_m}\right)^2\right]}{\left[1+(F-2)\left(\frac{s}{s_m}\right)+G\left(\frac{s}{s_m}\right)^2\right]} \tag{2.2}$$

where $\tau_m/f_t = A + B\left(1-exp\left[-\left(C\sigma/f_t\right)\right]\right)$, $s_m = D + E\sigma$ and τ_m, s_m, σ and f_t are the peak bond stress and slip at peak bond stress, confining axisymmetric radial pressure and tensile strength of concrete, respectively. A, B, C, D, E, F and G are

empirical constants determined for each bar type. The work involved an investigation of bond characteristics of GFRP bars with different surface configurations, and the influence of confining pressure on bond behaviour. The local bond stress-slip data and bond stress-radial deformation data were obtained for different confining pressures. The findings revealed that the radial pressure has a significant effect on bond strength, and by increasing the radial pressure bond strength can be increased threefold.

Cosenza *et al.* (1995) proposed a new model, named the Cozensa-Manfredi-Realfonzo (CMR) model which claimed to be better in defining the ascending branch of the bond-slip behaviour of FRP to concrete, and is given by,

$$\left(\frac{\tau}{\tau_m}\right)=\left[1-exp\left(-\frac{s}{s_r}\right)\right]^{\alpha} \tag{2.3}$$

where τ_m is the peak bond stress and s_r and α are curve-fitting parameters. Cosenza *et al.* (1995) compared the experimental results with the BEP, Malvar and CMR models and concluded that the Malvar model is less reliable compared to the other two models, that the CMR model has the closest agreement with the experimental results in the region of the ascending branch, while the BEP model shows good agreement with the experimental results throughout all regions.

Cosenza *et al.* (1996) modified the BEP model which was originally developed to model the concrete to steel bond, for the modelling of FRP to concrete bond. The Modified Bertero-Eligehausen-Popov (MBEP) model has three branches, eliminating the post-peak bond stress plateau of the four branched BEP model, as shown in Figure 2.6(c). The plateau was eliminated as the experimental results did not match the analytical curves, with the curves being more similar without the plateau. The MBEP model has an identical ascending branch as in Equation (2.1) and a linear descending branch given by,

$$\left(\frac{\tau}{\tau_m}\right)=1-\rho\left(\frac{s}{s_m}-1\right) \tag{2.4}$$

Malvar *et al.* (2003) modified the CMR model by introducing a non-dimensional parameter, β, replacing s_r by s_m/β where s_m is slip at peak bond stress. Malvar

analysed bond test results for four types of FRP bars with different deformation heights and deformation spacings using two bond models, namely the BEP model and the Modified CMR (MCMR) model. The local bond stress-slip and bond stress-radial displacement curves were obtained for various levels of radial confining pressure. Only the ascending branch of the τ - s relationship, i.e., the service state level was modelled. The peak bond stress and the corresponding slip were defined as a function of the confining pressure, σ, as follows.

$$\left(\frac{\tau_m}{f_t}\right) = A + \frac{B\sigma}{f_t} \tag{2.5a}$$

$$\left(\frac{s_m}{\phi}\right) = C + \frac{D\sigma}{f_t} \tag{2.5b}$$

where f_t is the tensile strength of concrete, ϕ is the nominal bar diameter, and A, B, C and D are empirical constants for each bar type.

Some of the above-mentioned bond models have also been used to model the bond stress-slip behaviour of NSM FRP bars. De Lorenzis (2002) modelled local bond stress-slip curves of NSM deformed FRP bars using the MBEP model. In modelling of bond for specimens which failed at the resin-concrete interface, the ascending branch was modelled using the MBEP model, while for the descending branch, the following equation was proposed,

$$\left(\frac{\tau}{\tau_m}\right) = \left(\frac{s}{s_m}\right)^{\alpha'} \text{ for } s \geq s_m \tag{2.6}$$

which is identical to the equation of the ascending branch, but replacing α with a negative value, α'.

τ_m, s_m, and α' were calibrated by best fitting the experimental results. Sena Cruz and Barros (2004) used the MBEP model to reproduce the bond behaviour of NSM FRP bars to concrete up to the peak bond stress while the post-peak branch was modelled using the analytical expression proposed by De Lorenzis *et al.*(2002). Focacci *et al.*(2000) defined a numerical method to calibrate parameters of any τ - s relationship. The method involves deriving the theoretical relationships between the applied pull-out load and the loaded end slip and that between the applied pull-out load and the free

end slip. By best fitting the theoretical curves with the experimental curves, the unknown bond parameters are obtained. Even though the method is applicable to any bond length, the most consistent results have been obtained for long bond lengths. Sena Cruz and Barros (2004) used this numerical method in finding the parameters of analytical τ - s relationships of NSM FRP bonded joints.

The bond parameters of the available analytical bond stress-slip relationships are generally found by best fitting the experimental curves or by various numerical and analytical methods involving use of experimental curves, for example, the numerical method of Focacci *et al.*(2000). Furthermore, the same analytical expression is not suitable for every bonded joint, i.e. applicability of an analytical expression to model a bonded joint is dependent on various factors such as type of FRP bar, surface texture and bond length. Therefore, bond analysis of FRP bars involves lots of influencing factors and the calibrated bond parameters are specific to the particular bonded joint. Therefore, generic analytical expressions/bond models are required to be developed based on the mechanics of bond behaviour.

2.3.2 Bond modelling in the transverse plane

The well-known theoretical model of Tepfers (1973) predicts the splitting resistance of steel-to-concrete bond, and relates the transverse and longitudinal bond modelling to each other, clarifying their mutual influences (De Lorenzis, 2002). Tepfers (1973) states that when the principal tensile stress caused by bond stresses reaches the tensile strength of concrete, micro-cracking starts and from then on bond stresses start radiating outwards from the bar. The angle between the bond forces and the bar axis, α, (Figure 2.1) depends on the direction of ribs in relation to the bar axis, rib face angle, etc. The radial stresses induce tensile hoop stresses in the concrete and will eventually cause splitting cracks along the anchored bar in the concrete cover. In the theoretical model, the radial stress on the concrete is regarded as a hydraulic pressure against a thick-wall concrete ring, and the concrete ring is assumed to approximate the effect of the surrounding concrete. The wall thickness of the concrete ring is determined by the thinnest part of the concrete cover.

A lower-bound to the cover splitting resistance was calculated assuming that the concrete acts entirely elastically, and the ultimate capacity is reached when the principal tensile stress exceeds the tensile strength of concrete. An upper-bound was estimated assuming perfectly plastic behaviour of concrete, i.e. the cylinder reaches its splitting resistance when the tangential stresses at every point along the cover reaches the tensile strength of concrete. An intermediate splitting resistance was derived for the partly cracked elastic stage. In this analysis, the plastic behaviour of concrete is disregarded, and it is assumed that concrete is completely elastic. When the principal tensile stress reaches the concrete tensile strength, an internal crack develops which does not split the entire cover if the load-carrying capacity of the concrete ring has not been reached by then. Generally, the elastic solution underestimates the actual bond capacity, as the concrete exhibits some form of plastic behaviour, thereby providing additional contribution to a higher capacity. The partly cracked elastic solution seems to provide a better estimation than the elastic solution but still underestimates the actual capacity as the softening behaviour of concrete is completely ignored. On the other hand, as concrete is not a perfectly plastic material, the actual capacity is overestimated when using the plastic solution (Tepfers, 1973). Therefore, experimental values are expected to lie between the partly cracked elastic solution and the plastic solution. The bond capacity of the concrete ring under the above three criteria were compared as a function of the concrete cover thickness (Figure 2.7) and the experimental values occurred between the partly cracked elastic and the plastic stages, as expected (Tepfers, 1973).

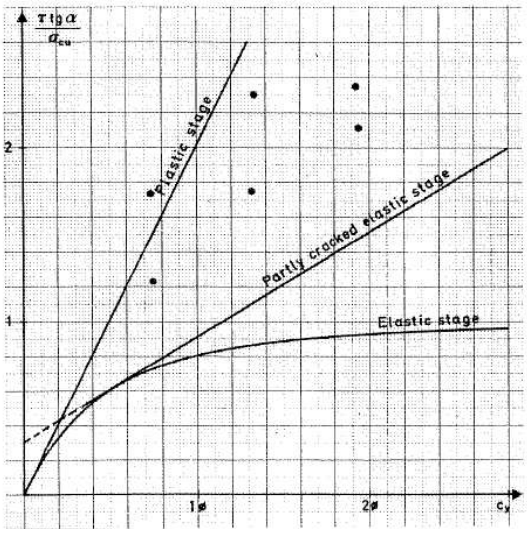

Figure 2.7 - Splitting resistance of the concrete cover at elastic, partly cracked elastic and plastic stages (Tepfers, 1973)

However, Tepfers identified that the experimental values were somewhat higher than expected and justified it by the fact that the theory is valid for cylinders, and the results were from a concrete body exceeding the dimensions of the cylinder.

By studying the fractures in an overlap splice in which the bars are laid side by side, six types of possible failure patterns were identified by Tepfers (1973) (Figure 2.8). The ultimate bond capacity of the joint has been obtained from equilibrium analysis of the ultimate splitting failure crack patterns. The ultimate crack pattern is determined by the geometry of the concrete member section and where the longitudinal cover cracks have appeared.

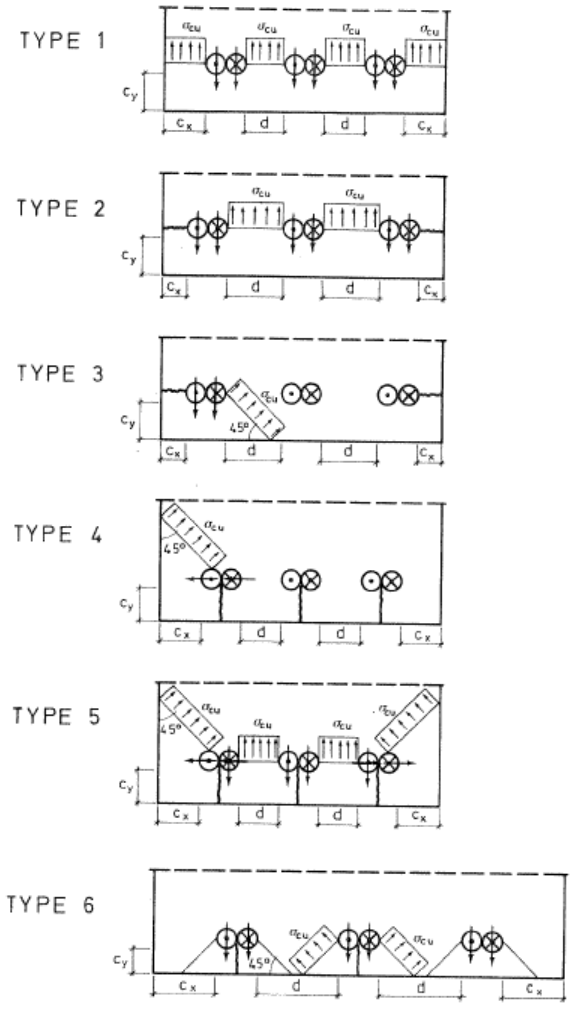

Figure 2.8 - Possible ultimate splitting failure crack patterns for overlapped steel bars (Tepfers, 1973)

Van der Veen (1990) derived a model for a thick-wall concrete ring subject to internal pressure, by modifying Tepfers (1973) partly cracked elastic solution. This model takes into account the softening behaviour of concrete after cracking so that the redistribution of tensile stresses is allowed along the crack. Therefore, the splitting bond capacity consists of the partly cracked elastic part and the softening contribution from the concrete. The models corresponding to different bar diameters seem to fall well within the experimental results (Figure 2.9).

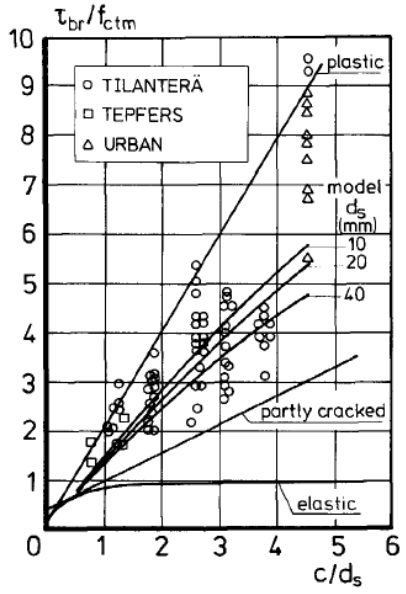

Figure 2.9 - Van der Veen's (1990) model for different bar diameters

All models predicting splitting resistance of the thick-wall concrete ring depend on the assumed angle α, and generally $\alpha =$ 45º has been assumed for simplicity and comparison purposes. Limited information is available for this angle when the bond of steel-to-concrete is concerned. The angle α seems to be independent of the concrete quality, to vary between 45º to 26º, and to decrease with increasing bar diameter and increasing cover to bar diameter ratio (Van der Veen, 1990). Also, the angle α increases to about 45º under increasing slip due to the wedge action of the crushed concrete in front of the ribs of deformed steel bars (Eligehausen, 1979, cited by Van der Veen (1990)).

De Lorenzis (2004) modelled the bond of NSM FRP bars in the transverse plane in the elastic stage by means of simplifying assumptions. Plane strain conditions were assumed due to the large thickness of the system. By reflecting on the geometry of the

tested specimens, grooves were assumed to have a square shape and the bar was assumed to be located in the middle of the groove. The system of the groove surrounded by the concrete, which is subjected to inner pressure, is assumed to be the superposition of the groove filling material plus the surrounding concrete, with mutual stresses acting on them. An analytical model predicting resin cover cracking pressure has been developed and the method is presented in Chapter 5 because part of the theoretical analysis of the current research is based on it. The analytical model was compared with the predictions from a finite element analysis and the predictions were in good agreement with the analytical model. Further, De Lorenzis calculated an upper-bound and a lower-bound to the local bond strength by analysing possible failure patterns of a NSM FRP system, similar to the analysis of ultimate failure crack patterns by Tepfers (1973). The models were consistent with the experimental results.

2.4 Anchorage length

The anchorage length ("development length") is the length over which an FRP bar can transfer bond stresses to resist a tensile force equal to its ultimate tensile strength. Therefore, to facilitate the development of full tensile capacity of the FRP reinforcement, a sufficient length should be provided beyond a critical section so that the reinforcement may not be susceptible to any premature debonding failure. The anchorage design of NSM FRP reinforcement is different to that of steel bars because in addition to the common parameters that influence the bond behaviour such as bonded surface area and concrete strength, there are other factors that affect the bond behaviour between FRP bars and concrete. For instance, transverse elastic modulus, mechanical and geometrical properties of the bar and resin properties are all additional factors.

The anchorage behaviour of FRP bars seems to be different from one strengthening technique to another. In the case of the EBR technique, a very important aspect is the existence of an "effective bond length", beyond which a further increase of bond length cannot influence the ultimate bond strength (De Lorenzis *et al.*, 2001; Lu *et al.*, 2005; Neubauer and Rostasy, 1999; Ueda and Dai, 2005). However, unlike in the EBR technique, generally, there exists a development length for NSM FRP bars, the minimum bond length required to transfer the maximum bond strength. As mentioned

in Section 2.2, experimental evidence exists to show that it is possible to achieve full tensile capacity of NSM CFRP strips. From the theoretical models for the maximum reinforcement stress resisted by an NSM bonded joint of De Lorenzis *et al.*(2002), σ_{max} , it has been identified that generally there exists a development length if σ_{max} is greater than the tensile strength of the bar, particularly for bond-slip curves with infinite values of fracture energy. When σ_{max} is lower than the tensile strength of the rod, there exists an effective length beyond which a further increment in bond length does not have any effect.

Cosenza *et al.* (2002) reviewed the available formulations for evaluating basic development length in various codes and guidelines, such as those found in the design guidelines of Japan Society of Civil Engineers (JSCE,1997) and guide for the design of concrete structures reinforced with FRP bars (ACI, 2003). Cosenza *et al.* (2002) concluded that all formulations given in these documents seem to be unsuitable for FRP bars as they have been derived under the assumption of a linear relationship between the bond strength and the square root of the concrete compressive strength, and by assuming a uniform bond stress distribution along the bond length, which is normally the case for deformed steel bars.

Some research studies present analytical approaches yielding closed-form solutions to the differential equation of bond, employing different kinds of bond stress-slip models to predict the effective bond length (Cosenza *et al.*, 2002; Mohamed Ali *et al.*, 2008; Yuan *et al.*, 2004). Further details on such studies are discussed in Chapter 6 where an analytical method to predict full range behaviour and anchorage length of NSM FRP-to-concrete joints has been presented.

It is a well-known fact that the anchorage length requirements established for deformed steel bars as well as that proposed for FRP bars in the available guidelines (ACI, 2003; JSCE, 1997), have been defined in terms of number of bar diameters. However, as the FRP technology emerges, different bar shapes other than circular bars become available and it is questionable that the definition of anchorage length in terms of bar diameter/equivalent bar diameter which is an indication of the strength rather than of bond, is still valid for non-circular bars. To the best of the author's knowledge, there has not been any study investigating this problem.

2.5 Concluding remarks

In recent years, as the use of NSM FRP bars has emerged, lots of research was conducted to characterise the bond behaviour of NSM FRP bars-to-concrete as the behaviour was notably different from that observed for the case of steel bars-to-concrete. A comprehensive review of the literature on bond behaviour of NSM FRP bars has been presented including experimental studies, failure modes, bond modelling and gaps of knowledge. Even though, a significant amount of research has already been conducted on bond behaviour of NSM FRP bars, some areas of research such as bond behaviour of square bars, effect of internal reinforcement and effect of bond length, still need further attention.

Bond analysis of FRP bars involves lots of influencing factors and the available analytical expressions/bond models are empirical/semi-empirical. The knowledge of anchorage length requirements is still limited and the existing design rules for the steel-to-concrete case cannot be directly extended to the FRP-to-concrete case. Therefore, generic analytical expressions/bond models predicting bond capacity and anchorage length requirements are required to be developed based on bond mechanics.

CHAPTER 3 – EXPERIMENTAL TEST PROGRAM

From a rigorous review of existing literature, some of possible critical factors affecting bond of NSM FRP bars-to-concrete such as bond length, groove dimensions, bar shape, bar size, bar surface texture, concrete strength, resin type, type of loading and edge distance, were identified. An extensive experimental study investigating this large number of bond parameters was needed in characterising the bond behaviour of NSM FRP bars. This chapter presents the details of bond tests investigating some of the above-mentioned critical bond parameters, including test configuration, test program and material properties.

3.1 Specimen configuration

After reviewing advantages/disadvantages of available bond test configurations such as direct pull-out tests and beam tests, a test set-up similar to cantilever beam test (Nanni *et al.*, 1995) was adopted in the current research. The specimen details and reinforcement details are shown in Figure 3.1. It is widely accepted that beam-type bond tests are more representative of actual stress fields in beams as the concrete surrounding the reinforcement is subjected to tension unlike in the case with direct pull-out tests. In addition, they can be used not only for the determination of bond strength but also for crack width and crack spacing (Nanni *et al.*, 1995). Further, the specimen configuration allowed monitoring of both the loaded end and free end slips.

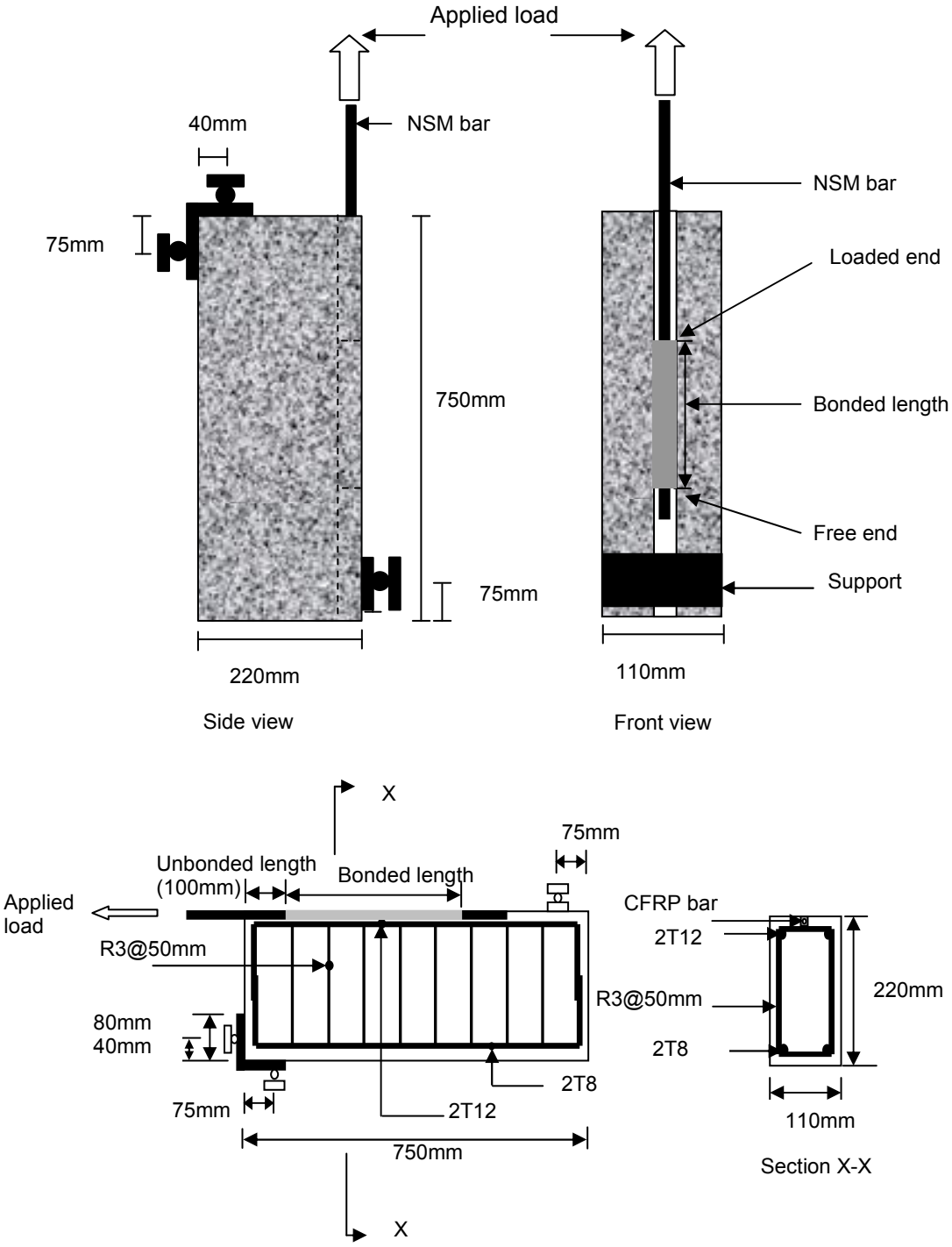

Figure 3.1 - Specimen and reinforcement details

The bond specimens were of 110mm x 220mm in cross-section and 750mm long. According to preliminary tests conducted (Section 3.3), it was found that internal steel reinforcement and shear stirrups were needed to prevent any bending or shear failure in the 'beam' portion before bond failure occurred, as the location and the size of the

bonded region were varied from one specimen to another, i.e. as the location of the load transfer area varied. The amount of flexural steel reinforcement was selected to avoid any flexural failure before bond failure occurred and also to resemble the usual percentage of internal steel reinforcement in practical situations (0.93%).The specimen was of easily manageable size and since the specimen was tested vertically, it was possible to visually inspect the bonded joint while loading progressed. A 100mm long region was left unbonded near the loaded end in order to prevent a cone type failure in the concrete when the bar is pulled out.

According to the specimen configuration, the bond tests can be classified as beam tests as far as the free body diagram is concerned since the free body diagram approximates that of the shear span of a beam test loaded under four-point bending. Therefore, the bond specimen was considered as a normal beam when the internal steel reinforcement and shear links were designed. Furthermore, this is more representative of the real situation of strengthening a beam with NSM FRP reinforcement, than previous studies (De Lorenzis, 2002; Sena Cruz, 2004) which omitted internal steel reinforcement. In those studies, beam-type bond tests were carried out ensuring that no flexural cracking occurred before the bond failure so that pure bond behaviour could be investigated. As a result, the maximum bond length possible was limited in those tests, owing to the limitation of specimen geometry. As the maximum bond length in the current research was as high as 510mm, there was no way that flexural cracking could be controlled with the limited length of the bond specimen (750mm). Therefore, it was expected that these bond tests may exhibit different behaviour to that found in the literature, especially when the ultimate capacities of the specimens were found to be high.

3.2 Test matrix

Table 3.1 lists the test matrix. Only CFRP bars were selected for the investigation due to its superior properties and widespread use for retrofitting applications. The experimental program consisted of 11 series, each composed of four bond specimens, investigating the effect of the following parameters on bond between NSM CFRP bars and concrete:

- Bond length (in terms of the number of bar perimeters, varying from 1.6 to 12.7)
- Bar shape (circular, rectangular and square)
- Bar cross-sectional area (varying from 64mm^2 to 114mm^2)
- Surface texture of the bar (smooth, sanded spirally wound and helical tape wrapping with small indentations)
- Groove size
- Concrete strength (nominal strengths of 30N/mm^2 and 60N/mm^2)
- Adhesive type (two different epoxy adhesives, Sikadur 30 and StoBPE Lim 465/464).

The bond length is expressed in terms of multiples of bar perimeter as the perimeters of 12mm diameter bars, 10mm square bars and 2 x 16mm rectangular bars were approximately the same so that it was possible to provide approximately the same bonded surface area for each bar shape. The multiples of bar perimeter considered here were 1.6, 3.2, 6.4 and 12.7 for all circular and non-circular sections so that the bond behaviour of various bar shapes could be directly compared with each other. Furthermore, non-circular bar sections were converted into an equivalent circular cross-section by equating cross-sectional areas, thereby obtaining bond lengths of non-circular sections in terms of equivalent bar diameters. Two nominal compressive cube strengths of concrete, 30N/mm^2 and 60N/mm^2, were selected to represent the usual extremes of concrete strength typically encountered in the strengthening of existing reinforced concrete structures. It was reviewed in the previous chapter how bond resisting mechanisms and failure modes change as the bar surface texture varies. Therefore, two different bar surface textures were employed in the current investigation to study this effect.

It was also evident from the reviewed literature that there exist differences in bond mechanisms as the bar shape varies. For example, resin cover splitting failure is a common failure mode for round NSM bars whereas it is a less likely failure mode for rectangular strips, owing to thicker lateral sides of the groove. Therefore, three most common FRP bar shapes, circular, rectangular and square, were selected for the investigation.

Groove size plays an important role in determining whether failure occurs in the resin cover or the surrounding concrete (De Lorenzis and Teng, 2007). Various groove dimensions, allowing a range of adhesive thickness around the bar, from 1mm to 6mm adhesive thicknesses, were found in the existing literature (De Lorenzis, 2002; Hassan *et al.*, 2001; Yan *et al.*, 1999). However, there is insufficient research and guidelines on groove detailing and an optimum value for groove size has not yet been proposed. Therefore, groove size was identified as one of the critical bond parameters and adhesive thicknesses ranging from 2mm to 4.5mm were considered in the current study.

The same adhesive (Sikadur 30) was used throughout Series 1 to 10 and StoBPE Lim 465/464 was used in Series 11. The effect of adhesive type was investigated by the comparison of Series 10 and 11 as the other bond parameters were the same. Cross-sectional area from 64mm^2 to 114mm^2 was varied in round bars and for the other bar shapes the same bar size was used throughout.

Specimen number	**Bar shape**	**Surface texture/ commercial name**	**Bar size**	**Nominal cube compressive strength of concrete (N/mm^2)**	**Groove dimensions (mm x mm)**	**Bonded length (number of bar perimeters)**	**Resin type**
1	Circular	Spirally wound and sand coated (Carbopree)	12mm dia.	60	16 x 16 (Small)	1.6	Sikadur 30
2						3.2	
3						6.4	
4						12.7	
5				30		1.6	
6						3.2	
7						6.4	
8						12.7	
9		Helical tape wrapping with surface indentations (Aslan 200)	9mm dia.	60	13 x 13 (Small)	1.6	
10						3.2	
11						6.4	
12						12.7	
13				30		1.6	
14						3.2	
15						6.4	
16						12.7	
17				60	18 x 18 (Large)	1.6	
18						3.2	
19						6.4	
20						12.7	
21			12mm dia.		16 x 16 (Small)	1.6	
22						3.2	
23						6.4	
24						12.7	
25	Rectangular	Tape wrapped with surface indentations (Aslan 500)	2mm x 16mm	60	6 x 20 (Small)	1.6	
26						3.2	
27						6.4	
28						12.7	
29					10 x 24 (Large)	1.6	
30						3.2	
31						6.4	
32						12.7	
33	Square	Smooth (Sto FRP)	10mm x 10mm	60	14 x 14 (Small)	1.6	
34						3.2	
35						6.4	
36						12.7	
37					18 x 18 (Large)	1.6	
38						3.2	
39						6.4	
40						12.7	
41						1.6	Sto BPE Lim 464/465
42						3.2	
43						6.4	
44						12.7	

Table 3.1 - Test matrix

3.3 Preliminary tests

Some preliminary tests were done to identify whether internal steel reinforcement and steel stirrups were needed. These specimens were tested horizontally and the test set-up and failure modes of two preliminary tests are shown in Figure 3.2. Their details are listed in Table 3.2.

Description	Bar type and size	Bond length (mm)	Ultimate load (kN)	Average bond strength (MPa)	Ultimate load/ tensile strength%	Failure mode
Specimen A - without any internal steel reinforcement	7.5mm diameter Carbopree	300	30.1	4.26	29	Flexural failure of concrete in tension
Specimen B - containing internal steel reinforcement with no shear stirrups			49.9	7.06	49	Resin-concrete interface failure

Table 3.2 - Details of preliminary tests

Specimen A failed in flexure at a low load as there was no reinforcement to withstand tensile stresses beyond the termination point of the CFRP bar (Figure 3.2(b)). Even though specimen B did not fail in shear, considerable shear cracking was observed (Figure 3.2(c)). Therefore, preliminary tests revealed the necessity of internal steel reinforcement and shear links in order that bond failure would precede any flexural/shear failure.

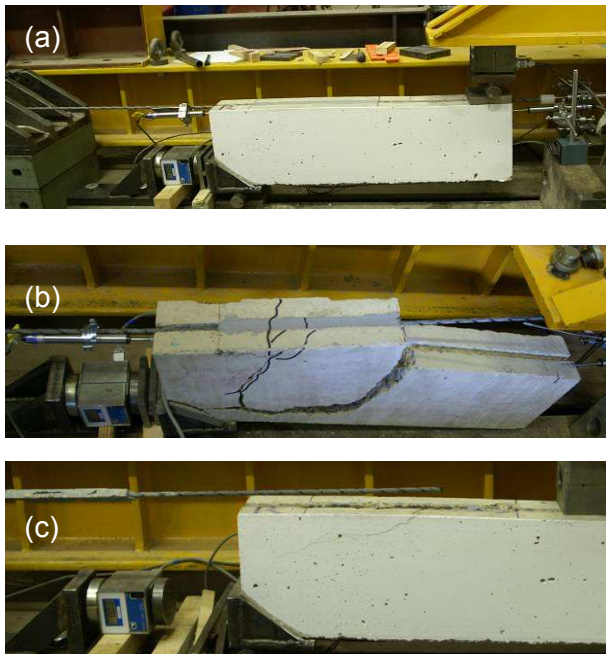

Figure 3.2 - Preliminary tests: (a) test set-up, (b) flexural failure of concrete in tension and (c) resin-concrete interface failure

3.4 Bond specimens with circular bars

Table 3.3 lists the specimen number and designation of the first six series of bond tests which considered circular bars, along with the bond length in millimetres and in terms of bar diameters. The multiples of bar perimeter were 1.6, 3.2, 6.4 and 12.7 and the corresponding multiples of bar diameter were 5, 10, 20 and 40, respectively. The designation of the specimens is of the form of "*series number - specimen number [bar type (A - Aslan or C - Carbopree) and bar diameter/ nominal cube compressive strength of concrete/ groove size (S - small or L - large)/ bond length in terms of number of bar perimeters (p)]*". Two nominal compressive strengths of concrete of 30N/mm^2 and 60N/mm^2 were considered. Two bar diameters of 9mm and 12mm were considered. Two types of CFRP bars with different surface textures, namely, CARBOPREE and ASLAN 200 manufactured by Sireg, (Italy) and Hughes Brothers, (USA), respectively, were used. The groove size was classified as small/large depending on how large it was compared with the bar diameter. When the groove dimension (the groove width and depth were the same because all the grooves were square in cross-section) was 4mm wider than the bar diameter, it was regarded as

'small' and when the groove dimension was 8mm wider than the bar diameter, it was classified as 'large'.

Series number	Specimen number	Specimen designation	Bond length (mm)	Bond length (number of bar diameters)
1	1	*1-1[C12/60/S/1.6p]*	60	5
	2	*1-2[C12/60/S/3.2p]*	120	10
	3	*1-3[C12/60/S/6.4p]*	240	20
	4	*1-4[C12/60/S/12.7p]*	480	40
2	17	*2-17[A9/60/L/1.6p]*	45	5
	18	*2-18[A9/60/L/3.2p]*	90	10
	19	*2-19[A9/60/L/6.4p]*	180	20
	20	*2-20[A9/60/L/12.7p]*	360	40
3	21	*3-21[A12/60/S/1.6p]*	60	5
	22	*3-22[A12/60/S/3.2p]*	120	10
	23	*3-23[A12/60/S/6.4p]*	240	20
	24	*3-24[A12/60/S/12.7p]*	480	40
4	9	*4-9[A9/60/S/1.6p]*	45	5
	10	*4-10[A9/60/S/3.2p]*	90	10
	11	*4-11[A9/60/S/6.4p]*	180	20
	12	*4-12[A9/60/S/12.7p]*	360	40
5	5	*5-5[C12/30/S/1.6p]*	60	5
	6	*5-6[C12/30/S/3.2p]*	120	10
	7	*5-7[C12/30/S/6.4p]*	240	20
	8	*5-8[C12/30/S/12.7p]*	480	40
6	13	*6-13[A9/30/S/1.6p]*	45	5
	14	*6-14[A9/30/S/3.2p]*	90	10
	15	*6-15[A9/30/S/6.4p]*	180	20
	16	*6-16[A9/30/S/12.7p]*	360	40

Table 3.3 - Designation and bond length of bond tests containing circular bars

Some tests had to be repeated due to some unexpected circumstances and errors. The maximum bond length in Series 1 started from the end of the unbonded region as can be seen in Figure 3.3(a). When the bond length was reduced to 1/2 and 1/4 of the maximum (i.e. in specimens *1-3[C12/60/S/6.4p]* and *1-2[C12/60/S/3.2p]*), the corresponding bond lengths also started from the end of the unbonded region as in Figure 3.3(b). As this caused a cone-type failure in the concrete, as shown in Figure 3.4, the bonded region was repositioned according to Figure 3.3(c) to prevent that sort of failure in the concrete, where the bond length started from the further end of the

maximum bond length. From there onwards, the later configuration was used for all the other tests including all the tests with non-circular bars.

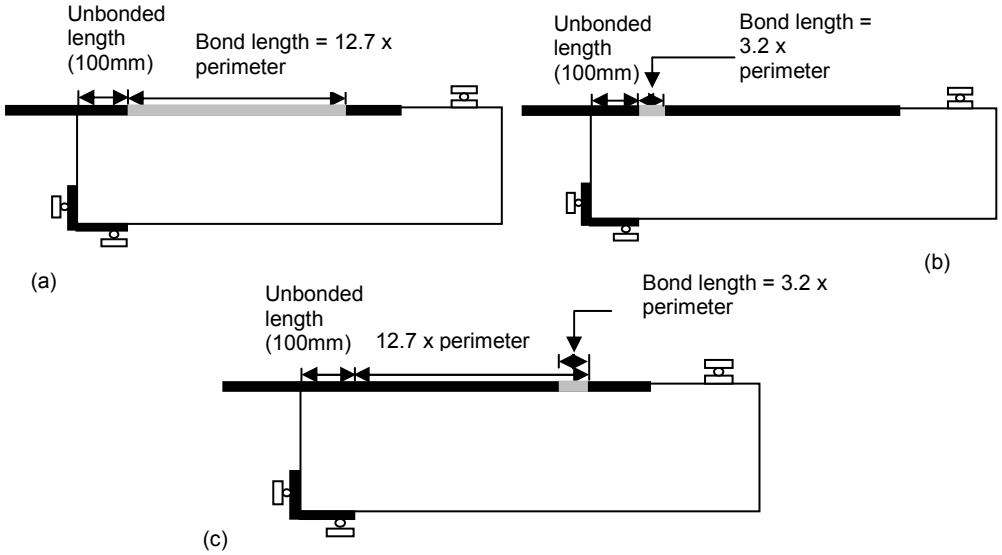

Figure 3.3 - Positioning the bonded region

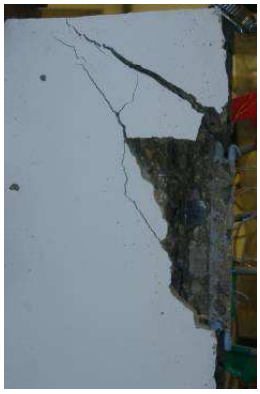

Figure 3.4 - Cone-type failure in the concrete in specimen *1-2[C12/60/S/3.2p]*

Secondly, in all four tests in Series 1, testing was aborted just after the failure load; consequently, their mode of failure could not be clearly identified as there were not obvious traces of failure in the concrete, FRP bar or resin. Therefore, these four tests were repeated and for all the other tests, testing was continued after the failure until the bar was completely pulled out or until the maximum displacement capacity of the loading machine was reached.

Lastly, specimen *4-11[A9/60/S/6.4p]* had to be repeated as it failed prematurely at the grips due to misalignment. The results of tests *1-3[C12/60/S/6.4p]*, *1-2[C12/60/S/3.2p]* configured according to Figure 3.3(b), and test *4-11[A9/60/S/6.4p]* which failed prematurely, were not analysed and discussed further and only their repeated test results were taken into consideration. However, the test results of all the four original tests in Series 1, were analysed, discussed further and compared against their repeat tests in the next chapter, as there was nothing inherently wrong with them, except for the uncertainty of the mode of failure.

3.5 Bond specimens with rectangular bars

Table 3.4 comprises the specimen number and designation of bond tests of Series 7 and 8 which considered rectangular bars, along with the bond length in millimetres and in multiples of the equivalent bar diameter (equal to $\sqrt{(4 \text{ x breadth x depth}/\pi)} \approx 6.4$mm). Variables considered within these series were bond length and groove size only. Bond length was expressed in terms of the same multiples of bar perimeter, i.e. 1.6, 3.2, 6.4 and 12.7 and the corresponding multiples of the equivalent bar diameter were 9, 18, 36 and 72, respectively. The nominal cube compressive strength of concrete was 60N/mm^2 for all the specimens. The bars used were ASLAN 500 strips of 2 x 16mm. When the groove dimensions (width and depth) were 4mm wider than that of the bar, it was regarded as 'small' and when the groove dimensions were 8mm wider than that of the bar, it was classified as 'large'. The designation of the specimens is of the form of "*series number - specimen number [shape (R - rectangular)/ nominal cube compressive strength of concrete/ groove size (S - small/ L - large)/ bond length in terms of number of bar perimeters (p)*]".

In Series 8, the specimen containing a bond length of 12.7 times the bar perimeter was not tested, as the results of the preliminary tests investigating the effect of strain gauges (described below) confirmed that the failure would also have been by tensile rupture of the bar for bond lengths greater than 6.4 times the bar perimeter.

Series number	Specimen number	Specimen designation	Bond length (mm)	Bond length (number of equivalent bar diameters)
7	25	*7-25[R/60/S/1.6p]*	58	9
	26	*7-26[R/60/S/3.2p]*	115	18
	27	*7-27[R/60/S/6.4p]*	230	36
	28	*7-28[R/60/S/12.7p]*	460	72
8	29	*8-29[R/60/L/1.6p]*	58	9
	30	*8-30[R/60/L/3.2p]*	115	18
	31	*8-31[R/60/L/6.4p]*	230	36
	32	*8-32[R/60/L/12.7p]*	460	72

Table 3.4 - Designation and bond length of bond tests containing rectangular bars

The application of strain gauges on the bar surface was a significant issue as it is likely that strain gauges would affect the bond performance. Therefore, strain gauges were aligned along the bar as explained in Section 3.9 in order to minimise the possible effects of strain gauging on bond behaviour. As the thickness of the rectangular strip was very small, it was not possible to position the gauges in the way shown later on in Section 3.9. Therefore, strain gauges had to be positioned on one of the side surfaces, which in turn was expected to have had a greater influence on bond behaviour than the former configuration. Therefore, two preliminary tests, one of which was *8-31[R/60/L/6.4p]* were conducted to investigate the effect of strain gauging on the side surfaces of rectangular strips. The other test was the control specimen which had no strain gauges.

3.6 Bond specimens with square bars

Series 9, 10 and 11 considered square bars, and the specimen numbers and designation can be seen in Table 3.5, along with the bond length in millimetres and in multiples of the equivalent bar diameter $(\text{equal to} \sqrt{(4 \text{ x breadth x depth}/\pi)} \approx 11.3\text{mm})$.

The investigated variables were bond length, groove size and resin type. The bond length was defined in terms of the same multiples of bar perimeter, i.e. 1.6, 3.2, 6.4 and 12.7, and the corresponding ratios of bond length to equivalent bar diameter were 6, 11, 23 and 45, respectively. The bars used were of 10mm x 10mm and commercially named as StoFRP bar E 10 C. All the grooves were square in shape and when the

groove dimension was 4mm wider than the bar dimension (width or depth), it was regarded as 'small' and when the groove dimension was 8mm wider than the bar diameter it was classified as 'large'. The designation of the specimens is of the form of "*series number - specimen number [shape (S - square)/ nominal cube compressive strength of concrete/ groove size (S - small/ L - large)/ resin type (Sika - Sikadur30/ Sto - StoBPE Lim 465/464)/ bond length in terms of number of bar perimeters (p)*]".

Series number	**Specimen number**	**Specimen designation**	**Bond length (mm)**	**Bond length (number of equivalent bar diameters)**
9	33	*9-33[S/60/S/Sika/1.6p]*	64	6
	34	*9-34[S/60/S/Sika/3.2p]*	128	11
	35	*9-35[S/60/S/Sika/6.4p]*	255	23
	36	*9-36[S/60/S/Sika/12.7p]*	510	45
10	37	*10-37[S/60/L/Sika/1.6p]*	64	6
	38	*10-38[S/60/L/Sika/3.2p]*	128	11
	39	*10-39[S/60/L/Sika/6.4p]*	255	23
	40	*10-40[S/60/L/Sika/12.7p]*	510	45
11	41	*11-41[S/60/L/Sto/1.6p]*	64	6
	42	*11-42[S/60/L/Sto/3.2p]*	128	11
	43	*11-43[S/60/L/Sto/6.4p]*	255	23
	44	*11-44[S/60/L/Sto/12.7p]*	510	45

Table 3.5 - Designation and bond length of bond tests containing square bars

Specimens *10-39[S/60/L/Sika/6.4p]* and *11-44[S/60/L/Sto/12.7p]* were repeated due to the inconsistency in their results as discussed in Chapter 4.

3.7 Material properties

3.7.1 Concrete

The mix proportions of the materials for each concrete grade are shown in Table 3.6. The correct mix proportions for the required nominal strengths were found by several trial mixes. The maximum size of the coarse aggregate (crushed limestone) was 14mm and the maximum size of the fine aggregate (yellow pit sand) was 5mm. Concrete cubes of 100mm x 100mm x 100mm were cast from each concrete batch, and the

compressive cube strength of the concrete was found by crushing these cubes on the day of testing the corresponding bond specimen. The average compressive strength of three or more cubes has been taken as the actual compressive strength of the particular concrete batch. The compression tests were conducted at a loading rate of 1000kPa/s on a 200tonne capacity testing machine.

Cylinders of 150mm in diameter and 300mm long were used to obtain the split-tensile strength of concrete. The results of compressive and split-tensile tests are shown in Table 3.7. Lack of available cylinder moulds prevented the possibility of casting cylinders for each and every concrete mix, when several batches were done in the same day. The split-tensile strength values of specimens with circular bars were deduced from one sample per specimen due to the limited number of moulds. Since such tensile strength results seemed to be less reliable than cube strength results, for specimens with rectangular and square bars split-tensile strength values were obtained from the average of three samples. The cylinder splitting tests were performed at a loading rate of 3.2tonnes per minute on a 250tonne capacity testing machine. Figure 3.5 illustrates the compression test set-up and the cylinder split-tensile test set-up.

Material	**C 30**	**C 60**
Ordinary Portland Cement (kg)	459	750
Fine aggregate (kg)	370	700
Sand (kg)	370	151
Coarse aggregate (kg)	1096	700
Water (kg)	193	165
Super plasticizer (l)	0	4.2

Table 3.6 - Material quantities for $1m^3$ of concrete

Series number	Specimen number	Specimen designation	Nominal concrete strength (N/mm^2)	Actual concrete strength (N/mm^2)	Splitting tensile strength (N/mm^2)
1	1	*1-1[C12/60/S/1.6p]*	60	58.9	2.81
	2	*1-2[C12/60/S/3.2p]*			
	3	*1-3[C12/60/S/6.4p]*			
	4	*1-4[C12/60/S/12.7p]*		N/A	N/A
	1-repeat	*1-1[C12/60/S/1.6p]repeat*		72.5	N/A
	2-repeat	*1-2[C12/60/S/3.2p]repeat*			
	3-repeat	*1-3[C12/60/S/6.4p]repeat*		70.6	3.04
	4-repeat	*1-4[C12/60/S/12.7p]repeat*		72.5	N/A
2	17	*2-17[A9/60/L/1.6p]*		56.6	2.26
	18	*2-18[A9/60/L/3.2p]*			
	19	*2-19[A9/60/L/6.4p]*		59.0	2.96
	20	*2-20[A9/60/L/12.7p]*		56.6	2.26
3	21	*3-21[A12/60/S/1.6p]*		59.0	2.96
	22	*3-22[A12/60/S/3.2p]*			
	23	*3-23[A12/60/S/6.4p]*		62.4	
	24	*3-24[A12/60/S/12.7p]*			
4	9	*4-9[A9/60/S/1.6p]*		54.2	2.78
	10	*4-10[A9/60/S/3.2p]*		62.4	2.96
	11	*4-11[A9/60/S/6.4p]*		54.2	3.04
	11-repeat	*4-11[A9/60/S/6.4p]repeat*		70.6	2.78
	12	*4-12[A9/60/S/12.7p]*		54.2	
5	5	*5-5[C12/30/S/1.6p]*	30	34.0	2.18
	6	*5-6[C12/30/S/3.2p]*			
	7	*5-7[C12/30/S/6.4p]*			
	8	*5-8[C12/30/S/12.7p]*		36.3	
6	13	*6-13[A9/30/S/1.6p]*		34.0	
	14	*6-14[A9/30/S/3.2p]*		36.3	
	15	*6-15[A9/30/S/6.4p]*			
	16	*6-16[A9/30/S/12.7p]*			
7	25	*7-25[R/60/S/1.6p]*	60	71.9	3.76
	26	*7-26[R/60/S/3.2p]*		69.6	N/A
	27	*7-27[R/60/S/6.4p]*			
	28	*7-28[R/60/S/12.7p]*		62.4	
8	29	*8-29[R/60/L/1.6p]*		70.3	N/A
	30	*8-30[R/60/L/3.2p]*		71.9	3.76
	31	*8-31[R/60/L/6.4p]*		70.3	N/A
	31-control	*8-31[R/60/L/6.4p]control*			
9	33	*9-33[S/60/S/Sika/1.6p]*		64.8	3.76
	34	*9-34[S/60/S/Sika/3.2p]*			
	35	*9-35[S/60/S/Sika/6.4p]*		60.7	3.71
	36	*9-36[S/60/S/Sika/12.7p]*			
10	37	*10-37[S/60/L/Sika/1.6p]*		61.5	N/A
	38	*10-38[S/60/L/Sika/3.2p]*			
	39	*10-39[S/60/L/Sika/6.4p]*		61.5	
	39-repeat	*10-39[S/60/L/Sika/6.4p]repeat*		62.4	
	40	*10-40[S/60/L/Sika/12.7p]*		64.8	3.76
11	41	*11-41[S/60/L/Sto/1.6p]*		69.6	N/A
	42	*11-42[S/60/L/Sto/3.2p]*		60.0	
	43	*11-43[S/60/L/Sto/6.4p]*		60.0	
	44	*11-44[S/60/L/Sto/12.7p]*		70.6	3.04
	44-repeat	*11-44[S/60/L/Sto/12.7p]repeat*		60.0	N/A

Table 3.7 - Mechanical properties of concrete

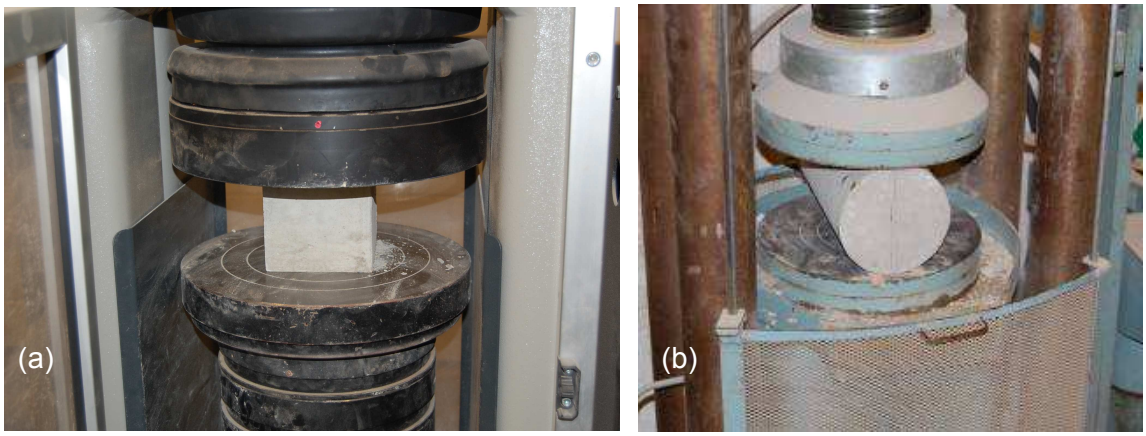

Figure 3.5 - (a) Compression test set-up and (b) split-tensile test set-up

3.7.2 Steel

High yield steel bars of 12mm were used as the tensile reinforcement, and 8mm high yield steel bars were used in the compression zone to hold the stirrups. The stirrups were of 3mm mild steel. Material tests for steel bars were not conducted because the internal steel reinforcement was not investigated as a bond parameter. Moreover, the same reinforcement arrangement was used for all the specimens. But the yield stress and the ultimate strength of the mild steel bars had previously been found to be 700N/mm^2 and 869N/mm^2, respectively (Valerio, 2005).

3.7.3 FRP bars

Two types of circular bars with different surface textures, Carbopree bars (from Sireg, Italy) and Aslan 200 bars (from Hughes Brothers, US) were selected. Carbopree bars had a spirally wound and sand coated surface whereas Aslan 200 bars had a helical tape wrapping with small indentations on it. The diameter of Carbopree bars was 12mm and the diameters of Aslan 200 bars were 9mm and 12mm. The rectangular bars (or strips) were 2mm thick and 16mm wide and commercially called Aslan 500 strips (from Hughes Brothers, US). The square bars were of 10mm x 10mm in cross-section and called StoFRP bar E 10 C (from Sto, Sweden). Figure 3.6 shows all the types of CFRP bars used, and Table 3.8 lists the geometric properties of the bars.

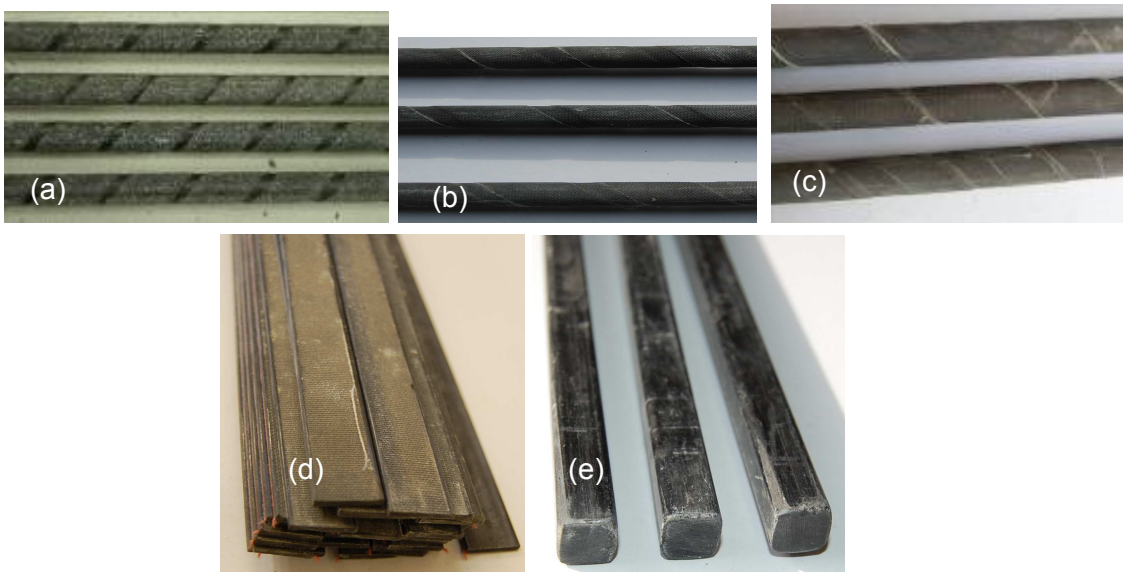

Figure 3.6 - Different shapes of CFRP bars: (a) 12mm Carbopree, (b) 9mm Aslan 200, (c) 12mm Aslan 200, (d) 2 x 16 mm Aslan 500 strips and (e) 10 x 10 mm Sto FRP bar E 10 C

Bar type	12mm Carbopree	12mm Aslan 200	9mm Aslan 200	2mm x 16mm Aslan 500	10mm x 10mm StoFRP
Diameter	12.2 (0.7%)	12 (0.7%)	9.42 (0.4%)	N/A	N/A
Width	N/A	N/A	N/A	15.9 (0.2%)	9.94 (0.2%)
Thickness	N/A	N/A	N/A	2.16 (0.5%)	9.95 (0.3%)

Table 3.8 - Geometric properties of the CFRP bars
(Note: Values within parentheses are coefficients of variation)

Tensile tests were performed in accordance with BS: EN: ISO: 527-5 (BSI, 1997) on all the types of FRP bars in order to verify the mechanical properties such as Young's modulus, tensile strength and ultimate strain. Conventional anchor devices such as steel grip jaws could not be used to grip the FRP bars as they are anisotropic materials. Generally, the transverse compressive strength (controlled by the resin properties) is significantly less than the longitudinal tensile strength. Therefore, FRP bars are susceptible to transverse crushing due to the hydraulic pressure at the grips, so that adopting a proper gripping system was critical to prevent any premature failure of the bar at the grips. As the standard methods for proper gripping are not yet fully characterised, several methods were initially adopted. Firstly, an anchor system

consisting of the bar cast inside a steel tube and filled with an epoxy adhesive was used. However, it did not work well and premature failure occurred with the bar slipping out of the steel tube. De Lorenzis (2002) had been able to grip FRP bars using this technique, but by replacing the epoxy with an expansive cement grout. The internal pressure due to the expansion of the grout prevented slippage of the bar. However, expansive cement grout was not considered here.

Secondly, different types of steel and aluminium wedges were used, and all of these trials ended up in premature anchorage failure. Finally, 190mm long and 2mm thick aluminium tabs were used at both grips to hold the FRP bars, avoiding some of the stress concentration. For circular and square bars, jaws with a v-shaped groove were used whereas for rectangular bars, flat jaws with indentations were used (Figure 3.7). The aluminium tabs were pre-bent slightly to fit into the groove when jaws with a v-shaped groove were used. Even with this gripping system, circular bars could not be gripped completely until their ultimate tensile strength was achieved, unlike encountered with the square and rectangular bars. Therefore, the ultimate tensile strength and the ultimate strain values are not available for circular bars in Table 3.9, where the experimental values of the mechanical properties of the bars are reported. However, all these tensile tests on the circular bars reached load levels higher than the ultimate capacities of the bond tests containing circular bars. Therefore, it was possible to study the stress-strain behaviour of circular bars until the required limit, as tensile rupture never occurred in bond tests containing the circular bars. Some of the supplier specified bar properties are listed in Table 3.10.

Bar size (mm)	Commercial name	Coupon number	Tensile strength (N/mm^2)	Ultimate load/ manufacture specified tensile strength%	Young's modulus (kN/mm^2)	Ultimate strain (%)
12	Carbopree	1	N/A	59	143	N/A
		2		61	138	
		3		60	141	
Average				**60**	**141**	
Standard deviation				**1.0**	**2.5**	
coefficient of variation				**2%**	**2%**	
12	Aslan 200	1	N/A	74	128	N/A
		2		73	128	
		3		77	124	
Average				**74.7**	**127**	
Standard deviation				**2.1**	**2.3**	
coefficient of variation				**3%**	**2%**	
9	Aslan 200	1	N/A	70	149	N/A
		2		63	122	
		3		77	147	
		4		58	140	
		5		59	148	
		6		85	158	
Average				**68.7**	**144**	
Standard deviation				**10.8**	**12.2**	
coefficient of variation				**16%**	**8%**	
2 x 16	Aslan 500	1	2058	99	127	1.59
		2	1976	96	123	1.48
		3	2096	101	120	1.51
Average			**2043**	**98.7**	**123**	**1.53**
Standard deviation			**61.3**	**2.5**	**3.5**	**0.1**
coefficient of variation			**3%**	**3%**	**3%**	**4%**
10 x 10	StoFRP	1	2533	127	137	1.61
		2	2738	137	136	1.61
		3	2893	145	139	1.60
Average			**2721**	**136**	**137**	**1.61**
Standard deviation			**181**	**9.0**	**1.5**	**0.0**
coefficient of variation			**7%**	**7%**	**1%**	**0%**

Table 3.9 - Mechanical properties of the CFRP bars (experimental values)

Bar Type	Surface configuration	Cross sectional area (mm^2)	Tensile strength (N/mm^2)	Modulus of elasticity (kN/mm^2)	Ultimate strain (%)
Carbopree	Spirally wounded and sand coated	113	2300	130	1.8
12mm Aslan 200	Helically wrapped tape with surface indentations	108	2068	124	1.7
9mm Aslan 200	Helically wrapped tape with surface indentations	65	2068	124	1.7
Aslan 500	Spirally wounded and sand coated	31	2068	124	1.7
Sto FRP	Plain smooth surface	100	2000	155	1.5

Table 3.10 - Properties of the CFRP bars (Manufacturer specified values (Hughes Brothers, 2006a; Hughes Brothers, 2006b; Carbopree, 2003))

Unlike with the circular bars, the rectangular and square bars could be tested properly using the chosen anchorage until their ultimate tensile strength was reached. The square bars were aligned parallel with the sides of the v-shaped groove because had they not been aligned parallel, they would have been susceptible to transverse crushing at the grips. The total length of the tensile specimens was 1000mm, including the test region and gripping lengths (2 x 190mm). Specimens were equipped with one or two strain gauges near the middle of the test region. The tests were conducted in displacement control mode at a rate of 2mm/min. The initial gripping pressure was around 3.5MPa. Figure 3.8 depicts the test set-up and the failed specimens.

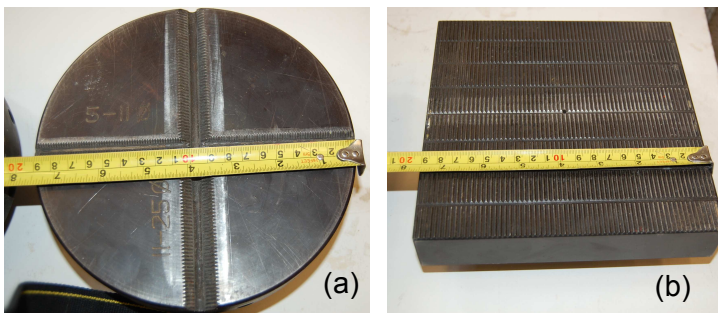

Figure 3.7 - Types of jaws: (a) jaws with a v-shaped groove and (b) flat jaws with indentations

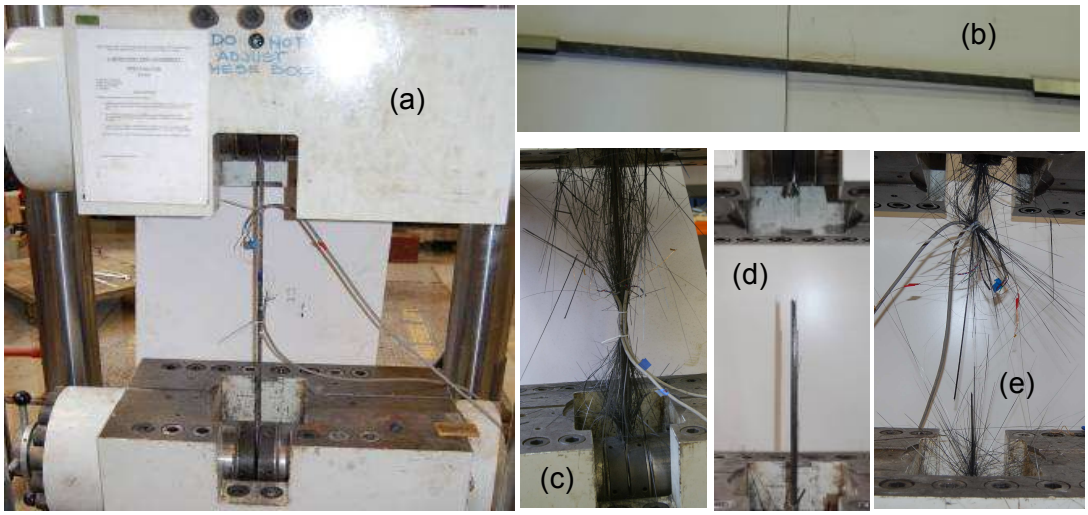

Figure 3.8 - (a) Tensile test set-up, (b) 12mm diameter Aslan 200 bar before testing, (c) failure of a circular bar, (d) failure of a square bar and (e) failure of a rectangular bar

All the tensile tests involving circular bars failed prematurely by fibre splitting, which started from the ends and spread towards the middle region, during the final stages of the load application. The square bars indicated a sharp brittle ultimate tensile failure, as can be seen in Figure 3.8(d), whereas the rectangular bars also exhibited a fibre splitting type failure around their ultimate tensile strength. Experimental tensile strength values of the square bars seemed to be about 45% higher than that provided by the supplier. Figure 3.9 shows the stress-strain plots for the tensile test specimens up to failure. For specimens failing prematurely, the stress-strain curve only up to the maximum load level recorded is plotted. Sometimes, the strain gauges stopped working before the maximum load was reached due to local fibre splitting. In that case, the stress-strain curves were plotted from the available strain gauge readings only. The deviations in some of the specimens near their end region of the curve were due to the slight dropping of the load, when fibre splitting or slipping of the bar from the jaws occurred.

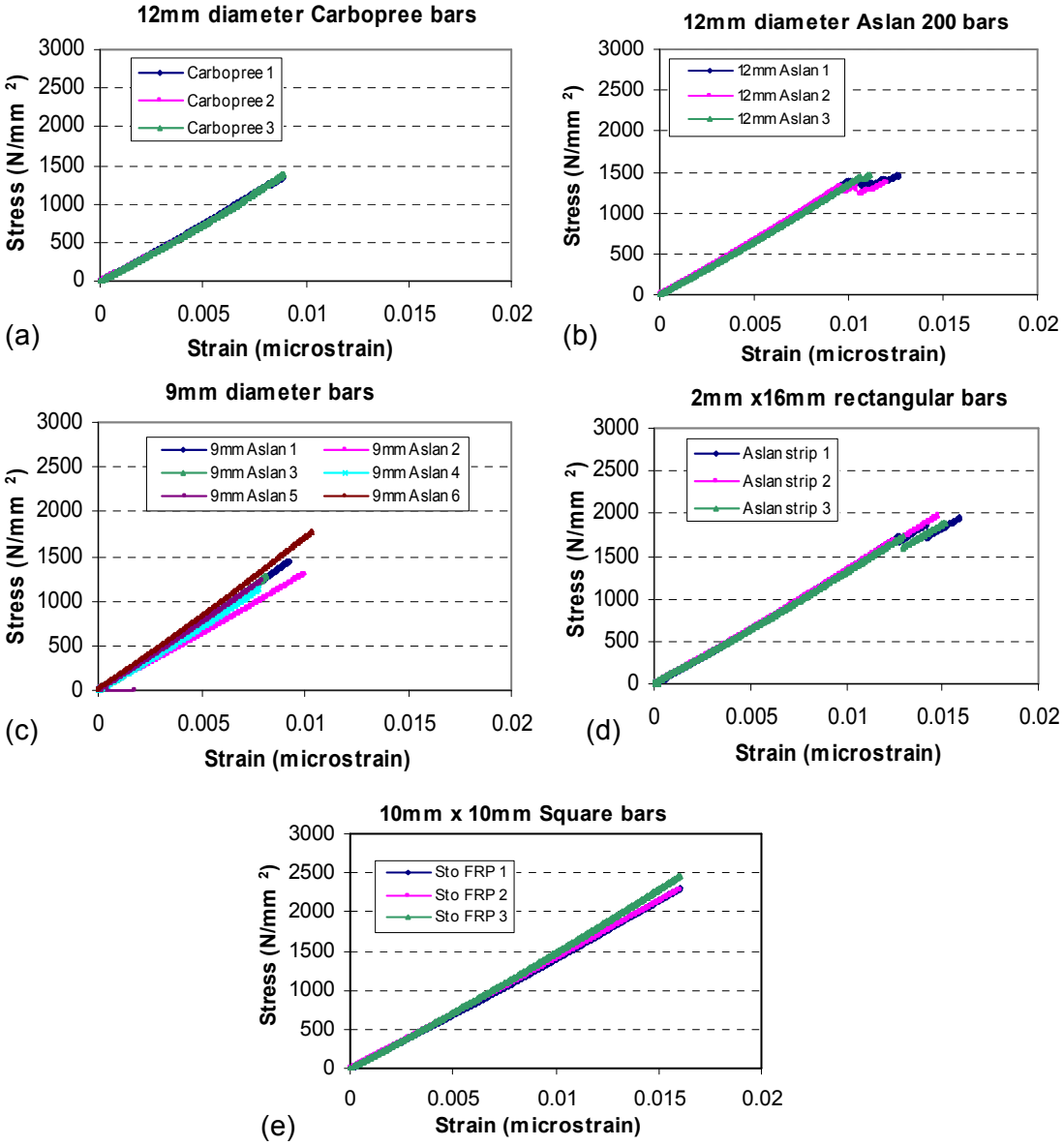

Figure 3.9 - Stress-strain relationships: (a) 12mm Carbopree bars, (b) 12mm Aslan 200 bars, (c) 9mm Aslan 200 bars, (d) 2mm x 16mm Aslan 500 strips and (e) 10mm x 10mm Sto FRP

It can be seen from Figure 3.9(c) and Table 3.9 that experimental elastic modulus values of the tested samples of 9mm Aslan 200 bars vary significantly ranging from 122kN/mm^2 to 158kN/mm^2. Due to this inconsistency, even the number of coupons tested was increased from three to six. However, still with the increased number of samples, there was a significant variation in the elastic modulus. Therefore, Young's modulus was also calculated from the nominal tensile strain, i.e., based on the elongation over the distance between grips, and found to be around an average of

120kN/mm^2 which is closer to the manufacturer specified value (124kN/mm^2). Local effects near the middle region due to fibre splitting and slipping at the grips could have affected the strain gauge readings leading to this erroneous behaviour.

3.7.4 Epoxy resins

The main adhesive used was a high modulus, high strength two-part structural epoxy paste which is commercially called Sikadur 30. Another type of resin, StoBPE Lim 465/464 which comes with a primer, was used only for the specimens with square bars which was the compatible resin recommended by the manufacturer of the square bars. The primer is called StoBPE Primer 50 Super/StoBPE Hardare 50. Some of the adhesive properties according to the supplier are listed in Table 3.11 and the experimental values found from flexural tests and compression tests are listed in Tables 3.12 and 3.13, respectively.

Resin type	**Compressive strength (N/mm^2)**	**Tensile strength (N/mm^2)**	**Shear strength (N/mm^2)**	**Modulus of elasticity (kN/mm^2)**
Sikadur 30	85-95 (EN 196)	26-31(DIN 53455)	16-19 (FIP)	12.8 (FIP)
StoBPE Lim 465/464	103	31	17.6	7

Table 3.11 - Properties of epoxy adhesives (Manufacturer specified values (Sika, 2006; Sto, 2007))

3.7.4.1 Flexural tests

To characterise some mechanical properties of the epoxy adhesives experimentally, flexural and compressive tests were carried out in accordance with BS: EN: 196-1 (BSI, 2005). The specimen dimensions were 40mm x 40mm x 160mm. The two components of the epoxy were mixed together using an electric drill with a blade attached to it and poured in to phenolic coated plywood moulds. All specimens were cured under laboratory conditions, at about 20ºC and 70% relative humidity. Testing was conducted after 7 days of casting. Five specimens from each adhesive were tested and the

average values were calculated. The flexural tests were conducted in a 100kN universal testing machine under load control at a rate of 50N/s (Figure 3.10).

Trial number	**Bending strength (N/mm^2)**	
	Sikadur 30	**Sto BPE Lim 465/464**
1	43.3	35.5
2	48.3	38.5
3	49.4	35.6
4	39.8	40.2
5	39.3	36.8
Average	**44.0**	**37.3**
Standard deviation	**4.7**	**2.0**
Coefficient of variation	**10.6%**	**5.5%**

Table 3.12 - Flexural strength of the adhesives

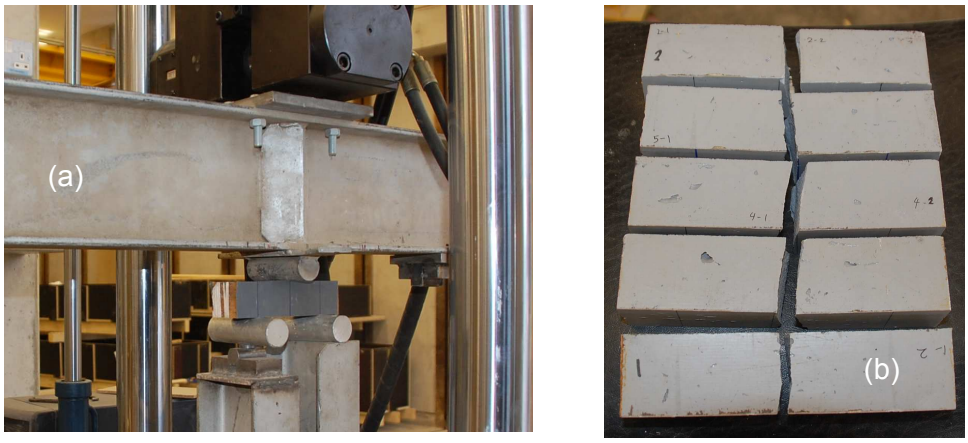

Figure 3.10 - Flexural tests: (a) set-up and (b) failed specimens

3.7.4.2 Compressive tests

Compressive tests were carried out on halves of the prisms broken in the flexural tests, and tested in a 200tonne universal testing machine under load control at a rate of 2400N/s using 40mm x 40mm loading platens (Figure 3.11).

Trial number	Compressive strength (N/mm^2)	
	Sikadur 30	**Sto BPE Lim 465/464**
1	94.8	89.0
2	88.9	87.2
3	87.5	82.9
4	89.0	88.0
5	87.3	92.5
6	91.8	92.0
7	90.0	94.0
8	91.2	93.2
9	90.5	94.6
10	88.6	93.5
Average	**90.0**	**90.7**
Standard deviation	**2.3**	**3.8**
Coefficient of variation	**2.5%**	**4.1%**

Table 3.13 - Compressive strength of the adhesives

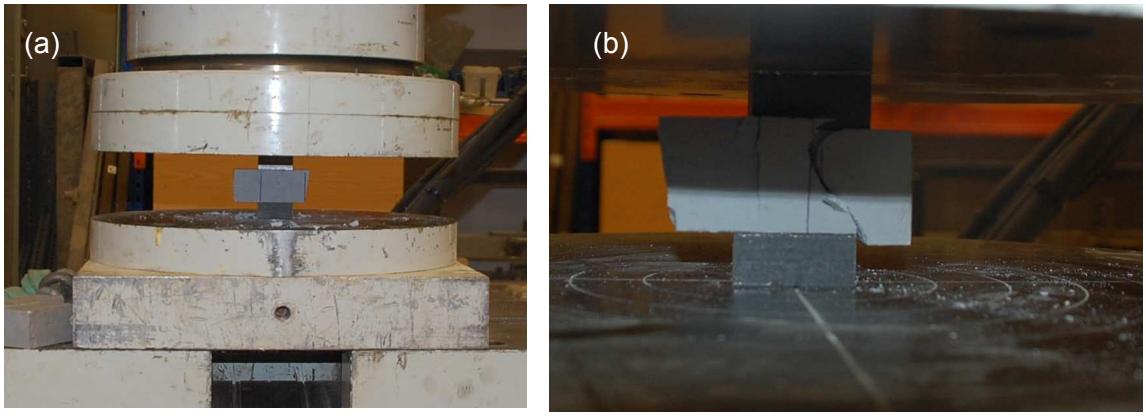

Figure 3.11 - Compression tests: (a) test set-up and (b) a failed specimen

3.8 Specimen preparation

The main bond specimens were cast in the concrete laboratory at the University of Bath. The formwork used was of steel, ensuring straight edges and a high surface quality. After making the reinforcement cages, they were positioned inside the formwork using 30mm plastic spacers (Figure 3.12(a)). Concrete was mixed using a

mechanical concrete mixer and three bond specimens, at least three concrete cubes and three concrete cylinders were cast per batch. After the casting, the exposed concrete surfaces of the specimens, cubes and cylinders were immediately wrapped with polythene sheets to allow initial curing by controlling the moisture. After two days of this curing, the specimens, cubes and cylinders were removed from the moulds and wrapped completely with damp clothes for continued curing. After a further 5 days, the wrappings were removed. In the first six test series, grooves were cut on the surface of the concrete blocks to the required size using a table-mounted concrete saw (Figure 3.12(b)). In the other series, a different concrete saw was used which was more flexible in manual handling and more accurate in dimensioning the groove (Figures 3.12(c) and (d)). Maximum care was taken to avoid any deviations while cutting the slots. The concrete area contained between two narrow grooves (Figure 3.12(d)) was chiselled out up to the required depth. After cleaning the slot with compressed air, the required bond length was marked on the surface of the block and the CFRP bar was bonded into the groove using the adhesive.

Figure 3.12 - (a) Reinforcement cages, (b), (c) and (d) saw cutting of the grooves on the concrete cover

The positioning of NSM CFRP bars was centrally within the groove as shown in Figure 3.13(a). However, rectangular (Blaschko and Zilch, 1999; Hassan and Rizkalla, 2003) and square bars (Carolin and Taljsten (2002) cited by De Lorenzis and Teng (2007)) have also been bonded along only three sides as in Figure 3.13(b).

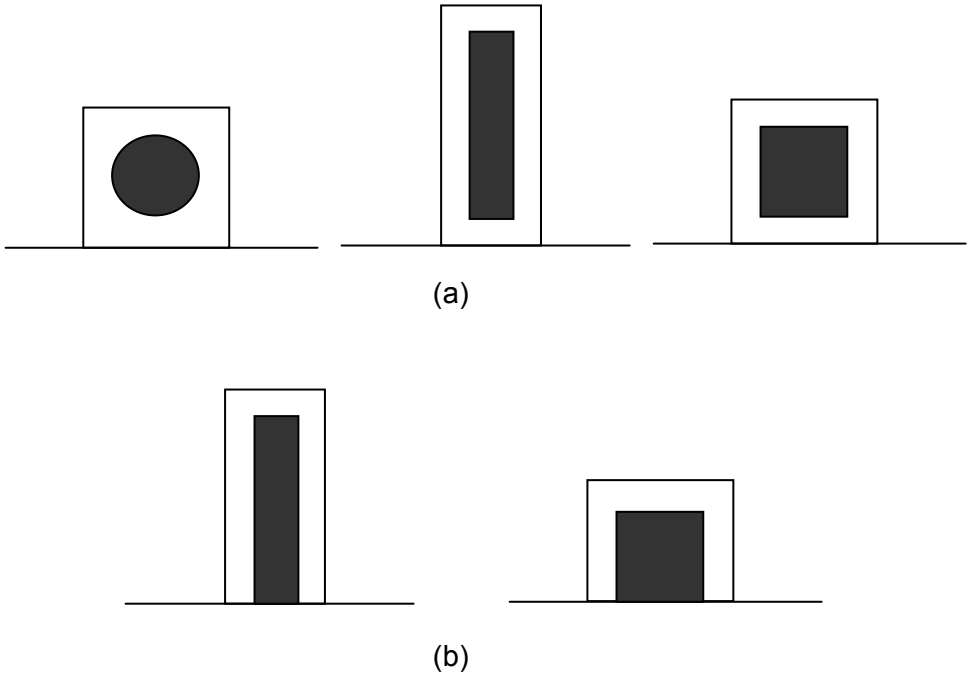

Figure 3.13 - Positioning of various shapes of FRP bars within the groove: (a) central positioning and (b) bonding along three sides only

The strain gauges were aligned along the CFRP bar before being bonded into the groove. The sand coating of the bars was removed using abrasion paper at the spots where the strain gauges were to be applied. When applying the resin, firstly, the groove was filled halfway with the resin, and then the bar was placed over the resin and slightly pressed into the resin. More resin was applied until the groove was completely filled. Finally, the surface was levelled as neatly as possible. Some modelling clay was used at the two ends of the bonded zone to limit the spilling of the adhesive so that the resin would not flow beyond the desired length. Two strips of masking tape were applied parallel with the slot before bonding the bar. After the application of the resin, the tapes were removed so that a neatly finished bonded surface was obtained.

When the resin StoBPE Lim 465/464 was used, the resin was applied 24 hours after application of the primer. However, some small shrinkage cracks could be seen on the concrete surface where the primer had been applied (Figure 3.14(c)). After allowing the adhesive to cure for 7 days, the blocks were painted white for better observation of cracks, and were tested normally on or after 14 days of age. Various steps involved in preparing the specimens are shown in Figures 3.12 and 3.14.

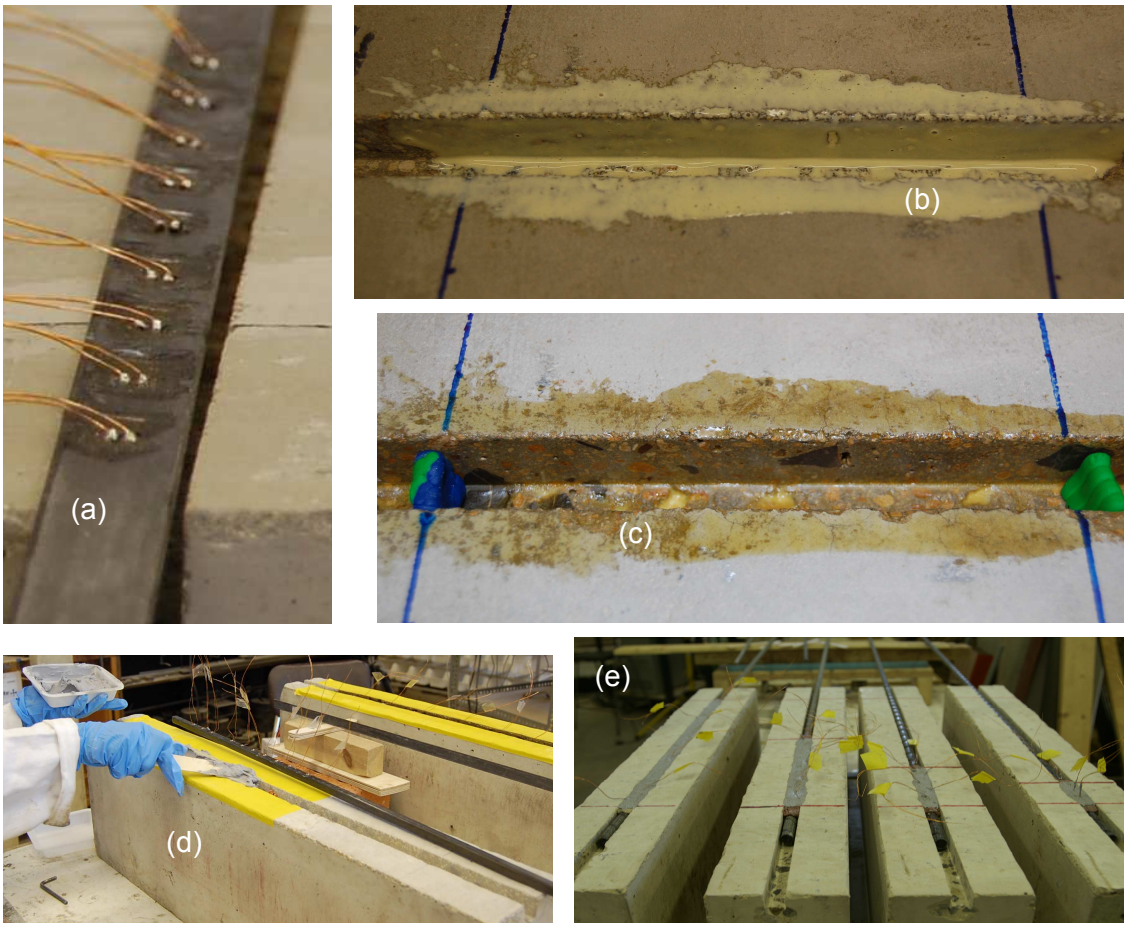

Figure 3.14 - (a) Strain gauges on a CFRP rectangular bar, (b) application of the primer, (c) after the curing of the primer, (d) bonding CFRP bars into the concrete member and (e) specimens set for testing

3.9 Instrumentation and loading arrangement

The strain distribution along the bar in the bonded region was monitored by suitably placed several strain gauges, whose gauge length was 6mm, while one strain gauge was positioned in the unbonded region. The number of strain gauges used from one specimen to another was different, depending on the length of bond. The strain gauge positioning for 12mm diameter bars is shown in Figure 3.15 and alignment of strain gauges for the other bars can be found in Appendix A. The CFRP bar with strain gauges was placed in the groove as in Figure 3.16, i.e. on the side from which there is the least contribution to bond action, in order to minimise the disturbance from the strain gauges to bond. The CFRP bar was gripped to the machine jaws, by placing two

2mm thick aluminium tabs in between the bar and the jaws, as described in Section 3.7.3.

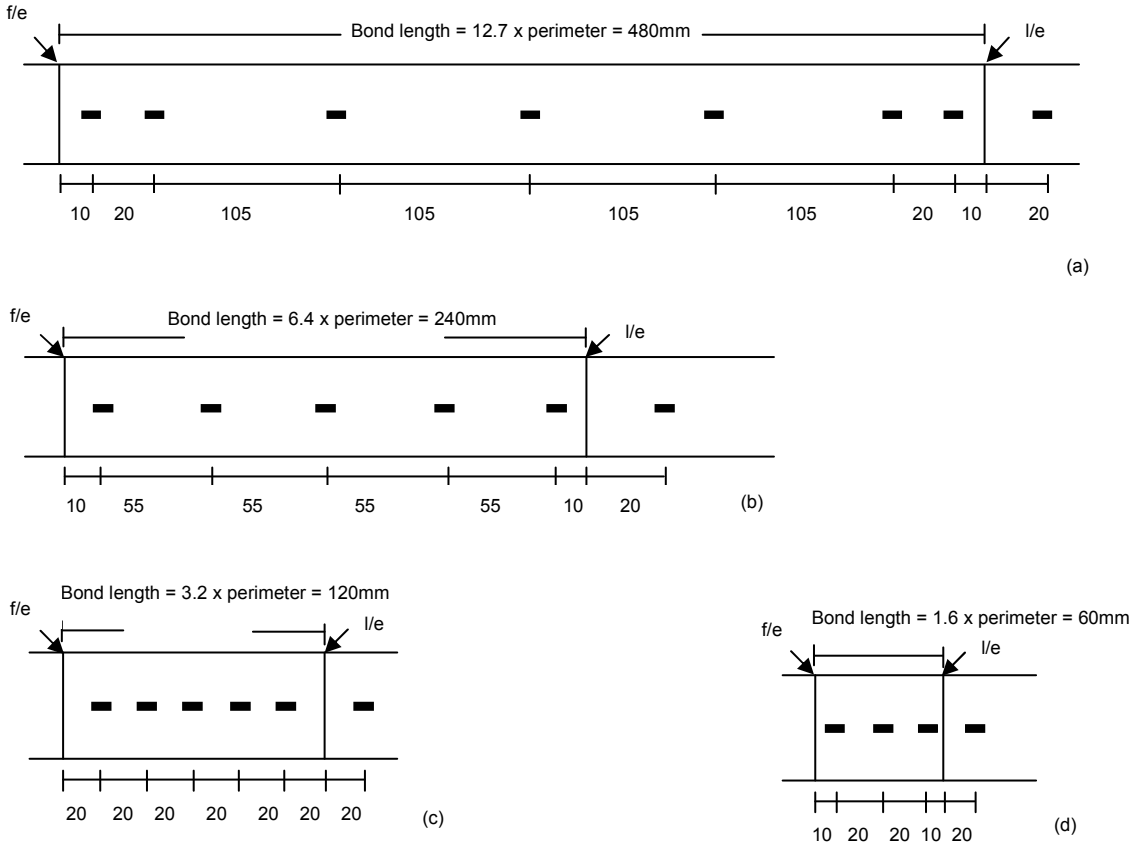

Figure 3.15 - Alignment of strain gauges for 12mm diameter bars: (a) 480mm, (b) 240mm, (c) 120mm and (d) 60mm (all dimensions are in mm)
(Note: f/e-free end and l/e-loaded end)

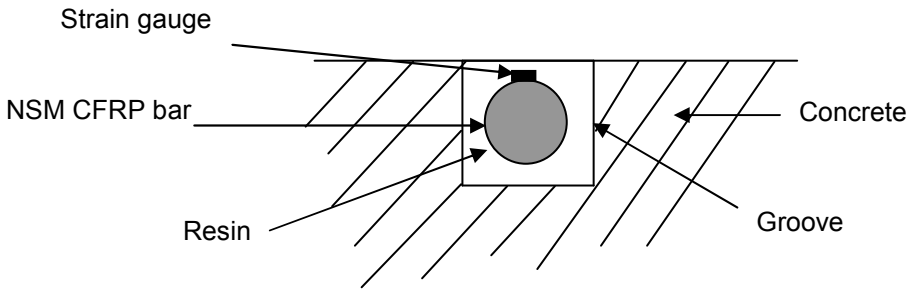

Figure 3.16 - Alignment of the CFRP bar with strain gauges

The load was applied by a universal testing machine with a capacity of 2000kN, at a cross-head displacement rate of 0.5mm/min. Linear Variable Displacement Transducers (LVDTs) were used to measure the free end and the loaded end slips.

The external compressive force and the reaction of the bottom support were monitored by two load cells of 500kN and 200kN capacities, respectively. The applied load, slips and strains were all recorded using System 5000 Data Logger and a recording software, Strainsmart. Figure 3.17 indicates the test set-up.

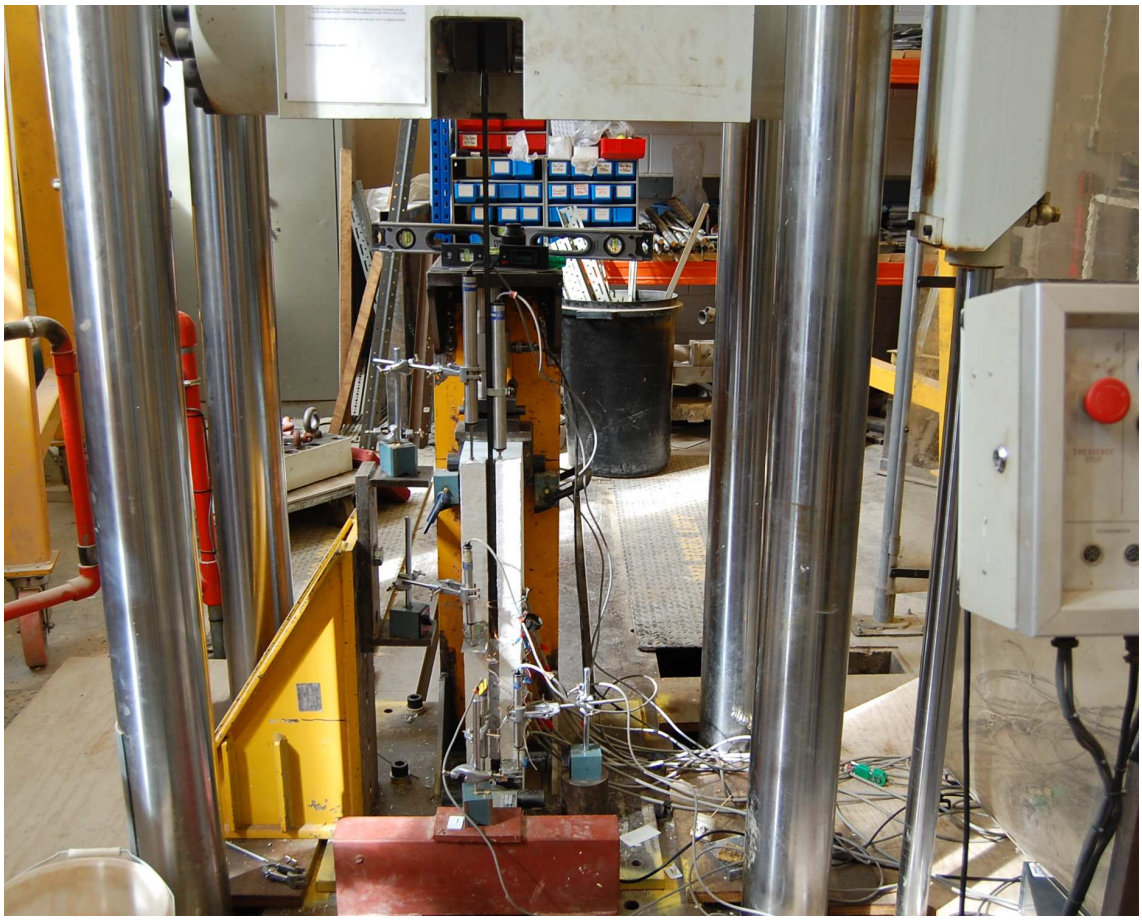

Figure 3.17 - Bond test set-up

3.10 Concluding remarks

To assess the bond performance between NSM CFRP bars and concrete, small scale beam-type bond tests were carried out. Several critical bond parameters such as bond length, bar shape, bar surface texture, bar cross-sectional area, concrete strength, groove size and resin type, were investigated. Next chapter presents the results of the bond tests and discusses the effect of the investigated variables.

CHAPTER 4 – TEST RESULTS & DISCUSSION

This chapter presents a detailed description of the results obtained from the bond tests on circular, rectangular and square CFRP bars, along with their failure modes and the underlying mechanics. The effect of the investigated variables on bond behaviour of NSM CFRP bars is discussed in detail. Furthermore, critical failure modes are identified depending on the bar shape.

4.1 Circular CFRP bars

Table 4.1 summarises the main results of the bond tests containing circular bars, in terms of the ultimate capacity, ultimate load as a percentage of tensile strength of the bar, strain of the bar at the unbonded region when the ultimate capacity is reached, average bond strength and failure mode.

4.1.1 Repeat tests

Specimens *1-1[C12/60/S/1.6p]*, *1-2[C12/60/S/3.2p]*, *1-3[C12/60/S/6.4p]*, *1-4[C12/60/S/12.7p]* and *4-11[A9/60/S/6.4p]* were repeated due to the reasons mentioned in Section 3.4.

4.1.2 Failure modes

Figure 4.1 details the interfacial failure modes associated with the two interfaces (bar-resin interface and resin-concrete interface) of NSM FRP bonded joints, along with the critical factors in determining the failure. These failure modes are generally defined as pull-out failures because they cause the bar to be pulled out of the joint.

Several failure modes were identified in the bond tests: shearing off of the outer layer of the bar (SOOL), resin splitting alone or with fracture in the concrete along inclined planes, resin-concrete interface failures, concrete cover separation failure (CCSF) and

fracture of edge concrete (edge concrete splitting). Sometimes the failure was a discrete mode and sometimes it was a combined failure of the above modes. Shear cracking could be seen in specimens containing longer bond lengths. Some of the above failure modes have previously been identified as the common failure modes observed in NSM FRP systems (De Lorenzis and Teng, 2007).

Series number	Specimen number	Specimen designation	Ultimate load (kN)	Ultimate load as a % of nominal tensile strength	Strain at ultimate load (%)	Average bond strength (N/mm^2)	Failure mode
1	1	*1-1[C12/60/S/1.6p]*	22.0	8.45	0.129	9.72	N/A
	2	*1-2[C12/60/S/3.2p]*	32.9	12.7	0.202	7.27	Splitting[1]
	3	*1-3[C12/60/S/6.4p]*	57.8	22.2	0.295	6.39	Splitting[1]
	4	*1-4[C12/60/S/12.7p]*	70.8	27.2	0.479	3.91	SOOL
	1-repeat	*1-1[C12/60/S/1.6p]repeat*	27.7	10.7	0.186	12.3	SOOL
	2-repeat	*1-2[C12/60/S/3.2p]repeat*	39.7	15.3	0.301	8.78	SOOL+Splitting[2]
	3-repeat	*1-3[C12/60/S/6.4p]repeat*	51.5	19.8	0.300	5.69	SOOL
	4-repeat	*1-4[C12/60/S/12.7p]repeat*	73.1	28.1	0.498	4.04	SOOL
2	17	*2-17[A9/60/L/1.6p]*	19.1	14.5	0.174	15.0	Splitting[2]
	18	*2-18[A9/60/L/3.2p]*	34.9	26.4	0.415	13.7	Splitting[1]
	19	*2-19[A9/60/L/6.4p]*	58.2	44.1	0.531	11.4	CCSF
	20	*2-20[A9/60/L/12.7p]*	79.0	59.8	0.793	7.76	CCSF
3	21	*3-21[A12/60/S/1.6p]*	26.1	11.2	0.127	11.6	RCIF[1]
	22	*3-22[A12/60/S/3.2p]*	46.9	20.1	0.300	10.4	Splitting[2]
	23	*3-23[A12/60/S/6.4p]*	70.5	30.1	0.487	7.79	Splitting[2]
	24	*3-24[A12/60/S/12.7p]*	76.0	32.5	0.474	4.20	CCSF
4	9	*4-9[A9/60/S/1.6p]*	21.6	16.4	0.199	17.0	Splitting[2]+ECS
	10	*4-10[A9/60/S/3.2p]*	33.1	25.1	0.303	13.0	Splitting[2]+ECS
	11	*4-11[A9/60/S/6.4p]*	48.8	37.0	0.502	9.59	PF
	11-repeat	*4-11[A9/60/S/6.4p]repeat*	52.9	40.1	0.642	10.4	Splitting[2]
	12	*4-12[A9/60/S/12.7p]*	68.4	51.8	0.649	6.72	Splitting[2]+ECS
5	5	*5-5[C12/30/S/1.6p]*	28.6	11.0	0.142	12.7	RCIF[2]+ECS
	6	*5-6[C12/30/S/3.2p]*	37.3	14.3	0.215	8.24	Splitting[1]
	7	*5-7[C12/30/S/6.4p]*	66.2	25.5	0.381	7.32	RCIF[2]
	8	*5-8[C12/30/S/12.7p]*	69.0	26.6	N/A	3.82	CCSF
6	13	*6-13[A9/30/S/1.6p]*	20.1	15.3	0.186	15.8	RCIF[1]
	14	*6-14[A9/30/S/3.2p]*	27.6	20.9	0.287	10.8	Splitting[2]
	15	*6-15[A9/30/S/6.4p]*	44.8	33.9	0.437	8.80	Splitting[1]
	16	*6-16[A9/30/S/12.7p]*	50.7	38.4	0.462	4.98	CCSF

Table 4.1 - Test results of specimens containing circular bars

(Note: SOOL– shearing off of the outer layer of the bar, Splitting[1]- resin splitting, Splitting[2]- resin splitting accompanied by fracture in the concrete along inclined planes, RCIF[1]- resin-concrete interface failure (interfacial failure), RCIF[2]- resin-concrete interface failure (cohesive shear failure in the concrete), PF- Premature failure at the grips, ECS- edge concrete splitting and CCSF- concrete cover separation failure)

Shearing off of the outer layer of the bar (SOOL) was observed for Carbopree bars and this type of failure can be classified as one of the interface failures (or pull-out failures) as detailed in Figure 4.1. Pure interfacial failure of the bar-resin interface occurs when the bond is primarily dependent on the chemical adhesion between the adherends and the degree of surface deformations is not strong enough to provide sufficient mechanical interlocking to resist bond stresses. However, pure bar-resin interfacial failure was not observed in any of the circular bars tested as they consisted of a moderate degree of surface texture. As shown in Figure 4.1 cohesive shear failure within the resin can be classified as a common failure mode for both the interfaces and was not observed in any of the specimens comprising circular bars as the shear strength of the selected adhesive was reasonably high. Both pure resin-concrete interfacial failure and cohesive shear failure in the concrete were observed in some specimens containing circular bars and are further described in Section 4.1.2.2.

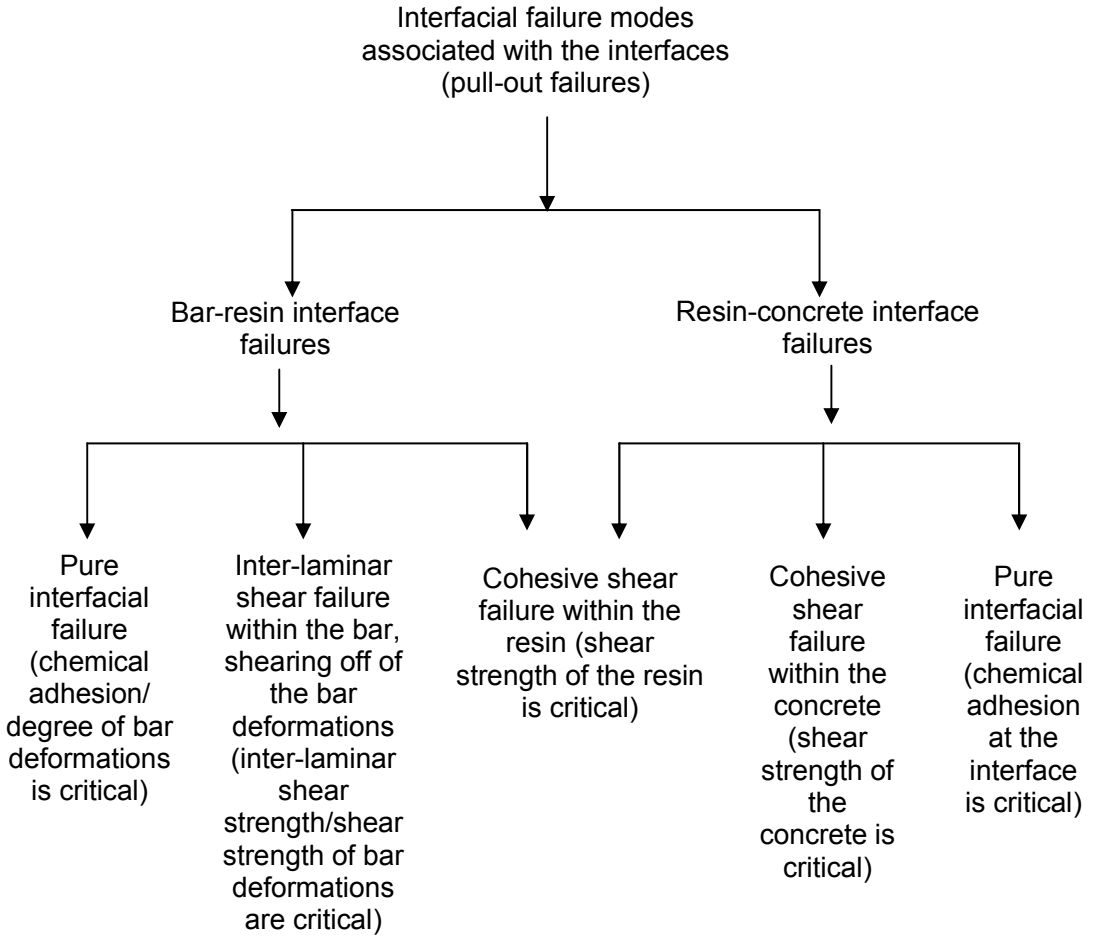

Figure 4.1 - Interfacial failure modes associated with the two interfaces of NSM FRP joints

4.1.2.1 Shearing off of the outer layer of the bar (SOOL)

Shearing off of the outer layer of the bar was observed only for Series 1 tests containing Carbopree bars, which were spirally wound and sand coated. Failure was caused by the shear stresses exceeding the inter-laminar shear strength of the bar. All the repeat specimens in Series 1 failed in SOOL or in a combined mode of SOOL and resin/concrete splitting. However in many cases there was no sign of failure, except a small amount of slippage at the loaded end with or without some resin splitting near the loaded end. Specimen *1-2[C12/60/S/3.2p]repeat* experienced a mixed mode of SOOL and resin/concrete splitting. All the other specimens, *1-4[C12/60/S/12.7p]repeat*, *1-3[C12/60/S/6.4p]repeat* and *1-1[C12/60/S/1.6p]repeat*, did not show any obvious signs of failure. Therefore, the primary failure mode was not clear by only observing the failed specimens. After the bond failure, loading was continued until the bar was completely pulled out. Pulled out bars of specimens *1-4[C12/60/S/12.7p]repeat* and *1-3[C12/60/S/6.4p]repeat* revealed that the outer layer of the bar was sheared off severely as it pulled out, especially for long bond lengths (Figure 4.2).

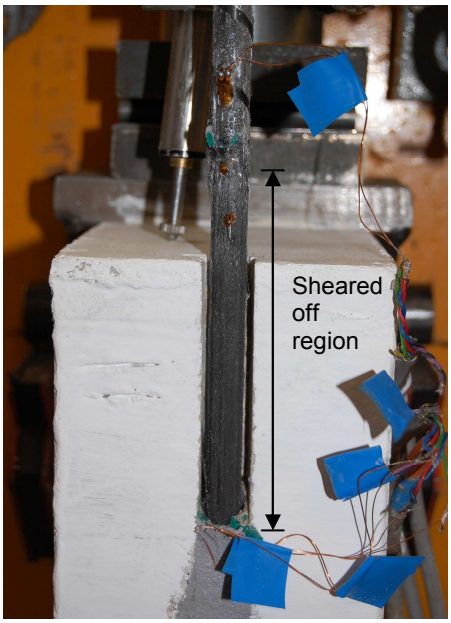

Figure 4.2 - Shearing off of the outer layer of the Carbopree bar in specimen *1-4[C12/60/S/12.7p]repeat*

In specimen *1-4[C12/60/S/12.7p]repeat*, it was found that the shearing of the outer layer occurred at some locations near the loaded end at a load level of about 80% of its ultimate capacity when the strain gauge readings were analysed. The strain gauge readings at these locations started to decrease at that load level (80% of the ultimate capacity) onwards as the applied load increased. This reduction of strain gauge reading was due to the release of stress in the sheared off fibres on which the strain gauges were attached. A release of stress at these intermediate locations between the loaded end and the free end can occur only due to the separation of the outer layer of bar (shearing off) at these strain gauge locations. This scenario was seen in most of the repeat specimens of Series 1. Further, in the original specimen, *1-4[C12/60/S/12.7p]*, the strain gauge readings revealed the same scenario. Figure 4.3 clearly depicts this state with the strain gauges remaining underneath the sheared off outer layer of the bar.

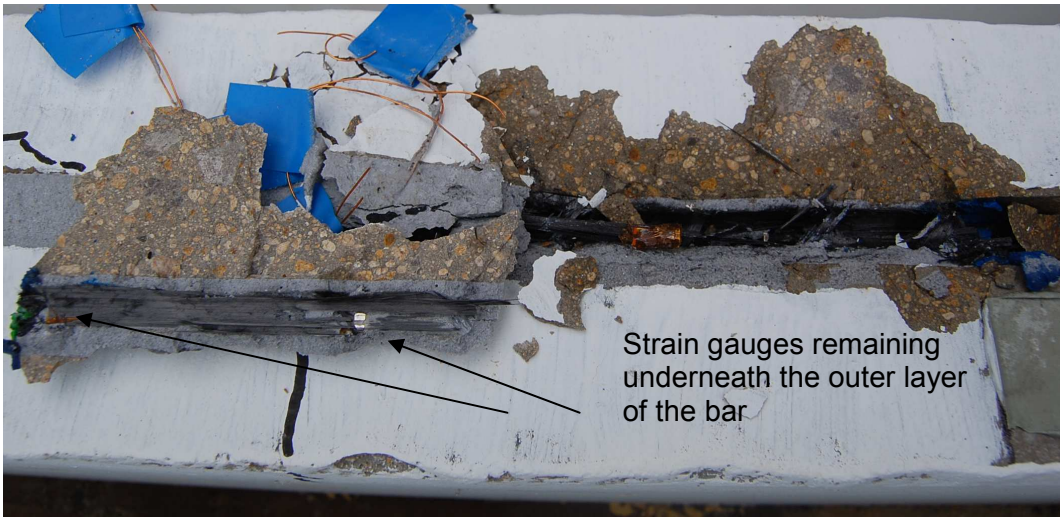

Figure 4.3 - Specimen *1-3[C12/60/S/6.4p]repeat* after complete pulling-out of the bar

When the loading was continued after the initial failure in specimens *1-4[C12/60/S/12.7p]repeat* and *1-3[C12/60/S/6.4p]repeat*, load increased up to a considerable level (about 70% of the ultimate capacity) and was sustained at that load level until the bar was completely pulled out. Further, specimen *1-4[C12/60/S/12.7p]* resisted a residual load level of about 60% of the ultimate load at the time of aborting the loading. This is probably because the failure occurred along only part of the bonded joint so that the rest of the joint could again pick the load up considerably until the joint failed completely.

While SOOL dominated failure of Series 1 containing Carbopree bars, the specimens in Series 5, also containing Carbopree bars, did not experience SOOL since their failure mode was controlled by the concrete failure as the low concrete strength was more critical than the inter-laminar shear strength of the bar.

4.1.2.2 Resin-concrete interface failures

Pure resin-concrete interfacial failure was observed in specimens *3-21[A12/60/S/1.6p]* and *6-13[A9/30/S/1.6p]* as witnessed by the absence of concrete aggregate particles attached to the resin block (Figure 4.4(a) to (d)). Only the traces of cement mortar can be seen on the bottom surface of the resin block. However, evidence of shearing could be seen on side surface of the pulled out resin block due to frictional stresses (Figure 4.4(a) and (c)). This failure mode generally results when the resin-concrete interface is weak, for example when there are impurities in the interface or when the grooves are pre-formed. This failure mode was previously observed and found to be critical for round bars bonded into pre-formed grooves due to the smooth surface of the groove (De Lorenzis et al., 2002).

Specimens *5-5[C12/30/S/1.6p]* and *5-7[C12/30/S/6.4p]* failed in cohesive shear failure in the concrete and the resin block had concrete particles attached to it, as can be seen in Figure 4.4(e) to (h). Cohesive shear failure of the concrete was previously observed in bond tests conducted on NSM CFRP strips (Seracino *et al.*, 2007).

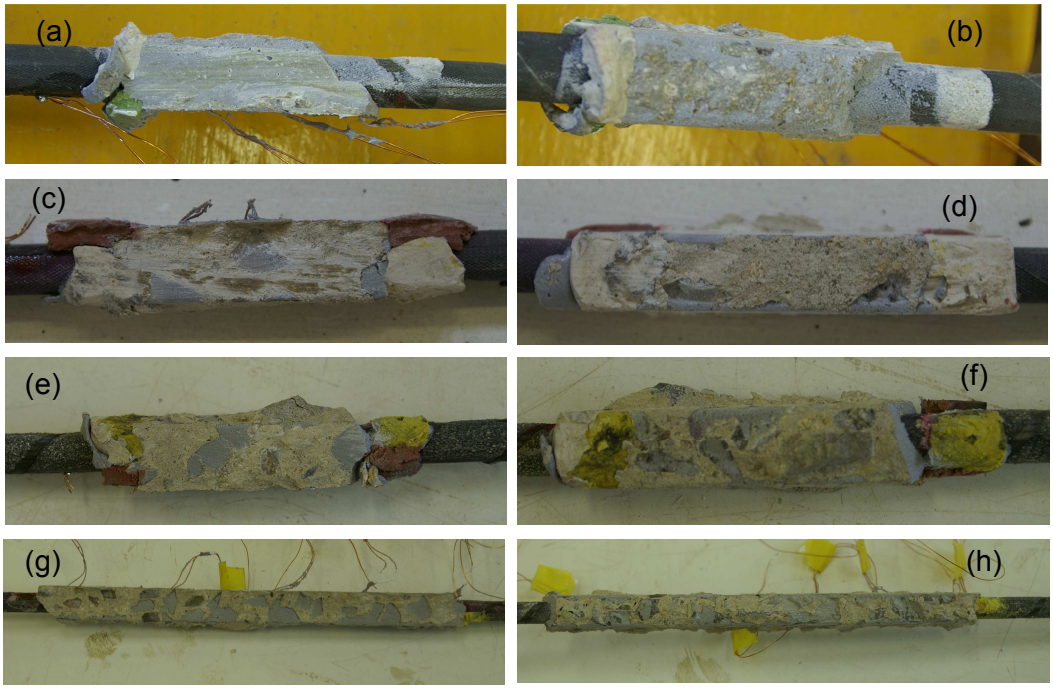

Figure 4.4 - Resin-concrete interfacial failures: in specimen *3-21[A12/60/S/1.6p]* (a) side surface and (b) bottom surface, in specimen *6-13[A9/30/S/1.6p]* (c) side surface and (d) bottom surface, in specimen *5-5[C12/30/S/1.6p]* (e) side surface and (f) bottom surface, and in specimen *5-7[C12/30/S/6.4p]* (g) side surface and (h) bottom surface

4.1.2.3 Splitting failures

Splitting failures, resin splitting and/or fracture in the concrete along inclined planes, (Figure 4.5) were the dominant failure modes for specimens containing moderate bond lengths and moderate concrete strengths. The mechanics of resin cover splitting is similar to that of splitting bond failure of deformed steel bars in concrete. The radial component of the bond stresses are balanced by hoop tensile stresses in the epoxy cover which may eventually split longitudinally if the tensile strength of the epoxy is exceeded. The concrete surrounding the groove is also subjected to tensile stresses and cracks along inclined planes may occur when the tensile strength of the concrete is reached. Whether a fracture in the concrete occurs before or after the appearance of splitting cracks in the resin cover depends on the groove size and the tensile strength of the two materials (De Lorenzis and Teng, 2007).

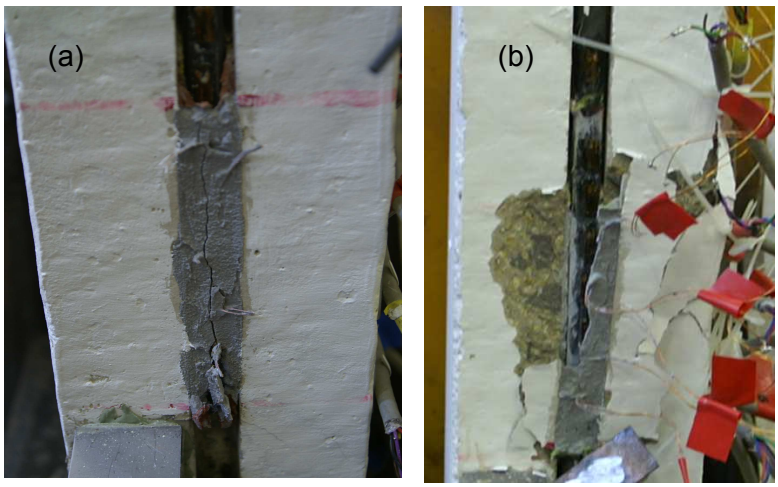

Figure 4.5 - (a) Resin splitting in specimen *5-6[C12/30/S/3.2p]* and (b) resin splitting with fracture in the concrete along inclined planes in specimen *3-22[A12/60/S/3.2p]*

Concrete splitting with no visible cracking in the resin cover has also been observed previously and is classified as one of the splitting failure modes of NSM FRP systems (De Lorenzis, 2002). For large groove depths and/or when the tensile strength ratio between concrete and resin is small, fractures in the concrete can occur before the resin crack has reached the external surface (De Lorenzis and Teng, 2007).

4.1.2.4 Concrete cover separation failure

Two types of cover separation failures were observed: localised cover separation near the high moment region forming triangular or trapezoidal concrete wedges (Figure 4.6(c), (d), and (e)) and separation of the entire cover from the free end to the far edge of the concrete specimen (Figure 4.6(a) and (b)). Further details on this failure mode can be found in Section 4.4.4.

(a) (b) (c) (d) (e)

Figure 4.6 - CCSF in specimens: (a) *2-19[A9/60/L/6.4p]*, (b) *2-20[A9/60/L/12.7p]*, (c) *6-16[A9/30/S/12.7p]*, (d) *5-8[C12/30/S/12.7p]* and (e) *3-24[A12/60/S/12.7p]*

4.1.2.5 Fracture of edge concrete

Edge concrete splitting was seen in specimens *4-9[A9/60/S/1.6p]*, *4-10[A9/60/S/3.2p]*, *4-12[A9/60/S/12.7p]* and *5-5[C12/30/S/1.6p]* (Figure 4.7). This failure mode did not occur by itself however; it was accompanied by some other failure modes. For example, it accompanied resin splitting with fracture in the concrete along inclined planes in specimens *4-9[A9/60/S/1.6p]*, *4-10[A9/60/S/3.2p]* and *4-12[A9/60/S/12.7p]* and it accompanied resin-concrete interface failure (cohesive shear failure in the concrete) in specimen *5-5[C12/30/S/1.6p]*.

Edge concrete splitting of specimen *4-12[A9/60/S/12.7p]* was different to that of the other specimens listed here. After the complete pulling out of the bar, it could be seen that the resin remaining on the groove had split longitudinally (Figure 4.7(b)) and the crack then spread towards the side face (110 x 220mm face) of the concrete specimen (Figure 4.7(c)). Furthermore, unlike in the other specimens, the local splitting crack that runs from the loaded end to the edge of the concrete specimen could not be seen in specimen *4-12[A9/60/S/12.7p]*. Therefore, the splitting crack in this specimen can not be regarded as a local concrete edge splitting around the bonded region and it is more likely a development of longitudinal splitting cracks globally in the concrete. This reveals that the surrounding concrete also splits longitudinally due to radial bond stresses in addition to the fracture along inclined planes.

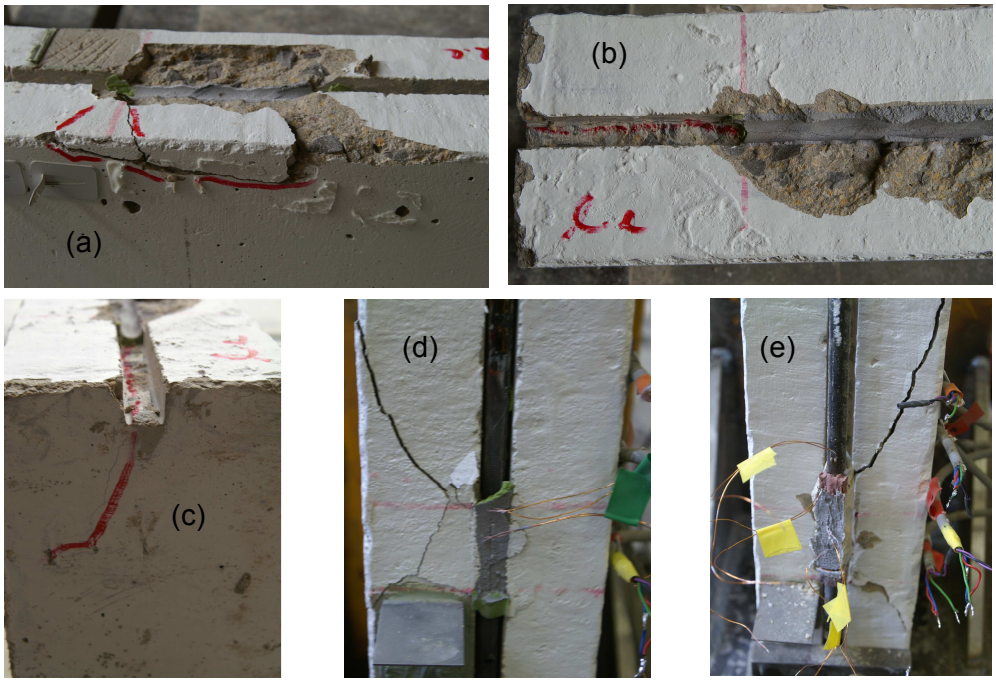

Figure 4.7 - Edge concrete splitting in specimens: (a) *4-10[A9/60/S/3.2p]*, (b) and (c) *4-12[A9/60/S/12.7p]*, (d) *4-9[A9/60/S/1.6p]* and (e) *5-5[C12/30/S/1.6p]*

4.1.3 Flexural/shear cracks

A crack at the free end was observed in almost all of the specimens, which is attributed to strain incompatibility between CFRP bar and the concrete at the termination point. Flexural/shear cracking could be seen for most of the specimens containing long bond lengths (6.4 and 12.7 times the bar perimeter). Deep shear cracks could be seen in specimens containing the maximum bond length (12.7 times the bar perimeter). When the failure mode was CCSF, cracks started from the free end and spread longitudinally towards the loaded end at the internal steel reinforcement level. Further, flexural cracks could also be seen near the maximum moment regions, which often had the effect of causing the local concrete cover separation to form into concrete wedges. However, a shear failure in the specimen was never observed as the specimens were designed not fail in shear. Figure 4.8 shows flexural/shear cracks formed in some of the specimens.

As expected, the flexural/shear cracking occurred for long bond lengths, which alters the pure bond behaviour between NSM CFRP bars and concrete. It has been reported that debonding mechanisms of NSM FRP bond tests are different to those of actual

beams strengthened with NSM FRP systems (De Lorenzis and Teng, 2007). For example, CCSF has not been previously observed for NSM FRP bond tests, which is primarily because of limitations imposed on the bond length to avoid flexural cracking. However, CCSF has been observed for tests where NSM FRP systems have been used for flexural strengthening of beams (Corden *et al.*, 2008; De Lorenzis, 2002; Soliman *et al.*, 2008; Teng *et al.*, 2006). Therefore, results such as bond stress-slip curves of NSM FRP bond tests carried out in previous investigations (De Lorenzis, 2002; Sena Cruz, 2004), cannot be directly transferred into predictive models for actual beams. This is because there is no simple or direct relationship between the debonding modes of those bond tests and that of beam tests due to presence of flexural/shear cracks altering the bond stress-slip distribution. As the failure modes of the bond tests carried out in the current research resemble the real situation, allowing flexural/shear cracking to occur, the results obtained will have a wider applicability once the size-effect issues are addressed quantitatively as discussed in Section 4.4.4.

Even though the specimens of the current study included internal reinforcement, most of the failure modes were similar to those observed for bond tests for NSM FRP reinforcement (De Lorenzis and Teng, 2007), for specimens containing moderate bond lengths and comprised quite high bond strength values as listed in Table 5.1. However, for relatively long bond lengths the bond behaviour was affected by flexural/shear cracking and was different to that of the previous NSM bond tests. CCSF was observed in these beam type bond tests for long bond lengths unlike in the previous NSM bond tests which did not have any internal steel reinforcement. Bond mechanisms of CCSF are discussed in Section 4.4.4. CCSF seemed to play an important role as the critical failure mode for NSM FRP bars with relatively high cross-sectional area/perimeter ratios, by limiting the bond capacity of beams strengthened with such NSM FRP systems. It was seen that the real beam behaviour can be qualitatively investigated in small scale beam-type bond tests with internal reinforcement as they fail in similar modes to those of real beams. The observed effects of flexural/shear cracking on local bond stress-slip relationship are discussed in Chapter 5. However, because the effect of internal reinforcement was not investigated as a parameter in this study, the differences in bond behaviour of specimens containing and not containing internal reinforcement could not be directly quantified.

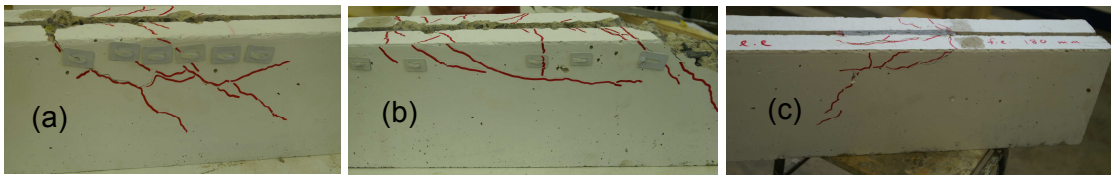

Figure 4.8 - Flexural/shear cracking in specimens: (a) *5-7[C12/30/S/6.4p]*, (b) *5-8[C12/30/S/12.7p]* and (c) *6-15[A9/30/S/6.4p]*

4.1.4 Effect of the test variables

4.1.4.1 Bond length

In all series, the ultimate load was seen to increase as the bond length increased. However, the relationship between the ultimate load and the bond length is not linear due to the non-uniform distribution of bond stresses. Consequently, average bond strength reduces as the bond length increases. Figure 4.9 depicts the effect of bond length on the ultimate load and the average bond strength. For Series 3, 5 and 6, ultimate load seems to increase as the bond length increases and stays uniform after a certain length, for further increments of bond length. In these series, the final points of these curves are characterised by CCSF while the penultimate points are characterised by one of the other debonding modes listed previously, frequently by splitting failures. However, this trend does not occur for Series 2, where both the final point and the penultimate point represent CCSF. The final points of these curves represent CCSF, which is a failure mode limiting the actual bond capacity so that the conclusion that a constant load level can be attained beyond a certain bond length is not valid. This shows that the ultimate capacity can be increased when the bond length is increased for specimens failing in CCSF, although without a change in the failure mode. In addition, Series 1 and Series 4 do not follow the trend of attaining a uniform load level beyond a certain bond length where the final points of the curves are not characterised by CCSF. Therefore, it seems that the existence of an effective bond length beyond which there is no further increase in ultimate load is not necessarily applicable to NSM FRP bonded joints, unlike with externally bonded FRP systems.

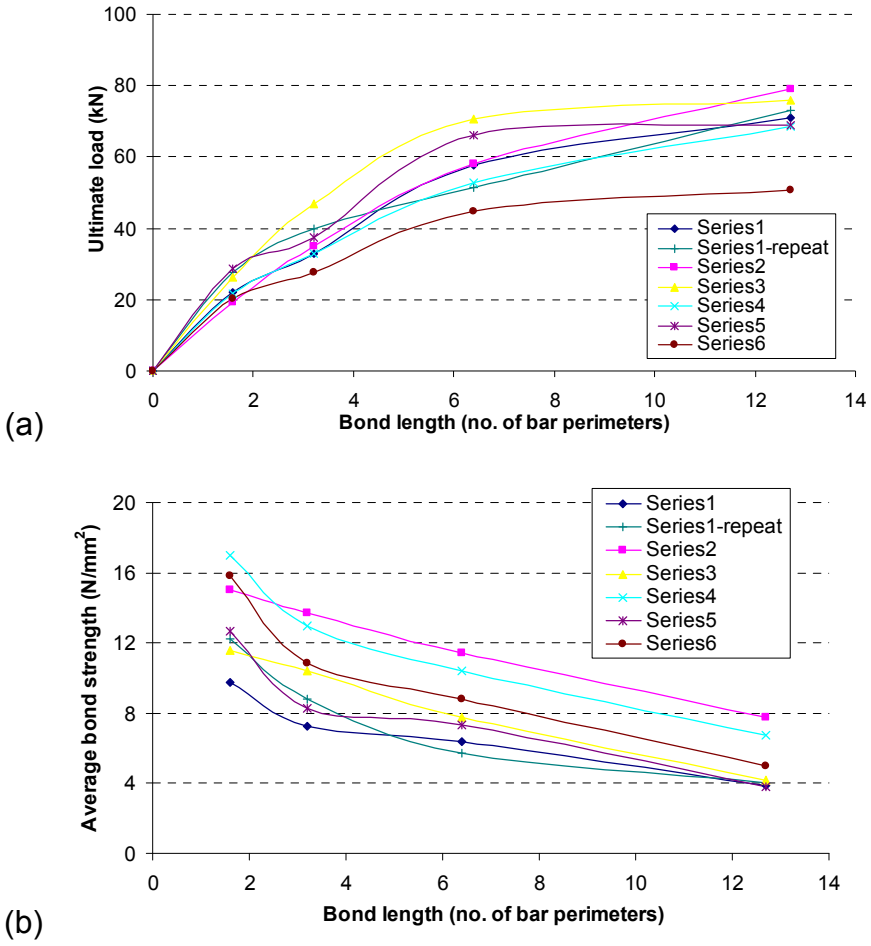

Figure 4.9 - (a) Ultimate load vs. bond length and (b) average bond strength vs. bond length for specimens containing circular bars

4.1.4.2 Groove size

A comparison between Series 2 and 4 allows the effect of groove size on bond behaviour to be examined. When the groove size was large, in Series 2, the thickness of the resin cover was also large so that the resistance to splitting of the resin cover increased, therefore, in general, the ultimate load capacity increased correspondingly. The increase/decrease in the ultimate load due to increase in groove size were -13.1%, 5.1% and 9% for specimens containing bond lengths of 1.6, 3.2 and 6.4 times the perimeter, respectively. The maximum percentage of increase in the ultimate load (15.5%) was observed between specimens *2-20[A9/60/L/12.7p]* and *4-12[A9/60/S/12.7p]*, which had the longest bond length. The mechanics of cover splitting

bond failure of a NSM FRP-concrete bonded joint is similar to that of a deformed steel bar in concrete (De Lorenzis and Teng, 2007). The radial component of bond stresses induces hoop tensile stresses in the resin cover, which leads to longitudinal splitting of the resin cover once the tensile strength of the resin is exceeded. Consequently, resin cover splitting failure depends on the thickness of the resin cover and the tensile strength of the resin. This explains how the ultimate capacity of specimens increased as the resin cover thickness increased because resin splitting is prevented or delayed when the resin cover thickness is increased. Further, when the groove size increases, perimeter of the resin-concrete interface also increases so that the stresses acting on the concrete are less, resulting in a delay of concrete splitting. The proposed theoretical models in Chapter 5 are consistent with this behaviour of both resin splitting and concrete splitting failures.

The change in the resin cover thickness influenced the mode of failure of specimens containing long bond lengths (6.4 and 12.7 times the bar perimeter), whereas specimens having short bond lengths (1.6 and 3.2 times the perimeter) had no significant difference in the failure modes. Both specimens *4-11[A9/60/S/6.4p]repeat* and *4-12[A9/60/S/12.7p]*, with the small groove size, failed by resin splitting accompanied by fracture in the concrete along inclined planes, whereas specimens *2-19[A9/60/L/6.4p]* and *2-20[A9/60/L/12.7p]*, with the large groove size, did not fail in resin splitting as resin splitting is prevented due to higher cover thickness and failed in a different mode, CCSF. Furthermore, specimen *2-20[A9/60/L/12.7p]* had the highest ultimate load recorded within all the specimens containing circular bars. This CCFS mode seemed to be the critical failure mode for specimens containing circular bars and is further explained in Section 4.4.4. The increase in the resin cover thickness was able to change the failure mode to a critical state provided that the bond length is equal or more than the optimum bond length as explained in Section 4.4.4.

4.1.4.3 Concrete strength

Series 4 and 6 compare the effect of the concrete strength on bond behaviour of Aslan 9mm bars and repeat tests of series 1 and 5 compare that of 12mm Carbopree bars. The effect of the concrete strength on the ultimate capacity seems to be dependent on the type of the bar. For Aslan 200 bars, the ultimate load tends to increase as the

concrete strength increases, whereas there was a marginal effect on the ultimate capacity of Carbopree bars. Percentage increments were 34.8, 18.1, 19.5 and 7.3 for specimens containing Aslan bars for bond lengths of 12.7, 6.4, 3.2 and 1.6 times the bar perimeter, respectively. Corresponding increments/decrements of specimens containing Carbopree bars were 5.9%, -22.3%, 6.5% and -3.2%, respectively.

The concrete strength seemed to influence the failure mode notably, especially for specimens having long bond lengths. Specimen *4-12[A9/60/S/12.7p]* containing the largest bond length failed in resin splitting accompanied by fracture in the concrete along inclined planes. After complete pulling out of the bar, it could be seen that both the resin cover remaining in the groove and the surrounding concrete had split longitudinally, spreading towards the edge of the concrete specimen (Figures 4.7(b) and (c)). This failure mode was caused by the tensile stresses induced on the resin cover and the concrete. The corresponding specimen in Series 6 with a low concrete strength, specimen *6-16[A9/30/S/12.7p]*, failed in CCSF owing to the low concrete strength, which is explained in Section 4.4.4.

The two specimens containing a bond length of 6.4 times the bar perimeter in both Series 4 and 6 (specimens *6-15[A9/30/S/6.4p]* and *4-11[A9/60/S/6.4p]repeat*) failed in the same mode and experienced deep shear cracks. However, some of the shear cracks in specimen *6-15[A9/30/S/6.4p]* spread horizontally from the free end towards the loaded end, at the level of the internal steel reinforcement. This explains that the concrete cover was approaching CCSF. Further, specimen *6-14[A9/30/S/3.2p]* also had a horizontal crack propagating from the free end, unlike the corresponding specimen in Series 4.

Similarly with Series 4 and 6, the comparison between Series 1 and 5 reveals that the failure modes of Series 5 were governed by concrete failure, while those of Series 1, which had high strength concrete failed in general, by shearing off of the outer layer of the bar. Two specimens in Series 5 (*5-5[C12/30/S/1.6p]* and *5-7[C12/30/S/6.4p]*) failed in resin-concrete interface failure (cohesive shear failure in the concrete). As the compressive strength of concrete reduces, shear strength also reduces so that it offers low shear resistance explaining the failure of these specimens. However, specimen *5-6[C12/30/S/3.2p]* was not influenced by the low concrete strength and failed by resin splitting. Observations following the bond failure revealed the presence of cracks in the

concrete along the groove edges spreading beyond the loaded end up to a certain distance. This demonstrates that the surrounding concrete can split longitudinally in addition to frequently observed fracture along inclined planes. In this case, the longitudinal splitting cracks in the concrete did not spread up to the edge of the specimen, unlike in Specimen *4-12[A9/60/S/12.7p]* (Figure 4.7(c)).

Similar to specimen *6-16[A9/30/S/12.7p]* in Series 6, specimen *5-8[C12/30/S/12.7p]* containing the longest bond length in Series 5 also failed in CCSF, the critical mode for circular bars, owing to low concrete strength. Therefore, it can be seen that as the concrete strength is reduced (by about half in this case), for a long bond length, the failure mode changes to a limiting mode, which depends on the concrete strength. The effect of concrete strength on this critical mode is further explained in Section 4.4.4.

4.1.4.4 Bar diameter (bar size)

Series 3 and 4 compare specimens with different sizes of bars, and show that the specimens containing 12mm bars could reach higher ultimate capacities than those containing 9 mm bars. Percentage increases of the ultimate capacity for the increase in bar diameter are 20.9, 42.4, 44.4 and 11.2 for specimens containing bond lengths of 1.6, 3.2, 6.4 and 12.7 times the bar perimeter, respectively. However, utilisation of the capacity of the tensile strength of the bar reduces notably as the bar size increases (Table 4.1). In general, it can be said that there was little difference in the failure modes except in the specimens containing the longest bond length. The dominant failure mode in these two series seems to be resin splitting accompanied by fracture in the surrounding concrete along inclined planes. However, specimen *3-24[A12/60/S/12.7p]* experienced a different mode, which is the critical (limiting) failure mode for specimens containing circular and square bars, CCSF. Therefore, it can be inferred that this limiting failure mode has restricted the possible increase in the ultimate load for this increase in bar diameter, as witnessed by the relatively low percentage increase (11.2%) for the longest bond length.

4.1.4.5 Surface deformations of bars

There is a noticeable difference between the failure modes of the specimens in Series 1 and 3, due to the difference in the surface texture and/or shear strength of the bar deformations of the bars. In general, Aslan 200 bars could develop higher ultimate capacities than Carbopree bars. The ultimate capacities of the specimens containing Aslan bars having bond lengths of 1.6, 3.2, 6.4 and 12.7 times the bar perimeter had percentage increments/decrements of -5.7, 18.1, 37 and 3.9, respectively, compared to those containing Carbopree bars.

The failure of all the specimens in Series 1 was controlled by the inter-laminar shear strength of the bar, while in Series 3, splitting failures were dominant. However, the specimen with the longest bond length, specimen *3-24[A12/60/S/12.7p]*, failed in CCSF, which is the limiting failure mode for specimens containing circular bars (further explained in Chapter 5, with respect to the local bond strength). This phenomenon demonstrates the ability of Aslan bars to produce a sound bar-resin interface, which remains intact until the critical failure mode occurs.

Normally, in any failure mode (except CCSF), failure occurs by damage to the top half of the bonded joint, leaving the bottom half intact or slightly damaged. Irrespective of the failure mode, the bottom surface of the completely pulled out Aslan bars had a resin layer stuck on it, whereas the pulled out bar surface of Carbopree bars revealed shearing off of the outer layer of the bar. In both cases, this confirms that the interface adhesion of both Aslan and Carbopree bars with the resin material was generally strong owing to the quality of the bar surface texture.

4.2 Rectangular CFRP bars

Table 4.2 summarises the main results obtained in the tests using rectangular bars. The first two specimens to be tested were specimen *8-31[R/60/L/6.4p]* and its control beam (*8-31[R/60/L/6.4p]control*) with no strain gauges, and both specimens failed in tensile rupture of the bar. Therefore, it was obvious that for any bond length greater than 6.4 times the bar perimeter, the failure and the ultimate load will be the same

because increasing the bond length beyond the development length has no effect on the mode and load at failure. Therefore, specimen *8-32[R/60/L/12.7p]* was not tested but it can be assumed that it would also fail in tensile rupture at the same load capacity as specimen *8-31[R/60/L/6.4p]*.

Series number	Specimen number	Specimen designation	Ultimate load (kN)	Ultimate load as a % of experimental tensile strength	Strain at ultimate load (%)	Average bond strength (N/mm^2)	Failure mode/ observations at failure
7	25	*7-25[R/60/S/1.6p]*	28.1	43.1	0.680	13.4	Splitting[1]
	26	*7-26[R/60/S/3.2p]*	34.3	52.7	0.823	8.29	Splitting[1]
	27	*7-27[R/60/S/6.4p]*	50.8	78.0	1.190	6.13	Splitting[1]
	28	*7-28[R/60/S/12.7p]*	57.1	87.7	1.400	3.45	FS+splitting[1]
8	29	*8-29[R/60/L/1.6p]*	26.2	40.3	0.613	12.6	Splitting[1]
	30	*8-30[R/60/L/3.2p]*	43.4	66.6	1.040	10.5	Splitting[1]
	31	*8-31[R/60/L/6.4p]*	61.6	94.6	1.440	7.44	TR
	31-control	*8-31[R/60/L/6.4p]control*	62.1	95.3	N/A	7.50	TR

Table 4.2 - Test results of specimens containing rectangular bars

(Note: TR- tensile rupture, FS- fibre splitting, Splitting[1]- partial splitting and/or cracking in the resin cover)

4.2.1 Preliminary tests

Specimen *8-31[R/60/L/6.4p]* failed in bar snapping without any damage in resin cover and the surrounding concrete at a load of 61.6kN. Only the common free end crack could be seen. The mode of failure of the control beam without any strain gauges was the same and the ultimate load was 62.1kN. Figure 4.10 indicates both the failed specimens showing no damage in the resin or the concrete. It can therefore be concluded that the application of several strain gauges on one of the side surfaces of the rectangular strip has little effect on bond behaviour of the specimen (as the mode of failure and the ultimate load for both specimens are identical).

Figure 4.10 - Specimens (a) *8-31[R/60/L/6.4p]* and (b) *8-31[R/60/L/6.4p]control* with no strain gauges (no damage in the resin or the concrete in both specimens)

4.2.2 Failure Modes

Some modes of failure were the same as observed in the specimens with circular bars, the only exception being the possibility of achieving tensile rupture of the CFRP bar without any premature bond failure. Observed failure modes included partial splitting and/or cracking in the resin, a combined fibre splitting and partial resin splitting/ cracking mode and, finally, tensile rupture. Unlike with circular bars, it was not possible to continue pulling the bar out after the bond failure (or the ultimate load) because the bar snapped simultaneously due to the shock of the failure, irrespective of failure mode. Specimen *8-29[R/60/L/1.6p]* was the only specimen that was not broken due to the shock and continued to resist load as it was pulled out after initial failure.

In short bond length specimens (1.6 and 3.2 times the bar perimeter), only partial resin splitting, especially near the loaded end was seen at failure with little sign of damage (Figure 4.11).

Figure 4.11 - Partial resin splitting in specimen *8-30[R/60/L/3.2p]*

Specimen *7-27[R/60/S/6.4p]* showed partial resin splitting/cracking near the loaded end (Figure 4.12(a)). Specimen *7-28[R/60/S/12.7p]* showed a combined mode of splitting of fibres in the CFRP bar and longitudinal resin splitting and resin cracking, as can be seen in Figure 4.12(b), at a load close to the ultimate tensile capacity of the bar. In NSM systems of rectangular FRP bars, the transverse component of the bond stresses acts on thick lateral sides of the groove as the strips are thin compared to their width, so that splitting failures are less likely to occur compared to NSM systems containing circular FRP bars (Blaschko, 2003; De Lorenzis and Teng, 2007).

Partial or complete splitting occurring in the external resin cover could not be the sole cause of failure in these specimens because the majority of the bond stresses are resisted by the thick lateral sides and only a small proportion of the bond stress is resisted by the external cover as explained above. Therefore, the exact cause of failure of specimens showing partial splitting/cracking of the resin, was identified as the macro-cracking in the resin, by analyzing the local bond stress-slip relationship as discussed in Section 5.1.6.

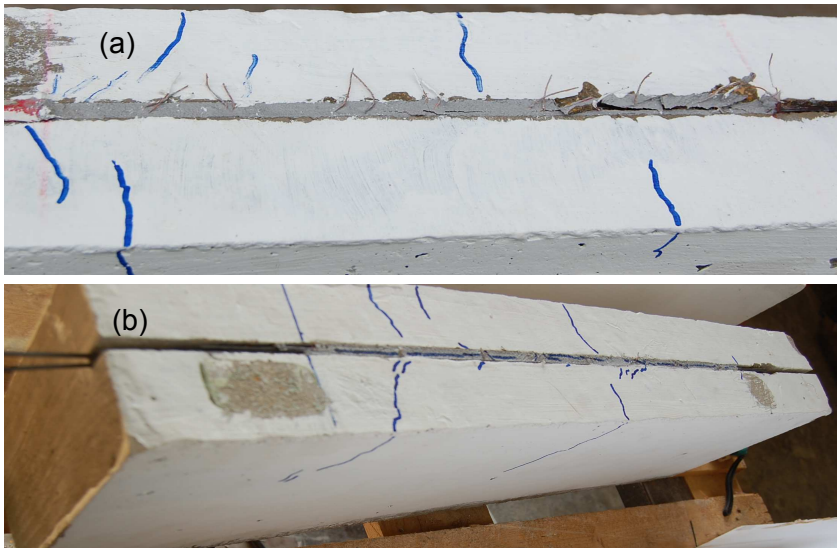

Figure 4.12 - (a) Splitting/cracking in the resin cover in specimen *7-27[R/60/S/6.4p]* and (b) longitudinal resin splitting in specimen *7-28[R/60/S/12.7p]*

Figure 4.13 depicts a specimen failed in tensile rupture.

Figure 4.13 - Tensile rupture in specimen *8-31[R/60/L/6.4p]control* with no strain gauges

4.2.3 Flexural/shear cracks

A crack at the free end was observed in some of the specimens, as in the case with circular bar tests. Few flexural/shear cracks were observed and cracking only occurred in a few specimens, unlike with circular bars (Figure 4.14), because the specimens carried lower ultimate loads due to the smaller cross-sectional area of the bar compared to specimens containing larger circular bars.

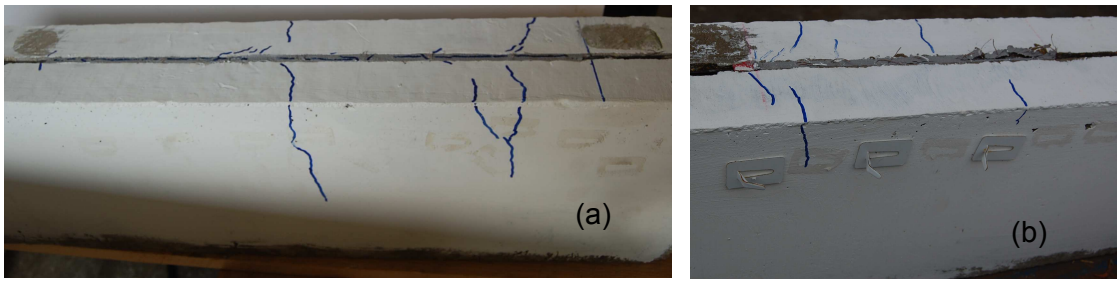

Figure 4.14 - Flexural/shear cracking in specimens: (a) *7-28[R/60/S/12.7p]* and (b) *7-27[R/60/S/6.4p]*

4.2.4 Effect of the investigated parameters

4.2.4.1 Groove size

The increase of the groove size changed the mode of failure as well as the ultimate load in specimens containing long bond lengths. The effect was marginal on specimens containing the shortest bond length (1.6 times the perimeter). However, specimen *8-30[R/60/L/3.2p]* that failed in macro-cracking in the resin, showed a 27% increase in the ultimate load for an increase in resin cover thickness, compared to specimen *7-26[R/60/S/3.2p]* that failed in the same mode. This is because, when the resin cover thickness is increased, the widening of the micro-cracks is delayed. The effect of resin cover thickness on the local bond strength of these specimens is discussed in Section 5.1.6.

Specimen *7-27[R/60/S/6.4p]* failed in macro-cracking in the resin. The corresponding specimen with the large groove, specimen *8-31[R/60/L/6.4p]*, failed by tensile rupture of the bar, indicating the effectiveness of increasing the groove size when the other influencing parameters are met. The corresponding increase in the ultimate load was 22% because the widening of the micro-cracks (macro-cracking) was delayed due to the greater adhesive thickness. When the bond length of specimen *7-27[R/60/S/6.4p]* was doubled (specimen *7-28[R/60/S/12.7p]*) failure occurred in a combined mode of fibre splitting and macro-cracking in the resin. The ultimate load of the specimen was about 88% of the tensile strength of the bar. Generally, some fibre splitting occurs as the stress of the bar approaches its ultimate strength, as observed in tensile tests of

rectangular bars (refer to Chapter 3). If the adhesive thickness was optimised as in specimen *8-31[R/60/L/6.4p]*, then the bar would have survived until its ultimate strength was reached, even with some fibre splitting. This means specimen *7-28[R/60/S/12.7p]* was not as effective as specimen *8-31[R/60/L/6.4p]*, even though the bond length of the former was twice that of the latter. In other words, the increase of bond length itself is not effective unless the thickness of the resin cover is thick enough to delay the widening of the micro-cracks in the resin until the tensile rupture is achieved. This observation clearly indicates that ideally all the influencing parameters should be optimised in order to achieve a perfect bond until rupture of the bar is achieved.

4.2.4.2 Bond length

As bond length increases so the ultimate load increases (Figure 4.15(a)) and the mode of failure changes in both Series 7 and 8. In Series 8, when the bond length was as high as 6.4 times the bar perimeter, tensile rupture of the bar was achieved, indicating that it is an upper-bound of the development length for rectangular strips, provided that the other influencing parameters like groove size are optimised. A reduction in average bond strength as bond length increases can be observed, similar to the case with circular bars due to a non-uniform bond stress distribution along the bond length. (Figure 4.15(b))

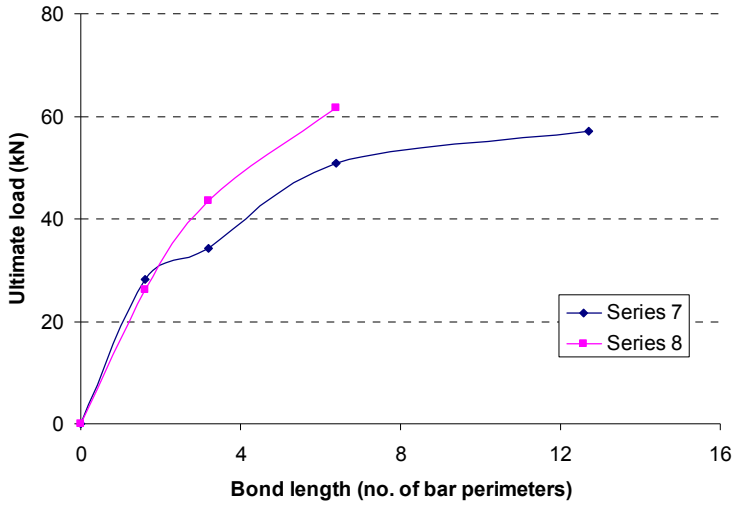

(a)

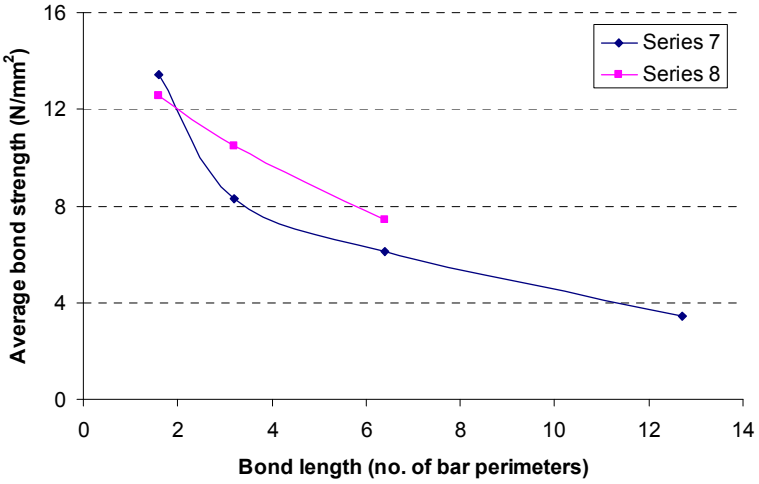

(b)

Figure 4.15 - (a) Ultimate load vs. bond length and (b) average bond strength vs. bond length for specimens containing rectangular bars

4.3 Square CFRP bars

Table 4.3 lists the results obtained in the specimens containing square bars.

Series number	Specimen number	Specimen designation	Ultimate load (kN)	Ultimate load as a % of nominal tensile strength	Strain at ultimate load (%)	Average bond strength (N/mm^2)	Failure mode
9	33	*9-33[S/60/S/Sika/1.6p]*	31.8	15.9	0.217	12.4	PO+splitting^3
	34	*9-34[S/60/S/Sika/3.2p]*	50.1	25.0	0.353	9.81	PO+splitting^2
	35	*9-35[S/60/S/Sika/6.4p]*	73.4	36.7	0.518	7.20	PO+splitting^2
	36	*9-36[S/60/S/Sika/12.7p]*	94.2	47.1	0.688	4.62	PO+splitting^2
10	37	*10-37[S/60/L/Sika/1.6p]*	33.7	16.8	0.245	13.2	PO+splitting^3
	38	*10-38[S/60/L/Sika/3.2p]*	56.2	28.1	0.403	11.0	PO+splitting^3
	39	*10-39[S/60/L/Sika/6.4p]*	40.7	20.4	0.268	3.99	PO
	39-repeat	*10-39[S/60/L/Sika/6.4p]repeat*	56.7	28.4	0.378	5.56	PO
	40	*10-40[S/60/L/Sika/12.7p]*	109.3	54.6	0.754	5.36	CCSF
11	41	*11-41[S/60/L/Sto/1.6p]*	28.8	14.4	0.205	11.2	PO+splitting^3
	42	*11-42[S/60/L/Sto/3.2p]*	50.5	25.2	0.343	9.90	PO+splitting^2
	43	*11-43[S/60/L/Sto/6.4p]*	87.1	43.6	0.636	8.54	PO+splitting^2
	44	*11-44[S/60/L/Sto/12.7p]*	77.4	38.7	0.513	3.79	CCSF
	44-repeat	*11-44[S/60/L/Sto/12.7p]repeat*	64.4	32.2	0.409	3.16	CCSF

Table 4.3 - Results of specimens with square bars

(Note: PO- pull-out failure (pure bar-resin interfacial failure), CCSF- concrete cover separation failure, Splitting^2- partial resin splitting accompanied by fracture in the concrete along inclined planes, Splitting^3- concrete splitting with no visible cracking in the resin cover)

4.3.1 Repeat tests

Specimens *10-39[S/60/L/Sika/6.4p]* and *11-44[S/60/L/Sto/12.7p]* were repeated due to the reasons mentioned in Sections 4.3.4.1 and 4.3.4.2.

4.3.2 Failure modes

Observed modes of failures were, pull-out (pure bar-resin interfacial failure), concrete cover separation failure and mixed modes of pull-out failure accompanied by splitting failures. Pull-out failure was the dominant failure mode due to the smooth surface texture of the bar.

4.3.2.1 Pull-out failure (pure bar-resin interfacial failure)

All the specimens, except the specimens which failed in CCSF, experienced pull-out failure (Figure 4.16(a)) or a combined failure mode of pull-out and splitting. Two types of accompanying splitting failure were identified; partial splitting of both the resin cover and the concrete (Figure 4.16(b)) and concrete splitting with no visible cracking in the resin (Figure 4.16(c)). Splitting in the concrete was not as extensive as in the case with circular bars.

Figure 4.16 - (a) Pull-out failure in specimen *10-39[S/60/L/Sika/6.4p]repeat*, (b) pull-out failure accompanied by splitting of the resin cover and the concrete in specimen *9-36[S/60/S/Sika/12.7p]* and (c) pull-out failure accompanied by splitting in the concrete with no visible cracks in the resin cover in specimen *10-38[S/60/L/Sika/3.2p]*

4.3.2.1 Concrete cover separation failure

CCSF was observed in specimens containing the longest bond length in Series 10 and 11. Localised cover separation near the free end could be seen in specimen *10-40[S/60/L/Sika/12.7p]* (Figure 4.17(a)), whereas in specimens *11-44[S/60/L/Sto/12.7p]* and *11-44[S/60/L/Sto/12.7p]repeat*, the failure occurred locally near the loaded end (Figures 4.17(b) and (c)).

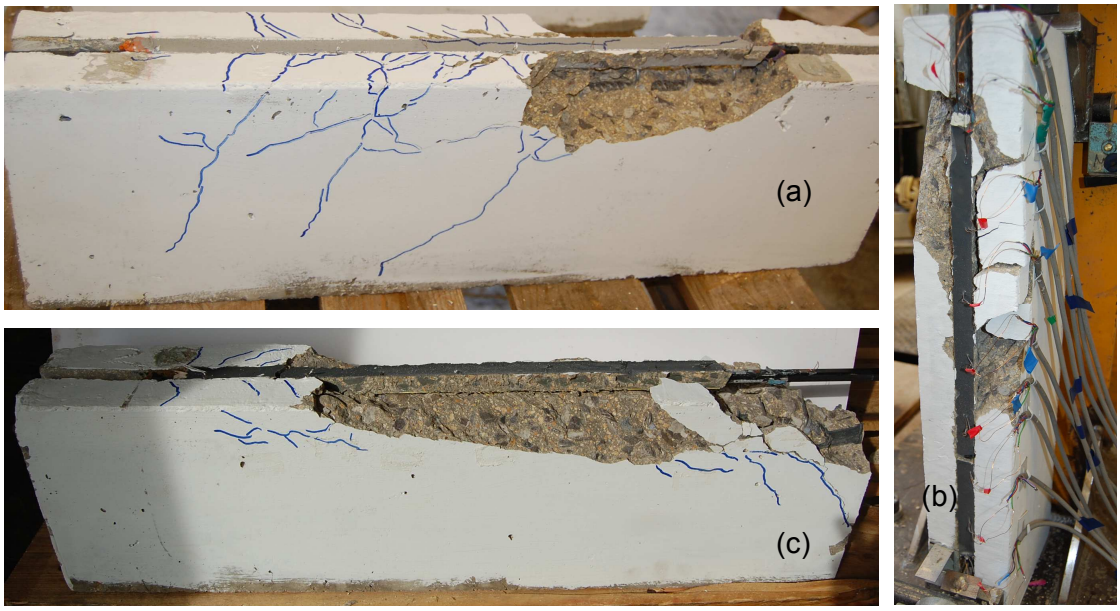

Figure 4.17 - CCSF in specimens: (a) *10-40[S/60/L/Sika/12.7p]*, (b) *11-44[S/60/L/Sto/12.7p]repeat* and (c) *11-44[S/60/L/Sto/12.7p]*

4.3.3 Flexural/shear cracks

Extensive flexural/shear cracking was seen especially in specimens containing long bond lengths (6.4 and 12.7 times the perimeter), due to the higher ultimate loads which were sustained, compared to those containing circular and rectangular bars**.** Figure 4.18 shows specimens with deep flexural/shear cracks. The common crack at the free end was observed in most of the specimens, even for short bond lengths as in the case with specimens containing circular and rectangular bars.

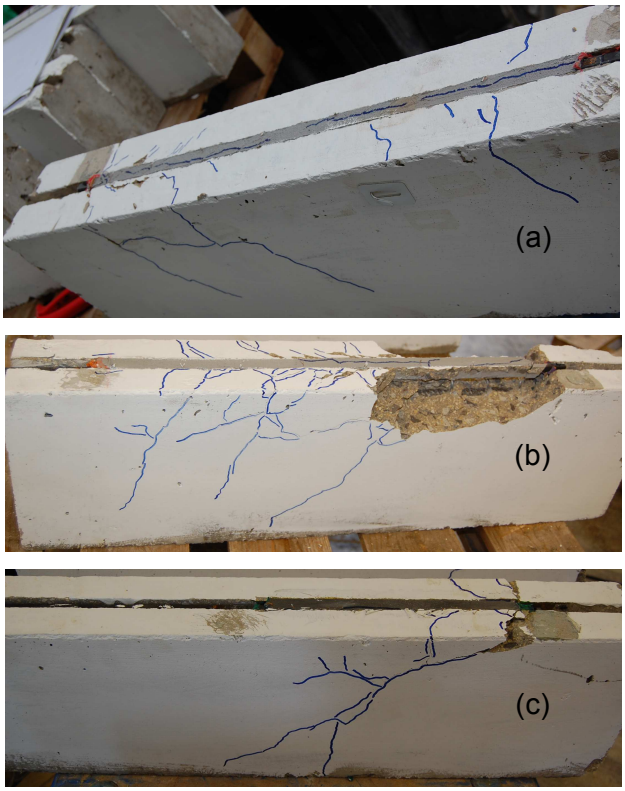

Figure 4.18 - Flexural/shear cracks in specimens containing square bars: (a) *9-36[S/60/S/Sika/12.7p]*, (b) *10-40[S/60/L/Sika/12.7p]* and (c) *11-43[S/60/L/Sto/6.4p]*

4.3.4 Effect of the parameters

4.3.4.1 Groove size

Series 9 and 10 compare the effect of groove size on bond behaviour of square bars. When the groove size increased, the ultimate load also increased by 6%, 12% and 16 % for bond lengths of 1.6, 3.2 and 12.7 times the perimeter, respectively. In contrast, as the groove size increased there was a significant decrease (45%) in the ultimate load of the specimen corresponding to a bond length of 6.4 times the perimeter. This is because the ultimate load of specimen *10-39[S/60/L/Sika/6.4p]* was governed by a pure interfacial failure at the bar-resin interface with out any sort of failure in the resin cover or the concrete. After reaching the maximum load of the specimen, the load dropped gradually. All other specimens, including the ones with circular and rectangular bars, showed a sudden failure at the peak value. The corresponding

specimen in Series 9 with a small groove and the same bond length, specimen *9-35[S/60/S/Sika/6.4p]*, failed in a mixed mode of pull-out and splitting failure. Furthermore, this was the only occasion within the whole sets of experiments that showed a very significant decrease in ultimate load when the groove size was increased.

In fact, this situation is even more surprising given that the ultimate load of specimen *10-39[S/60/L/Sika/6.4p]* was 28% lower than specimen *10-38[S/60/L/Sika/3.2p]*, which had half the bond length of the former specimen. This is the only case where a reduction in the ultimate load occurred when the bond length was doubled suggesting that there is a defect in specimen *10-39[S/60/L/Sika/6.4p]*. Therefore, this specimen was repeated to see whether there were any defects. However, it turned out that the behaviour of the repeat test, specimen *10-39[S/60/L/Sika/6.4p]repeat* was very similar to that of the original specimen, by failing in the same mode but with a 39% higher load than that of the original. However, the comparison between the ultimate load of specimen *10-39[S/60/L/Sika/6.4p]repeat* and that of specimen *10-38[S/60/L/Sika/3.2p]* shows that the increase in the ultimate capacity was just 1%, indicating the effect of doubling the bond length is still marginal, which is not the case for all the other specimens. Further, the ultimate load of the repeat test is still 23% lower than that of the corresponding specimen in Series 9, *9-35[S/60/S/Sika/6.4p]*. This means the increment of groove thickness has a negative effect, which is again not the case for all the other specimens. It remains unclear why the bonded joint was not more effective experimentally, when the bond length was doubled compared to specimen *10-38[S/60/L/Sika/3.2p]* and when the groove thickness was increased compared to specimen *9-35[S/60/S/Sika/6.4p]*.

The increase of groove size influenced the mode of failure of specimens *9-34[S/60/S/Sika/3.2p]* and *9-36[S/60/S/Sika/12.7p]*, which had bond lengths of 3.2 and 12.7 times the perimeter, respectively. Specimen *9-34[S/60/S/Sika/3.2p]* failed in a combined mode of pull-out and partial splitting in both the resin cover and the concrete. The corresponding specimen in Series 10 with the large groove failed in pull-out failure accompanied by partial concrete splitting. There was no visible damage in the resin cover as the resin cover was thicker than that of specimen *9-34[S/60/S/Sika/3.2p]*. By a similar comparison between specimen *9-36[S/60/S/Sika/12.7p]* and *10-40[S/60/L/Sika/12.7p]*, it can be seen that greater thickness of the resin cover was able

to prevent pull-out dominant failure behaviour and ended up in a catastrophic concrete cover separation failure. However, there was not much difference in the failure modes of specimens *9-33[S/60/S/Sika/1.6p]* and *10-37[S/60/L/Sika/1.6p]*, which correspond to the shortest bond length.

4.3.4.2 Resin type

Series 10 and 11 compare the effect of resin type on the bond behaviour of square bars. There was a significant increase in ultimate loads of specimens using Sikadur 30 compared to those using StoBPE Lim 465/464. The percentage increments were 17, 11 and 41 for specimens with bond lengths of 1.6, 3.2 and 12.7 times the perimeter, respectively indicating Sikadur 30 is better than StoBPE Lim 465/464 as far as the ultimate capacity is concerned. However, resin type had a minor effect on the failure modes. Modes of failure were the same in the both series for specimens with 1.6 and 12.7 times the perimeter. The effect of resin type on the behaviour of the specimen with a bond length of 6.4 times the perimeter cannot be concluded as the behaviour of specimen *10-39[S/60/L/Sika/6.4p]* was doubtful as described in Section 4.3.4.1.

Another exception was seen with specimens *11-44[S/60/L/Sto/12.7p]* and *11-43[S/60/L/Sto/6.4p]*, where the ultimate load of the former is 11% lower than that of the latter. This is again inconsistent as a reduction in bond strength would not be expected when the bond length is doubled. As the unusual strength reduction was observed, it was thought that it might be worth repeating the test to see whether there was anything wrong that might have influenced the ultimate load of the specimen. The repeat test, specimen *11-44[S/60/L/Sto/12.7p]repeat*, failed in the same mode, catastrophic failure in the concrete cover, with a lower load, a 17% decrease from the original. As the failure in both specimens was governed by the concrete failure, the decrease in the ultimate load was thought to be attributed to the lower concrete strength of the latter compared to that of the former (Table 3.7). However, it remains unclear why there is a negative difference in the ultimate load of specimen *11-44[S/60/L/Sto/12.7p]* and *11-43[S/60/L/Sto/6.4p]*, when the bond length was doubled.

According to the manufacture's specifications, and experimental tests on the adhesives, the mechanical properties of both adhesives (Table 3.11) were more or less

the same except the modulus of elasticity, *E*, of Sikadur 30 was about double that of StoBPE Lim 465/464. The modes of failures corresponding to each bond length seemed to be approximately the same. The significant Increase in ultimate loads of Series 10 over Series 11 could be attributed to the higher stiffness of Sikadur 30. Despite the fact that StoBPE Lim 465/464 is the compatible adhesive recommended by the manufacturer, Sikadur 30 seemed to be more effective.

4.3.4.3 Bond length

As the bond length increased so the ultimate load increased as for circular and rectangular bars, although with some exceptions as explained in Sections 4.3.4.1 and 4.3.4.2. Figure 4.19 depicts the relationships between the bond length and both the ultimate capacity and the average bond strength.

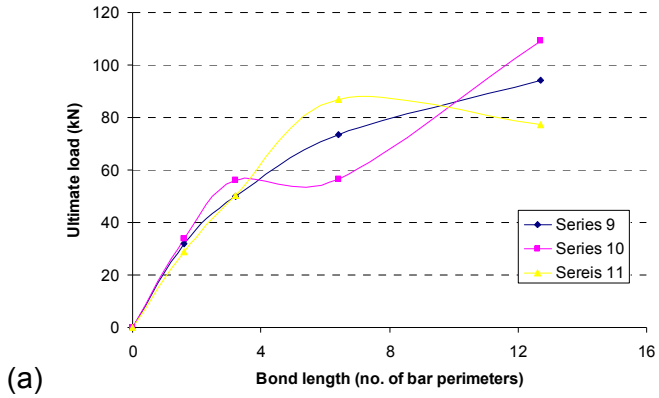

(a)

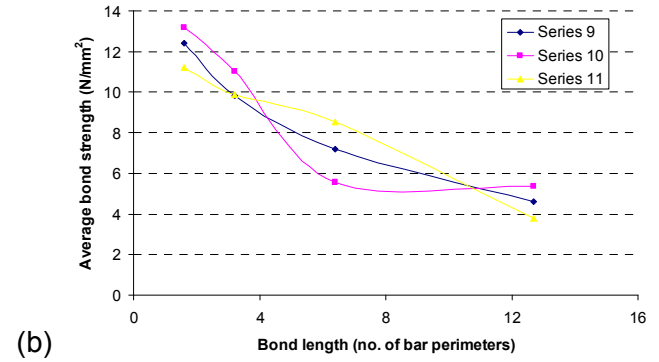

(b)

Figure 4.19 - (a) Ultimate load vs. bond length and (b) average bond strength vs. bond length of specimens containing square bars

The discrepancies can be seen in curves representing Series 10 and 11, due to the inconsistent results of specimens *10-39[S/60/L/Sika/6.4p]* and *11-44[S/60/L/Sto/12.7p]*. Similar to the behaviour of circular and rectangular bars, if the other parameters such as the resin cover thickness, have been optimised, then as the bond length increases the mode of failure changes to a critical (limiting) mode as further explained in Sections 4.4.3 and 4.4.4. In both circular and square bars this critical failure mode was CCSF, whereas for rectangular bars the critical failure mode was tensile rupture of the bar, which is the desired mode of failure for any bar shape.

4.4 General Results

4.4.1 Effect of bar shape

Series 3, 7 and 9 compare the bond behaviour of various shapes of CFRP bars. Table 4.4 lists the details of the specimens in these series. As the perimeters of the each bar shape were approximately the same, bond length of each shape was varied in terms of the same multiples of bar perimeters. Therefore, it was possible to provide approximately equal bonded surface areas for each bar shape for a given bond length in terms of the bar perimeter. Therefore, with the other variables kept constant, the only variable is the bar shape allowing a direct comparison of bond behaviour of specimens containing different bar shapes. Within these series, the other variables that have been kept constant were nominal concrete compressive strength, adhesive type, bar type and size of groove (“small”- 2mm adhesive thickness around the perimeter). It should be noted that even though the nominal concrete strength was the same for all the specimens, the actual strengths vary slightly (Table 3.7). Also the bar properties (strength, stiffness and surface texture) of circular and rectangular bars were the same, whereas those of square bars were different as they were from a different manufacturer.

Figure 4.20(a) shows the relationship between the bond length and the ultimate load whereas Figure 4.20(b) depicts the ultimate load as a percentage of the tensile strength of the bars against the bond length, for the various bar shapes. According to the Figure 4.20(a), it is shown that square bars achieved higher ultimate capacities

whereas rectangular bars achieved lower ultimate capacities. However, Figure 4.20(b) shows that rectangular bars achieved the highest ratio of ultimate load to tensile strength, whereas circular bars achieved the lowest percentage, for a given bond length. Therefore, it is clear that even though rectangular bars cannot sustain high ultimate loads, due to their relatively low cross-sectional area/perimeter ratio, the tensile capacity of the bar is more fully utilised compared to the other shapes. The tensile strength values of the bars were taken from the manufacturer's specifications as the experimental values were only available for the rectangular and square bars. For the highest bond length, the utilization of tensile capacity of rectangular bars was as high as 90%, almost double that of square bars and treble that of circular bars. For the lowest bond length, utilisation of tensile capacities of rectangular, square and circular bars were 43%, 16% and 11%, respectively.

The bar shape has influenced the mode of failure of specimens for a given bond length. As mentioned previously, the different surface texture of square bars affected the mode of failure. However, any direct comparison of failure modes of Series 3 and 7 is viable because of their identical bar properties. Specimens corresponding to the maximum bond length exhibited the key variation in mode of failure due to the differences in the bar shape. Specimen *3-24[A12/60/S/12.7p]* failed catastrophically in the concrete cover whereas specimen *7-28[R/60/S/12.7p]* failed in a combined mode of fibre splitting and resin splitting. As explained in Section 4.2.4.1, specimen *7-28[R/60/S/12.7p]* would have failed in tensile rupture of the bar if the right amount of resin cover thickness had been provided. Therefore, it seems that rectangular shape leads the specimen towards the most desired failure mode (tensile rupture of the bar) due to its beneficial cross-sectional area/ perimeter ratio. It can be seen that the failure mode of specimen *3-24[A12/60/S/12.7p]*, CCSF, is the critical limiting mode experienced by both circular and square bars, which is described in Section 4.4.4.

The mode of failure of all the specimens in Series 9 was pull-out governed due to the smooth surface texture of the bar. Therefore, any variation in the change of failure mode compared to circular and rectangular bars in Series 3 and 7, might be attributed to both surface texture and the square bar shape. However, by comparing failure modes of specimens *9-36[S/60/S/Sika/12.7p]* and *10-40[S/60/L/Sika/12.7p]*, as explained in Section 4.3.4.1, it can be concluded that if the adhesive thickness was optimised in specimen *9-36[S/60/S/Sika/12.7p]*, it would have failed in the critical failure

mode, CCSF, which is not affected by the smoothness of the bar surface. This assumption can also be confirmed by comparing the amount of utilisation of the tensile capacities of specimens *10-40[S/60/L/Sika/12.7p]* and *9-36[S/60/S/Sika/12.7p]*, which are 55% and 47%, respectively. As these percentage values are close to one another it can be suggested that the mode of failure of specimen *9-36[S/60/S/Sika/12.7p]* was approaching its critical mode of failure. Furthermore, there were shear cracks in the specimen running horizontally at the level of internal reinforcement level, which confirms this possibility.

The bar perimeters of Series 3, 7 and 9 are approximately the same (Table 4.4). For a given perimeter, the cross-sectional area is lower in rectangular bars compared to circular and square bars so that the generated load capacity is also lower in rectangular bars. Consequently, specimens containing rectangular bars are not likely to develop high stresses in the concrete cover leading to CCSF unlike circular and square bars. Therefore, it can be concluded that when the other parameters like bond length, and groove size have been optimised, rectangular bars can be properly anchored until the tensile rupture of the bar occurs due to its relatively low cross-sectional area/ perimeter ratio, unlike circular and square bars where the premature failure is governed by CCSF. Similar bond behaviour was seen between circular and square bars in terms of ultimate capacities as can be seen in Figures 4.20(a) and (b) and in terms of their failure modes.

Series number	Specimen number	Specimen designation	Bar shape	Commercial name	Bar size	Cross-sectional area (mm^2)	Perimeter (mm)	Bond length (mm)	Bonded surface area (mm^2)
3	21	*3-21[A12/60/S/1.6p]*	Circular	Aslan 200	12mm diameter	113	38	480	18098
	22	*3-22[A12/60/S/3.2p]*						240	9049
	23	*3-23[A12/60/S/6.4p]*						120	4524
	24	*3-24[A12/60/S/12.7p]*						60	2262
7	25	*7-25[R/60/S/1.6p]*	Rectangular	Aslan 500	2mm x 16mm	32	36	460	16499
	26	*7-26[R/60/S/3.2p]*						230	8250
	27	*7-27[R/60/S/6.4p]*						115	4125
	28	*7-28[R/60/S/12.7p]*						58	2062
9	33	*9-33[S/60/S/Sika/1.6p]*	Square	StoFRP Bar E10C	10mm x 10mm	100	40	510	20369
	34	*9-34[S/60/S/Sika/3.2p]*						255	10185
	35	*9-35[S/60/S/Sika/6.4p]*						128	5092
	36	*9-36[S/60/S/Sika/12.7p]*						64	2546

Table 4.4 - Details of specimens containing different bar shapes

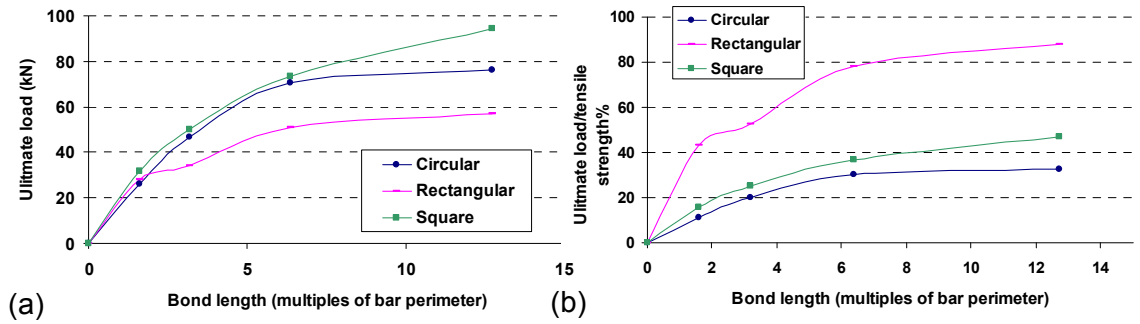

Figure 4.20 - (a) Ultimate load vs. bond length and (b) ultimate load/tensile strength (%) vs. bond length, for different bar shapes

4.4.2 Effect of cross - sectional area/perimeter ratio

Table 4.5 lists the cross-sectional area/ perimeter ratio and the maximum ultimate load achieved by each bar type, bar size and bar shape, as a percentage of the tensile strength. Even though, the actual maximum ultimate load/tensile strength (%) for rectangular bars is 95% of its experimental tensile strength, here it is taken as 100% as the actual failure mode was the tensile rupture of the bar. It is evident that the utilization of tensile capacity of CFRP bars depends on the cross-sectional area/perimeter ratio. As the ratio increases, effectiveness of utilising the full tensile capacity reduces. Full tensile capacity of CFRP bars was achieved only by the rectangular bars, with the lowest cross-sectional area/perimeter ratio. Therefore, rectangular bars seem to be the most efficient shape. The identical behaviour of circular and square bars can again be confirmed from Table 4.5. The 9mm diameter Aslan 200 bars and the square bars with approximately equal cross-sectional area/ perimeter ratios (2.25 and 2.5, respectively) achieved approximately the same maximum ultimate load/tensile strength percentages (59% and 55%). However, 12mm diameter Carbopree bars with a higher ratio of 3, achieved a relatively low percentage of its ultimate strength (28%) compared to that of the square bars.

According to Figure 4.21, the relationship between the cross-sectional area/ perimeter ratio and the percentage of maximum ultimate load/ tensile strength seems to be approximately a linear relationship, for the range of CFRP bars tested. When the equation of this relationship is empirically defined, the likely maximum bond strength achieved by a particular type of bar might easily be estimated.

Bar shape	Commercial name	Size	Cross-sectional area (mm^2)	Perimeter (mm)	Cross sectional area/ perimeter ratio	Maximum ultimate load capacity/tensile strength (%)
Circular	Carbopree	12mm diameter	113	38	3	28
	Aslan 200	12mm diameter	113	38	3	32
	Aslan 200	9mm diameter	64	28	2.25	59
Rectangular	Aslan 500	2mm x 16mm	32	36	0.89	100
Square	StoFRP Bar E10C	10mm x 10mm	100	40	2.5	55

Table 4.5 - Cross-sectional area/perimeter ratio and maximum load capacity/ tensile strength

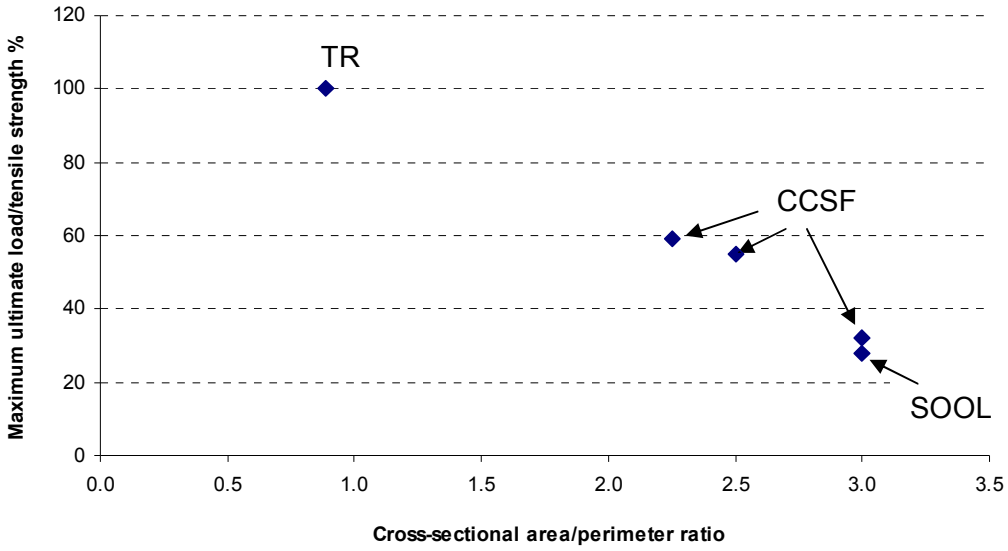

Figure 4.21 - Relationship between cross-sectional area/perimeter ratio and maximum ultimate load/tensile strength (%)

4.4.3 Critical limiting failure modes

Two types of critical limiting failure modes were identified, depending on the shape of the CFRP bar. For both circular and square bars this critical failure mode was brittle concrete cover separation failure (CCSF), whereas for rectangular bars, the critical failure mode was tensile rupture of the bar, the desired mode of failure for any type of bar. These critical failure modes demonstrate full bond of the CFRP has been

maintained to failure. The highest ultimate loads sustained by specimens containing square, circular and rectangular bars were 109.3kN, 79kN and 62.1kN, respectively. It should be noted that the highest ultimate capacity achieved by rectangular bars, 62.1kN, was governed by tensile rupture, whereas those achived by circular and square bars, 79kN and 109.3kN, respectively, were controlled by CCSF. Depending on the bar shape, as the bond length increases, the mode of failure of specimens changes to one of the above critical modes provided that the other parameters (like resin cover thickness and bar surface texture) have been optimised, which can otherwise potentially cause other failure modes, such as resin splitting and bar-resin interface failure.

The corresponding bond length at which CCSF first occurs is the optimum bond length for the particular bar. There will be no change of the critical failure mode for further increments of bond length beyond this optimum bond length. However, the ultimate capacity may increase with an increase of the bond length. This scenario can be confirmed by the tests from Series 2. The optimum bond length for the particular bar, 9mm Aslan 200, can be found by comparing the failure modes of specimens *2-19[A9/60/L/6.4p]* and *2-18[A9/60/L/3.2p]* where all the parameters except the bond length were the same. Through comparison of failure modes of specimens *2-20[A9/60/L/12.7p]* and *2-19[A9/60/L/6.4p]*, it can be seen that there is no effect of further increments of bond length on the critical failure mode once the optimum bond length is exceeded, as both specimens failed in CCSF. However, the ultimate capacity of the specimen corresponding to the longer bond length increased because the average bond stresses were lower due to the longer length so that the induced longitudinal shear stresses in the concrete were also lower than that of the specimen with shorter bond length. Consequently, the specimen containing the longer bond length can sustain a higher load until it fails in CCSF. However, there is not a linear increase in strength with bond length since the bond stresses are not uniform but reduce towards the free end.

By comparing each of the specimens in Series 2 with the corresponding specimen in Series 4, i.e. *4-12[A9/60/S/12.7p]* and *4-11[A9/60/S/6.4p]repeat*, respectively, where all the parameters except the groove size are constant, the importance of optimising the resin cover thickness in order for the critical mode to occur can be justified. Similarly, comparison of the failure modes of specimens *8-31[R/60/L/6.4p]* and *7-*

27[R/60/S/6.4p], where all the parameters except the groove size were kept constant, confirms the nessecity of optimising the groove size in order for the critical failure mode of rectangular bars (tensile rupture of the bar) to occur. The optimum bond length at which the critical failure mode occurs for the particular rectangular bar was 6.4 times the bar perimeter, which is 230mm. This optimum bond length becomes the developement length of the particular bar when the critical failure mode is tensile rupture of the bar.

4.4.4 Concrete cover separation failure (CCSF)

CCSF sometimes started from the free end and propagated towards the loaded end at the internal steel reinforcement level and occurred simultaneously over the entire bonded region and the unbonded region of the specimen. Sometimes it was a localised cover separation at either the free end or the loaded end with separation of triangular or trapezoidal concrete wedges. Most of the time the 'resin prism' containing the epoxy cover and the CFRP bar remained intact as a combined unit, with localised resin splitting/cracking occurring. The two side surfaces and the bottom surface of the 'resin prism' had an aggregate-particle layer stuck to them, indicating that there was a sound bond between concrete and epoxy. Similar results for CCSF can be found in the literature, where NSM systems have been used for flexural strengthening of beams (Corden *et al.*, 2008; De Lorenzis, 2002; Soliman *et al.*, 2008; Teng *et al.*, 2006). CCSF has also been observed in EBR systems and it is one of the main debonding failure modes observed in reinforced concrete beams strengthened with externally bonded FRP reinforcement (Smith and Teng, 2002).

The CCSF mode seems to be dependent on the concrete strength as this failure is associated with longitudinal shear stresses in concrete. Comparison of the failure modes of specimens *1-4[C12/60/S/12.7p]* and *5-8[C12/30/S/12.7p]*, where all the parameters except the concrete strength were kept constant, and similar experimental confirmation between specimens *4-12[A9/60/S/12.7p]* and *6-16[A9/30/S/12.7p]*, show that, on both occasions, as the concrete strength increased by about 30N/mm^2 the critical mode changed to a failure mode involving either splitting of the resin cover or shearing off of the outer layer of the bar. This change in failure mode also attracted an increase in the ultimate capacity, purely because of the significant increase in the

concrete strength. Further, by comparing the failure modes of specimens *1-4[C12/60/S/12.7p]* and *4-12[A9/60/S/12.7p]*, with those of specimens *3-24[A12/60/S/12.7p]* and *2-20[A9/60/L/12.7p]*, respectively, the complete behaviour of CCSF can be analysed as in Figure 4.22.

From Figure 4.22, it can be seen that for low strength concrete, if the bond length is optimised, CCSF occurs irrespective of bar surface texture, resin cover thickness and bar size as the low concrete shear strength is more critical than the other parameters, yielding the lowest ultimate load capacity. For relatively high strength concrete, if the bond length is optimised, concrete shear strength becomes less critical so that one of the most critical non-optimum parameters causes the failure. However, if all the influencing parameters are optimised, failure occurs by CCSF yielding the highest ultimate load capacity. Therefore, it seems that CCSF is the upper-bound debonding failure mode for NSM systems with circular CFRP bars in the range of 9mm to 12mm diameter. The adhesive should be strong enough to avoid either cohesive shear failure within the adhesive or resin cover splitting failure. Cohesive shear failure in the resin cover was not observed in any of the tests of the current research as the shear strength of the adhesive used was relatively high. Even if a weak adhesive was used for NSM systems, cohesive shear failure in the adhesive can be overcome by increasing the shear strength of the adhesive. Therefore, when the adhesive shear strength is considered as another variable, CCSF failure will still be the upper-bound debonding failure mode for relatively high strength concrete, which occurs when the other parameter are optimised. However, CCSF can also be the lower-bound failure mode yielding the lowest capacity, if the concrete strength is comparatively low as seen with specimens *5-8[C12/30/S/12.7p]* and *6-16[A9/30/S/12.7p]*.

For specimens with square bars, identical behaviour was observed for CCSF even though only few variables have been investigated. Specimen *11-44[S/60/L/Sto/12.7p]repeat* was tested as a repeat test of *11-44[S/60/L/Sto/12.7p]* and the actual concrete strength of the former was about 10N/mm^2 lower than that of the latter. Therefore, all the parameters were the same except the concrete strength. Both the specimens failed in the same mode, CCSF, with the former exhibiting a lower ultimate capacity, indicating the influence of the reduced concrete strength on CCSF. On the other hand that observation can be analysed from the reverse view point, i.e. it can be said that as the concrete strength increased by 10N/mm^2 the ultimate capacity

increased correspondingly, but there was no change in the critical failure mode. Therefore, it seems that by increasing the concrete strength CCSF cannot be prevented even though the load capacity increases. In other words, once the concrete strength exceeds a certain strength, the optimum concrete strength, CCSF becomes the upper-bound failure mode provided that the other parameters are also optimised.

Figure 4.23 further explains the behaviour of CCSF mode for square bars. By comparing the failure modes of specimens *9-36[S/60/S/Sika/12.7p]* and *10-40[S/60/L/Sika/12.7p]*, the necessity of optimising the groove size in order CCSF to occur can be justified. Similarly, the necessity of optimising the bond length can be explained by comparing the failure modes of specimens *10-39[S/60/L/Sika/6.4p]* and *10-40[S/60/L/Sika/12.7p]*. Through comparison of specimens *11-44[S/60/L/Sto/12.7p]* and *11-44[S/60/L/Sto/12.7p]repeat*, it can be seen that when the influencing parameters are optimised, even if the concrete strength is increased, still the failure mode is CCSF with some increment in the ultimate capacity, indicating that it is the upper-bound failure mode for square bars as well. It can also be said that CCSF occurs irrespective of the resin type provided that the adhesive shear strength is strong enough not to cause cohesive shear failure in the adhesive, and is strong enough not to split so that there is an optimum resin cover thickness where resin splitting does not take place before CCSF occurs.

From the considered variables, the ones which affect CCSF are bond length, groove size (resin cover thickness), concrete strength, bar surface texture and resin type (with a fairly high tensile strength and a shear strength), i.e. all the factors except bar size and bar shape need to be optimised in order CCSF to occur. CCSF occurs irrespective of the bar size and bar shape provided that the cross-sectional area/perimeter ratio is high enough to develop high stresses in the concrete cover (refer to Figure 4.20(a)). From the above mentioned five parameters affecting CCSF, degree of bar surface texture and resin properties are difficult to be physically quantified because there is a vast variety of FRP bar surface textures and resin properties. Therefore, it is difficult to define optimum values for the degree of surface texture or optimum properties of the resin or to investigate the influence of these parameters beyond their optimum values. It is only possible to say that in order for CCSF to occur, both the degree of surface texture should be strong enough to avoid bar-resin interface failure and the resin type should be strong enough to preclude resin splitting failure and the cohesive shear

failure within the resin cover. In contrast, the three variables, bond length, groove size and concrete strength can be easily quantified and their optimum values can be defined.

The effect of increasing the bond length and the concrete strength beyond their optimum values on the failure mode can be identified by studying the behaviour of the following specimens. By comparing the failure modes of specimens *2-19[A9/60/L/6.4p]* and *2-20[A9/60/L/12.7p]*, it can be seen that increasing the bond length beyond the optimum value has no effect on the failure mode, CCSF, even though there is an increase of the ultimate load. Similarly, by comparing failure modes of specimens *11-44[S/60/L/Sto/12.7p]* and *11-44[S/60/L/Sto/12.7p]repeat*, it is seen that increasing concrete strength above the optimum concrete strength has no effect on the failure mode, CCSF. However, there is an increase in the ultimate load as a result of the increase of concrete strength. This scenario could not be investigated experimentally for the resin cover thickness as only two groove sizes were considered.

The average shear stress in the concrete cover failure plane of specimens *5-8[C12/30/S/12.7p]* and *6-16[A9/30/S/12.7p]* at failure are approximately the same, 1.31N/mm^2 (equal to 69kN/480mm/110mm) and 1.29N/mm^2 (equal to 51kN/360mm/110mm), respectively. This similarity makes sense because the two specimens failed due to low concrete strength, yielding the lowest ultimate capacity amongst all the specimens which failed in CCSF. However, for other specimens with a relatively high concrete strength, i.e. when CCSF was no longer the lower-bound failure mode, there was no similarity in the average shear strength of the concrete cover failure plane of the specimens (Figures 4.22 and 4.23). This suggests that there is a complex behaviour causing CCSF, which is not necessarily dependent on shear stress of the concrete cover failure plane when the concrete strength is not the critical factor.

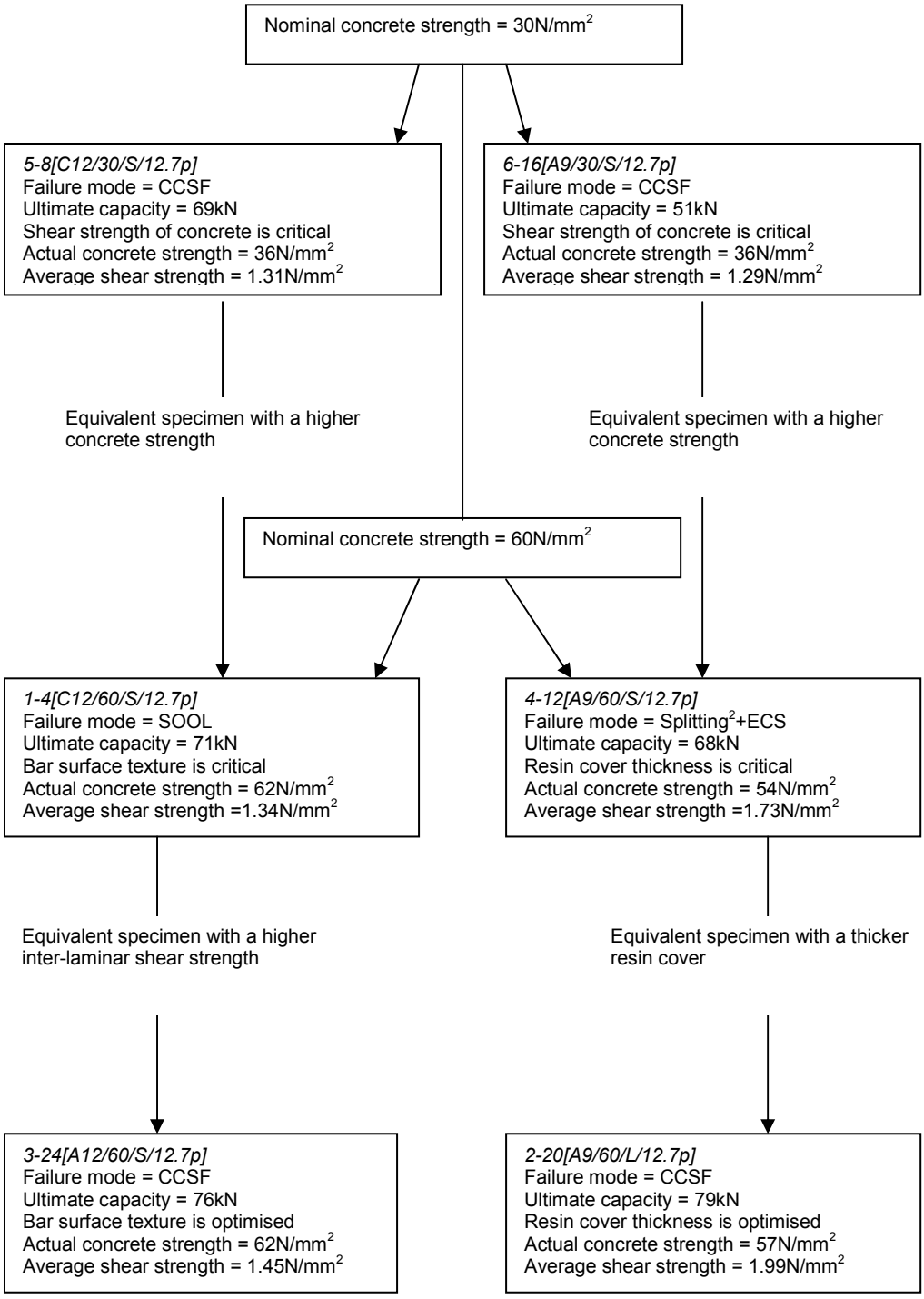

Figure 4.22 - Diagram showing the complete behaviour of CCSF for circular bars

Therefore, it is seen that for both the circular and square bars with relatively high cross-sectional area/perimeter ratios, the CCSF mode is the upper-bound failure mode (which gives the highest ultimate load capacity) for fairly high strength concrete, when the influencing parameters like bond length, resin cover thickness and concrete

strength are optimised. However, CCSF can occur as the lower-bound failure mode (which gives the lowest ultimate load capacity) if the concrete strength is relatively low. For successful design of NSM FRP bars for flexural strengthening, the possibility of predicting this upper-bound failure mode, CCSF is absolutely crucial. Therefore, development of appropriate debonding models for NSM FRP bars is required, as has been done for externally bonded FRP plates (Smith and Teng, 2002), where considerable amount of research has already been carried out.

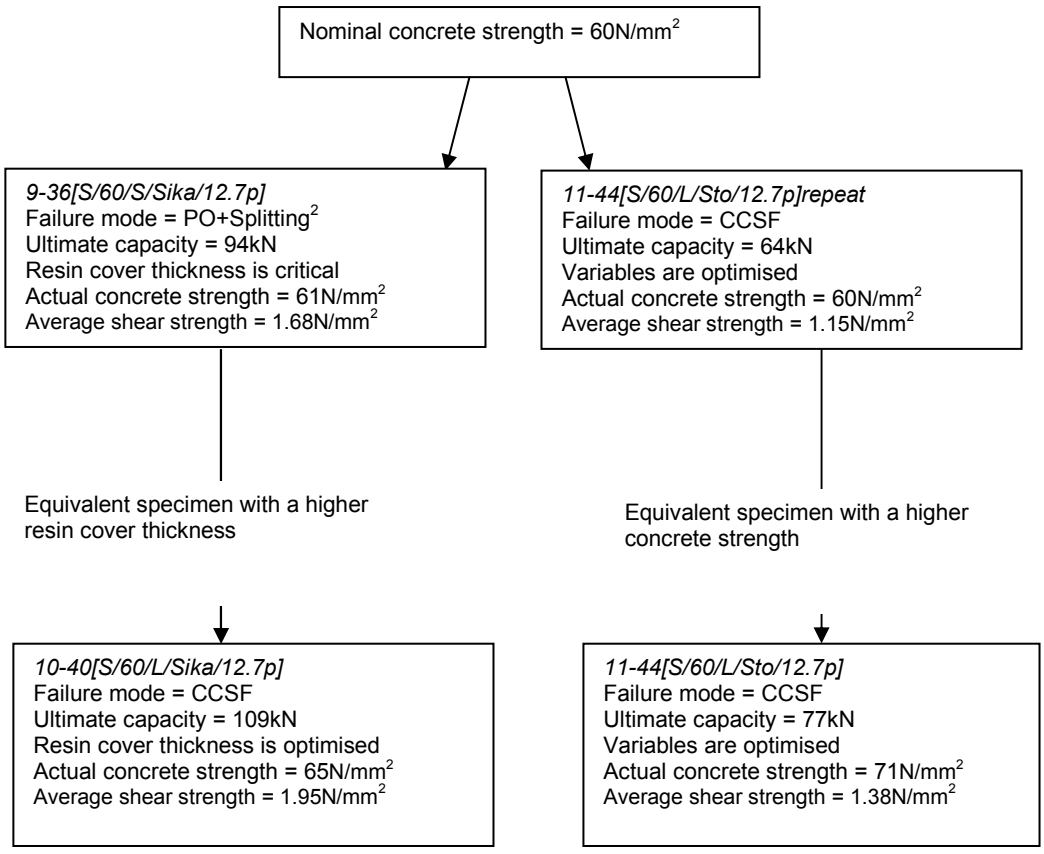

Figure 4.23 - Diagram showing the complete behaviour of CCSF for square bars

This research demonstrated that the real behaviour of flexurally strengthened beams with NSM FRP systems can be qualitatively correlated with the results of small scale beam-type bond tests containing internal reinforcement because the bond mechanisms such as CCSF are the same. However, at this stage, it is not possible to incorporate these bond stress-slip results for predictive models for real beams as these results are specimen size dependent. Therefore, it is required to investigate size-effect phenomenon in relation to bond behaviour of NSM FRP bars and concrete and establish correct quantitative correlations between bond test results and beam test

results using both extensive experimental studies and analytical modelling. Once the size-effect issues are addressed, it will then be possible to apply the results of these small scale beam-type bond tests for predicting debonding failures in real beams.

4.4.5 Dominant failure mode

The splitting failures, resin splitting and resin splitting accompanied with concrete splitting were the dominant failure mode for circular and square bars. Splitting failures are less likely to occur for rectangular bars as the transverse bond stresses are acting against thick lateral sides of the concrete block (De Lorenzis and Teng, 2007). Splitting failures generally occurred for specimens with moderate bond lengths and comprised relatively high bond capacities.

4.4.6 Definition of bond length in terms of bar perimeters and bar diameters

It has been a convention that anchorage length be expressed in terms of multiples of bar diameter in the case of steel-to-concrete bond. This convention is sensible for steel-to-concrete bond as it generally involves circular bars only. There is no difference in defining bond length in terms of bar diameter or bar perimeter as long as only circular bars are involved, as there is a linear relationship between the bar diameter and bar perimeter, π, for circular bars. However, as the FRP technology emerges, different bar shapes such as square and rectangular bars become available. Therefore, it is crucial that guidelines on anchorage length requirements be representative of all the different shapes. As a result, it is questionable that the definition of anchorage in terms of bar diameter/equivalent bar diameter is still valid. The current study investigated this problem and made the following observations.

Figure 4.24(a) depicts the ultimate capacities of the bond specimens vs. bond length, in terms of number of bar perimeters whereas Figure 4.24(b) shows the ultimate capacity vs. bond length, in terms of number of bar diameters for circular bars and in terms of equivalent bar diameters for non-circular bars (by converting the non-circular cross-section into a circle of the same cross-sectional area). It can be seen that, there is a

considerable difference between the two plots. If comparison is made only between the curves representing specimens containing circular bars, it can be seen that there is no change in behaviour, as mentioned before, unlike for the specimens representing non-circular bars, where there is no linear relationship between the bar perimeter and equivalent bar diameter.

.

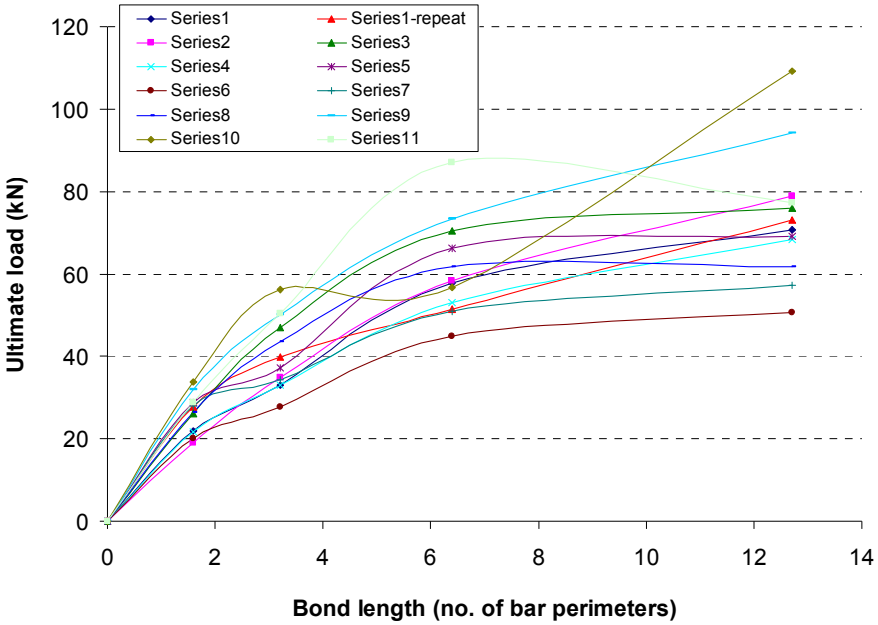

(a)

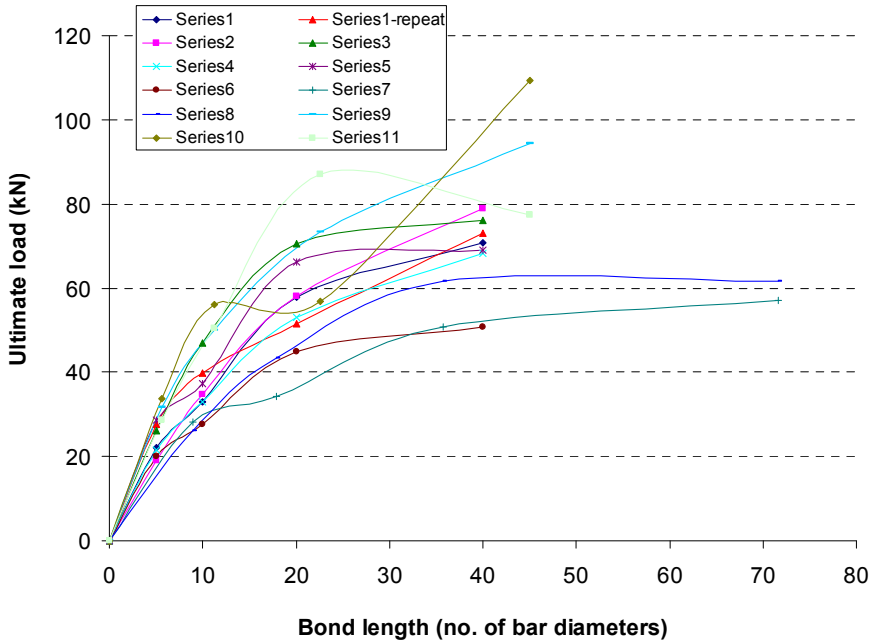

(b)

Figure 4.24 - (a) Ultimate load vs. bond length (no. of bar perimeters) and (b) ultimate load vs. bond length (no. of bar diameters)

It can be seen in Figure 4.24(a) that Series 8 (containing rectangular bars) has a higher ultimate load compared to Series 1-repeat (containing circular bars) in the range of bond length from 2-10 times bar perimeter. However, according to Figure 4.24(b), Series 1-repeat has a higher ultimate load than Series 8 for any given bond length which is contradictory to the observation from Figure 4.24(a). Similar contradictory observations can be made with other series containing non-circular bars by careful comparison of the two plots. Therefore, the differences in the two plots for non-circular bars are evident. Furthermore, bar perimeter is obviously one of the parameters directly related to bond whereas bar diameter/equivalent bar diameter is more related to the strength of the bar rather than being an indication of bond. For circular bars, bar diameter can be a substitution for bar perimeter as there is a linear relationship between them. However, with non-circular sections this substitution no longer makes sense as there is no linear relationship between them.

4.4.7 Load-slip behaviour

Figure 4.25 illustrates the typical load-loaded end slip behaviour of long bond length specimens containing different bar shapes whereas Figure 4.26 depicts the typical load-loaded end slip behaviour of short bond length specimens. It can be seen that in both cases, displacement ranges are quite similar for circular and square bars owing to their similar failure modes, while the range for rectangular bars reaches almost double the range for circular and square bars. Further, for both long and short bond length specimens, rectangular bars display a quite ductile load-slip behaviour compared to the other shapes due to the slip promoted by the common bond mechanism of rectangular bars, macro-cracking in the resin (refer to Section 5.1.6). The curves displayed in Figure 4.25 correspond to specimens *1-4[C12/60/S/12.7p]repeat* (circular), *7-28[R/60/S/12.7p]* (rectangular) and *9-36[S/60/S/Sika/12.7p]* (square) whereas the curves in Figure 4.26 represent *5-5[C12/30/S/1.6p]* (circular), *8-29[R/60/L/1.6p]* (rectangular) and *11-41[S/60/L/Sto/1.6p]* (square). Load-slip behaviour of other specimens can be found in Appendix B.

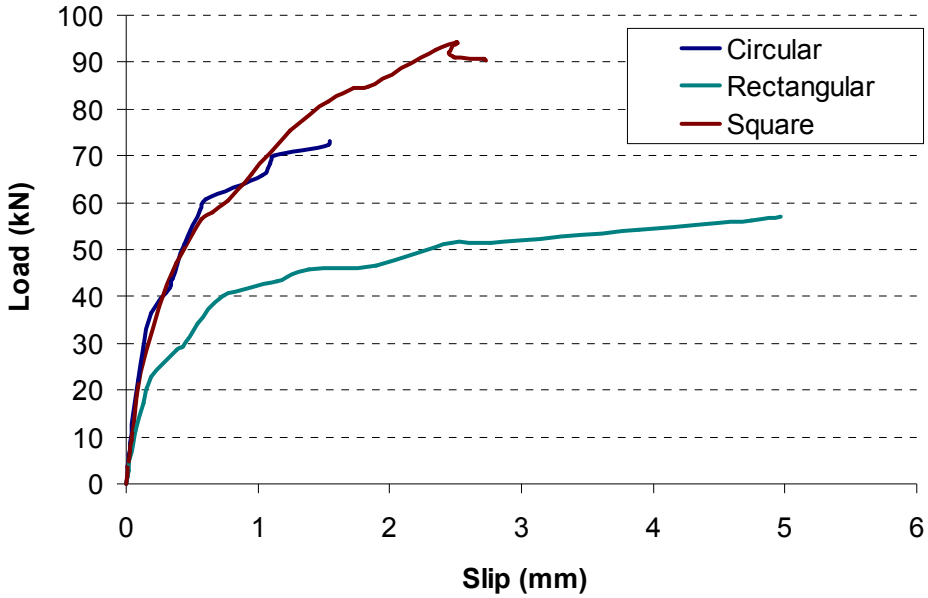

Figure 4.25 - Typical load-slip behaviour of long bond length specimens

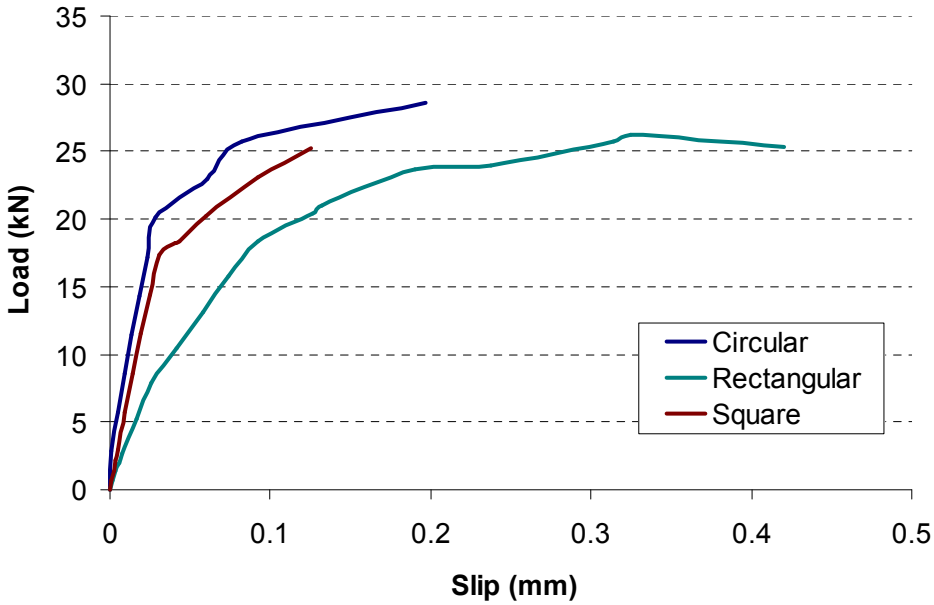

Figure 4.26 - Typical load-slip behaviour of short bond length specimens

4.5 Summary

The utilisation of tensile capacity of CFRP bars depends on cross-sectional area/perimeter ratio. Rectangular bars seem to be the most effective shape owing to the fact that they have a beneficial cross-sectional area/perimeter ratio. The utilised

tensile capacity of circular and square bars is considerably lower than their ultimate tensile capacity due to premature debonding unlike rectangular bars where tensile rupture of bars can be achieved. The definition of bond length in terms of number of bar perimeters appears to be more sensible than defining it in terms of number of bar diameters.

Among all the types of failures, splitting failures are the dominant mode for moderate concrete strengths, bond lengths and groove sizes. When all of these parameters reach their optimum values, the bond failure is controlled by CCSF for circular and square bars with fairly high cross-sectional area/ perimeter ratios as the upper-bound failure mode yielding the highest possible load capacity. The other less critical failure modes observed in the current research can be overcome by optimising the relevant variable responsible for the low capacity bond failure modes. For example, pull-out failure can be precluded by increasing the quality of degree of surface deformations. However, low capacity failure modes occurring in the concrete such as cohesive shear failure in the concrete cannot be prevented by optimising the concrete properties because in a strengthening situation, the concrete already exists and there is no control over the properties of the concrete. Resin splitting and cohesive shear failure within the resin can be overcome until CCSF occurs by providing an optimum groove size for a resin type with a high tensile strength and high shear strength. However, CCSF can occur as the lower-bound failure mode if the concrete strength is relatively low yielding the lowest possible load capacity.

For relatively short bond lengths, the bond behaviour was not affected by flexural/shear cracking and was similar to that of the previous NSM FRP bond tests with no internal steel reinforcement whereas for relatively long bond lengths, the bond behaviour was affected by flexural/shear cracking and was different to that of the previous NSM FRP bond tests and was similar to that of flexurally strengthened large scale beams. It was seen that the real beam behaviour can be qualitatively investigated in small scale beam-type bond tests with internal reinforcement as they fail in similar modes to those of real beams. At this stage, it is not possible to incorporate these bond stress-slip results for predictive models for real beams as these results are specimen size dependent. Therefore, it is required to investigate size effects in relation to bond behaviour of NSM FRP bars and concrete and establish correct quantitative correlations between bond test results and beam test results.

For both long and short bond length specimens, displacement ranges are quite similar for circular and square bars owing to their similar failure modes, while the range for rectangular bars reaches almost double the range for circular and square bars. Further, for both long and short bond length specimens, rectangular bars display a quite ductile load-slip behaviour compared to the other shapes due to the slip promoted by the common bond mechanism of rectangular bars, macro-cracking in the resin.

The next chapter presents the analysis of bond test data such as strain, slip and bond stress distributions along the bond length. Local bond stress-slip curves are developed and theoretical models addressing the dominant failure modes for circular and square bars (splitting failure and CCSF) are developed and compared with the experimental results.

CHAPTER 5 – ANALYTICAL METHODS

This chapter presents analysis of local bond stress-slip relationships, theoretical models addressing splitting failure modes, resin splitting and concrete splitting, and bounds for splitting resistance. Further, an upper-bound plasticity model to predict CCSF has been developed. All the models have been compared with the experimental results and the reliability of each model is discussed.

5.1 Local bond stress-slip curves

5.1.1 Analysis of slip and strain data to obtain local bond stress - slip relationship

The local bond stress-slip distributions have been obtained by analysing the strain gauge readings and the measured free end slip, by considering the equilibrium of an infinitesimal element of length dx and assuming linear elastic behaviour of the bar. Thus, the local bond stress, τ, is given by;

$$\tau(x) = \frac{A_f E_f}{p_f} \frac{d\varepsilon_f(x)}{dx} \tag{5.1}$$

where x = coordinate along the bond length starting from the free end, p_f = perimeter of the bar, A_f = cross-sectional area of the bar, E_f = Young's modulus of the bar and ε_f = axial strain of the bar.

By assuming the concrete strain is negligible compared to FRP strain, the local slip of the bar along the bond length can be obtained as follows,

$$s(x) = s_{fe} + \int_0^x \varepsilon_f(x)\, dx \tag{5.2}$$

where s_{fe} is the free end slip.

The strain versus location graphs have been plotted for different load levels as a percentage of the ultimate load, assuming that the strain at the free end is zero. The local bond stress and slip distributions along the bond length at different load levels have been obtained, by approximating Equations (5.1) and (5.2) for discrete strain gauge readings. Finally, the bond stress versus location and the slip versus location data have been combined to plot the bond stress versus slip curves at each strain gauge location, presented next.

5.1.2 Bond behaviour of circular bars

5.1.2.1 Bond behaviour of specimens containing long bond lengths and short bond lengths

Figure 5.1 depicts strain, bond stress and slip distributions along the bond length in two specimens, namely specimen *4-12[A9/60/S/12.7p]* and specimen *6-13[A9/30/S/1.6p]*, at different load levels, as a percentage of the ultimate load. Specimen *4-12[A9/60/S/12.7p]* represents the general behaviour of specimens containing a long bond length and specimen *6-13[A9/30/S/1.6p]* illustrates the common behaviour of specimens having a short bond length, irrespective of the other variables. There is a clear difference between the behaviour of specimens having long bond lengths and those having short bond lengths. The strain distribution of specimen *4-12[A9/60/S/12.7p]* is generally non-linear at low load levels, and tends to follow a more linear shape as the load approaches the ultimate, whereas that of specimen *6-13[A9/30/S/1.6p]* shows some linearity even at low load levels. It seems that bond stresses tend to become more even at final load levels in the specimens with long bond lengths, due to the redistribution of bond stresses after local bond degradation occurs at the loaded end. The approximate linearity of the strain distribution, even at low load levels, suggests that the bond stresses are generally fairly constant along the bond length in specimens containing short bond lengths. Generally, it is believed that bond stresses along the bond length are even for short bond length specimens (Stratford, 2001). Further, in specimens containing short bond lengths, there are gradual strain increments during all the load increments (or almost equal strain increments during the equal load increments), at all strain gauge locations, unlike in the case with specimens

containing long bond lengths, where the largest increment of strain always occurs during the final load increment (90 -100%).

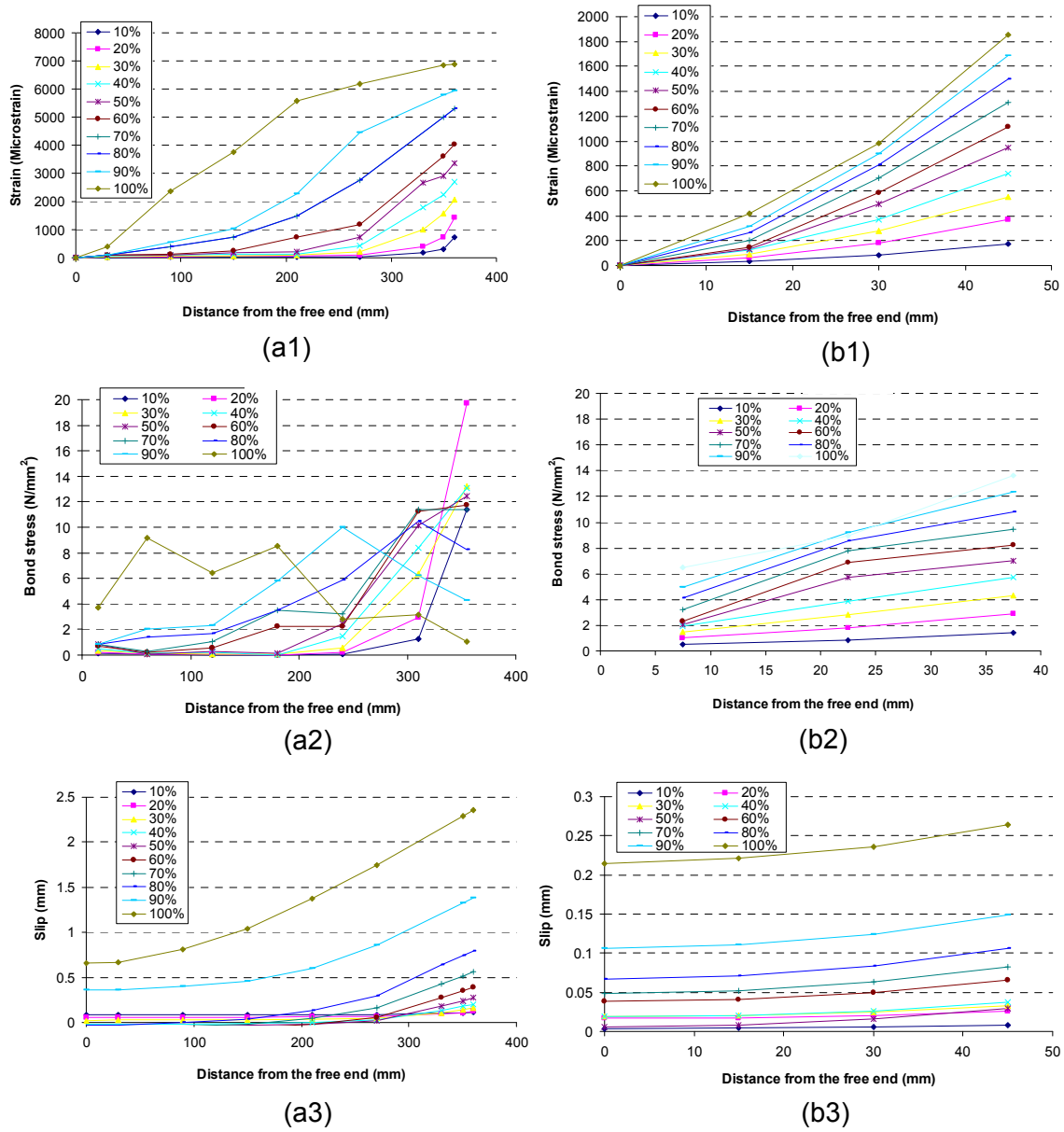

Figure 5.1 - Strain, bond stress and slip distributions along the bond length: (a1-a3) specimen *4-12[A9/60/S/12.7p]* and (b1-b3) specimen *6-13[A9/30/S/1.6p]*

At low load levels, in specimen *4-12[A9/60/S/12.7p]*, the bond stress at the free end is almost zero and at the ultimate load level it increases considerably, showing that the whole bond length contributes to the bond action at final load levels. Initially, only a part of the bond length, which is close by to the loaded end, is resisting the pulling action,

and once the bond resistance is lost there, the remaining part of the bond length starts resisting the applied load, thereby increasing the bond stresses towards the free end. This is clearly indicated by the peak value moving towards the free end, and by the bond stress at the loaded end decreasing during the final load levels. This phenomenon is completely different for specimens containing short bond lengths, where the bond stress at the free end gradually increases from the beginning of the load application. That means the whole bond length is contributing to the bond resistance from the start to the end of the pull-out action.

The free end slip of specimens containing long bond lengths is almost zero at low load levels. The specimens with short bond lengths show an almost constant slip distribution along the whole bond length at all load levels, confirming the previous findings (Stratford, 2001). Consequently, as the load increases, gradual slip increments can be seen everywhere along the bond length in those specimens, unlike in the case with specimens containing long bond lengths.

Figure 5.2 illustrates the bond stress versus slip distribution at the location of each strain gauge along the bond length in specimens *4-12[A9/60/S/12.7p]* and *6-13[A9/30/S/1.6p]*, which represent the general bond stress-slip behaviour of long bond lengths and short bond lengths, respectively. These graphs are obtained from the bond stress and slip values at each load level up to the ultimate load level. In other words, the bond stress-slip behaviour at each strain gauge location, up to the ultimate load level, is considered. The bond stress-slip relationships are quite irregular because both the bond stress and the slip values are based on a limited number of strain gauge readings, and affected by imperfections in the interface conditions. In spite of the irregularity, the basic shape of the bond stress-slip curve is clearly visible in both graphs. Since the free end slip readings of specimen *4-12[A9/60/S/12.7p]* were highly irregular during the initial stages of loading, the bond stress-slip curves at locations closer to the free end (for example, the 15 mm, 60mm and 120mm locations) have been affected significantly by that. Therefore, the bond stress-slip curves at those locations show a significant deviation from the desired shape of the bond stress-slip curve, whereas this effect is marginal on the bond stress-slip curves at locations away from the free end.

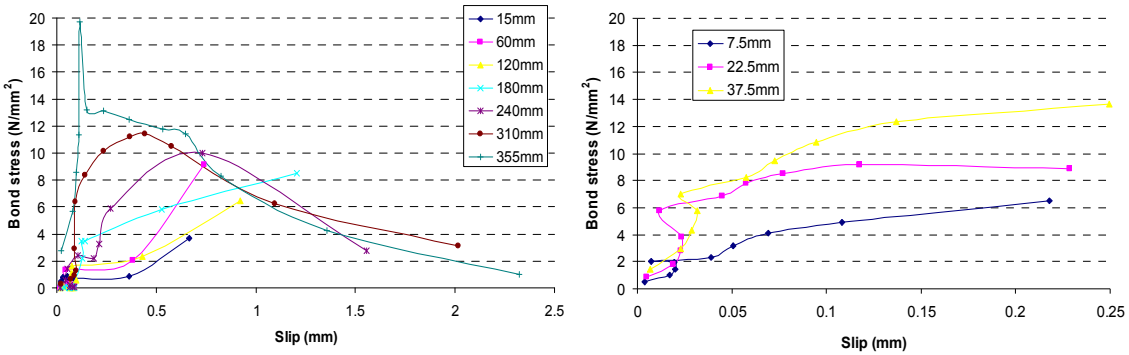

Figure 5.2 - Bond stress-slip curves: (a) specimen *4-12[A9/60/S/12.7p]*, (b) specimen *6-13[A9/30/S/1.6p]*

The main difference between the shapes of the two graphs is that there is no post-peak branch for the specimens with short bond lengths because the bond length is not long enough for redistribution of bond stresses to occur by the time the ultimate load is reached, unlike in the case with long bond lengths. Further, there is a significant difference between the bond behaviour at the 15mm location of specimen *4-12[A9/60/S/12.7p]* and the 7.5mm location of specimen *6-13[A9/30/S/1.6p]*. The 15mm location, being the closest point to the free end of specimen *4-12[A9/60/S/12.7p]*, has not reached the peak bond stress at all. The 7.5mm location, being the closest point to the free end of specimen *6-13[A9/30/S/1.6p]* has almost reached the peak value, and behaves almost the same as the other points along the bond length, confirming that the whole bond length of specimens containing short bond lengths contributes to the bond action from the very beginning to the end.

5.1.2.2 Local bond behaviour at different locations along the bond length

Generally, in all the specimens, local bond stress-slip curves were slightly different from one location to another along the bond length. In many cases of specimens having long bond lengths, only the locations close to the loaded end showed high bond stresses. Bond softening was seen only at the locations close to the loaded end, whereas the locations near the free end had just attained the peak bond stress or even a lower bond stress. Generally, a gradual failure mechanism, such as resin splitting, first causes the failure at the loaded end, causing bond degradation at the loaded end.

Then, the peak bond stress moves towards the free end allowing bond redistribution, provided that the bond length is long enough for bond redistribution to occur.

Therefore, whenever a failure occurs in these specimens (long bond length specimens), local bond stress-slip curves at the loaded end and the adjacent locations show similar behaviour with a post-peak branch appearing with approximately the same local bond strength. However, if specimens are failing in one of the brittle failure modes such as CCSF (for example, specimen *3-24[A12/60/S/12.7p]*), local bond stress-slip curves at the loaded end and the adjacent locations vary significantly from each other (Figure 5.3). The reason is that bond redistribution, which is a gradual process, is not possible as the failure is brittle. As a result, as soon as the bond fails locally at the loaded end, the bond failure spreads abruptly into the remaining area, towards the free end, without allowing bond stresses at adjacent locations to rise up to the peak value. However, in some of the specimens failing in CCSF, the bond redistribution had taken place before the brittle CCSF occurred, as described later on. In that case, local bond stress-slip curves at the loaded end and at the adjacent locations should generally look alike, provided that there is no influence from flexural/shear cracking on pure bond behaviour. The effect of flexural/shear cracking on pure bond behaviour is discussed in Section 5.1.5.

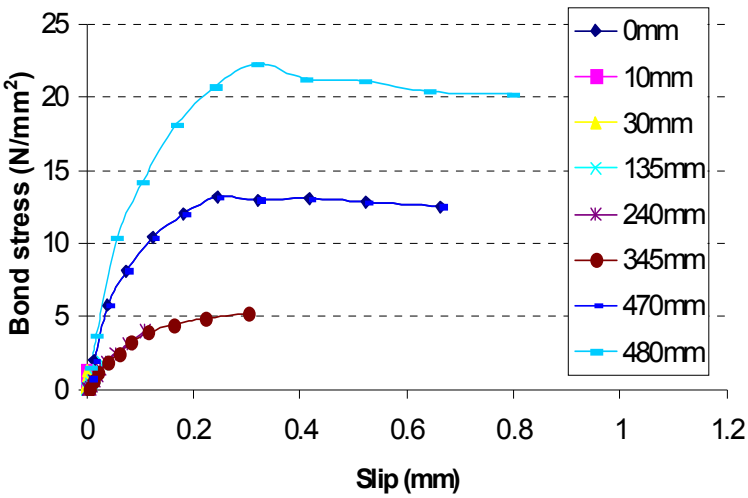

Figure 5.3 - Bond stress-slip behaviour of specimen *3-24[A12/60/S/12.7p]*

5.1.2.3 Behaviour of specimens attaining the highest local bond strength

The local bond strength of specimens failing in SOOL (Specimen *1-4[C12/60/S/12.7p]*, Specimen *1-4[C12/60/S/12.7p]repeat* and *1-3[C12/60/S/6.4p]repeat*) was significantly higher than that of the specimens failing in other failure modes (around 30 N/mm^2), because this is the highest possible bond resistance achievable by an FRP bar embedded in concrete. As explained in Chapter 2, the bond mechanism offering the highest bond resistance for an FRP bar is shearing off of the bar deformations, inter-laminar shear failure, or shear failure of the concrete in front of bar deformations, depending on the relative shear strengths. The first two modes and the shear failure in the resin are possible failure mechanisms for an NSM FRP bar, depending on the relative shear strengths. When achieving such a high bond strength, there should be enough resistance in the surrounding resin cover to avoid resin splitting failure. The provided cover was able to prevent splitting failure so that the specimens considered here were able to attain the highest possible bond resistance.

However, there was some partial resin splitting near the loaded end in specimen *1-4[C12/60/S/12.7p]*. Also, in specimen *1-4[C12/60/S/12.7p]repeat*, some resin splitting near the loaded end was observed with a very narrow crack width. These examples show that even though there was partial resin splitting near the loaded end, it was not critical enough to cause failure by spreading over the entire bond length. Further, in specimen *1-3[C12/60/S/6.4p]repeat* no resin splitting near the loaded end was observed. However, it is possible that even in specimen *1-3[C12/60/S/6.4p]repeat*, some resin splitting might have occurred when the bond stresses exceeded the splitting strength, but with no visible resin splitting on the outer surface, i.e. either resin splitting occurred in the internal cover or the splitting cracks occurred in the external cover without reaching the outer surface.

These specimens could carry significant load (up to 70% of the ultimate capacity) after initial failure, unlike other specimens, as discussed in Chapter 4. This is probably because of the failure occurred by shearing off of only a part of the bonded joint so that the rest of the joint could maintain significant capacity before complete failure occurred.

5.1.2.4 Relationship between local bond strength and ultimate load capacity

The local bond strength of specimen *1-3[C12/60/S/6.4p]repeat* is significantly higher than that of specimen *3-23[A12/60/S/6.4p]*. Both specimens had similar bond parameters with different bar surface textures. However, the ultimate capacity of the latter was considerably higher than that of the former, indicating the non-linear bond stress distribution along the bond length. Further, locations close to the free end of the former developed noticeably lower bond stress values, compared to that of the latter, by the time the ultimate capacity was reached. This confirms that even though the latter had lower local bond strength, as the whole bond length was effectively contributing, it was possible to gain a higher capacity than that of the specimen with higher local bond strength.

5.1.2.5 Relationship between local bond strength and resin cover thickness

Local bond strength of specimens in Series 2 failing in resin splitting was considerably higher than that of the specimens in other series failing in the same mode, because Series 2 had the highest resin cover thickness amongst all the series so that the resistance to resin cover splitting was higher.

5.1.3 Assumptions in analysing slip and strain readings

The free end slip was calculated from the difference in the readings of two LVDTs measuring displacements of the CFRP bar and the concrete at the free end. However, most of the time concrete displacement appeared to be higher than the bar displacement, which is counter-intuitive. Consequently, free end slip was determined to be negative in these cases. The exact reason for this happening is not clear and it may be due to an experimental error. Sometimes, it was clearly seen that there was an initial error in one of the displacement readings, in which case the correct free end slip had to be taken after deducting that initial error. Because of this inconsistency in displacement readings, it was not reliable to use them in the analysis. Therefore, free end slip is assumed as zero for all the tests. On the other hand, in many un-erroneous cases, free end slip was almost zero throughout testing, except at load levels closer to

the ultimate load, in specimens containing long bond lengths. Therefore, this assumption is believed to have little effect on long bond length specimens. However, for short bond lengths, there is a considerable free end slip even from low load levels as discussed earlier, and omitting the free end slip in bond stress-slip analysis seems to yield lower slip values than actual.

5.1.4 Bond behaviour of rectangular and square bars

A similar procedure was adopted for specimens containing rectangular and square bars in local bond stress-slip analysis.

5.1.4.1 Rectangular bars

The local bond stress-slip behaviour of short bond length specimens containing rectangular bars was different to that of short bond length specimens containing circular and square bars. That is to say, specimens containing rectangular bars exhibited a post-peak branch even for the shortest bond length (1.6 times the bar perimeter), unlike the specimens containing circular and square bars for the same bond length, indicating the effectiveness of rectangular bars compared to square and circular bars because of its beneficial cross-sectional area/perimeter ratio. Another difference between the bond behaviour of circular and square bars and that of rectangular bars is that there is a relatively ductile response at the peak bond stress, as can be seen in many of the plots in Figure 5.4. This ductile behaviour was common to all the specimens containing rectangular bars irrespective of the failure mode, except for specimen *8-30[R/60/L/3.2p]* (Figure 5.4(d)) and the reasons for this behaviour is explained in Section 5.1.6.

Bond stress-slip curves at different locations along the bond length are quite different from each other as far as the local bond strength is concerned, unlike those of circular and square bars. Local bond strength at different locations along the bond length vary from about 10-20N/mm^2 (Figure 5.4). Therefore, it was difficult to fit them into an analytical expression due to the large scatter. Generally, local bond strength of specimens containing rectangular bars was higher than that of the specimens containing circular and square bars, when the maximum local bond strength achieved

by Carbopree bars in Series 1 is disregarded. However, the shape of the local bond stress-slip relationship at different locations along the bond length are quite similar (all locations showing ductile behaviour at the peak bond stress value).

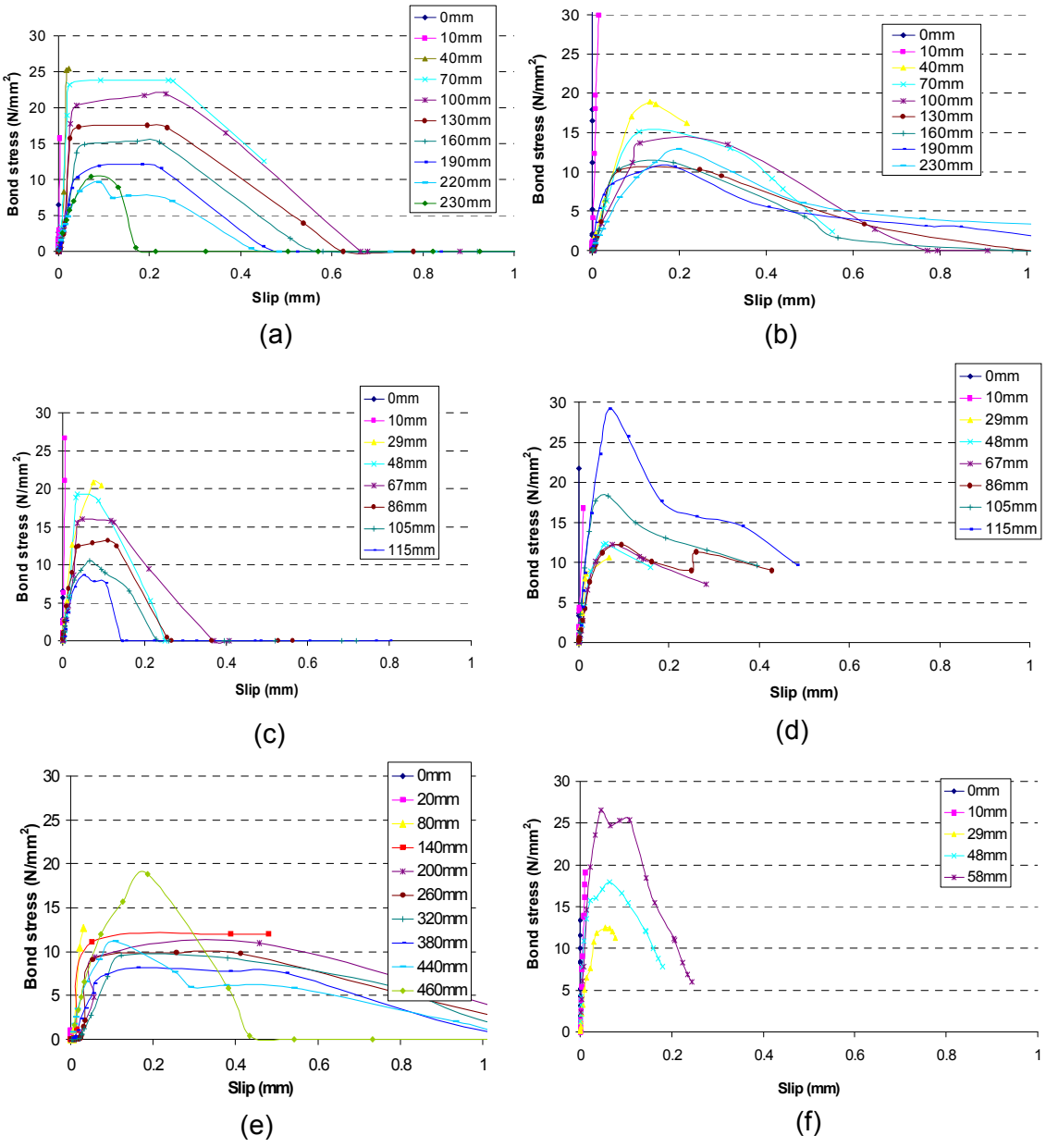

Figure 5.4 - Bond stress-slip relationship of specimens containing rectangular bars: (a) *8-31[R/60/L/6.4p]* (tensile rupture), (b) *7-27[R/60/S/6.4p]* (partial resin splitting/cracking), (c) *7-26[R/60/S/3.2p]* (partial resin splitting/cracking), (d) *8-30[R/60/L/3.2p]* (partial resin splitting/cracking), (e) *7-28[R/60/S/12.7p]* (fibre splitting and resin splitting) and (f) *7-25[R/60/S/1.6p]* (partial resin splitting/cracking)

5.1.4.2 Square bars

The local bond strength of specimens in Series 10 failing in pure bar-resin interfacial failure (pull-out failure) (Figure 5.5) is notably lower than that of the other specimens containing square bars and failing in other failure modes. Generally, the local bond strength of all the specimens containing square bars was comparatively low because the bond properties, and thereby the failure modes, were governed by the smoothness of the bar surface texture. An important fact to note is that none of the specimens containing square bars failed in resin splitting, which offers higher local bond strength. The poor bond in specimens containing square bars, due to a smooth bar surface texture, was not able to sustain a stress level as high as that otherwise achievable due to resin splitting resistance. Instead, partial splitting either in the resin or the concrete (or in both) was observed, combined with pull-out failure.

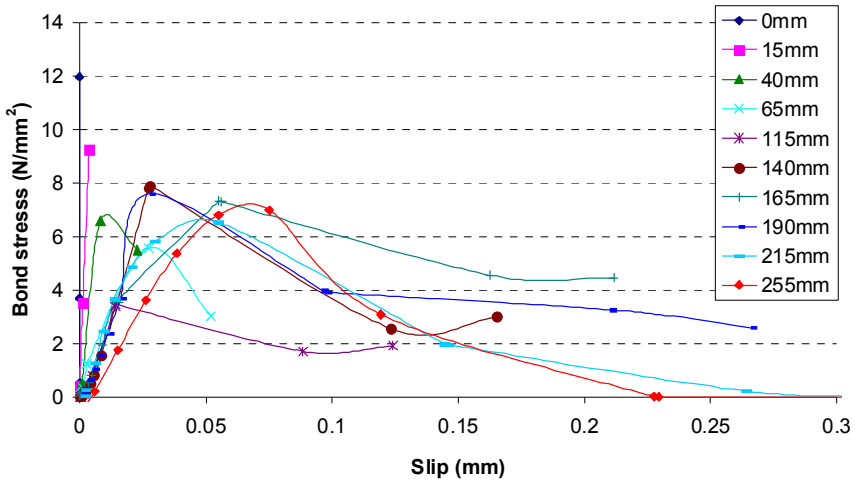

Figure 5.5 - Local bond stress-slip behaviour of specimen *10-39[S/60/L/Sika/6.4p]* failing in pure bar-resin interfacial failure

5.1.5 Effect of flexural/shear cracking on pure bond behaviour

Sometimes there was local cracking in the bonded joint, at a gauge location close to the loaded end (high moment regions), particularly with long bond lengths and in specimens failing in CCSF, which is a result of flexural/shear cracking in the adjacent concrete propagating to the bonded joint. When local cracking occurred at a point close

to the loaded end (but not at the immediate gauge location to the loaded end), bond stresses were released locally, and the strain in the bar at that point increased more than that at the immediate gauge location at the loaded end, unlike in the case of pure bond behaviour. When there is pure bond behaviour, release of bond stress (bond degradation) starts from the loaded end and debonding gradually propagates towards the free end. Consequently, when local cracking starts, bond softening occurs at the point before the bond softening occurs at the immediate locations to the loaded end and the initial strain gradient of the locations near the loaded end remains approximately the same while the strain gradient at the local cracking location reduces considerably. In other words, bond stresses at locations near the loaded end remain roughly the same (so that there is ductile bond behaviour), while the local bond stress at the cracking point reduces. This ductile bond behaviour near the loaded end was clearly visible in the specimens failing in CCSF, for example, in specimens *5-8[C12/30/S/12.7p]*, *6-16[A9/30/S/12.7p]* and *11-44[S/60/L/Sto/12.7p]* (Figure 5.6), as well as in some of the specimens containing long bond lengths where local cracking was observed, for example, in specimen *4-12[A9/60/S/12.7p]* (Figure 5.2(a)).

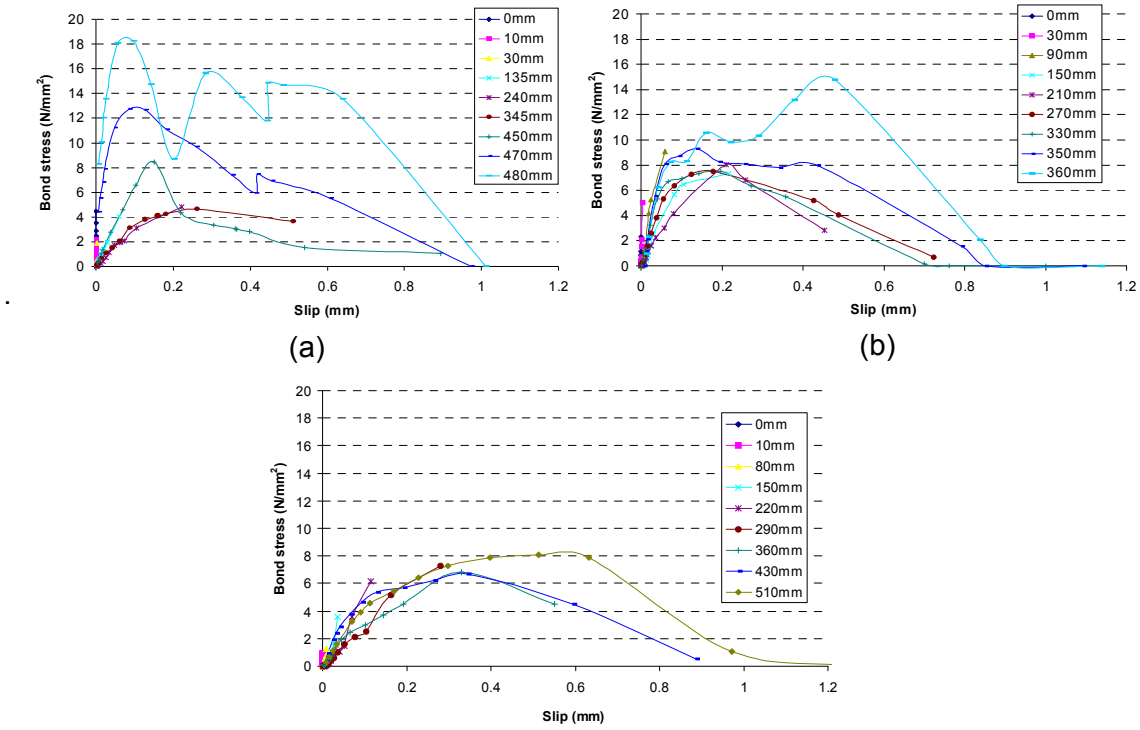

Figure 5.6 - Ductile bond stress-slip behaviour at some locations along the bond length (a) specimen *5-8[C12/30/S/12.7p]*, (b) specimen *6-16[A9/30/S/12.7p]* and (c) *11-44[S/60/L/Sto/12.7p]*

Consequently, the local bond stress-slip relationships at different locations along the bond length differ significantly from each other depending on where there is pure bond behaviour and where the pure bond behaviour is affected by flexural/shear cracking.

5.1.6 Ductile bond behaviour of specimens containing rectangular bars

As described earlier, different bond behaviour (ductile behaviour at almost all the gauge locations) was observed in specimens containing rectangular bars. A ductile behaviour was observed also in specimens containing circular bars and square bars when there was local cracking close to the loaded end, as described in Section 5.1.5. The local cracking was due to the influence of the extensive flexural/shear cracks and occurred only for long bond lengths at high moment regions (i.e. near the loaded end). Therefore, on those occasions, the local bond stress-slip relationship at locations near the free end was not affected by local cracking, so that there was no ductile behaviour at the peak value. However, in the case with rectangular bars, the ductile behaviour was consistent throughout the bond length suggesting that this is not due to local cracking resulting from flexural/shear cracks. On the other hand, there was mild flexural/shear cracking in specimens containing rectangular bars even for long bond lengths, because lower ultimate loads were acting owing to the smaller cross-sectional area of the bar (refer to Section 4.2.3 for further details and figures of flexural/shear cracking). Besides, this ductile behaviour could be seen even in the specimen containing the shortest bond length (1.6 times the perimeter) (Figure 5.4(f)). Therefore, this ductile behaviour could be due to macro-cracking forming in the bonded joint itself, rather than a local effect resulting from flexural/shear cracking.

Generally, micro-cracks form when the principal tensile stress caused by the tangential bond stress exceeds the tensile strength of the resin. Then transverse bond stresses also form, and resin splitting will occur once the principal tensile stress caused by transverse bond stresses exceeds the tensile strength of the resin. However, it is unlikely that splitting failures will occur in the case with rectangular bars, unlike the case with circular bars, because the lateral bond forces now act on thicker lateral sides of the concrete specimens (Blaschko, 2003). Therefore, the bond stresses in this case (with rectangular bars) are likely to be able to rise above the normal resin splitting bond strength of circular bars, for a given resin. Therefore, for rectangular bars, it is possible

for micro-cracks to widen while the bond stresses are rising beyond the normal resin splitting bond strength of circular bars. Generally, the local bond strength of almost all the specimens containing rectangular bars was higher than that of the specimens containing circular bars that failed in resin splitting, where the same resin was used (confirming the assumed behaviour). Once the cracks near the loaded end are wide enough to cause the bond softening, the debonding process is believed to start from the loaded end and to spread towards the free end. However, when a gauge is located exactly on a crack location, the local bond stress-slip behaviour does not show ductile behaviour at the peak value; instead it behaves similar to the normal case, because as soon as the macro-crack forms, the bond stresses at that location soften, while the bond stresses at the adjacent locations towards the loaded end remain the same for a while. That is why the local bond stress-slip relationship at the loaded end of some of the specimens in Figure 5.4 did not show ductile response, while that of the other specimens in the figure indeed showed ductile behaviour, exhibiting the influence of the crack location on the local bond stress-slip relationship.

The local bond stress-slip relationship of specimen *8-31[R/60/L/6.4p]* that failed in tensile rupture also showed similar behaviour, indicating that bond degradation started from the loaded end by macro-cracking and had already propagated towards the free end when tensile rupture occurred. As explained in Chapter 4, even though resin splitting occurred partially in the external cover in many of the specimens, splitting could not be the sole mode of failure. Therefore, these specimens are believed to have failed when macro-cracking occurred in the resin along the whole bond length. Traces of macro-cracking could not be observed as pull-out could not be continued (refer to Chapter 4). This assumed behaviour can be confirmed because when both specimen *8-31[R/60/L/6.4p]* and its control specimen failed in tensile rupture, there was no trace of resin splitting/cracking or concrete splitting/cracking or indeed any other form of damage. But the local bond stress-slip relationship (Figure 5.4(a)) shows how bond softening had already occurred along a considerable portion of the bond length. So the conclusion is that the specimens that showed signs of partial resin splitting or cracking in the external resin cover actually failed by macro-cracking in the resin (when micro-cracks became macro-cracks).

In general, similar bond behaviour (the range of the local bond strength and the shape of the curve) was observed in all the specimens containing rectangular bars

irrespective of the failure mode, because bond softening started from the loaded end by the same mechanism, namely macro-cracking. The effect of resin cover thickness on local bond strength of specimens containing rectangular bars that failed in macro-cracking can be seen by comparing Figures 5.4(a) vs. 5.4(b) and Figures 5.4(c) vs. 5.4(d) where in both occasions, as the resin cover increased, local bond strength also increased noticeably, because widening of micro-cracks (macro-cracking) was delayed correspondingly. This also attracted an increase in the load capacity as discussed in Chapter 4.

5.1.7 Bond behaviour of specimens failing in CCSF

In many of the series (eight out of the eleven), failure of the specimen containing the maximum bond length occurred by CCSF, sometimes limiting the local bond strength of the bonded joint (Case 1) or sometimes limiting the ultimate capacity of the specimen (Case 2 or Case 3).

5.1.7.1 Case 1

In a few of the cases failing in CCSF (for example, specimen *3-24[A12/60/S/12.7p]*), there was no softening branch in the bond stress-slip law, even though the bond length was relatively long, indicating that there was no bond redistribution taking place when the ultimate load was reached. In other words, there was no bond degradation when the CCSF occurred (Figure 5.3). This specimen showed quite a ductile response before CCSF occurred because of the influence of flexural/shear cracking, as explained in Section 5.1.5.

5.1.7.2 Case 2

In many cases of CCSF, the bond redistribution occurred near the end of the test, unlike in the general case of a bond test where bond redistribution occurs gradually throughout loading, normally from about half of the maximum load capacity if the bond length is fairly long, for example, in specimen *10-40[S/60/L/Sika/12.7p]* (Figure 5.7(a)).

5.1.7.3 Case 3

This case represents the situation when the bond redistribution had already taken place over a considerable portion of the bond length when the CCSF occurred, in only one case (specimen *2-19[A9/60/L/6.4p]*), possibly because of the shorter bond length compared to the other specimens that failed in CCSF (Figure 5.7(b)). This specimen also showed ductile bond behaviour at the gauge locations near the loaded end.

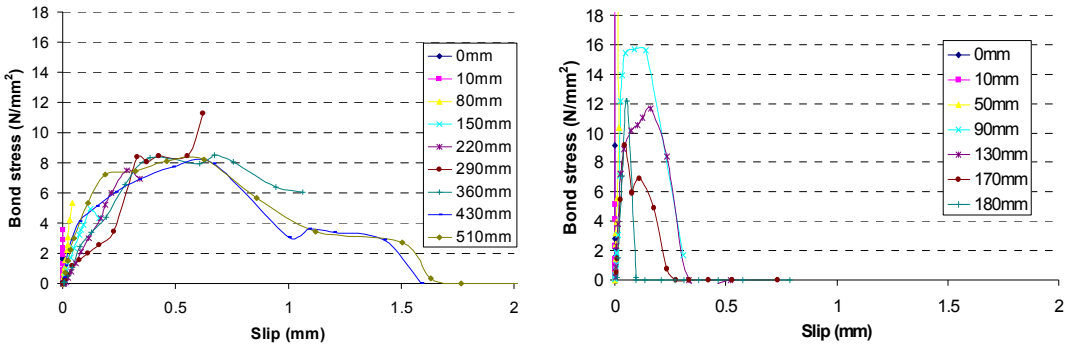

Figure 5.7 - Local bond stress-slip behaviour of specimens failing in CCSF: (a) specimen *10-40[S/60/L/Sika/12.7p]* and (b) specimen *2-19[A9/60/L/6.4p]*

From Case 1, it is clear that the bonded joint would have developed higher local bond strength if the failure had not been prematurely caused by CCSF. From Case 2 and Case 3, it is evident that local bond strength would not have exceeded the current value, as the bond degradation had already taken place locally by a different failure mechanism, such as local resin splitting. Local resin splitting in either the internal or external resin cover, or in both covers, was observed in the failed specimens. It was not possible to observe them while the loading progressed as the failure was explosive. For Case 1, the local bond degradation did not occur before the ultimate load capacity was reached by CCSF, whereas for Cases 2 and 3, local bond degradation did indeed occur before the ultimate load capacity was reached by CCSF. In both Cases 2 and 3, it would have been possible to achieve a higher ultimate load capacity if the failure had not been caused prematurely by CCSF, and the real failure would have occurred after the debonding had occurred along the whole bond length, from the loaded end to the free end. These examples confirm that CCSF is a critical failure mode that starts away

from the bonded joint, normally limiting either local bond strength or ultimate load capacity of the specimen.

5.2 Analytical bond stress - slip relationships

The following analytical bond stress-slip relationships were selected to model the experimental bond stress-slip curves at the loaded end. Firstly, the ascending branch of all the specimens was modelled using the BEP model (refer to Chapter 2) because of its ability to simulate the bond behaviour up to the peak bond stress;

$$\tau = \tau_m (s/s_m)^{\alpha} \text{ for } 0 \le s \le s_m \quad (5.3)$$

where τ, s, τ_m, s_m, and α are local bond stress, local slip, local bond strength, slip at local bond strength and a bond parameter which varies between 0 and 1, respectively.

For the modelling of the descending branch of all the specimens (with few exceptions described below), the model adopted by De Lorenzis (2002) was used because the post-peak bond behaviour is well represented by the model within the experimentally available range of slip values;

$$\tau = \tau_m (s/s_m)^{\alpha'} \text{ for } s \ge s_m \quad (5.4)$$

The model is identical to the equation of the ascending branch, with a negative value for α, α'.

The bond stress-slip behaviour of specimens containing Carbopree bars that failed in shearing off of the outer layer (in Series 1) seemed to be well interpreted by the softening branch of the MBEP model (refer to Chapter 2) and by introducing a constant branch after the softening branch, which represents the friction along the failed interface;

$$\tau = \tau_m + k'(s - s_m) \text{ for } s_m \le s \le s_f \quad (5.5)$$

$$\tau = \tau_f \text{ for } s \ge s_f \quad (5.6)$$

where k' is the slope of the linear branch, τ_f is the frictional bond stress, and s_f is the value of slip when bond stress reaches the frictional bond stress level. The same models were used to model the post-peak behaviour for square CFRP bars (Series 9 and 10) because these specimens also showed a clear frictional plateau. Even though, Series 11 contained the same CFRP bars, the specimens in Series 11 did not show a frictional plateau possibly because the different adhesive might have changed the bond behaviour.

When the bond fails in SOOL, the only mechanism available to resist bond stresses afterwards is friction, so that the softening branch falls rapidly from the peak value to the residual stress level. Similarly, failure modes like pure bar-resin interface failure and pure resin-concrete interface failure should exhibit the same swift behaviour in bond degradation because the next available resisting mechanism is the friction of the corresponding interface. However, when the failure is by resin splitting in the external cover, there is still a considerable contribution to bond resistance from the resin cover of the other un-split sides. Consequently, the softening branch falls gradually until the resin cover in all directions is completely broken and will reach the frictional stress level thereafter. Similarly, in the cases of concrete splitting and resin-concrete interface failure (cohesive shear failure of the concrete), again there is a gradual softening branch up to the residual bond stress level, as the aggregate interlocking of the concrete fracture surfaces also contributes to bond resistance. The above features of bond stress-slip behaviour were observed experimentally in the specimens that failed in the described failure modes, provided that the bond length was long enough to redistribute bond stresses so that a softening branch was available.

The parameters of the bond models were determined by best fitting the average bond stress - loaded end slip behaviour for each series and are listed in Table 5.1. Two examples of analytical bond stress-slip relationships are illustrated in Figure 5.8. In most of the specimens, near the ultimate load level, strain gauges stopped functioning with increasing slip. Consequently, softening branches were highly irregular. When there was large scatter in softening branches, only the ascending branch has been modelled, for example, in specimens failing in CCSF.

Series	Failure mode	τ_m (N/mm^2)	s_m (mm)	α	α'	τ_f (N/mm^2)	s_f (mm)	k' (N/mm^3)
Series 1 (12/Carbopree/1.33)	SOOL	29.0	0.060	0.810	-	3.11	0.101	-827
Series 2 (9/Aslan/2)	Splitting[1]	28.3	0.048	0.708	-1.870	-	-	-
Series 3 (ascen. branch only) (12/Aslan/1.33)	CCSF	23.7	0.320	0.533	N/A	-	-	-
Series 3 (12/Aslan/1.33)	Splitting[2]	14.8	0.047	0.722	-0.617	-	-	-
Series 4 (9/Aslan/1.44)	Splitting[2]	15.7	0.051	0.667	-0.394	-	-	-
Series 5 (ascen. branch only) (12/Carbopree/1.33)	Splitting[1]	12.5	0.069	0.504	N/A	-	-	-
Series 6 (ascen. branch only) (9/Aslan/1.44)	Splitting[2]	15.4	0.061	0.607	N/A	-	-	-
Series 9 (10x10/Sto/1.4)	PO+splitting[2]	10.5	0.071	0.948	-	2.80	0.622	-14.7
Series 10 (10x10/Sto/1.8)	CCSF	8.33	0.381	0.595	-	3.32	1.170	-6.60
Series 10 (10x10/Sto/1.8)	PO	6.90	0.047	0.980	-	2.63	0.124	-54.9

Table 5.1 - Calibrated bond parameters

(Note: the description within the parentheses includes bar diameter, bar type and groove depth/bar diameter (or bar depth) ratio, respectively, and N/A-not available)

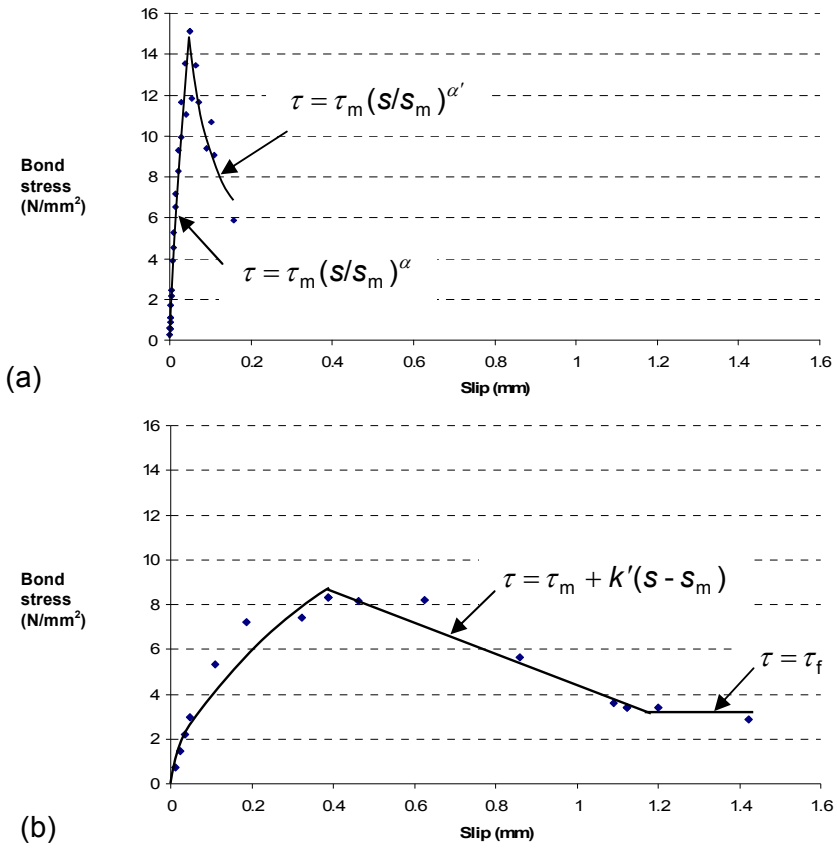

Figure 5.8 - Analytical bond stress-slip relationships: (a) *3-22[A12/60/S/3.2p]* and (b) specimen *10-40[S/60/L/Sika/12.7p]*

The values of local bond strength range from 6.9N/mm^2 to 29N/mm^2 and the slip at the maximum bond stress vary from a minimum of 0.047mm to a maximum of 0.381mm. In the previous studies of De Lorenzis (2002) and Sena Cruz (2004), the values of local bond strength vary from 4.67N/mm^2 to 17.03N/mm^2 and from 18N/mm^2 to 21.5N/mm^2, respectively, while corresponding slip values at the maximum bond stress vary from 0.069mm to 0.481mm and from 0.14mm to 0.43mm, respectively. It can be seen that the upper limit of the bond strength in the current study, 29N/mm^2, is quite high while the lower limit of the corresponding slip is quite low, 0.047mm compared to those of the other studies. The lower slip value limit is probably caused by the assumption of zero free end slip (refer to Section 5.1.3).

The local bond strength of CFRP bars in each series was mainly dependent on resin cover thickness, bar type and failure mode. Specimens that failed in SOOL within the bar and resin splitting showed the highest local bond strengths (Table 5.1). However, it is difficult to determine the actual relationship between local bond strength and ultimate capacity of the bond specimens as bond stress distribution along the bond length is not constant.

5.3 Ultimate capacity for CCSF using plasticity theory

As discussed in the previous chapter, CCSF was identified as the critical failure mode, which often limits further bond development for circular and square bars that have a relatively high cross-sectional area/perimeter ratio. Therefore, it is important that suitable theoretical models are available to predict the CCSF capacity to avoid catastrophic bond failure in NSM CFRP strengthened concrete structures. The following analysis is an attempt to develop a theoretical model to cater for that issue, by using the theory of plasticity.

5.3.1 Theory of Plasticity

Generally, there are two approaches in plasticity theory, lower-bound analysis and upper-bound analysis. In lower-bound analysis, only equilibrium is considered whereas

in upper-bound analysis, only kinematic compatibility is considered. They are sometimes called the static approach and the kinematic approach, respectively.

- In the lower-bound theorem, an estimate for the capacity of the structure is found by considering any internal stress system that is in equilibrium with the external loads without violating the yield condition. The capacity obtained in this approach is always equal to or lower than the actual collapse load so that the lower-bound theorem is often known as the safe, or conservative, method.

- In the upper-bound theorem, an estimate for the load capacity of the structure is found for any compatible collapse mechanism by equating internal energy dissipation to the external work done by the applied loads. This estimate will always be equal to or higher than the actual collapse load. This theorem is theoretically unsafe as it overestimates the actual capacity. However, by considering several possible collapse mechanisms or by minimising the solution with respect to geometrical parameters defining the yield line, it is possible to find the critical load capacity.

If an upper-bound solution and a lower-bound solution happen to yield the same load capacity, then the solution is called an exact solution.

5.3.2 Concrete Plasticity

A comprehensive review of concrete plasticity, including the theory and solutions to a wide range of problems, can be found in Nielsen (1998). In reality, concrete is not a perfectly-plastic material that can undergo large deformations at a constant stress level. The stress-strain curve for concrete has a softening branch after the ultimate strength, and therefore ductility is limited so that softening effects need to be taken into account (Nielsen, 1998). Therefore, strength parameters that need to be applied in theoretical solutions using plasticity theory are called effective strengths and are lower than the peak strength values. An effectiveness factor, ν_c, is introduced to define this reduced strength (effective compressive strength of concrete, f_c) as follows.

Effective compressive strength of concrete $f_c = \nu_c f_{cu}$ (5.7)

where f_{cu} is the peak cube compressive strength of concrete.

In a similar way, an effectiveness factor, ν_t, is used to reduce the tensile strength of concrete, f_t' to f_t (effective tensile strength). The effectiveness factor, ν_c, may vary from problem to problem as it is dependent on many factors such as concrete strength, steel reinforcement ratio and loading arrangement (Shave, 2005). The application of plasticity theory into concrete structures sometimes may not seem straightforward as concrete is not a perfectly-plastic material. However, the theory has been applied to both reinforced concrete structures and pre-stressed concrete structures over many years with excellent predictions. The use of suitable effectiveness factors seems to have made it possible to apply this theory to concrete structures, even in situations of limited ductility. For the current analysis, the Modified Mohr-Coulomb failure criterion with non-zero tension cut-off is assumed for the concrete. The energy dissipation formula for Modified Mohr-Coulomb materials for both plane stress and plane strain conditions is as follows (Nielsen, 1998) if the tensile strength of concrete is assumed to be zero.

The dissipation per unit length of the yield line,

$$W_l = \frac{1}{2} f_c \delta (1 - \sin\alpha) b \qquad (5.8)$$

where f_c = effective concrete compressive strength, δ = magnitude of the relative displacement vector, b = thickness of the body, α = angle between the direction of the relative displacement vector and the yield line (discontinuity) and $0 \le \alpha \le 2\pi$ for plane stress and $\Phi \le \alpha \le (\pi - \Phi)$ plane strain. Φ is the angle of friction of concrete and usually assumed to be 37º.

In plane stress conditions, relative displacement can occur in the full range of 0 to π from the direction of the yield line, i.e. $0 \le \alpha \le 2\pi$, because concrete aggregates are free to move in a lateral direction so that they can move around each other even if the angle $\alpha < \Phi$, enabling sliding in the full range. However, under plane strain conditions, the aggregates cannot move in the lateral direction so that the only way they can move over each other is when $\alpha \ge \Phi$. Consequently, in plane strain problems, $\Phi \le \alpha \le (\pi - \Phi)$.

5.3.3 An upper - bound plasticity model for CCSF

An upper-bound plasticity model is developed based on the specimen geometry and the observed concrete cover failure patterns (Figure 5.9). Three types of failure patterns, namely concrete cover separation over the entire bonded region, local failure near the loaded end and local failure near the free end, were observed, hence three models each involving rotation about Point C are initially considered. If Model 2 is considered, it can be assumed that the relative displacement component in the direction of the applied load is nearly zero, as the angle between the relative displacement and the FRP bar is approximately 90º. Therefore, internal energy dissipated by the CFRP bar can be ignored. Even if this quantity is not ignored, as the CFRP bar behaves elastically the energy dissipated is half the equivalent plastic energy, were the CFRP bars able to yield. Consequently, this quantity will still be a small amount and hence negligible. Therefore, if this assumption is made, there is no difference between Model 1 and Model 2. Similarly, if Model 3 is considered, it can be assumed that there is no concrete crushing along line CD as in this tensile zone, tensile cracks are forming and compressive stresses are closing these tensile cracks. Based on these assumptions, Models 1, 2 and 3 would yield the same results, and hence Model 1 is considered as the basic plasticity model.

However, it is questionable whether it is possible to use plasticity theory for a brittle failure like CCSF, which occurs in the cover region, as the concrete cover only contains plain concrete with no ductility contribution from the internal steel reinforcement or shear stirrups, which in turn affect the value of effectiveness factor, ν_c. For the current analysis ν_c is calculated from the formulations given in Ibell *et al* (1997) and the calculated values are as follows.

$$\nu_c = 0.24 \text{ (for C60)} \tag{5.9}$$

$$\nu_c = 0.30 \text{ (for C30)} \tag{5.10}$$

The model is a rotational model, which assumes the block to be rotated about point C (Figure 5.10).

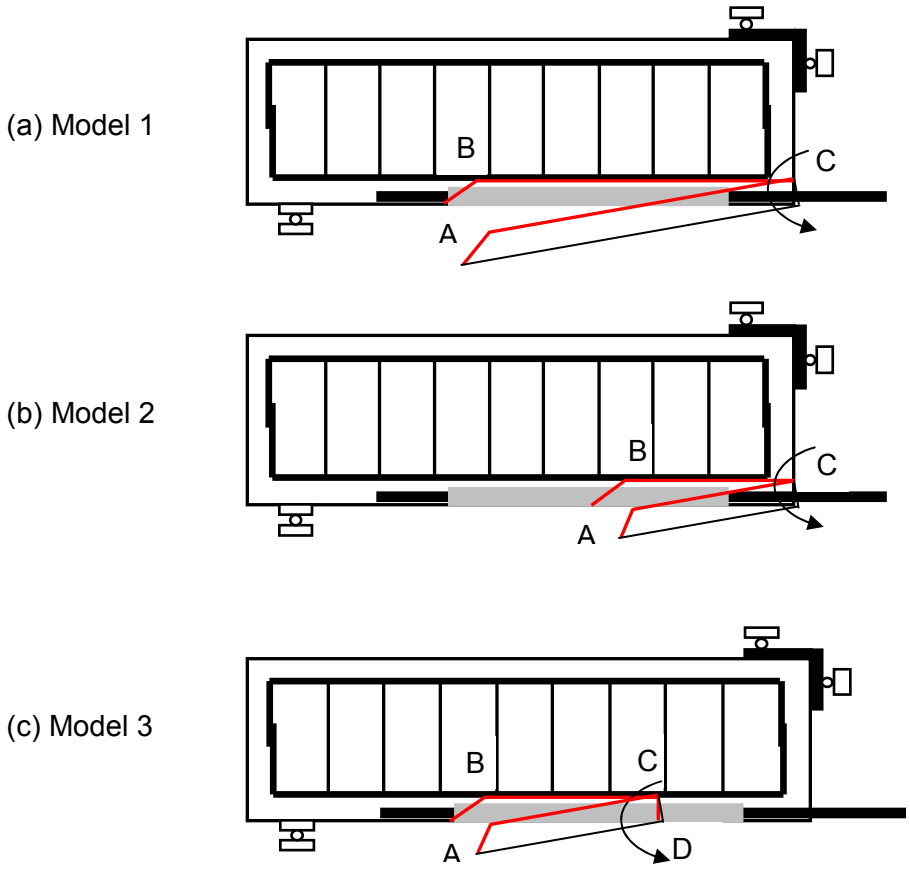

Figure 5.9 - CCSF failure patterns: (a) Model 1- CCSF over the entire bond length, (b) Model 2- local CCSF near the loaded end and (c) Model 3- local CCSF near the free end

No energy is dissipated along the yield line BC (as α = 90°). By applying Equation (5.8), the internal energy dissipation, ED, can be obtained as,

$$ED = \int_0^{h/\sin\theta} W_l \, dl = \int_0^{h/\sin\theta} \frac{1}{2} f_c r \beta (1 - \sin\alpha) b \, dl \tag{5.11}$$

Assuming the CFRP bar is located centrally within the groove, the external work, W_E is given by,

$$W_E = P\left(h - \frac{h_g}{2}\right)\beta \tag{5.12}$$

where P = applied load, h = concrete cover and h_g = groove depth.

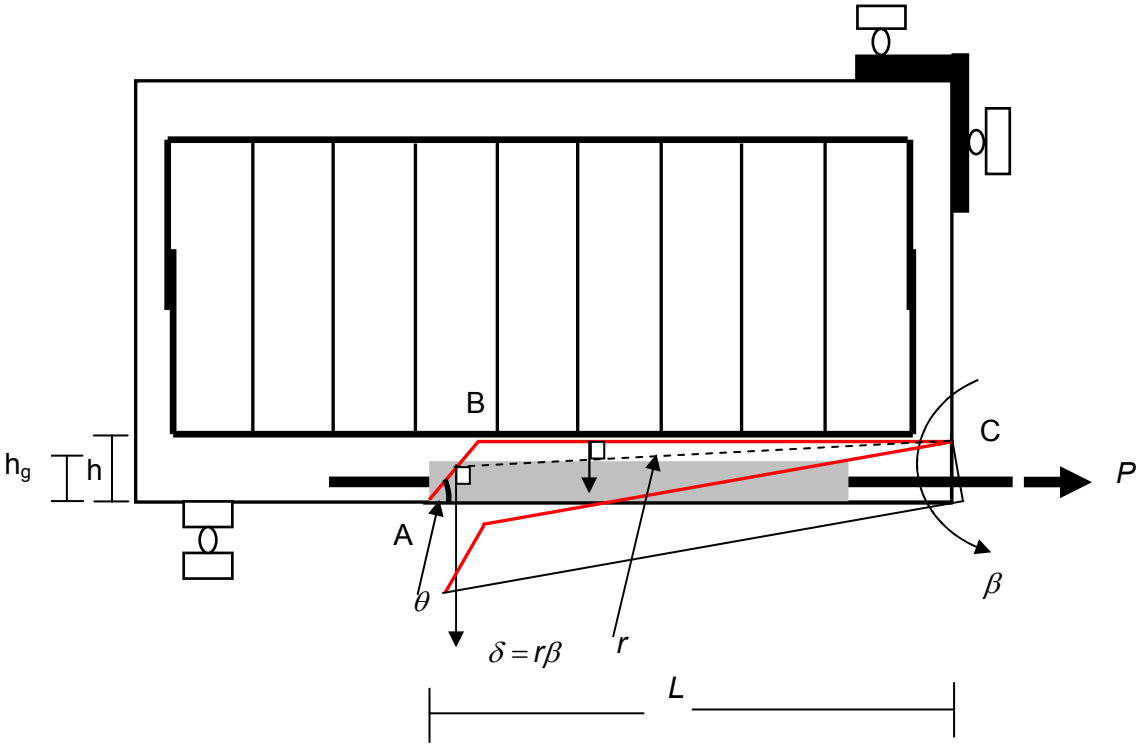

Figure 5.10 - Rotational plasticity model for CCSF

By equating these expressions, the following upper-bound solution is obtained,

$$P = \frac{f_c b}{4\left(h - \frac{h_g}{2}\right)}\left\{c_2^2 \sinh^{-1}\left[\frac{\left(\frac{h}{\sin\theta} + c_1\right)}{c_2}\right] - c_2^2 \sinh^{-1}\left(\frac{c_1}{c_2}\right) + \left(\frac{h}{\sin\theta} + c_1\right)\left[\left(\frac{h}{\sin\theta} + c_1\right)^2 + c_2^2\right]^{1/2} - c_1\left(c_1^2 + c_2^2\right)^{1/2} - \frac{h^2}{\sin^2\theta} - \frac{2c_1 h}{\sin\theta}\right\} \quad (5.13)$$

where $c_1 = (L\tan\theta - h)\cos\theta\cot\theta$, $c_2 = (L\tan\theta - h)\cos\theta$, θ = angle between the yield line AB and the horizontal direction and L = distance from the edge of the concrete specimen to the free end.

It is not possible to find an optimum value for load P, by minimising the solution with respect to angle θ, as the function P does not have a minimum value. The critical angle θ is found by varying the angle θ until the mean squared error reaches a minimum. i.e. $\frac{1}{n}\sum_{i=1}^{n}\left(P - P_{\exp}\right)^2$ is a minimum, where $P_{\exp}$ is the actual failure load and n is number of specimens failing in CCSF.

The critical angle is found to be 19º and the predicted failure load of each specimen is then found when θ = 19º. The experimentally observed angles of failure plane seem to

vary from 20º to 45º in all the three models 1, 2 and 3. The results from the upper-bound analysis are illustrated in Figure 5.11.

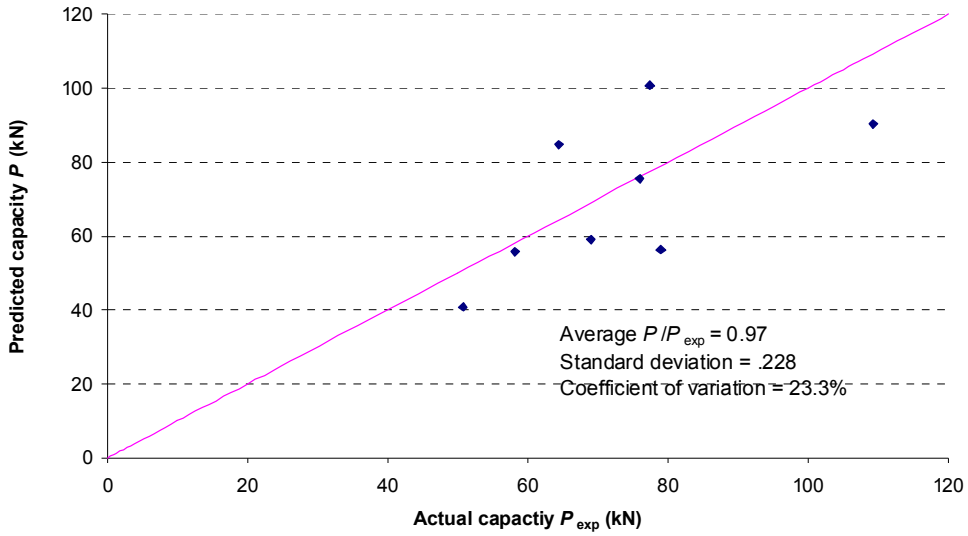

Even though the average is good, there is a large experimental scatter. It seems that the observed brittle behaviour at CCSF cannot be approximated by this plasticity model since the model assumes the ductile behaviour in concrete. Hence, plasticity theory approaches do not seem to be able to accurately predict the capacity at CCSF.

5.4 Local bond strength for splitting failures

The dominant failure mode for circular bars was splitting either in the resin cover or in the adjacent concrete, or in both. Therefore, what follows is the evaluation of an existing theoretical model of De Lorenzis (2002) for the prediction of resin cover splitting resistance. The model is then used to develop a new model to forecast the concrete splitting resistance in the elastic stage. Further, an upper-bound and a lower-bound for the local bond strength of NSM FRP bars failing in splitting failure modes, developed by De Lorenzis (2002), are employed here for comparison with the experimental results.

5.4.1 Theoretical model for resin splitting resistance

De Lorenzis (2004) modelled the bond of NSM bars in the transverse plane in the elastic stage by means of simplifying assumptions. Plane strain conditions have been assumed due to the large thickness of the system. Consequently, Young's modulus, E, and Poisson's ratio, ν, of the groove filling material are replaced by $E' = E/(1-\nu^2)$ and $\nu' = \nu/(1-\nu)$, respectively. By reflecting on the geometry of the tested specimens, grooves were assumed to have a square shape and the bar has been assumed to be located in the middle of the groove. The system of the groove surrounded by the concrete, which is subjected to inner pressure, is assumed to be the superposition of the groove filling material plus the surrounding concrete, with mutual stresses per unit thickness X_1 and X_2 (Figure 5.12).

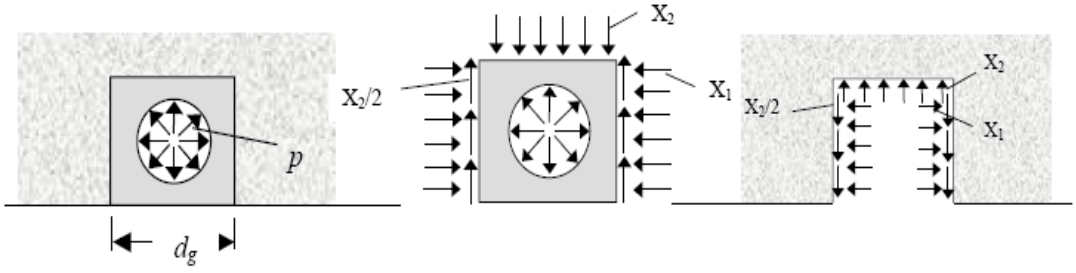

Figure 5.12 - Schematic representation of bond stresses in the system of groove filling material plus the surrounding concrete (De Lorenzis, 2004)

The displacements of the groove filling material are computed by superposition of the displacements induced by the stress systems shown in Figure 5.13. Below are the formulations of De Lorenzis's (2002) model for stresses ($\sigma_x, \sigma_y, \tau_{xy}$), strains ($\varepsilon_x, \varepsilon_y, \gamma_{xy}$), displacements ($u_x, u_y$) and the horizontal and vertical displacements along the sides of the block $\left[u_x\left(\frac{d_g}{2}, y\right), u_y\left(x, -\frac{d_g}{2}\right)\right]$ in each Scheme (a), (b) and (c), where d_g is groove depth/width, d_b is bar diameter, tension is positive and compression is negative. The sign of the displacements are relative to the positive directions of x and y - axes.

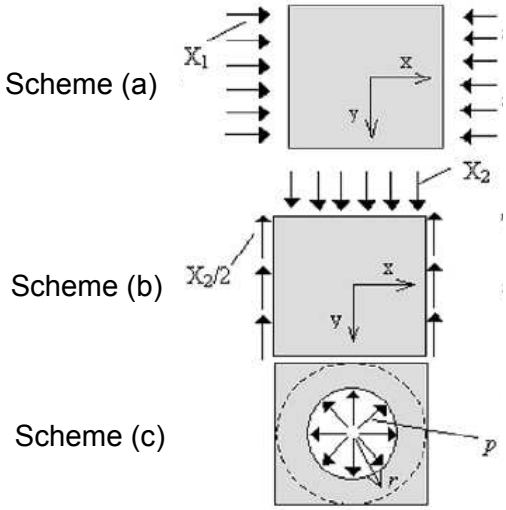

Figure 5.13 - Superposition of stress systems for calculating the displacements of the groove filling material (De Lorenzis, 2004)

- Scheme (a)

$$\sigma_x = -X_1 \tag{5.14}$$

$$\sigma_y = 0 \tag{5.15}$$

$$\tau_{xy} = 0 \tag{5.16}$$

$$\varepsilon_x = \frac{1}{E'}\left(\sigma_x - \nu'\sigma_y\right) = -\frac{X_1}{E'} \tag{5.17}$$

$$\varepsilon_y = \frac{1}{E'}\left(\sigma_y - \nu'\sigma_x\right) = \frac{\nu' X_1}{E'} \tag{5.18}$$

$$\gamma_{xy} = \frac{2(1+\nu')}{E'}\tau_{xy} = 0 \tag{5.19}$$

$$u_x = -\frac{X_1}{E'}x \tag{5.20}$$

$$u_y = \frac{\nu' X_1}{E'}y \tag{5.21}$$

$$u_x\left(\frac{d_g}{2},y\right)=-\frac{X_1}{E'}\frac{d_g}{2} \tag{5.22}$$

$$u_y\left(x,-\frac{d_g}{2}\right)=-\frac{\nu' X_1}{E'}\frac{d_g}{2} \tag{5.23}$$

- Scheme (b)

$$\sigma_x=6X_2\left(\frac{1}{4}-\frac{x^2}{{d_g}^2}\right)\frac{y}{d_g}+X_2\left(4\frac{y^3}{{d_g}^3}-\frac{3y}{5d_g}\right) \tag{5.24}$$

$$\sigma_y=\frac{X_2}{2}\left(-1+3\frac{y}{d_g}-4\frac{y^3}{{d_g}^3}\right) \tag{5.25}$$

$$\tau_{xy}=-6X_2\frac{x}{{d_g}^3}\left(\frac{{d_g}^2}{4}-y^2\right) \tag{5.26}$$

$$\varepsilon_x=\frac{1}{E'}\left[6X_2\left(\frac{1}{4}-\frac{x^2}{{d_g}^2}\right)\frac{y}{d_g}+X_2\left(4\frac{y^3}{{d_g}^3}-\frac{3y}{5d_g}\right)-\nu'\frac{X_2}{2}\left(-1+3\frac{y}{d_g}-4\frac{y^3}{{d_g}^3}\right)\right] \tag{5.27}$$

$$\varepsilon_y=\frac{1}{E'}\left[\frac{X_2}{2}\left(-1+3\frac{y}{d_g}-4\frac{y^3}{{d_g}^3}\right)-\nu' 6X_2\left(\frac{1}{4}-\frac{x^2}{{d_g}^2}\right)\frac{y}{d_g}-\nu' X_2\left(4\frac{y^3}{{d_g}^3}-\frac{3y}{5d_g}\right)\right] \tag{5.28}$$

$$\gamma_{xy}=-\frac{12(1+\nu')}{E'}X_2\frac{x}{{d_g}^3}\left(\frac{{d_g}^2}{4}-y^2\right) \tag{5.29}$$

$$u_x=\frac{X_2}{E'}\left[6y\left(\frac{x}{4d_g}-\frac{x^3}{3{d_g}^3}\right)+x\left(4\frac{y^3}{{d_g}^3}-\frac{3y}{5d_g}\right)-\nu'\frac{x}{2}\left(-1+3\frac{y}{d_g}-4\frac{y^3}{{d_g}^3}\right)-6(1+\nu')x\left(\frac{y}{4d_g}-\frac{y^3}{3{d_g}^3}\right)\right] \tag{5.30}$$

$$u_y=\frac{X_2}{E'}\left[-3(1+\nu')\frac{x^2}{d_g}\left(\frac{1}{4}-\frac{y^2}{{d_g}^2}\right)+\frac{d_g}{2}\left(-\frac{y}{d_g}+\frac{3y^2}{2{d_g}^2}-\frac{y^4}{{d_g}^4}\right)-3\nu'\frac{y^2}{d_g}\left(\frac{1}{4}-\frac{x^2}{{d_g}^2}\right)-\nu' d_g\left(\frac{y^4}{{d_g}^4}-\frac{3y^2}{10{d_g}^2}\right)\right] \tag{5.31}$$

$$u_x\left(\frac{d_g}{2},y\right)=\frac{X_2}{E'}\left[\frac{y}{2}+\frac{d_g}{2}\left(4\frac{y^3}{{d_g}^3}-\frac{3y}{5d_g}\right)-\nu'\frac{d_g}{4}\left(-1+3\frac{y}{d_g}-4\frac{y^3}{{d_g}^3}\right)-3(1+\nu')d_g\left(\frac{y}{4d_g}-\frac{y^3}{3{d_g}^3}\right)\right] \tag{5.32}$$

$$u_y\left(x,-\frac{d_g}{2}\right)=\frac{X_2}{E'}d_g\left[\frac{13}{32}+\frac{\nu'}{80}-\frac{3}{4}\nu'\left(\frac{1}{4}-\frac{x^2}{{d_g}^2}\right)\right] \tag{5.33}$$

- Scheme (c)

The radial and circumferential stresses in a thick wall cylinder subjected to an inner pressure, p, with an internal radius, r_i, and an external radius, r_e, are as follows (Timoshenko and Goodier, 1970),

$$\sigma_r(r)=\frac{p{r_i}^2}{{r_e}^2-{r_i}^2}\left(1-\frac{{r_e}^2}{r^2}\right) \tag{5.34}$$

$$\sigma_\theta(r)=\frac{p{r_i}^2}{{r_e}^2-{r_i}^2}\left(1+\frac{{r_e}^2}{r^2}\right) \tag{5.35}$$

$$u_r(r)=\frac{1}{E'}\frac{p{r_i}^2}{{r_e}^2-{r_i}^2}\left((1-\nu')r+(1+\nu')\frac{{r_e}^2}{r}\right) \tag{5.36}$$

where $r_i \le r \le r_e$.

By substituting $r_i=\frac{d_b}{2}$ and $r_e=\frac{d_g}{2}$ into Equations (5.34) to (5.36),

$$\sigma_r(r)=\frac{p{d_b}^2}{{d_g}^2-{d_b}^2}\left(1-\frac{{d_g}^2}{4r^2}\right) \tag{5.37}$$

$$\sigma_\theta(r)=\frac{p{d_b}^2}{{d_g}^2-{d_b}^2}\left(1+\frac{{d_g}^2}{4r^2}\right) \tag{5.38}$$

$$u_r(r)=\frac{1}{E'}\frac{p{d_b}^2}{{d_g}^2-{d_b}^2}\left((1-\nu')r+(1+\nu')\frac{{d_g}^2}{4r}\right) \tag{5.39}$$

where $\frac{d_b}{2} \le r \le \frac{d_g}{2}$.

$$u_x\left(\frac{d_g}{2}, y\right) = \frac{p}{E'} \frac{d_g {d_b}^2}{{d_g}^2 - {d_b}^2} \tag{5.40}$$

$$u_y\left(x, -\frac{d_g}{2}\right) = -\frac{p}{E'} \frac{d_g {d_b}^2}{{d_g}^2 - {d_b}^2} \tag{5.41}$$

The displacements in the concrete surrounding the groove are assumed to be small, as the same stresses act on thicker lateral sides of the concrete block and the modulus of elasticity of concrete is an order of magnitude higher than that of a typical resin. Hence, the concrete displacements are neglected when global compatibility is considered.

$$\frac{1}{d_g} \int_{-\frac{d_g}{2}}^{\frac{d_g}{2}} u_x\left(\frac{d_g}{2}, y\right) dy = 0 \tag{5.42}$$

$$\frac{1}{d_g} \int_{-\frac{d_g}{2}}^{\frac{d_g}{2}} u_y\left(x, -\frac{d_g}{2}\right) dx = 0 \tag{5.43}$$

The stress components, X_1 and X_2, are found by substituting the superposition of horizontal and vertical displacement components along the sides of the groove, obtained from each scheme, in Equations (5.42) and (5.43), as follows,

$$X_1 = k_1(\nu') \frac{p {d_b}^2}{{d_g}^2 - {d_b}^2} = k_1(\nu') \frac{p}{k^2 - 1} \tag{5.44}$$

$$X_2 = k_2(\nu') \frac{p {d_b}^2}{{d_g}^2 - {d_b}^2} = k_2(\nu') \frac{p}{k^2 - 1} \tag{5.45}$$

where $k_1(\nu') = \frac{\nu'(1+\nu')}{\frac{13}{16} - \frac{9}{40}\nu' - \frac{\nu'^2}{2}} + 2$, $k_2(\nu') = \frac{(1+\nu')}{\frac{13}{32} - \frac{9}{80}\nu' - \frac{\nu'^2}{4}}$ and $k = \frac{d_g}{d_b}$.

Then the stresses along the x and y - axes can thus be calculated, and particularly important are the stresses along the positive y - axis, .i.e. along the external resin cover, to predict resin cover splitting resistance.

σ_x, σ_y and τ_{xy} along the y - axis are,

$$\sigma_x(0,y)=\left[-k_1(\nu')+k_2(\nu')\left(4\frac{y^3}{{d_g}^3}+\frac{9y}{10d_g}\right)+1+\frac{{d_g}^2}{4y^2}\right]\frac{p}{k^2-1} \tag{5.46}$$

$$\sigma_y(0,y)=\left[\frac{1}{2}k_2(\nu')\left(-1+\frac{3y}{d_g}-4\frac{y^3}{{d_g}^3}\right)+1-\frac{{d_g}^2}{4y^2}\right]\frac{p}{k^2-1} \tag{5.47}$$

$$\tau_{xy}(0,y)=0 \tag{5.48}$$

where $-1\le 2y/d_g\le -1/k$ and $1/k\le 2y/d_g\le 1$.

σ_x, σ_y and τ_{xy} along the x - axis are,

$$\sigma_x(x,0)=\left[-k_1(\nu')+1-\frac{{d_g}^2}{4x^2}\right]\frac{p}{k^2-1} \tag{5.49}$$

$$\sigma_y(x,0)=\left[-\frac{1}{2}k_2(\nu')+1+\frac{{d_g}^2}{4x^2}\right]\frac{p}{k^2-1} \tag{5.50}$$

$$\tau_{xy}(x,0)=-\frac{3}{2}\frac{x}{d_g}k_2(\nu')\frac{p{d_b}^2}{{d_g}^2-{d_b}^2} \tag{5.51}$$

where $-1\le 2x/d_g\le -1/k$ and $1/k\le 2x/d_g\le 1$.

The principal stresses along the y -axis coincide with the stresses given in Equations (5.46) and (5.47) as $\tau_{xy}(0,y)=0$. Principal stresses along the x - axis can be calculated from Equations (5.49)-(5.51) and below are the maximum principal stresses along the x and y - axes.

$$\sigma_1(0,y)=\left[-k_1(\nu')+k_2(\nu')\left(4\frac{y^3}{{d_g}^3}+\frac{9y}{10d_g}\right)+1+\frac{{d_g}^2}{4y^2}\right]\frac{p}{k^2-1} \quad (5.52)$$

$$\sigma_1(x,0)=\left[1-\frac{1}{2}k_1(\nu')-\frac{1}{4}k_2(\nu')+\frac{1}{2}\sqrt{\left(-k_1(\nu')+\frac{1}{2}k_2(\nu')-\frac{{d_g}^2}{2x^2}\right)^2+9{k_2}^2(\nu')\frac{x^2}{{d_g}^2}}\right]\frac{p}{k^2-1} \quad (5.53)$$

De Lorenzis (2002) plotted Equations (5.52) and (5.53) for different values of k and ν, and Figure 5.14 illustrates the plot corresponding to the y - axis. The plot also shows results from a finite element analysis, although these results are not discussed here. From the plots, De Lorenzis (2002) concluded that lower k values and higher ν values result in higher principal tensile stresses. However, such a conclusion is not valid unless the radial pressure, p, is constant for all the considered k values and ν values or else the conclusion should be for principal tensile stress/radial pressure ratio. It is unlikely that p would remain constant as k and ν values change, because the change in these bond parameters will change the value of radial pressure. The plot corresponding to stresses along the y - axis also showed that for low values of k, the principal tensile stress is maximum at the external fibre of the cover and, for high values of k, the stress is maximum at the innermost fibre.

De Lorenzis (2002) calculated the radial pressures at external cover cracking and internal cover cracking (cover along the y - axis) at $y=d_b/2$ and $x=d_b/2$, respectively, from Equations (5.52) and (5.53) and by setting the equations equal to the tensile strength of the groove-filling material, individually (Figure 5.15). De Lorenzis (2002) concluded that for a given resin tensile strength, the cracking radial pressure, p_{cr} increases with k, but its rate of increase slows at higher k values, consistent with test results. Between the two pressures producing cracking of the external and internal cover, the lower value will be the more critical. The first to crack is generally the external cover, except for high values of k and when Poisson's ratio for the resin is 0.2. Hence, for a Poisson's ratio of the resin of 0.3 (corresponding to the epoxy used in De Lorenzis (2002)'s experiments) and a k ranging between 1 and 3 (as higher values would be impractical), the cracking pressure of the external cover will be critical.

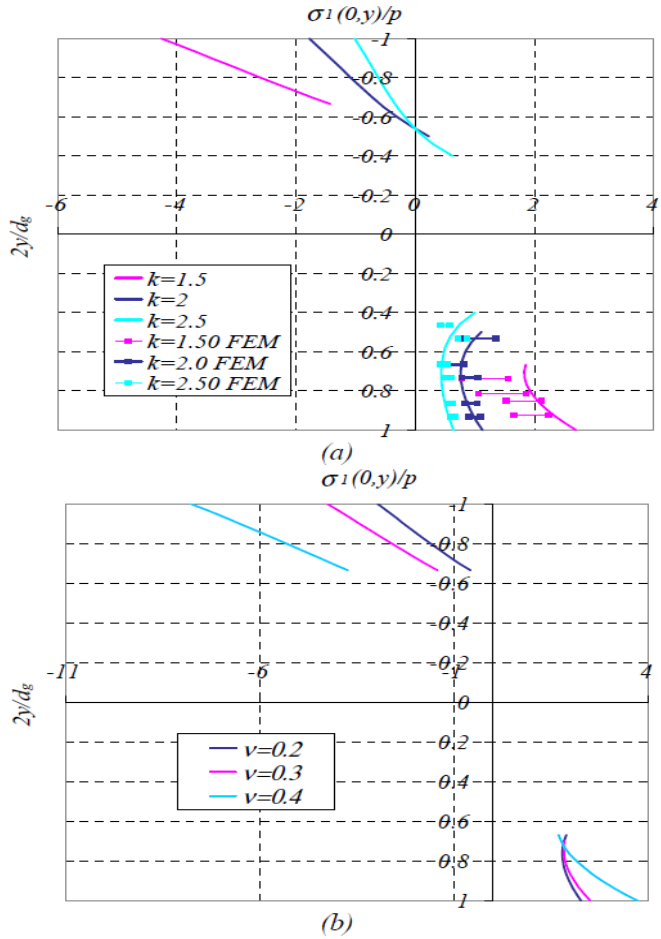

Figure 5.14 - Principal tensile stress distribution along the y -axis: (a) for different k values and (b) for different ν values (De Lorenzis, 2002)

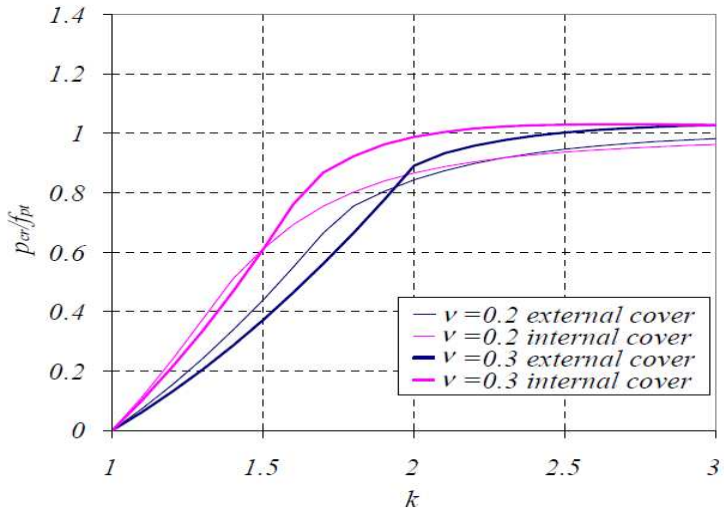

Figure 5.15 - Cover cracking pressure/tensile strength of the resin vs. k ratio for different ν values (De Lorenzis, 2002)

In all the following analytical work, similar to De Lorenzis's assumptions, the groove is assumed to be of square shape and the bar is assumed to be located in the middle of the groove. Further, the shape of the bar is assumed to be circular, for simplicity.

5.4.1.1 The model

In the current analysis, the above model predicting the radial pressure at which the external resin cover cracks is used. As explained in Chapter 2, the relationship of radial pressure, p = tangential bond stress (τ) x $tan\alpha$ (Tepfers, 1973), is used to convert the function of critical radial pressure (p_{cr}) vs. k into that of local bond strength (τ_m) vs. k. Generally, for steel-to-concrete bond, α = 45º is assumed, even though it depends on several factors, as explained in Chapter 2. As there is no information on an appropriate value of α for NSM FRP to concrete bond, α = 45º is also assumed in the current analytical work. The Poisson's ratio of the groove filling material is assumed to be equal to the two extreme values for the Poisson's ratio of epoxy resins (0.38 and 0.40) listed in Hull and Clyne (1996), as the actual value of the Poisson's ratio of the resin used is not available. The model is compared with the results of the bond tests (Figure 5.16). The tensile strength of the resin, f_{pt} is taken as 24.8MPa (from the manufacturer's specifications).

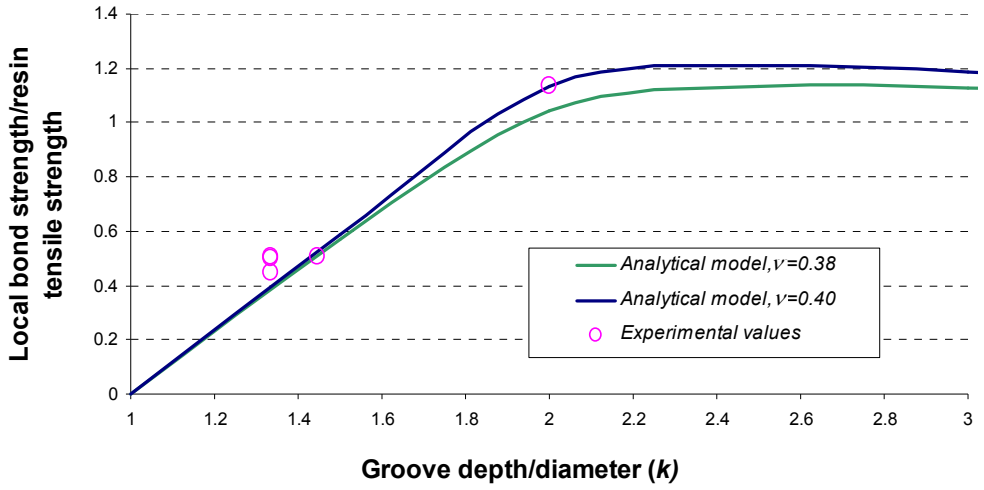

Figure 5.16 - Comparison of the analytical model and the experimental values for resin splitting strength

5.4.1.2 Results

The experimental points in Figure 5.16 represent the specimens failing in resin splitting. It can be seen that there is good correlation between the experimental results and the theoretical model when the assumed values of Poisson's ratio are considered within a specific range of k. However, more experimental points corresponding to k values over 2, and when k is close to 1, are needed to be more certain about the analytical model. Further, the model represents the fact that there should be an optimum k value beyond which there is no significant increase in bond strength, as the rate of increase in bond strength becomes lower at higher k values and τ_m / f_{pt} stabilises at $\tau_m / f_{pt} = 1$ as k approaches infinity. Also, it is likely that as k values become higher, failure may not occur by resin splitting and may involve the adjacent concrete, as observed in De Lorenzis (2002).

5.4.2 Theoretical models for concrete splitting resistance

An NSM FRP bonded joint involves two interfaces, namely the bar-resin interface and resin-concrete interface, and the tangential bond stress at each interface can be taken as τ and τ', respectively. τ is calculated based on the perimeter of the bar, p_1, whereas τ' is calculated based on the perimeter of the groove, p_2. τ and τ' vary along the corresponding interface. However, at a given location along the two interfaces, $\tau > \tau'$ for a given load because $p_2 > p_1$ and the ratio of τ / τ' at any location along the bond length should be p_2 / p_1 for any given load (this can be shown by considering equilibrium of an infinitesimal element of the resin cover of length dx and by assuming that resin cover carries only shear with no tension).

Transverse bond stresses develop in the resin-concrete interface due to the effect of radial pressure arising from the bar-resin interface. Also, another contribution to transverse pressure at the resin-concrete interface is based on the interface itself, as soon as micro-cracking starts in the concrete similarly to the mechanics at the bar-resin interface. Even though the surface of the resin block does not possess any surface

deformations, microscopic irregularities at the interface can be thought to develop mechanical interlocking once the adhesion between the two materials is lost. Therefore, once the principal tensile stress caused by tangential bond stress, τ', reaches the tensile strength of concrete, micro-cracking starts.

When analysing the bond at the resin-concrete interface in the transverse plane, three cases have to be considered depending on the occurrence of micro-cracking at each interface, as follows:

Case 1 - Only the transverse pressure arising from the bar-resin interface (after micro-cracking starts in the resin) is considered.

Case 2 - Only the transverse pressure arising from the resin-concrete interface (after micro-cracking occurs in the concrete) is considered.

Case 3 - Transverse pressure contributions from both the interfaces are considered.

In all the cases, splitting failure in the concrete is assumed to occur when the principal tensile stress reaches the splitting tensile strength of concrete. Micro-cracking in the concrete is likely to occur significantly before micro-cracking occurs in the resin, as the ratio of resin tensile strength/concrete tensile strength is considerably higher than practical p_2/p_1 ratios. Therefore, only Case 2 and Case 3 seem to be appropriate.

Initially, a model for concrete splitting resistance (Analytical model 1) was developed based on the stress distribution considered in De Lorenzis (2002) as below (Figure 5.17), because the stress scheme seemed to be good enough to yield a consistent model for resin splitting strength.

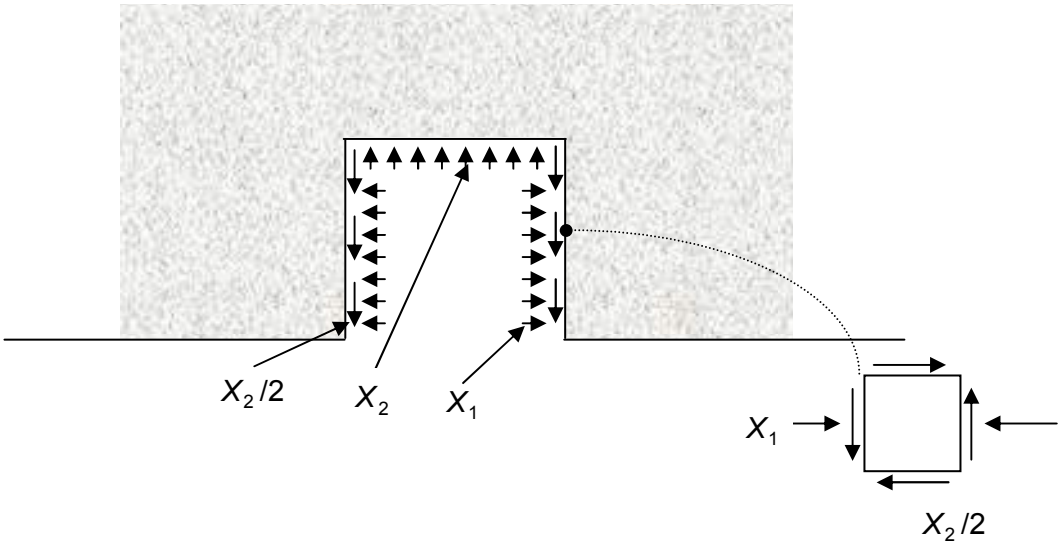

Figure 5.17 - Stress distribution acting on the concrete

It is assumed that concrete splitting failure occurs when the principal tensile stress equals the splitting tensile strength of concrete at the point of failure. By considering the stress condition of a point on the vertical side of the groove can be approximated as in Figure 5.17, the principal tensile stress at that point can be calculated. By setting the principal tensile stress equal to the splitting tensile strength of concrete, f_{tsplit}, the elastic solution for concrete splitting resistance can be obtained as follows.

$$\frac{\tau_m}{f_{tsplit}} = \frac{2(k^2 - 1)}{\left(- k_1(\nu') + \left[k_1(\nu')^2 + k_2(\nu')^2 \right]^{1/2} \right)} \tag{5.54}$$

where τ_m is the local bond strength at the bar-resin interface.

The angle of the failure plane to the horizontal direction is $\frac{tan^{-1}\left[k_2(\nu') / k_1(\nu') \right]}{2}$. By using the relationships of $\tau' = \tau \, p_1 / p_2$ and $p_1 / p_2 = \pi / 3k$ (for a square groove with the dimension d_g and a circular NSM FRP bar with the diameter d_b), the bond strength at the resin-concrete interface when concrete splitting failure occurs, can be obtained,

$$\frac{\tau'_m}{f_{tsplit}} = \frac{2(k^2 - 1)}{\left(- k_1(\nu') + \left[k_1(\nu')^2 + k_2(\nu')^2 \right]^{1/2} \right)} \frac{\pi}{3k} \tag{5.55}$$

Among the possible types of splitting failures, namely resin splitting with no or little damage in the concrete (mode I), concrete splitting accompanied by resin splitting, where resin splitting occurs before concrete splitting (mode II) and finally, concrete splitting with no visible cover cracking in the resin (mode III), the analytical models predicting concrete splitting resistance assumes the failure to be either of mode II or mode III. In the current tests, only modes I and II were observed, whereas in De Lorenzis (2002) all three modes were observed. Figure 5.18 depicts the analytical model 1 and the model corresponding to Case 2 (described in the next section) which are dimensionless with respect to the splitting tensile strength of concrete and the experimental local bond strength/splitting tensile strength ratio of specimens failing in concrete splitting accompanied by resin splitting, in terms of the bond strength at the bar-resin interface.

The splitting tensile strength of the specimens were calculated from $f_{tsplit} = 0.32 f_c'^{2/3}$ (Nielsen, 1998) where f_c' is cylinder compressive strength of concrete in MPa. It should be noted that in this kind of splitting failure, it seems appropriate that for the tensile strength of concrete, splitting tensile strength should be used rather than the direct tensile strength or the modulus of rupture of concrete as the concrete splits when subjected to compressive stresses rather than in a direct tension failure or a flexural failure.

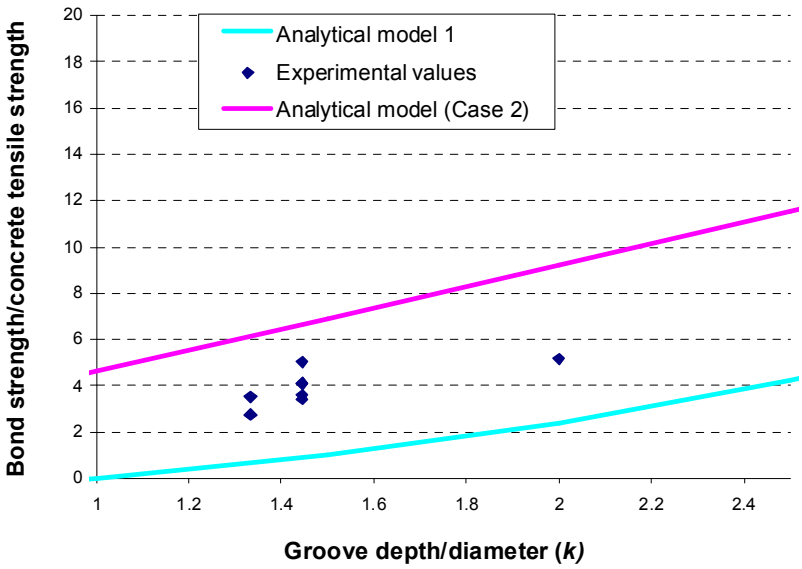

Figure 5.18 - Analytical model 1 for concrete splitting resistance and experimental values in terms of the bond strength at the bar-resin interface

However, the analytical model 1 suffers from some weaknesses. Firstly, it underestimates the experimental values considerably. Secondly, it predicts bond strength to be zero when k = 1. In reality, when k = 1, i.e. groove depth = bar diameter, the four corners of the resin cover, surrounded by the sides of the groove and the bar circumference, would be able to develop some sort of bond resistance so that bond strength cannot be zero. Finally, the model is highly dependent on the Poisson's ratio of the resin as X_1 and X_2 have been derived considering the deformations of the resin material only. Therefore, the following two new models were developed overcoming these weaknesses, for the above-mentioned Case 2 and Case 3.

5.4.2.1 Case 2

A new model is proposed based on the following approximated stress distribution along the sides of the concrete groove assuming that micro-cracking occurs in the concrete before that occurs in the resin (Figure 5.19). In other words, no transverse pressure arising from the bar-resin interface is applied to the concrete. Therefore, the analytical model corresponding to Case 2 is independent of the assumed radial stress distribution for the resin block subjected to inner pressure from the bar-resin interface. The same relationship between tangential bond stress and transverse bond stress is applied assuming α = 45º, i.e. $\tau' = p' tan\alpha$, where p' is the transverse pressure at the resin-concrete interface. As the interface conditions at the three sides of the groove are the same, the normal pressure on each side is assumed to be the same and uniformly distributed.

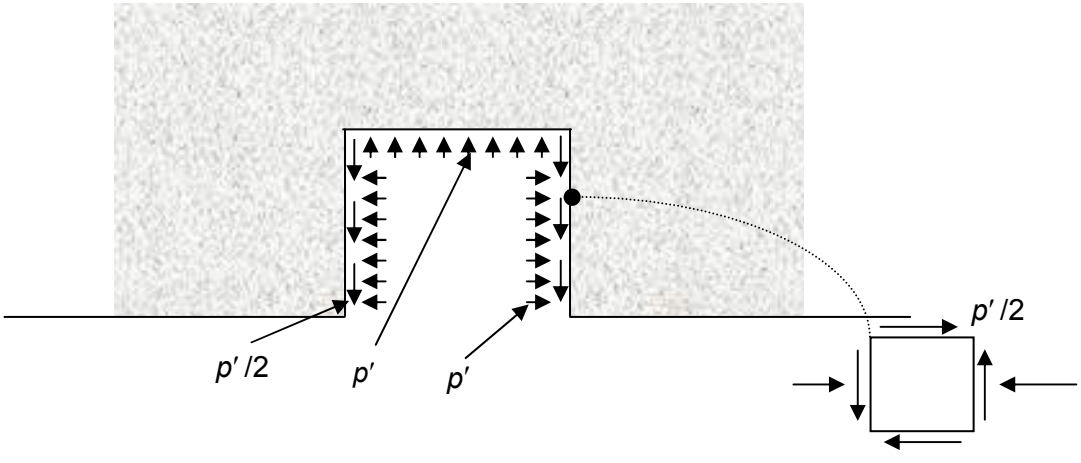

Figure 5.19 - Approximated stress distribution acting on the concrete in Case 2

The principal tensile stress at a point along a vertical side of the groove is calculated and, by setting it equal to the splitting tensile strength of concrete, the elastic solution for Case 2 can be obtained as before.

$$\frac{\tau'_{\mathrm{m}}}{f_{\mathrm{tsplit}}} = \frac{2}{\sqrt{2}-1} \tag{5.56}$$

where τ'_{m} is the local bond strength at the resin-concrete interface. The angle of the failure plane to the horizontal direction is 22.5º.

By using the relationships, $\tau' = \tau \, {p_1}/{p_2}$ and ${p_1}/{p_2} = {\pi}/{3k}$, bond strength at the bar-resin interface when concrete splitting failure occurs, can be obtained,

$$\frac{\tau_{\mathrm{m}}}{f_{\mathrm{tsplit}}} = \frac{1}{\pi}\frac{6k}{\sqrt{2}\text{-}1} \tag{5.57}$$

It is clear that the local bond strength at the resin-concrete interface (Equation (5.56)) is not dependent on k unlike the local bond strength of the bar-resin interface (Equation (5.57)), when concrete splitting failure occurs.

The model corresponding to Case 2 (Equation 5.57) seems to overestimate the actual capacity (Figure 5.18) indicating that there should be more transverse pressure on the concrete in order for splitting failure to occur. Therefore, Case 3 seems to be the most appropriate case with the contributions from both interfaces.

5.4.2.2 Case 3

The model defined by Equation (5.54) underestimates the actual capacity considerably (Figure 5.18) because the assumed theoretical stress distribution is higher than the actual stress distribution. This is also clear from the stress distribution of Scheme (c) (Figure 5.13) (De Lorenzis, 2002), in that the resistance offered by the resin material at the four corners of the groove surrounded by the groove and the outer circumference of the thick wall cylinder, is neglected so that the stresses on the remaining inner cylinder area are higher. Therefore, a new stress scheme is considered to calculate the transverse pressure resulting from the bar-resin interface in Case 3, which includes the

resistance from the four corners of the groove consisting of the resin. The new scheme assumes that the behaviour of the resin block subjected to inner pressure from the bar-resin interface is approximated by a thick wall cylinder with a diameter of $\sqrt{2}d_g$, as in Figure 5.20.

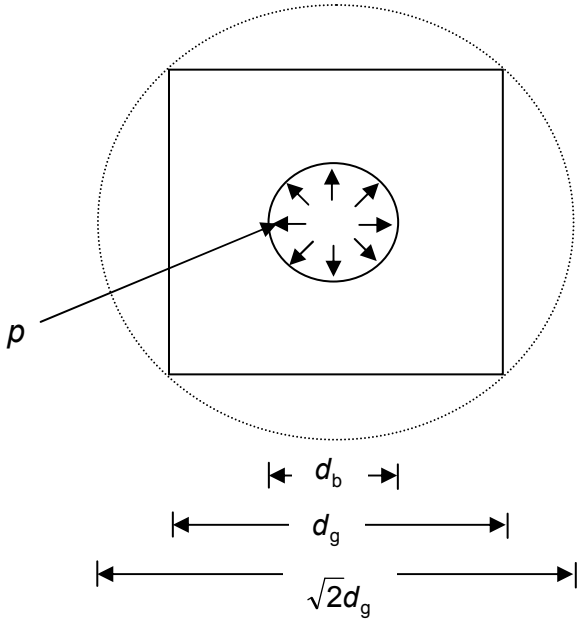

Figure 5.20 - Approximated radial stress distribution and the dimensions of the thick wall-cylinder

The radial and circumferential stresses in a thick wall cylinder subjected to an inner pressure, p, with an internal radius, $d_b/2$, and an external radius, $d_g/\sqrt{2}$, are as follows (Timoshenko and Goodier, 1970),

$$\sigma_r = \frac{p d_b^{\,2}}{2d_g^{\,2} - d_b^{\,2}}\left(1 - \frac{d_g^{\,2}}{2r^2}\right) \tag{5.58}$$

$$\sigma_\theta = \frac{p d_b^{\,2}}{2d_g^{\,2} - d_b^{\,2}}\left(1 + \frac{d_g^{\,2}}{2r^2}\right) \tag{5.59}$$

where tension is positive and compression is negative.

The radial compressive stress at $r = d_g/2$ is,

$$\sigma_{r_{d_g/2}} = \frac{p d_b^{\,2}}{2 d_g^{\,2} - d_b^{\,2}} (1-2) = -\frac{p}{2k^2 - 1} \tag{5.60}$$

The resultant vertical and horizontal bond stress components of the radial pressure at $r = d_g/2$ are assumed to act on the concrete along the three sides of the groove as in Figure 5.21.

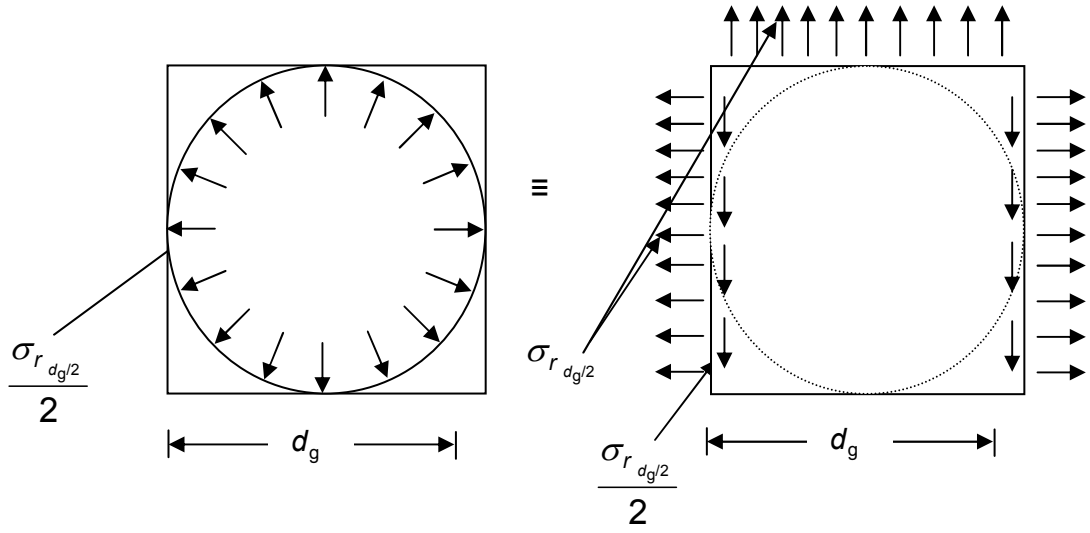

Figure 5.21 - Stress resultants on the concrete from the lateral pressure arising from the bar-resin interface

In addition, the lateral pressure from the resin-concrete interface is also applied on the concrete as in Figure 5.19. Therefore, when both contributions are considered, the stress distribution along the three sides of the groove is depicted in Figure 5.22.

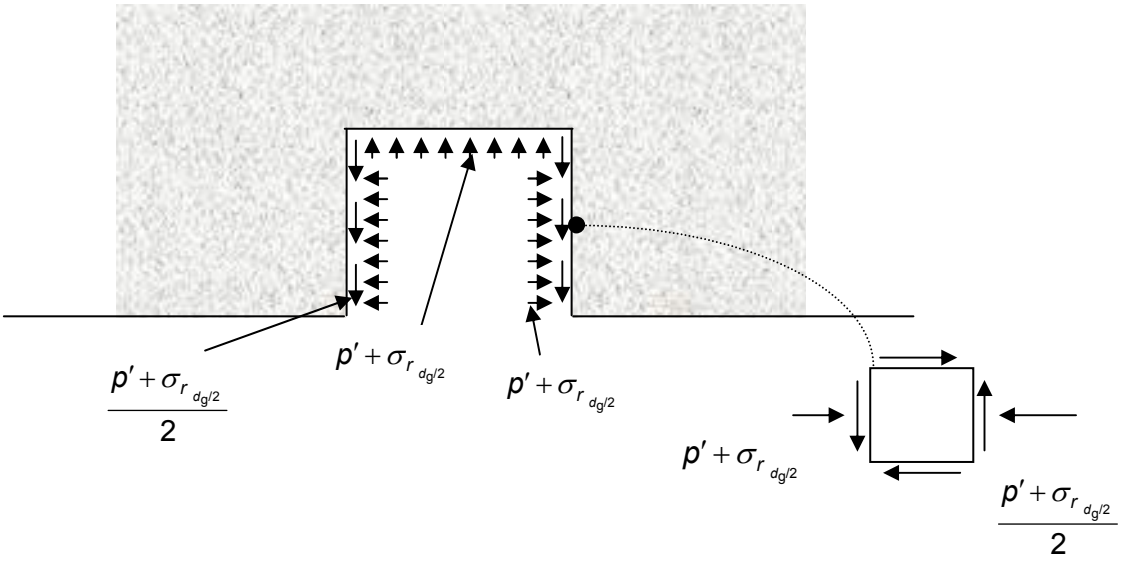

Figure 5.22 - Lateral pressure on the concrete from both interfaces

The principal tensile stress at a point along a vertical side of the groove is calculated and, by setting it equal to the splitting tensile strength of concrete, the elastic solution for Case 3 can be obtained as below.

$$\frac{\tau_m}{f_{tsplit}} = \left(\frac{6}{\sqrt{2}-1}\right)\frac{\left(2k^2-1\right)k}{\pi(2k^2-1)+3k} \tag{5.61}$$

By using the relationships, $\tau' = \tau\, {p_1}/{p_2}$ and ${p_1}/{p_2} = {\pi}/{3k}$, the bond strength at the resin-concrete interface when concrete splitting failure occurs, can be obtained,

$$\frac{\tau'_m}{f_{tsplit}} = \left(\frac{2\pi}{\sqrt{2}-1}\right)\frac{\left(2k^2-1\right)}{\pi(2k^2-1)+3k} \tag{5.62}$$

Figure 5.23(a) depicts the models corresponding to analytical model 1, Case 2 and Case 3 (Equations (5.54), (5.57) and (5.61), respectively) and the experimental values, in terms of the bond strength at the bar-resin interface. The model corresponding to Case 3 seems to match the experimental results reasonably, especially with low k values. Further, it possesses a bond strength even when k = 1 unlike the model I. Therefore, the assumed bond stress distribution for the concrete with the contributions from both the interfaces seems to be consistent. Figure 5.23(b) includes the models,

experimental values from the current study and experimental values of De Lorenzis (2002).

In general, the experimental values of De Lorenzis (2002) seem to increase with increasing k in a slope similar to that of the analytical model for Case 3. However, one set of data points in Series 2 of De Lorenzis (2002), corresponding to long bond lengths (24 times the bar diameter) do not quite follow the model unlike those corresponding to short bond lengths (4 times the bar diameter). In Series 2 of De Lorenzis (2002), the local bond stress-slip relationship has been approximated from the average bond stress-slip relationship, which is essentially the same for short bond lengths as there is no variation of bond stress and slip along the bond length for short bond lengths (Stratford, 2001). However, this assumption cannot be justified for use with long bond lengths as there is a significant variation in bond stress and slip along the bond length. The average bond strength reduces as the bond length increases due to non-linear bond stress distribution. Consequently, the local bond strength of specimens with long bond lengths is not accurately represented by taking the average bond strength. That is why the specimens containing long bond lengths of De Lorenzis (2002) (24 times the diameter) show considerably lower local bond strength values than those predicted by the model. When these experimental values are ignored, the model seems to be reasonably consistent with the rest of the experimental values of De Lorenzis (2002). The failure plane is 22.5º inclined to the horizontal direction and the experimentally observed angle of failure plane is about 30º (De Lorenzis, 2002).

The model corresponding to Case 2 seems to be a good upper-bound for the concrete splitting resistance. It would be interesting to perform an experiment when $k = 1$ where there is resin at the four corners of the groove only, not around the whole circumference of the bar, to see whether it matches the bond strength value predicted by the model.

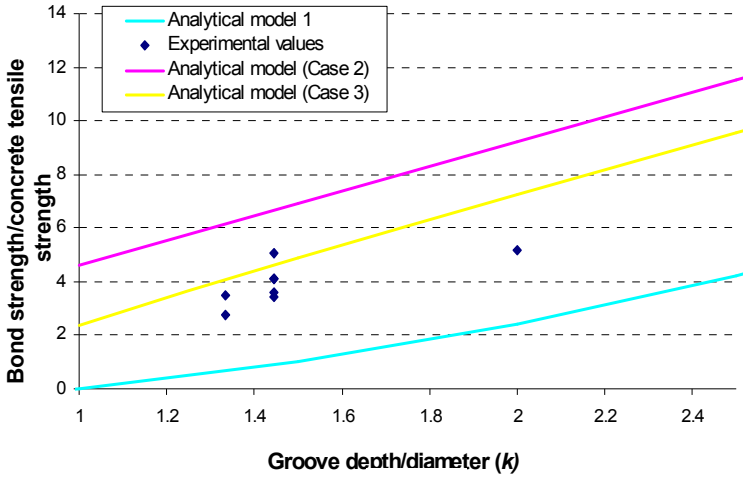

(a)

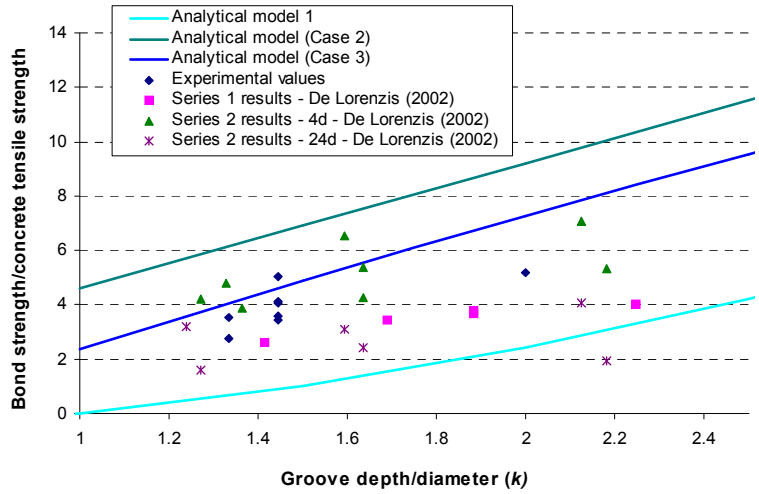

(b)

Figure 5.23 - Comparison of the analytical models (a) with the experimental values and (b) with the experimental results of De Lorenzis (2002) in terms of the local bond strength at the bar-resin interface

Figure 5.24 illustrates the analytical models (Equations (5.55), (5.56) and (5.62)) and the experimental results of the current study and of De Lorenzis (2002), in terms of the local bond strength at the resin-concrete interface. The experimental results do not show much dependence on k within the available range of k ratio. The proposed model (Case 3) initially increases alongside the increasing k with a gentle slope for small values of k and then the rate of increase seems to decrease and stabilise for higher values of k, being consistent with the experimental data. However, for high k values, some of the experimental points (Series 1 results of De Lorenzis (2002)) seem

to fall quite below the predicted values, whereas in the range of about $1.3 \le k \le 1.7$, the correlation between the model and the experimental results is fairly good. To verify the initial dependence on k, more experimental tests are needed in the range of k = 1 to about k = 1.3. As explained earlier, the model corresponding to Case 2 (Equation 5.56) does not depend on k because it only takes the lateral pressure arising from the resin-concrete interface into account. But the model representing Case 3 takes the lateral pressure contributions from both the interfaces so that it depends on k as the lateral pressure contribution from the bar-resin interface depends on k (Equation (5.62)). As already observed graphically from Figure 5.24, Equation (5.62) further explains the fact that as k Increases, the lateral pressure contribution from the bar-resin interface reduces so that the model (Case 3) approaches the model corresponding to Case 2. The model is physically reasonable because it depends noticeably on k only for low values of the k ratio. Model 1 has an ever increasing relationship with increasing k, which again confirms the limitations of the model.

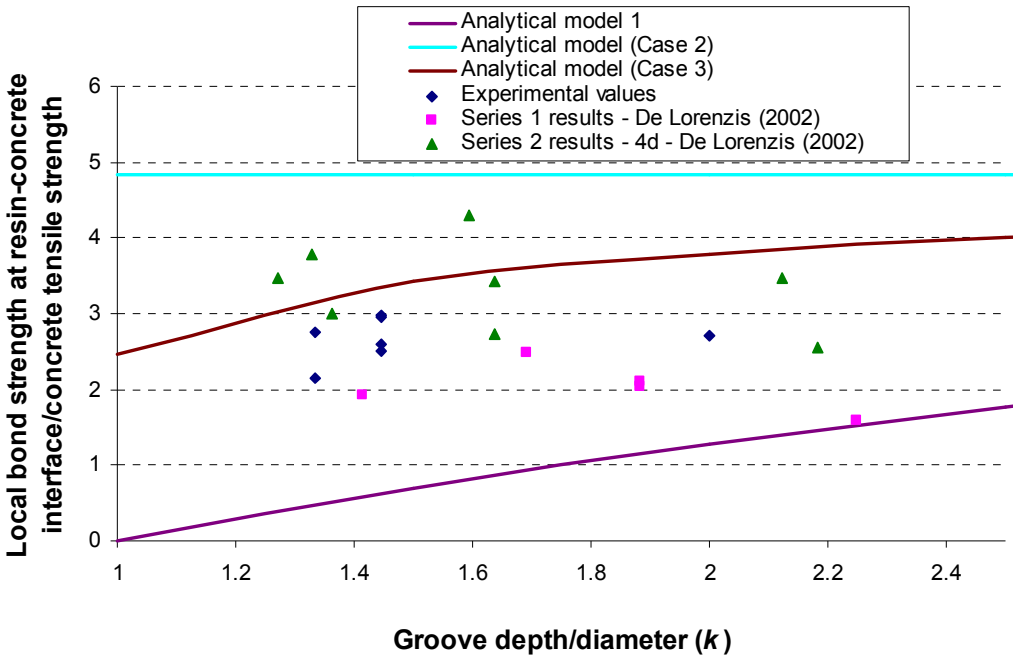

Figure 5.24 - Comparison of the analytical models with the experimental results, in terms of the local bond strength at the resin-concrete interface

5.4.3 Bounds for splitting strength

De Lorenzis (2002) calculated an upper-bound and a lower-bound to the local bond strength of specimens failing in splitting failures by analysing possible failure crack patterns of the NSM FRP system (Figure 5.25), in a similar approach to the analysis of ultimate failure crack patterns in steel-to-concrete bond conducted by Tepfers (1973). Such a study assumes uniform stress distribution along the crack surfaces, implying stress redistribution in the concrete in tension. Pattern (1-a) assumes the internal resin cover has already cracked and the failure is reached in the concrete along the crack lines whereas Pattern (2-a) assumes both the internal resin cover and external resin cover have already cracked when the failure occurs in the concrete. From the equilibrium analysis of each failure pattern, equations for local bond strength have been found where the angle α has been assumed to be 45º, and the angle of the failure plane, γ, has been assumed to be 30º (based on the experimental observations). However, Pattern (2-a) does not fully satisfy equilibrium. The models of De Lorenzis (2002) corresponding to Patterns (1-a) and (2-a) were compared with the experimental results of the current study and Figure 5.26 depicts the comparison for two different concrete splitting tensile strength/resin tensile strength ratios. The experimental points seem to lie well within the bounds for both concrete splitting tensile strength/resin tensile strength ratios so that the proposed bounds seem to be consistent with the experimental results.

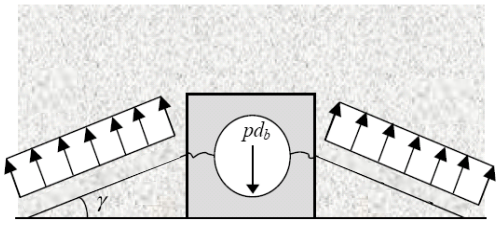

Pattern (1-a)

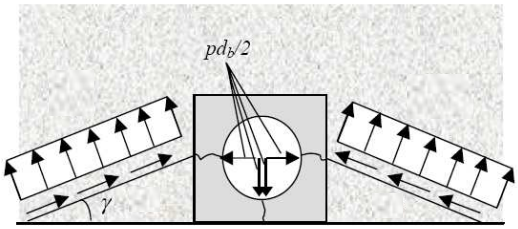

Pattern (2-a)

Figure 5.25 - Possible failure patterns of a NSM bonded joint (De Lorenzis, 2004)

(a)

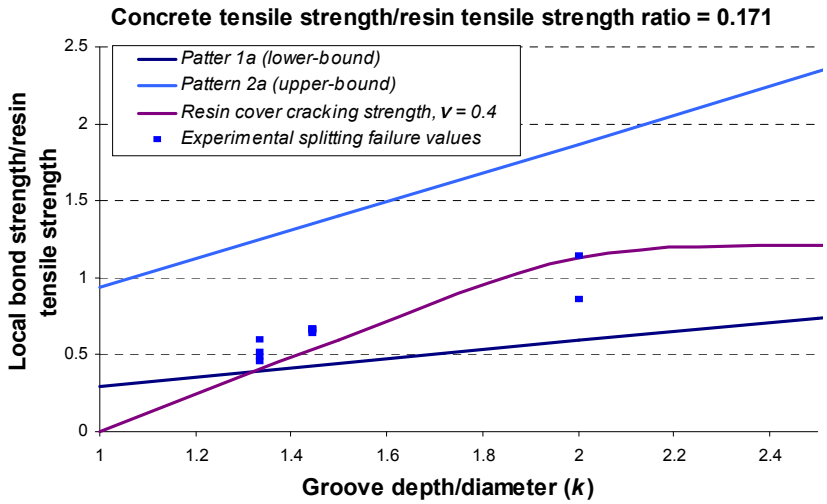

(b)

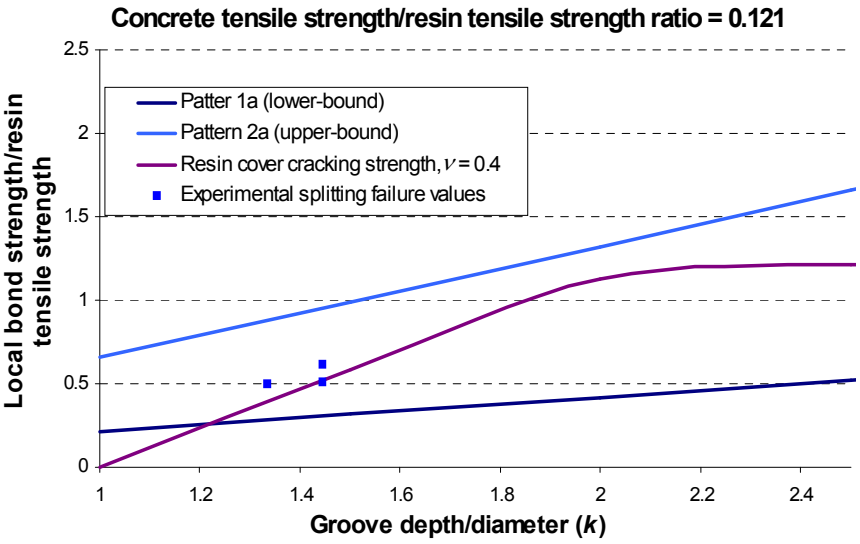

Figure 5.26 - Lower and upper-bounds for the local bond strength (De Lorenzis, 2002)

(a) $f_{tsplit}/f_{pt} = 0.171$ and (b) $f_{tsplit}/f_{pt} = 0.121$

5.5 Concluding remarks

Analysis of the bond behaviour of CFRP bars-to-resin and/or concrete is a complex problem involving many variables. Local bond stress-slip relationships of various bar shapes have been analysed along with the underlying mechanics. An upper-bound plasticity model has been developed to predict the CCSF, but it has not proved to be very accurate. An analytical model developed by De Lorenzis (2002) to predict resin

cover cracking bond strength seems to be consistent with the experimental results within the available groove depth/bar diameter ratios. Further, a consistent model has been developed to predict the concrete splitting resistance. The experimental local bond strength values failing in splitting failures seem to lie well within the upper and the lower-bounds developed by De Lorenzis (2002).

The next chapter presents an analytical method to predict the full range load-displacement behaviour of an NSM FRP-to-concrete bonded joint subjected to a direct pull-out force in a simple pull-push test, which involves solutions to the governing differential equation of bond.

CHAPTER 6 – FULL RANGE BEHAVIOUR OF NSM FRP BAR-TO-CONCRETE BONDED JOINTS

6.1 Introduction

This chapter presents an analytical solution to predict the full range behaviour of NSM FRP-to-concrete bonded joints which is based on a previous analytical method developed to predict full range behaviour of externally bonded FRP-to-concrete bonded joints (Yuan *et al.*, 2004). The solutions are developed based on a simple pull-push bond test containing a rectangular bar. However, the methodology and the solutions remain the same for any other bar shape.

6.2 Governing differential equation

Figure 6.1 shows a schematic diagram of a pull-push bond test containing a rectangular bar. The thickness and the width of the NSM FRP rectangular bar are denoted by t_f and h_f, respectively, the width and the depth of the concrete prism are b_c and h_c and those of the groove are b_g and h_g, respectively. The bond length of the joint is denoted by L, Young's modulus and the cross-sectional area of the FRP bar are E_f and A_f, respectively, and those of the concrete prism are E_c and A_c, respectively. The perimeter of the failure interface is denoted by L_{peri} while the applied load is denoted by P.

The following assumptions are made in the analytical approach,

- the FRP bar behaves linear elastically
- both adherends are subject to uniformly distributed axial stresses only, with any bending effects neglected
- concrete axial stresses are uniformly distributed over the concrete gross area ($b_c h_c$)

- the adhesive surrounding the FRP bar is subject to shear deformations only, i.e. the adhesive is subject to shear stresses only which are assumed to be constant across the thickness of the adhesive layer.

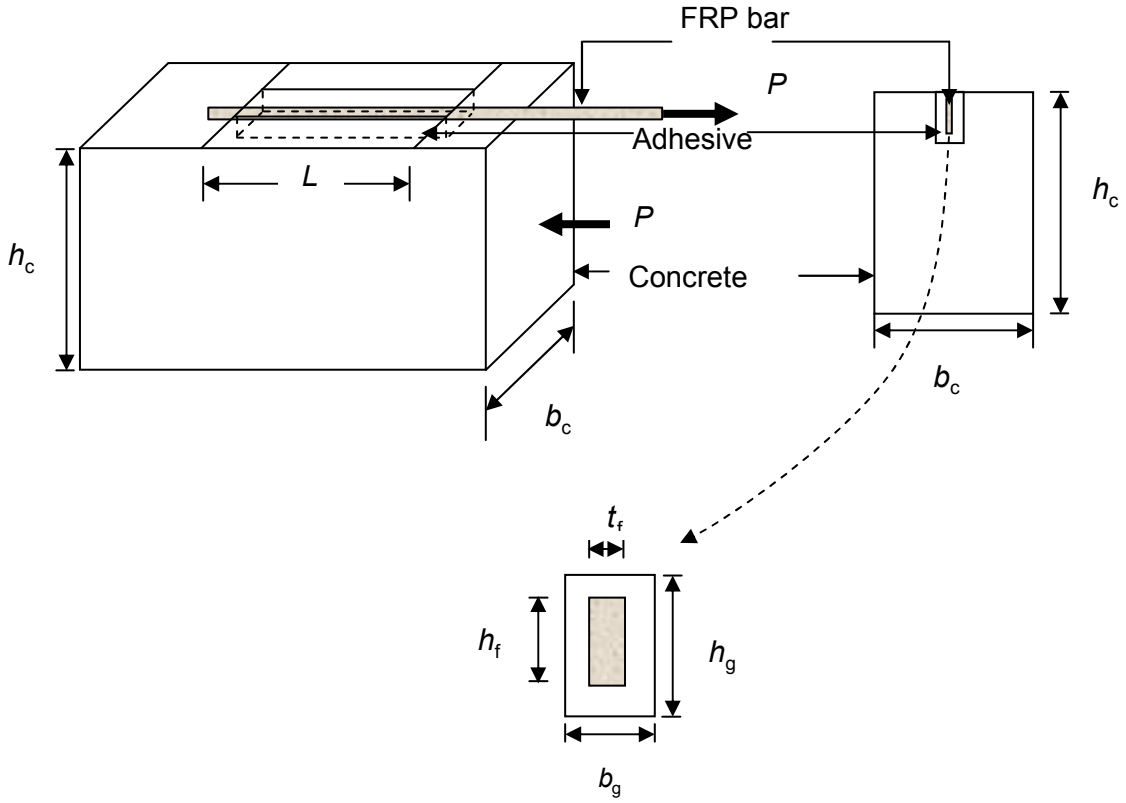

Figure 6.1 - Schematic diagram of a pull-out bond test

In accordance with the above assumptions, and considering equilibrium conditions of an infinitesimal element of length dx (Figure 6.2) and constitutive laws, the following equations can be derived, where τ is the tangential shear stress along the interface, u_f and σ_f are the displacement and the normal stress of the FRP bar, respectively, and u_c and σ_c are the displacement and normal stress of the concrete, respectively.

$$\tau = f(\delta) \tag{6.1a}$$

$$\sigma_f = E_f \frac{du_f}{dx} \tag{6.1b}$$

$$\sigma_c = E_c \frac{du_c}{dx} \tag{6.1c}$$

$$\frac{d\sigma_f}{dx}t_f h_f + \frac{d\sigma_c}{dx}b_c h_c = 0 \tag{6.1d}$$

$$\frac{d\sigma_f}{dx} = \frac{\tau L_{peri}}{t_f h_f} \tag{6.1e}$$

The interfacial slip, δ, is defined as the relative displacement between the two adherends, FRP bar and the concrete.

$$\delta = u_f - u_c \tag{6.2}$$

$$\frac{d\delta}{dx} = \frac{du_f}{dx} - \frac{du_c}{dx} = \frac{\sigma_f}{E_f} - \frac{\sigma_c}{E_c} \tag{6.3a}$$

$$\frac{d^2\delta}{dx^2} = \frac{1}{E_f}\frac{d\sigma_f}{dx} - \frac{1}{E_c}\frac{d\sigma_c}{dx} \tag{6.3b}$$

By substituting Equations (6.1d) and (6.1e) in to Equation (6.3b),

$$\frac{d^2\delta}{dx^2} = \tau L_{peri}\left[\frac{1}{(E_f A_f)} + \frac{1}{(E_c A_c)}\right] \tag{6.4}$$

Introducing the parameters of local bond strength, τ_f, and interfacial fracture energy, G_f, to Equation (6.4) gives,

$$\frac{d^2\delta}{dx^2} - \frac{2G_f\lambda^2 f(\delta)}{\tau_f^{\,2}} = 0 \tag{6.5}$$

where $\lambda^2 = \frac{\tau_f^{\,2} L_{peri}}{2G_f}\left[\frac{1}{(E_f A_f)} + \frac{1}{(E_c A_c)}\right] = \frac{\tau_f^{\,2} L_{peri}}{2G_f}\left[\frac{1}{(E_f t_f h_f)} + \frac{1}{(E_c b_c h_c)}\right]$ and $\sigma_f = \frac{L_{peri}\tau_f^{\,2}}{A_f 2G_f\lambda^2}\frac{d\delta}{dx}$.

The governing differential equation of the bonded joint, Equation (6.5), can be solved if the local bond stress-slip relationship, $f(\delta)$, is known.

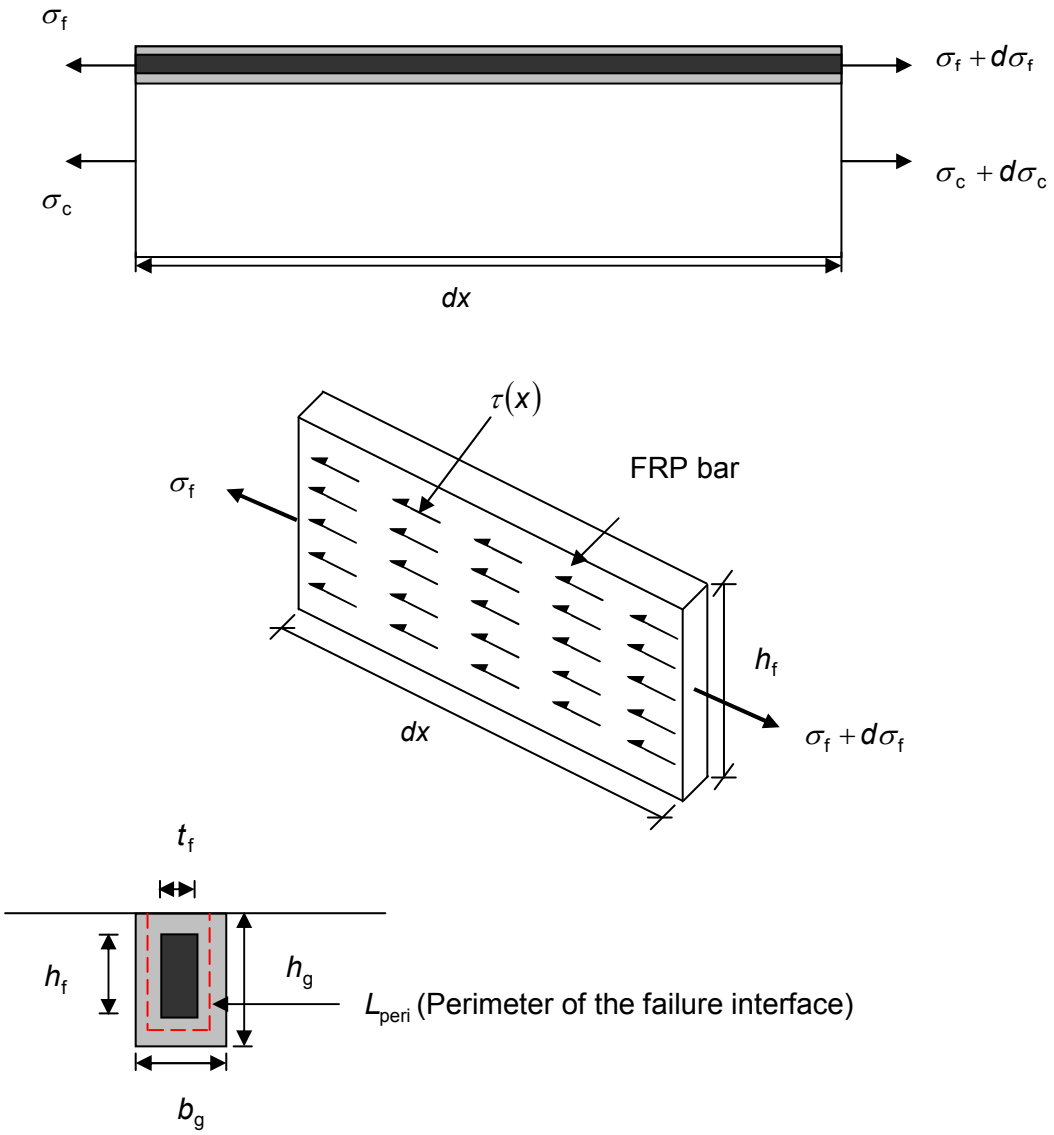

$L_{peri} = 2(h_f + t_f)$ = Perimeter of the FRP bar, if failure is at the bar-resin interface

$L_{peri} = (2h_g + b_g)$ = Perimeter of the groove, if failure is at the resin-concrete interface

Figure 6.2 - Equilibrium conditions of an infinitesimal element of length *dx*

6.3 Local bond stress - slip model

The following simple four-branched bond stress-slip model (Figure 6.3) was selected to model the bond between near surface mounted FRP bars and concrete. The applicability of more practical bond stress-slip models are discussed later. Various

bond stress-slip models have been used (Mohamed Ali *et al.*, 2008; Yuan *et al.*, 2004) to solve the differential equation even employing the non-linear MBEP model for the ascending branch (Cosenza *et al.*, 2002). Further, simple bi-linear and uni-linear models have been employed, especially to yield the solutions for the externally bonded FRP joints (Yuan *et al.*, 2004) as well as to solve the governing equation of bond in NSM FRP joints (Mohamed Ali *et al.*, 2008). Both the bi-linear and uni-linear models neglect the frictional resistance present along the failed interface. Further, both the models yield closed-form solutions to the differential equation. However, in strict terms the bi-linear model yields a closed-form solution for the debonding resistance (load capacity of the bonded joint) only for infinitely long bond lengths because the initial linear branch prevents a closed-form solution to the ultimate load capacity, in contrast to the uni-linear model.

A linear ascending branch was employed here because of simplicity and the fact that it provides a close approximation in the case of externally bonded FRP-to-concrete joints (Yuan *et al.*, 2004). Even the α value of the analytical equation (BEP model) of the modelled ascending branch was sometimes close to 1, indicating that the non-linear ascending branch approaches linearity, as observed in some of the bond tests in this research and in those of De Lorenzis (2002). Further, the linear descending branch and the frictional (residual) bond stress plateau also represent the actual bond behaviour of NSM FRP joints in many cases, depending on the bar type, as observed experimentally in this study and in De Lorenzis (2002). Finally, the last linearly descending branch was assumed to exist when the bonded joint fails completely so that there is a finite value for the interfacial fracture energy.

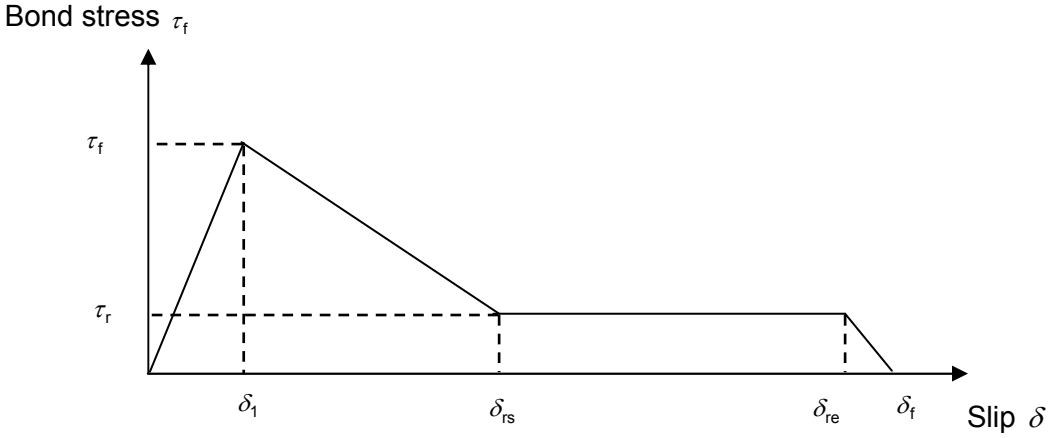

Figure 6.3 - Local bond stress-slip model

The bond stress-slip model is defined by the following equations,

$$f(\delta)=\begin{cases}\delta\tau_{\mathrm{f}}/\delta_1 \text{ for } 0\le\delta\le\delta_1\\ \tau_{\mathrm{r}}+(\tau_{\mathrm{f}}-\tau_{\mathrm{r}})(\delta_{\mathrm{rs}}-\delta)/(\delta_{\mathrm{rs}}-\delta_1) \text{ for } \delta_1\le\delta\le\delta_{\mathrm{rs}}\\ \tau_{\mathrm{r}} \text{ for } \delta_{\mathrm{rs}}\le\delta\le\delta_{\mathrm{re}}\\ \tau_{\mathrm{r}}(\delta_{\mathrm{f}}-\delta)/(\delta_{\mathrm{f}}-\delta_{\mathrm{re}}) \text{ for } \delta_{\mathrm{re}}\le\delta\le\delta_{\mathrm{f}}\\ 0 \text{ for } \delta>\delta_{\mathrm{f}}\end{cases} \tag{6.6}$$

The interfacial fracture energy is obtained from the area under the bond stress-slip curve as below.

$$G_{\mathrm{f}}=\frac{1}{2}\left[\tau_{\mathrm{f}}\delta_{\mathrm{rs}}+\tau_{\mathrm{r}}\left(\delta_{\mathrm{f}}+\delta_{\mathrm{re}}-\delta_{\mathrm{rs}}-\delta_1\right)\right] \tag{6.7}$$

6.4 Analysis of the debonding process

Because the bond stress-slip relationship consists of several branches, the debonding process also undergoes several stages corresponding to these branches. Therefore, Equation (6.5) has to be solved at each stage using relevant boundary conditions, and the solutions are presented below stage by stage. It should be noted that the following predictions for load-slip behaviour are only strictly correct for infinitely long bond lengths although the predictions are indistinguishable for bond lengths considerably longer than the effective bond length given later in Section 6.4.4. However, the general solutions of the differential equation during different stages of the debonding process are valid for any bond length.

6.4.1 Elastic stage

The bond stress distribution along the bond length at this stage is of the form shown in Figure 6.4.

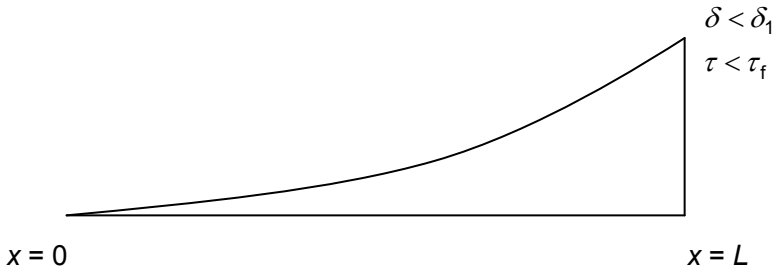

Figure 6.4 - Interfacial shear stress distribution during the elastic stage

Substituting the relevant relationship from Equation (6.6) into Equation (6.5), the following differential equation (Equation (6.8)) can be obtained and it can be solved by considering the boundary conditions (Equations (6.9) and (6.10)) to obtain the expressions for interfacial slip (Equation (6.11)), interfacial shear stress (Equation (6.12)) and axial stress in the FRP strip (Equation (6.13)) along the bonded length.

$$\frac{d^2\delta}{dx^2} - \lambda_1^2\delta = 0 \tag{6.8}$$

where $\lambda_1^2 = \frac{\lambda^2 2G_f}{\delta_1\tau_f} = \frac{\tau_f L_{peri}}{\delta_1}\left[\frac{1}{(E_f A_f)} + \frac{1}{(E_c A_c)}\right]$

$$\sigma_f = 0 \text{ at } x = 0 \tag{6.9}$$

$$\sigma_f = \frac{P}{A_p} \text{ at } x = L \tag{6.10}$$

$$\delta = \frac{P\delta_1\lambda_1 cosh(\lambda_1 x)}{L_{peri}\tau_f sinh(\lambda_1 L)} \tag{6.11}$$

$$\tau = \frac{P\lambda_1 cosh(\lambda_1 x)}{L_{peri} sinh(\lambda_1 L)} \tag{6.12}$$

$$\sigma_f = \frac{P sinh(\lambda_1 x)}{A_f sinh(\lambda_1 L)} \tag{6.13}$$

The slip at the loaded end (the value of δ at $x = L$) is defined as the displacement of the bonded joint and is denoted by Δ. Therefore, from Equation (6.11),

$$\Delta = \frac{P\delta_1\lambda_1 cosh(\lambda_1 L)}{L_{peri}\tau_f sinh(\lambda_1 L)} \tag{6.14}$$

In other words,

$$P = \frac{\Delta L_{peri}\tau_f tanh(\lambda_1 L)}{\delta_1 \lambda_1} \tag{6.15}$$

This represents the relationship between the slip and the applied load. By introducing two non-dimensional parameters, $\overline{P} = \frac{P}{\left[\frac{L_{peri}\tau_r}{\lambda_4 sin(\lambda_4 c_4)}\right]}$ and $\overline{\Delta} = \frac{\Delta}{\delta_f}$,

$$\overline{P} = \overline{\Delta}\frac{\delta_f \lambda_4 \tau_f}{\delta_1 \lambda_1 \tau_r} sin(\lambda_4 c_4) tanh(\lambda_1 L) \tag{6.16}$$

where $sin(\lambda_4 c_4) = \frac{\lambda_1}{\left\{\lambda_1^2 + \lambda_4^2\left[\frac{\tau_f^2}{\tau_r^2}\left(\frac{\lambda_1^2 + \lambda_2^2}{\lambda_2^2}\right) - \frac{\lambda_1^2}{\lambda_2^2} + 2\frac{\tau_f}{\tau_r}\left(\frac{\delta_{re} - \delta_{rs}}{\delta_1}\right)\right]\right\}^{1/2}}$, λ_2, λ_4 and c_4 are introduced later in Section 6.4.4.

The graph of the load vs. displacement at the loaded end (slip) is linear during the elastic stage and it is shown as segment OA in the typical full range load-displacement curve (Figure 6.5). The elastic stage ends and interfacial softening starts when the shear stress at the loaded end reaches the local bond strength at a slip values of δ_1, i.e., when $\tau = \tau_f$ and $\delta = \delta_1$ at $x = L$. Equation (6.15) gives the load at which the stage ends and interfacial softening begins, $P = P_1$,

$$P = P_1 = \frac{L_{peri}\tau_f}{\lambda_1} tanh(\lambda_1 L) \tag{6.17}$$

For an infinite bond length,

$$P_1 = \frac{L_{peri}\tau_f}{\lambda_1} \tag{6.18}$$

The length of the interface that is mobilised to resist the applied load is generally called the effective bond length. The effective bond length is defined here as the bond length over which the shear stresses offer a total resistance of at least 97% of the applied load for a joint with an infinite bond length (Yuan *et al.*, 2004). Based on this definition

and $tanh(2) \approx 0.97$, Equation (6.19) gives the effective bond length during the elastic stage and it is independent of the load level during this stage.

$$l_{eff} = \frac{2}{\lambda_1} \tag{6.19}$$

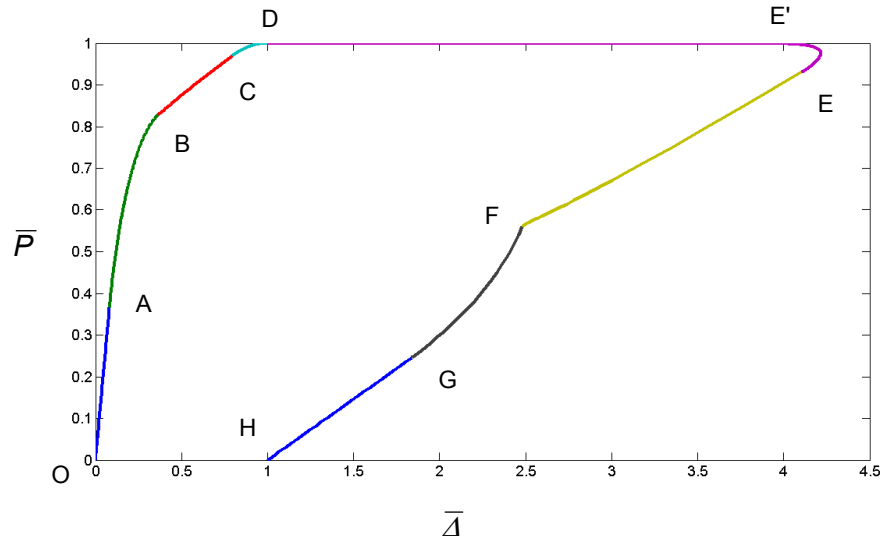

Figure 6.5 - Typical full range load-displacement curve for NSM FRP bar-to-concrete bonded joints

6.4.2 Elastic - softening stage

During this stage, a part of the bond length is in an elastic state while the other part ('*a*') is in a softening state (Figure 6.6). The expressions for interfacial slip, interfacial shear stress and axial stress in the FRP strip in each state, displacement (slip) at the loaded end and the applied load can be obtained solving the corresponding governing differential equation using the relevant boundary conditions, as in the previous stage.

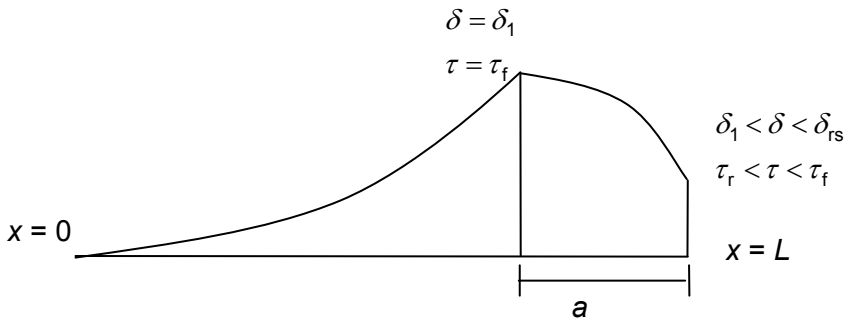

Figure 6.6 - Interfacial shear stress distribution during the elastic - softening stage

In the elastic region, $0 \le \delta \le \delta_1$, $0 \le x \le L - a$,

$$\frac{d^2\delta}{dx^2} - \lambda_1^2 \delta = 0 \tag{6.20a}$$

The solutions (Equations (6.20d) to (6.20f)) for the elastic state can be obtained from the following boundary conditions.

$$\sigma_f = 0 \text{ at } x = 0 \tag{6.20b}$$

$$\delta = \delta_1 \text{ at } x = L - a \tag{6.20c}$$

$$\delta = \frac{\delta_1 cosh(\lambda_1 x)}{cosh[\lambda_1 (L-a)]} \tag{6.20d}$$

$$\tau = \frac{\tau_f cosh(\lambda_1 x)}{cosh[\lambda_1 (L-a)]} \tag{6.20e}$$

$$\sigma_f = \frac{L_{peri}\tau_f sinh(\lambda_1 x)}{A_p \lambda_1 cosh[\lambda_1 (L-a)]} \tag{6.20f}$$

In the softening region, $\delta_1 \le \delta \le \delta_{rs}$, $L - a \le x \le L$,

$$\frac{d^2\delta}{dx^2} + \lambda_2^2 \delta = \lambda_3^2 \tag{6.21a}$$

where $\lambda_2^2 = \frac{\lambda^2 2G_f(\tau_f - \tau_r)}{\tau_f^2(\delta_{rs} - \delta_1)} = \frac{(\tau_f - \tau_r)L_{peri}}{(\delta_{rs} - \delta_1)}\left[\frac{1}{(E_f A_f)} + \frac{1}{(E_c A_c)}\right]$ and $\lambda_3^2 = \frac{\lambda^2 2G_f(\tau_f \delta_{rs} - \tau_r \delta_1)}{\tau_f^2(\delta_{rs} - \delta_1)}$.

The following boundary conditions are used to obtain the solutions (Equations (6.21d) to (6.21f)) in the softening state.

$$\sigma_f \text{ is continuous at } x = L - a \tag{6.21b}$$

$$\delta = \delta_1 \text{ at } x = L - a \tag{6.21c}$$

$$\delta = \frac{\tau_f(\delta_{rs} - \delta_f)}{(\tau_f - \tau_r)}\left\{\frac{\lambda_2}{\lambda_1} tanh[\lambda_1(L-a)] sin[\lambda_2(x - L + a)] - cos[\lambda_2(x - L + a)] + \frac{(\tau_f \delta_{rs} - \tau_r \delta_1)}{\tau_f(\delta_{rs} - \delta_f)}\right\} \tag{6.21d}$$

$$\tau = -\tau_f \left\{ \frac{\lambda_2}{\lambda_1} tanh[\lambda_1(L-a)] sin[\lambda_2(x-L+a)] - cos[\lambda_2(x-L+a)] \right\} \quad (6.21e)$$

$$\sigma_f = \frac{L_{peri}\tau_f}{A_p\lambda_2} \left\{ \frac{\lambda_2}{\lambda_1} tanh[\lambda_1(L-a)] cos[\lambda_2(x-L+a)] + sin[\lambda_2(x-L+a)] \right\} \quad (6.21f)$$

The relationship between the applied load and the loaded end slip is given by the following equations.

$$\text{Slip, } \Delta = \frac{\tau_f(\delta_{rs}-\delta_f)}{(\tau_f-\tau_r)} \left\{ \frac{\lambda_2}{\lambda_1} tanh[\lambda_1(L-a)] sin(\lambda_2 a) - cos(\lambda_2 a) + \frac{(\tau_f\delta_{rs}-\tau_r\delta_1)}{\tau_f(\delta_{rs}-\delta_f)} \right\} \quad (6.22)$$

$$\overline{\Delta} = \frac{\tau_f(\delta_{rs}-\delta_f)}{\delta_f(\tau_f-\tau_r)} \left\{ \frac{\lambda_2}{\lambda_1} tanh[\lambda_1(L-a)] sin(\lambda_2 a) - cos(\lambda_2 a) + \frac{(\tau_f\delta_{rs}-\tau_r\delta_1)}{\tau_f(\delta_{rs}-\delta_f)} \right\} \quad (6.23)$$

$$\text{Applied load, } P = \frac{\tau_f L_{peri}}{\lambda_2} \left\{ \frac{\lambda_2}{\lambda_1} tanh[\lambda_1(L-a)] cos(\lambda_2 a) + sin(\lambda_2 a) \right\} \quad (6.24)$$

$$\overline{P} = \frac{\tau_f\lambda_4}{\tau_r\lambda_2} \left\{ \frac{\lambda_2}{\lambda_1} tanh[\lambda_1(L-a)] cos(\lambda_2 a) + sin(\lambda_2 a) \right\} sin(\lambda_4 c_4) \quad (6.25)$$

Segment AB in Figure 6.5 relates the load and the displacement during this stage. At the initiation of the elastic-softening-frictional resistance stage (i.e., when $\tau = \tau_r$ at $x = L$) the value of '*a*' can be found from Equation (6.26a) through substitution of the above condition into Equation (6.21e).

$$\left\{ \frac{\lambda_2}{\lambda_1} tanh[\lambda_1(L-a)] sin(\lambda_2 a) - cos(\lambda_2 a) \right\} = -\frac{\tau_r}{\tau_f} \quad (6.26a)$$

For an infinite bond length, Equation (6.26a) converges to Equation (6.26b) yielding $a = a_2$.

$$\left\{ \frac{\lambda_2}{\lambda_1} sin(\lambda_2 a) - cos(\lambda_2 a) \right\} = -\frac{\tau_r}{\tau_f} \quad (6.26b)$$

$$a_2 = \frac{1}{\lambda_2} sin^{-1}\left[\frac{\tau_r}{\tau_f} \frac{\lambda_1}{\left(\lambda_1^2+\lambda_2^2\right)^{1/2}} + tan^{-1}\left(\frac{\lambda_1}{\lambda_2}\right) \right] \quad (6.27)$$

The corresponding load for an infinite bond length at the initiation of softening, P_2, is,

$$P_2 = \frac{L_{\text{peri}}}{\lambda_1 \lambda_2}\left[\tau_f^{\,2}\left(\lambda_1^{\,2} + \lambda_2^{\,2}\right) - \tau_r^{\,2}\lambda_1^{\,2}\right]^{1/2} \tag{6.28}$$

The effective bond length when the maximum load at the elastic-softening stage, P_2 is reached, defined in the same manner as before, can be obtained as below.

$$l_{\text{eff}} = a_2 + \frac{1}{2\lambda_1} ln\left[\frac{1.97\lambda_2 - 0.03\lambda_1 tan(\lambda_2 a_2)}{0.03\lambda_2 + 0.03\lambda_1 tan(\lambda_2 a_2)}\right] \tag{6.29}$$

6.4.3 Elastic - softening - frictional resistance stage

During this stage, part of the bond length, ('*L*-*a*-*b*'), is in an elastic state while another part, ('*a*'), is in a softening state and the other part, ('*b*'), is in a state of residual bond stress (frictional resistance) (Figure 6.7). The expressions for interfacial slip, interfacial shear stress and axial stress in the FRP bar in each state, the displacement (slip) at the loaded end and the applied load in the FRP strip can be obtained solving the corresponding governing differential equation.

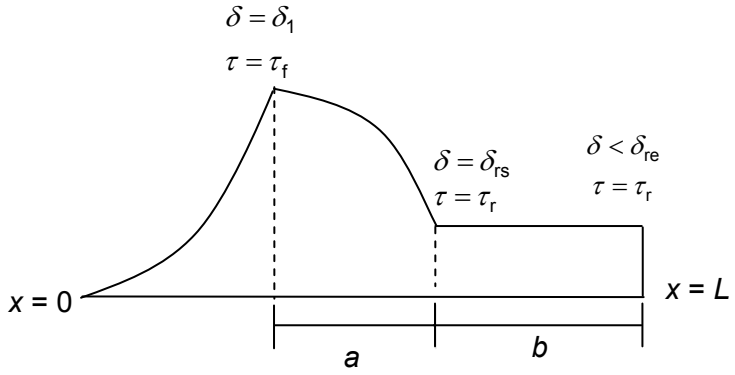

Figure 6.7 - Interfacial shear stress distribution during the elastic - softening - frictional resistance stage

In the elastic region, $0 \le \delta \le \delta_1$, $0 \le x \le (L - b) - a$,

$$\frac{d^2\delta}{dx^2} - \lambda_1^{\,2}\delta = 0 \tag{6.30}$$

Equations (6.20d) to (6.20f) will yield the solutions for this state of stress, when L is replaced by (L-b) as the boundary conditions are still the same.

In the softening region, $\delta_1 \le \delta \le \delta_{rs}$, $(L-b)-a \le x \le L-b$,

$$\frac{d^2\delta}{dx^2} + {\lambda_2}^2\delta = {\lambda_3}^2 \tag{6.31}$$

Equations (6.21d) to (6.21f) still yield the solutions for the softening state, when L is replaced by (L-b).

In the frictional resistance region, $\delta_{rs} \le \delta \le \delta_{re}$, $L-b \le x \le L$,

$$\frac{d^2\delta}{dx^2} - \frac{2G_f\lambda^2\tau_r}{{\tau_f}^2} = 0 \tag{6.32a}$$

The following boundary conditions are used to solve the differential equation and the solutions are given by Equations (6.32d) to (6.32f).

σ_f is continuous at $x = L-b$ (6.32b)

$\delta = \delta_{rs}$ at $x = L-b$ (6.32c)

$$\delta = \frac{{\lambda_1}^2\delta_1}{\tau_f}\left\{\frac{\tau_r}{2}[x-(L-b)]^2 - \frac{\tau_f}{\lambda_2}\left\{\frac{\lambda_2}{\lambda_1}tanh[\lambda_1(L-b-a)]cos(\lambda_2 a) + sin(\lambda_2 a)\right\}[x-(L-b)]\right\} + \delta_{rs} \tag{6.32d}$$

$$\tau = \tau_r \tag{6.32e}$$

$$\sigma_f = \frac{L_{peri}}{A_p}\left\{\tau_r x + \frac{\tau_f}{\lambda_2}\left\{\frac{\lambda_2}{\lambda_1}tanh[\lambda_1(L-b-a)]cos(\lambda_2 a) + sin(\lambda_2 a)\right\} - \tau_r(L-b)\right\} \tag{6.32f}$$

The load-displacement relationship is given by the following equations,

$$\Delta = \frac{{\lambda_1}^2\delta_1}{\tau_f}\left\{\frac{\tau_r b^2}{2} + \frac{\tau_f b}{\lambda_2}\left\{\frac{\lambda_2}{\lambda_1}tanh[\lambda_1(L-b-a)]cos(\lambda_2 a) + sin(\lambda_2 a)\right\}\right\} + \delta_{rs} \tag{6.33a}$$

$$\overline{\Delta} = \frac{{\lambda_1}^2\delta_1}{\tau_f\delta_f}\left\{\frac{\tau_r b^2}{2} + \frac{\tau_f b}{\lambda_2}\left\{\frac{\lambda_2}{\lambda_1}tanh[\lambda_1(L-b-a)]cos(\lambda_2 a) + sin(\lambda_2 a)\right\}\right\} + \frac{\delta_{rs}}{\delta_f} \tag{6.33b}$$

$$P = L_{\text{peri}}\left\{\tau_r b + \frac{\tau_f}{\lambda_2}\left\{\frac{\lambda_2}{\lambda_1}tanh\left[\lambda_1(L-b-a)\right]cos(\lambda_2 a) + sin(\lambda_2 a)\right\}\right\} \quad (6.33c)$$

The relationship between '*a*' and '*b*' is still given by Equation (6.26a) in which *L* should be replaced by (*L*-*b*),

$$b = L - a - \frac{1}{\lambda_1}tanh^{-1}\left\{\frac{\lambda_1}{\lambda_2}\left[-\frac{\tau_r}{\tau_f} + cos(\lambda_2 a)\right]\frac{1}{sin(\lambda_2 a)}\right\} \quad (6.34)$$

Equation (6.33c) can be simplified by applying Equation (6.34),

$$P = L_{\text{peri}}\left\{\tau_r b + \frac{\left[\tau_f - \tau_r cos(\lambda_2 a)\right]}{\lambda_2 sin(\lambda_2 a)}\right\} \quad (6.35a)$$

$$\overline{P} = \frac{\lambda_4 sin(\lambda_4 c_4)}{\tau_r}\left\{\tau_r b + \frac{\left[\tau_f - \tau_r cos(\lambda_2 a)\right]}{\lambda_2 sin(\lambda_2 a)}\right\} \quad (6.35b)$$

Segment BC is the corresponding branch of the load-displacement curve (Figure 6.5) for this stage. At the end of this stage, i.e., when $\delta = \delta_{\text{re}}$ at $x = L$, Equation (6.32d) yields another relationship between '*a*' and '*b*' so that the two unknowns can be found from Equations (6.34) and (6.36), at the end of the stage.

$$\delta_{\text{re}} - \delta_{\text{rs}} = \frac{\lambda_1^2 \delta_1}{\tau_f}\left\{\frac{\tau_r b^2}{2} + \frac{\tau_f b}{\lambda_2}\left\{\frac{\lambda_2}{\lambda_1}tanh\left[\lambda_1(L-b-a)\right]cos(\lambda_2 a) + sin(\lambda_2 a)\right\}\right\} \quad (6.36)$$

For an infinite bond length Equations (6.34) and (6.36) converge to Equations (6.37) and (6.38) whose solutions yield values of $a = a_3$ and $b = b_3$. During this stage, the value of '*a*' does not change from the previous value of $a = a_2$ since Equations (6.26b) and (6.37) are the same for an infinite bond length, while '*b*' increases form zero to $b = b_3$. In other words, for infinite bond lengths '*a*' remains constant during this stage (i.e., $a = a_2 = a_3$) as '*b*' increases. The corresponding load for an infinite bond length, $P = P_3$ is given by Equation (6.39b).

$$\left\{\frac{\lambda_2}{\lambda_1}sin(\lambda_2 a_3) - cos(\lambda_2 a_3)\right\} = -\frac{\tau_r}{\tau_f} \quad (6.37)$$

$$\delta_{re} - \delta_{rs} = \frac{\lambda_1^2 \delta_1}{\tau_f}\left\{\frac{\tau_r b_3^2}{2} + \frac{\tau_f b_3}{\lambda_2}\left[\frac{\lambda_2}{\lambda_1} cos(\lambda_2 a_3) + sin(\lambda_2 a_3)\right]\right\} \quad (6.38)$$

$$b_3 = \left[\frac{\tau_f^2}{\tau_r}\left(\frac{\lambda_1^2 + \lambda_2^2}{\lambda_1 \lambda_2}\right) - \tau_f^2 \lambda_1^2\right]^{1/2} + \frac{1}{\lambda_1}\left[\frac{\tau_f^2}{\tau_r^2}\left(\frac{\lambda_1^2 + \lambda_2^2}{\lambda_2^2}\right) - \frac{\lambda_1^2}{\lambda_2^2} + 2\frac{\tau_f}{\tau_r}\left(\frac{\delta_{re} - \delta_{rs}}{\delta_1}\right)\right]^{1/2} \quad (6.39a)$$

$$P_3 = \frac{L_{peri}\tau_r}{\lambda_1}\left[\frac{\tau_f^2}{\tau_r^2}\left(\frac{\lambda_1^2 + \lambda_2^2}{\lambda_2^2}\right) - \frac{\lambda_1^2}{\lambda_2^2} + 2\frac{\tau_f}{\tau_r}\left(\frac{\delta_{re} - \delta_{rs}}{\delta_1}\right)\right]^{1/2} \quad (6.39b)$$

The effective bond length when the maximum load at this stage, P_3, is reached, defined as before, is given below.

$$l_{eff} = a_3 + b_3 + \frac{1}{\lambda_1} tanh^{-1}\left[0.97 - \frac{0.03\lambda_1 tan(\lambda_2 a_3)}{\lambda_2} - \frac{0.03\lambda_1 \tau_r b_3}{\tau_f cos(\lambda_2 a_3)}\right] \quad (6.39c)$$

6.4.4 Elastic - softening - frictional resistance - frictional softening stage

There are four regions where there are four different states along the bond length, elastic state, softening state ('*a*'), residual bond stress state ('*b*') and frictional softening state ('*c*'). The expressions for interfacial slip, interfacial shear stress and axial stress in the FRP strip in each state, displacement (slip) at the loaded end and the applied load can be obtained by solving the corresponding governing differential equation. The bond stress distribution during this stage is of the form shown in Figure 6.8.

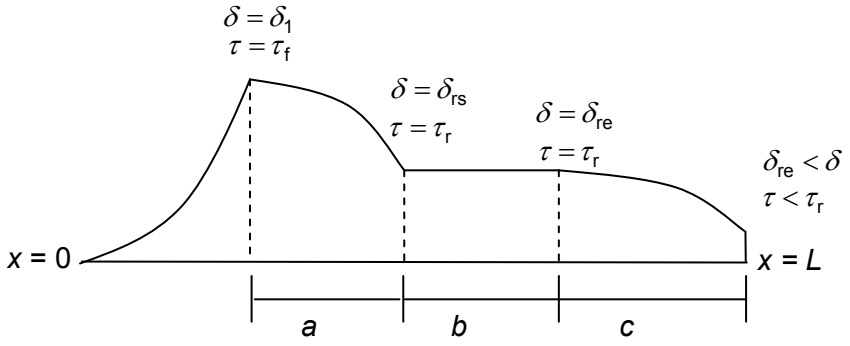

Figure 6.8 - Interfacial shear stress distribution during the elastic - softening - frictional resistance - frictional softening stage

In the elastic region, $0 \le \delta \le \delta_1$, $0 \le x \le (L - c - b) - a$,

$$\frac{d^2\delta}{dx^2} - \lambda_1^2 \delta = 0 \tag{6.40}$$

Equations (6.20d) to (6.20f) yield the solutions for this state of stress when *L* is replaced by (*L*-*c*-*b*), as the boundary conditions are still the same.

In the softening region, $\delta_1 \le \delta \le \delta_{rs}$, $(L - c - b) - a \le x \le L - c - b$,

$$\frac{d^2\delta}{dx^2} + \lambda_2^2 \delta = \lambda_3^2 \tag{6.41}$$

Equations (6.21d) to (6.21f) yield the solutions for the softening state when *L* is replaced by (*L*-*c*-*b*).

In the frictional resistance region, $\delta_{rs} \le \delta \le \delta_{re}$, $(L - c) - b \le x \le L - c$,

$$\frac{d^2\delta}{dx^2} - \frac{2G_f \lambda^2 \tau_r}{\tau_f^2} = 0 \tag{6.42}$$

Equations (6.32d) to (6.32f) still yield the solutions for the frictional resistance state, when *L* is replaced by (*L*-*c*).

In the frictional softening region, $\delta_{re} \le \delta \le \delta_f$, $L - c \le x \le L$,

$$\frac{d^2\delta}{dx^2} + \lambda_4^2 \delta = \lambda_4^2 \delta_f \tag{6.43a}$$

where $\lambda_4^2 = \dfrac{\lambda^2 2G_f \tau_r}{\tau_f^2 (\delta_f - \delta_{re})} = \dfrac{\tau_r L_{peri}}{(\delta_f - \delta_{re})} \left[\dfrac{1}{(E_f A_f)} + \dfrac{1}{(E_c A_c)} \right]$

Equations (6.43d) to (6.43f) are the solutions of the differential equation using the following boundary conditions.

σ_f is continuous at $x = L - c$ (6.43b)

$\delta = \delta_{re}$ at $x = L - c$ (6.43c)

$$\delta = (\delta_f - \delta_{re})\left\{\left[\tau_r b + \frac{\tau_f}{\lambda_2}\left\{\frac{\lambda_2}{\lambda_1}tanh[\lambda_1(L-c-b-a)]cos(\lambda_2 a)+sin(\lambda_2 a)\right\}\right]\frac{\lambda_4}{\tau_r}sin[\lambda_4(x-L+c)]-cos[\lambda_4(x-L+c)]+\frac{\delta_f}{(\delta_f-\delta_{re})}\right\} \quad (6.43d)$$

$$\tau = -\tau_r\left\{\left[\tau_r b + \frac{\tau_f}{\lambda_2}\left\{\frac{\lambda_2}{\lambda_1}tanh[\lambda_1(L-c-b-a)]cos(\lambda_2 a)+sin(\lambda_2 a)\right\}\right]\frac{\lambda_4}{\tau_r}sin[\lambda_4(x-L+c)]-cos[\lambda_4(x-L+c)]\right\} \quad (6.43e)$$

$$\sigma_f = \frac{L_{peri}\tau_r}{A_p\lambda_4}\left\{\left[\tau_r b + \frac{\tau_f}{\lambda_2}\left\{\frac{\lambda_2}{\lambda_1}tanh[\lambda_1(L-c-b-a)]cos(\lambda_2 a)+sin(\lambda_2 a)\right\}\right]\frac{\lambda_4}{\tau_r}cos[\lambda_4(x-L+c)]+sin[\lambda_4(x-L+c)]\right\} \quad (6.43f)$$

The following equations relate the applied load and the displacement,

$$\Delta = (\delta_f - \delta_{re})\left\{\left[\tau_r b + \frac{\tau_f}{\lambda_2}\left\{\frac{\lambda_2}{\lambda_1}tanh[\lambda_1(L-c-b-a)]cos(\lambda_2 a)+sin(\lambda_2 a)\right\}\right]\frac{\lambda_4}{\tau_r}sin(\lambda_4 c)-cos(\lambda_4 c)+\frac{\delta_f}{(\delta_f-\delta_{re})}\right\} \quad (6.44a)$$

$$\overline{\Delta} = \frac{(\delta_f - \delta_{re})}{\delta_f}\left\{\left[\tau_r b + \frac{\tau_f}{\lambda_2}\left\{\frac{\lambda_2}{\lambda_1}tanh[\lambda_1(L-c-b-a)]cos(\lambda_2 a)+sin(\lambda_2 a)\right\}\right]\frac{\lambda_4}{\tau_r}sin(\lambda_4 c)-cos(\lambda_4 c)+\frac{\delta_f}{(\delta_f-\delta_{re})}\right\} \quad (6.44b)$$

$$P = \frac{L_{peri}\tau_r}{\lambda_4}\left\{\left[\tau_r b + \frac{\tau_f}{\lambda_2}\left\{\frac{\lambda_2}{\lambda_1}tanh[\lambda_1(L-c-b-a)]cos(\lambda_2 a)+sin(\lambda_2 a)\right\}\right]\frac{\lambda_4}{\tau_r}cos(\lambda_4 c)+sin(\lambda_4 c)\right\} \quad (6.45a)$$

$$\overline{P} = sin(\lambda_4 c_4)\left\{\left[\tau_r b + \frac{\tau_f}{\lambda_2}\left\{\frac{\lambda_2}{\lambda_1}tanh[\lambda_1(L-c-b-a)]cos(\lambda_2 a)+sin(\lambda_2 a)\right\}\right]\frac{\lambda_4}{\tau_r}cos(\lambda_4 c)+sin(\lambda_4 c)\right\} \quad (6.45b)$$

Two relationships amongst '*a*', '*b*' and '*c*' are given by Equations (6.34) and (6.36) when *L* is replaced by (*L*-*c*) as below.

$$b = L - c - a - \frac{1}{\lambda_1}tanh^{-1}\left\{\frac{\lambda_1}{\lambda_2}\left[-\frac{\tau_r}{\tau_f}+cos(\lambda_2 a)\right]\frac{1}{sin(\lambda_2 a)}\right\} \quad (6.46)$$

$$\delta_{re} - \delta_{rs} = \frac{{\lambda_1}^2\delta_1}{\tau_f}\left\{\frac{\tau_r b^2}{2}+\frac{\tau_f b}{\lambda_2}\left\{\frac{\lambda_2}{\lambda_1}tanh[\lambda_1(L-c-b-a)]cos(\lambda_2 a)+sin(\lambda_2 a)\right\}\right\} \quad (6.47)$$

For an infinite bond length Equations (6.46) and (6.47) converge to Equations (6.51a) and (6.51b). During this stage the value of '*a*' and '*b*' do not change from the previous

value of a = a_3 since Equations (6.26b), (6.37) and (6.51a) as well as Equations (6.38) and (6.51b) are the same for an infinite bond length, while '*c*' increases from zero. In other words, '*a*' and '*b*' remain constant during this stage (i.e., $a = a_4 = a_3 = a_2$ and $b = b_4 = b_3$) as '*c*' increases, for infinite bond lengths.

At the end of this stage *P* reaches its maximum when $\frac{dP}{dc} = 0$ for infinite bond lengths,

$$P_{ult} = \frac{L_{peri}\tau_r}{\lambda_4 sin(\lambda_4 c)} \tag{6.48}$$

Further, it can be shown that for infinite bond lengths *P* reaches its maximum when $\tau = 0$ at $x = L$ (i.e. from the substitution of this condition in Equation (6.43e)) yielding,

$$P_{ult} = \frac{L_{peri}\tau_r}{\lambda_4 sin(\lambda_4 c)} \tag{6.49}$$

This substitution also yields another relationship amongst '*a*', '*b*' and '*c*',

$$tan(\lambda_4 c) = \frac{\tau_r}{\lambda_4\left\{\tau_r b + \frac{\tau_f}{\lambda_2}\left\{\frac{\lambda_2}{\lambda_1} tanh[\lambda_1(L-c-b-a)]cos(\lambda_2 a) + sin(\lambda_2 a)\right\}\right\}} \tag{6.50}$$

For an infinite bond length this converges to Equation (6.51c). The corresponding load for an infinite bond length, $P = P_4 = P_{ult}$ is given by Equation (6.51e).

$$\left\{\frac{\lambda_2}{\lambda_1} sin(\lambda_2 a_4) - cos(\lambda_2 a_4)\right\} = -\frac{\tau_r}{\tau_f} \tag{6.51a}$$

$$\delta_{re} - \delta_{rs} = \frac{\lambda_1^2 \delta_1}{\tau_f}\left\{\frac{\tau_r b_4^2}{2} + \frac{\tau_f b_4}{\lambda_2}\left[\frac{\lambda_2}{\lambda_1} cos(\lambda_2 a_4) + sin(\lambda_2 a_4)\right]\right\} \tag{6.51b}$$

$$tan(\lambda_4 c_4) = \frac{\tau_r}{\lambda_4\left\{\tau_r b_4 + \frac{\tau_f}{\lambda_2}\left[\frac{\lambda_2}{\lambda_1} cos(\lambda_2 a_4) + sin(\lambda_2 a_4)\right]\right\}} \tag{6.51c}$$

$$c_4 = \frac{1}{\lambda_4} tan^{-1}\left\{ \frac{\lambda_1}{\lambda_4\left[\frac{\tau_f^{\,2}}{\tau_r^{\,2}}\left(\frac{\lambda_1^{\,2}+\lambda_2^{\,2}}{\lambda_2^{\,2}}\right)-\frac{\lambda_1^{\,2}}{\lambda_2^{\,2}}+2\frac{\tau_f}{\tau_r}\left(\frac{\delta_{re}-\delta_{rs}}{\delta_1}\right)\right]^{1/2}} \right\} \quad (6.51d)$$

$$P_{ult} = \frac{L_{peri}\tau_r}{\lambda_4\lambda_1}\left\{\lambda_1^{\,2}+\lambda_4^{\,2}\left[\frac{\tau_f^{\,2}}{\tau_r^{\,2}}\left(\frac{\lambda_1^{\,2}+\lambda_2^{\,2}}{\lambda_2^{\,2}}\right)-\frac{\lambda_1^{\,2}}{\lambda_2^{\,2}}+2\frac{\tau_f}{\tau_r}\left(\frac{\delta_{re}-\delta_{rs}}{\delta_1}\right)\right]\right\}^{1/2} \quad (6.51e)$$

The relevant segment for this stage is CD in the load-displacement curve in Figure 6.5. The effective bond length when the maximum load, P_4, is reached, defined as before is given below.

$$l_{eff} = a_4 + b_4 + c_4 + \frac{1}{2\lambda_1} cosh^{-1}\left[\frac{4\tau_f cos(\lambda_2 a_4) cos^2(\lambda_4 c_4) - 0.06\tau_r}{0.06\tau_r}\right] \quad (6.52)$$

6.4.5 Elastic - softening - frictional resistance - frictional softening - debonding stage

There are five regions where there are five different states along the bond length, elastic state ('*L*-*a*-*b*-*c*-*d*'), softening state ('*a*'), residual bond stress state ('*b*'), frictional softening state ('*c*') and debonding state ('*d*') (Figure 6.9). The expressions for interfacial slip, interfacial shear stress and axial stress in the FRP strip in the previous stage are still valid if *L* is replaced by (*L*-*d*) for the first four zones.

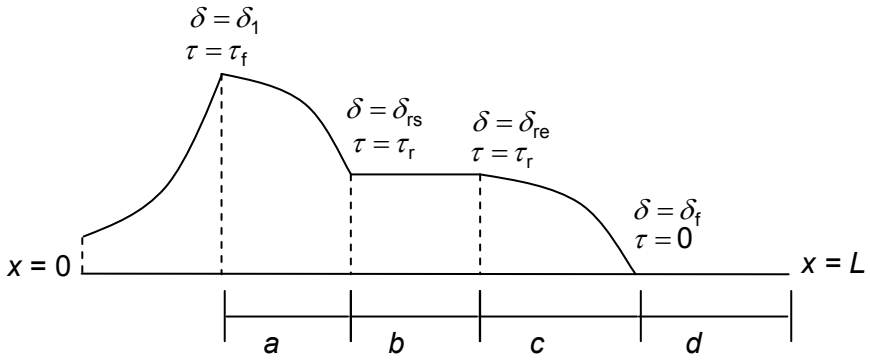

Figure 6.9 - Interfacial shear stress distribution during the elastic - softening - frictional resistance - frictional softening - debonding stage

The governing differential equation for the debonding zone ('*d*'), $\delta_f \le \delta,\ L-d \le x \le L$, is given by,

$$\frac{d^2\delta}{dx^2} = 0 \tag{6.53a}$$

Equations (6.53d) to (6.53f) are the solutions with the following boundary conditions.

$$\sigma_f = \frac{P}{A_p} \text{ at } x = L-d \tag{6.53b}$$

$$\delta = \delta_f \text{ at } x = L-d \tag{6.53c}$$

$$\delta = \frac{P(x-L+d)\lambda_1^{\,2}\delta_1}{L_{peri}\tau_f} + \delta_f \tag{6.53d}$$

$$\tau = 0 \tag{6.53e}$$

$$\sigma_f = \frac{P}{A_p} \tag{6.53f}$$

Equations (6.46), (6.47) and (6.50) are still valid when *L* is replaced by (*L*-*d*), and yield three relationships amongst '*a*', '*b*', '*c*' and '*d*' as below.

$$b = L-d-c-a-\frac{1}{\lambda_1}tanh^{-1}\left\{\frac{\lambda_1}{\lambda_2}\left[-\frac{\tau_r}{\tau_f}+cos(\lambda_2 a)\right]\frac{1}{sin(\lambda_2 a)}\right\} \tag{6.54}$$

$$\delta_{re}-\delta_{rs} = \frac{\lambda_1^{\,2}\delta_1}{\tau_f}\left\{\frac{\tau_r b^2}{2}+\frac{\tau_f b}{\lambda_2}\left\{\frac{\lambda_2}{\lambda_1}tanh[\lambda_1(L-d-c-b-a)]cos(\lambda_2 a)+sin(\lambda_2 a)\right\}\right\} \tag{6.55}$$

$$tan(\lambda_4 c) = \frac{\tau_r}{\lambda_4\left\{\tau_r b+\frac{\tau_f}{\lambda_2}\left\{\frac{\lambda_2}{\lambda_1}tanh[\lambda_1(L-d-c-b-a)]cos(\lambda_2 a)+sin(\lambda_2 a)\right\}\right\}} \tag{6.56}$$

The applied load in the strip is given by,

$$P = \frac{L_{peri}\tau_r}{\lambda_4}\left\{\left[\tau_r b+\frac{\tau_f}{\lambda_2}\left\{\frac{\lambda_2}{\lambda_1}tanh[\lambda_1(L-d-c-b-a)]cos(\lambda_2 a)+sin(\lambda_2 a)\right\}\right]\frac{\lambda_4}{\tau_r}cos(\lambda_4 c)+\sin(\lambda_4 c)\right\} \tag{6.57a}$$

The expression for the applied load can be simplified by applying Equation (6.56) to Equation (6.57a) as follows, which is essentially the same as Equation (6.49) with only the value of 'c' being varied,

$$P = \frac{L_{\text{peri}}\tau_{\text{r}}}{\lambda_4 sin(\lambda_4 c)} \tag{6.57b}$$

$$\overline{P} = \frac{sin(\lambda_4 c_4)}{sin(\lambda_4 c)} \tag{6.57c}$$

The displacement at the loaded end is given by,

$$\Delta = \frac{Pd\lambda_1^{\,2}\delta_1}{L_{\text{peri}}\tau_{\text{f}}} + \delta_{\text{f}} \tag{6.57d}$$

$$\overline{\Delta} = \frac{\overline{P}d\lambda_1^{\,2}\delta_1\tau_{\text{r}}}{\tau_{\text{f}}\delta_{\text{f}}\lambda_4 sin(\lambda_4 c_4)} + 1 \tag{6.57e}$$

At the end of this stage, the elastic zone disappears (i.e., *L*-*d*-*c*-*b*-*a* = 0) yielding another relationship amongst '*a*', '*b*', '*c*' and '*d*' and allowing solutions to be found for *a* = a_5, *b* = b_5, *c* = c_5 and *d* = d_5 at the end of this stage. Segment DE'E in Figure 6.5 represents the relationship between *P* and Δ during this stage. Point E' at the end of the plateau shows how the transferable load reduces slightly when the elastic zone starts diminishing in length while the length of the debonded zone increases.

$$a_5 = \frac{1}{\lambda_2} cos^{-1}\left(\frac{\tau_{\text{r}}}{\tau_{\text{f}}}\right) \tag{6.58a}$$

$$b_5 = -\frac{\left(\tau_{\text{f}}^{\,2} - \tau_{\text{r}}^{\,2}\right)^{1/2}}{\tau_{\text{r}}\lambda_2} + \left[\frac{\left(\tau_{\text{f}}^{\,2} - \tau_{\text{r}}^{\,2}\right)}{\tau_{\text{r}}^{\,2}\lambda_2^{\,2}} + \frac{2}{\lambda_1^{\,2}}\frac{\tau_{\text{f}}}{\tau_{\text{r}}}\left(\frac{\delta_{\text{re}} - \delta_{\text{rs}}}{\delta_1}\right)\right]^{1/2} \tag{6.58b}$$

$$c_5 = \frac{1}{\lambda_4} tan^{-1}\left\{\frac{\tau_{\text{r}}}{\lambda_4\left[\left(\frac{\tau_{\text{f}}^{\,2} - \tau_{\text{r}}^{\,2}}{\lambda_2^{\,2}}\right) + 2\frac{\tau_{\text{f}}\tau_{\text{r}}}{\lambda_1^{\,2}}\left(\frac{\delta_{\text{re}} - \delta_{\text{rs}}}{\delta_1}\right)\right]^{1/2}}\right\} \tag{6.58c}$$

$$d_5 = L - a_5 - b_5 - c_5 \tag{6.58d}$$

Equation (6.59) gives the load $P = P_5$ at which the stage ends.

$$P_5 = \frac{L_{peri}}{\lambda_4}\left\{\tau_r^{\,2} + \lambda_4^{\,2}\left[\left(\frac{\tau_f^{\,2} - \tau_r^{\,2}}{\lambda_2^{\,2}}\right) + 2\frac{\tau_f \tau_r}{\lambda_1^{\,2}}\left(\frac{\delta_{re} - \delta_{rs}}{\delta_1}\right)\right]\right\}^{1/2} \tag{6.59}$$

6.4.6 Softening - frictional resistance - frictional softening - debonding stage

The expressions for interfacial slip, interfacial shear stress and axial stress can be found by solving the corresponding governing differential equation following the same procedure as in the previous stages. The bond stress distribution is of the form shown in Figure 6.10.

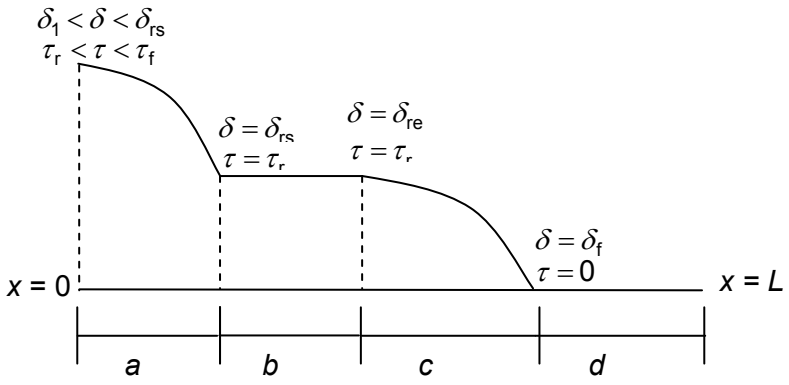

Figure 6.10 - Interfacial shear stress distribution during the softening - frictional resistance - frictional softening - debonding stage

In the softening region, $\delta_1 \le \delta \le \delta_{rs}$, $0 \le x \le L - d - c - b$,

$$\frac{d^2\delta}{dx^2} + \lambda_2^{\,2}\delta = \lambda_3^{\,2} \tag{6.60a}$$

Equations (6.60d) to (6.60f) yield solutions for the softening state using the following boundary conditions.

$$\sigma_f = 0 \text{ at } x = 0 \tag{6.60b}$$

$$\delta = \delta_{rs} \text{ at } x = a \tag{6.60c}$$

$$\delta = \frac{(\delta_{rs} - \delta_1)}{(\tau_f - \tau_r)}\left[\frac{-\tau_r cos(\lambda_2 x)}{cos(\lambda_2 a)} + \frac{(\tau_f \delta_{rs} - \tau_r \delta_1)}{(\delta_{rs} - \delta_1)}\right] \quad (6.60d)$$

$$\tau = \frac{-\tau_r cos(\lambda_2 x)}{cos(\lambda_2 a)} \quad (6.60e)$$

$$\sigma_f = \frac{L_{peri}\tau_r sin(\lambda_2 x)}{A_p \lambda_2 cos(\lambda_2 a)} \quad (6.60f)$$

In the frictional resistance region, $\delta_{rs} \le \delta \le \delta_{re}$, $L - d - c - b \le x \le L - d - c$,

$$\frac{d^2\delta}{dx^2} - \frac{2G_f \lambda^2 \tau_r}{\tau_f^2} = 0 \quad (6.61a)$$

Equations (6.61d) to (6.61f) yield solutions for the frictional resistance state using the following boundary conditions.

σ_f is continuous at $x = a$ (6.61b)

$\delta = \delta_{rs}$ at $x = a$ (6.61c)

$$\delta = \frac{\lambda_1^2 \delta_1}{\tau_f}\left\{\frac{\tau_r x^2}{2} + \frac{\tau_r}{\lambda_2}[tan(\lambda_2 a) - \lambda_2 a]x - \frac{\tau_r a}{2\lambda_2}[2tan(\lambda_2 a) - \lambda_2 a]\right\} + \delta_{rs} \quad (6.61d)$$

$$\tau = \tau_r \quad (6.61e)$$

$$\sigma_f = \frac{L_{peri}\tau_f}{A_p \lambda_2}[tan(\lambda_2 a) + \lambda_2 (x - a)] \quad (6.61f)$$

In the frictional softening region, $\delta_{re} \le \delta \le \delta_f$, $L - d - c \le x \le L - d$,

$$\frac{d^2\delta}{dx^2} + \lambda_4^2 \delta = \lambda_4^2 \delta_f \quad (6.62a)$$

Equations (6.62d) to (6.62f) are the solutions of the differential equation using the following boundary conditions.

σ_f is continuous at $x = L - d - c$ (6.62b)

$\delta = \delta_{re}$ at $x = L - d - c$ (6.62c)

$$\delta = (\delta_f - \delta_{re})\left\{\frac{\lambda_4}{\lambda_2}[tan(\lambda_2 a) + b\lambda_2]sin[\lambda_4(x - L + d + c)] - cos[\lambda_4(x - L + d + c)] + \frac{\delta_f}{(\delta_f - \delta_{re})}\right\} \quad (6.62d)$$

$$\tau = -\tau_r\left\{\frac{\lambda_4}{\lambda_2}[tan(\lambda_2 a) + b\lambda_2]sin[\lambda_4(x - L + d + c)] - cos[\lambda_4(x - L + d + c)]\right\} \quad (6.62e)$$

$$\sigma_f = \frac{L_{peri}\tau_r}{A_p\lambda_4}\left\{\frac{\lambda_4}{\lambda_2}[tan(\lambda_2 a) + b\lambda_2]cos[\lambda_4(x - L + d + c)] + sin[\lambda_4(x - L + d + c)]\right\} \quad (6.62f)$$

In the debonding zone, $\delta_f \le \delta$, $L - d \le x \le L$, Equations (6.53d) to (6.53f) are still valid as the boundary conditions are the same. The relationship between the displacement and the load is still the same as given by Equations (6.57d) and (6.57e), except the expression for the applied load is different as below.

$$P = \frac{L_{peri}\tau_r}{\lambda_4}\left\{\frac{\lambda_4}{\lambda_2}[tan(\lambda_2 a) + b\lambda_2]cos(\lambda_4 c) + sin(\lambda_4 c)\right\} \quad (6.63)$$

Two relationships amongst '*a*', '*b*', '*c*' and '*d*' can be obtained by substituting the following conditions into Equations (6.61d) and (6.62d), respectively.

$\delta = \delta_{re}$ at $x = L - d - c$ (6.64)

$\delta = \delta_f$ at $x = L - d$ (6.65)

$$b = \frac{1}{\lambda_2}\left\{-tan(\lambda_2 a) + \left[tan^2(\lambda_2 a) + 2\frac{\lambda_2^2}{\lambda_1^2}\frac{(\delta_{re} - \delta_{rs})}{\delta_1}\frac{\tau_f}{\tau_r}\right]^{1/2}\right\} \quad (6.66)$$

$$c = \frac{1}{\lambda_4}tan^{-1}\left\{\frac{\lambda_2}{\lambda_4[b\lambda_2 + tan(\lambda_2 a)]}\right\} \quad (6.67)$$

Further, $d = L - a - b - c$ (6.68)

By applying Equation (6.67) to Equation (6.63), the expression for the applied load can be simplified as below, yielding similar results to Equations (6.49) and (6.57b), with only the value of '*c*' being different in each stage.

$$P = \frac{L_{peri}\tau_r}{\lambda_4 sin(\lambda_4 c)} \tag{6.69}$$

$$\overline{P} = \frac{sin(\lambda_4 c_4)}{sin(\lambda_4 c)} \tag{6.70}$$

At the end of this stage the softening zone disappears, i.e., $a = 0$ and the values of $b = b_6$, $c = c_6$ and $d = d_6$ can be found by applying this condition to Equations (6.66), (6.67) and (6.68). Segment EF in Figure 6.5 represents the P vs. Δ relationship during this stage.

$$b_6 = \frac{1}{\lambda_1}\left[2\frac{(\delta_{re}-\delta_{rs})}{\delta_1}\frac{\tau_f}{\tau_r}\right]^{1/2} \tag{6.71}$$

$$c_6 = \frac{1}{\lambda_4} tan^{-1}\left\{\frac{\lambda_1}{\lambda_4\left[2\frac{(\delta_{re}-\delta_{rs})}{\delta_1}\frac{\tau_f}{\tau_r}\right]^{1/2}}\right\} \tag{6.72}$$

$$d_6 = L - \frac{1}{\lambda_1}\left[2\frac{(\delta_{re}-\delta_{rs})}{\delta_1}\frac{\tau_f}{\tau_r}\right]^{1/2} - \frac{1}{\lambda_4} tan^{-1}\left\{\frac{\lambda_1}{\lambda_4\left[2\frac{(\delta_{re}-\delta_{rs})}{\delta_1}\frac{\tau_f}{\tau_r}\right]^{1/2}}\right\} \tag{6.73}$$

Equation (6.74) gives the load, $P = P_6$ at which the stage ends.

$$P_6 = \frac{L_{peri}\tau_r}{\lambda_4}\left[1+2\frac{\lambda_4^{\,2}}{\lambda_1^{\,2}}\frac{(\delta_{re}-\delta_{rs})}{\delta_1}\frac{\tau_f}{\tau_r}\right]^{1/2} \tag{6.74}$$

6.4.7 Frictional resistance - frictional softening - debonding stage

There are only three regions remaining along the bond length, namely, frictional resistance zone, frictional softening zone and debonding zone, as in Figure 6.11.

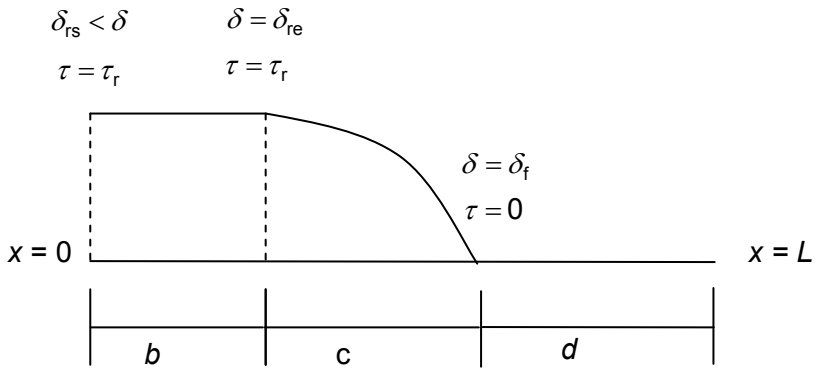

Figure 6.11 - Interfacial shear stress distribution during the frictional resistance - frictional softening - debonding stage

In the frictional resistance region, $\delta_{rs} \le \delta \le \delta_{re}$, $0 \le x \le L - d - c$,

$$\frac{d^2\delta}{dx^2} - \frac{2G_f\lambda^2\tau_r}{\tau_f^2} = 0 \tag{6.75a}$$

Equations (6.75d) to (6.75f) yield the solutions for the frictional resistance state using the following boundary conditions.

$$\sigma_f = 0 \text{ at } x = 0 \tag{6.75b}$$

$$\delta = \delta_{re} \text{ at } x = L - d - c \tag{6.75c}$$

$$\delta = \frac{\lambda_1^2\delta_1\tau_r}{2\tau_f}(x^2 - d^2) + \delta_{re} \tag{6.75d}$$

$$\tau = \tau_r \tag{6.75e}$$

$$\sigma_f = \frac{L_{peri}\tau_r x}{A_p} \tag{6.75f}$$

In the frictional softening region, $\delta_{re} \le \delta \le \delta_f$, $L - d - c \le x \le L - d$,

$$\frac{d^2\delta}{dx^2} + \lambda_4^2\delta = \lambda_4^2\delta_f \tag{6.76a}$$

Equations (6.76d) to (6.76f) are the solutions of the differential equation using the following boundary conditions.

$$\sigma_f = \frac{P}{A_p} \text{ at } x = L - d \tag{6.76b}$$

$$\delta = \delta_f \text{ at } x = L - d \tag{6.76c}$$

$$\delta = \frac{P\lambda_1^2\delta_1 sin\left[\lambda_4\left(x - L + d\right)\right]}{\lambda_4 L_{peri}\tau_f} + \delta_f \tag{6.76d}$$

$$\tau = -\frac{P\lambda_4 \sin\left[\lambda_4\left(x - L + d\right)\right]}{L_{peri}} \tag{6.76e}$$

$$\sigma_f = \frac{Pcos\left[\lambda_4\left(x - L + d\right)\right]}{A_p} \tag{6.76f}$$

In the debonding zone, $\delta_f \le \delta$, $L - d \le x \le L$, Equations (6.53d) to (6.53f) are still valid as the boundary conditions are the same.

The relationship between the displacement and the load is still the same as given by Equations (6.57d) and (6.57e), and the value of applied load is given below.

$$P = \frac{L_{peri}\tau_r b}{cos\left(\lambda_4 c\right)} \tag{6.77}$$

A relationship amongst '*b*', '*c*' and '*d*' can be obtained by substituting $\delta = \delta_{re}$ at *x* = *L*-*d*-*c* into Equation (6.76d), and from Equation (6.77),

$$b = \frac{1}{\lambda_4 tan\left(\lambda_4 c\right)} \tag{6.78}$$

The second relationship amongst 'b', 'c' and 'd' is given by,

$$d = L - c - b \tag{6.79}$$

By applying the condition in Equation (6.78) to Equation (6.77), the expression for the applied load can be simplified as below and this is similar to the results of Equations (6.49), (6.57b) and (6.69), with only the value of '*c*' being different in each stage.

$$P = \frac{L_{\text{peri}}\tau_{\text{r}}}{\lambda_4 sin(\lambda_4 c)} \tag{6.80}$$

$$\overline{P} = \frac{sin(\lambda_4 c_4)}{sin(\lambda_4 c)} \tag{6.81}$$

At the end of this stage, the frictional bond stress zone disappears, i.e., b = 0 and the values of $c = c_7$ and $d = d_7$ at the end of this stage can be found by applying this condition to Equations (6.78), (6.79) as follows.

$$c = c_7 = \frac{\pi}{2\lambda_4} \tag{6.82}$$

$$d = d_7 = L - \frac{\pi}{2\lambda_4} \tag{6.83}$$

Equation (6.84) gives the corresponding load $P = P_7$ at which the stage ends.

$$P_7 = \frac{L_{\text{peri}}\tau_{\text{r}}}{\lambda_4} \tag{6.84}$$

Segment FG in Figure 6.5 represents the P vs. Δ relationship during this stage.

6.4.8 Frictional softening - debonding stage

There are only two zones left along the bond length now (Figure 6.12). They are frictional softening and debonding zones.

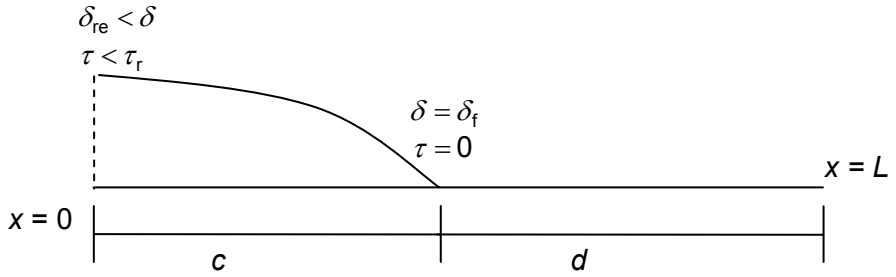

Figure 6.12 - Interfacial shear stress distribution during the frictional softening - debonding stage

In the frictional softening region, $\delta_{re} \le \delta \le \delta_f$, $0 \le x \le L - d$,

$$\frac{d^2\delta}{dx^2} + \lambda_4{}^2\delta = \lambda_4{}^2\delta_f \tag{6.85}$$

The following solutions can be found by solving the differential equation with the boundary conditions of $\sigma_f = 0$ at $x = 0$ and $\delta = \delta_f$ at $x = L\text{-}d$, as follows. .

$$c = c_7 = \frac{\pi}{2\lambda_4} \tag{6.86}$$

In other words, the length of the frictional softening zone, '*c*', remains constant throughout this stage. Consequently, the length of the debonding zone, $d = L\text{-}c$, also remains constant during this stage.

$$\delta = \delta_f - \frac{P\lambda_1{}^2\delta_1 cos(\lambda_4 x)}{\lambda_4 L_{peri}\tau_f} \tag{6.87}$$

$$\tau = \frac{P\lambda_4 cos(\lambda_4 x)}{L_{peri}} \tag{6.88}$$

$$\sigma_f = \frac{Psin(\lambda_4 x)}{A_p} \tag{6.89}$$

In the debonding zone, $\delta_f \le \delta$, $L - d \le x \le L$, Equations (6.53d) to (6.53f) are still valid as the boundary conditions are the same.

The relationship between the displacement and the load is still the same as given by Equations (6.57d) and (6.57e), but now $d = L - c = L - \frac{\pi}{2\lambda_4}$.

i.e., $$\Delta = \frac{P\lambda_1{}^2\delta_1\left(L - \frac{\pi}{2\lambda_4}\right)}{L_{peri}\tau_f} + \delta_f \tag{6.90}$$

$$\overline{\Delta} = \frac{\overline{P}\lambda_1{}^2\delta_1\tau_r\left(L - \frac{\pi}{2\lambda_4}\right)}{\tau_f\delta_f\lambda_4 sin(\lambda_4 c_4)} + 1 \tag{6.91}$$

Equation (6.90) shows that the displacement decreases linearly as the load decreases, as can be seen in Segment GH in Figure 6.5.

Figure 6.5 shows a snap-back behavior from the end of the elastic-softening-frictional resistance-frictional softening-debonding stage to the end of the last stage, frictional softening-debonding stage. This is due to progressive and rapid decaying of each portion of bond length at different stress states (portions at elastic state, softening state, frictional stress state, frictional softening state, respectively) until the complete debonding occurs. Figure 6.13 represents a typical full range load-displacement curve for an externally bonded plate-to-concrete bonded joint of a single lap pull-push test (Yuan *et al.*, 2004) resulting from the bi-linear bond stress-slip relationship, for comparison with Figure 6.5. Generally, both curves represent the same shape consisting an initially linear branch, then non-linear load-slip behaviour up to the peak load, a constant plateau after the peak load and snap-back behaviour in the softening region. However, the ascending region in Figure 6.5 represents four stages of the debonding process whereas that in Figure 6.13 corresponds to two stages only. Similarly, the snap-back region in Figure 6.5 represents three stages of the debonding process while that in Figure 6.13 represents only one stage.

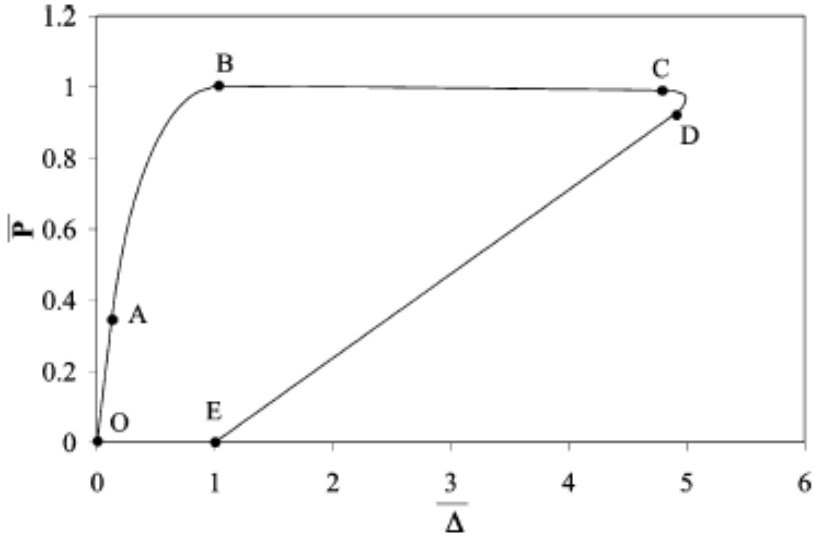

Figure 6.13 - Typical full range load-displacement curve of a plate-to-concrete bonded joint (Yuan *et al.*, 2004)

6.5 Practical local bond stress - slip curves

Two bond stress-slip curves which are likely to be more practical are considered in this section for modelling NSM FRP to concrete bonded joints (Figure 6.14). The expressions for interfacial slip, interfacial shear stress, axial stress in the FRP strip, slip and the applied load can be derived from those of the basic curve (Figure 6.3) using relevant substitutions.

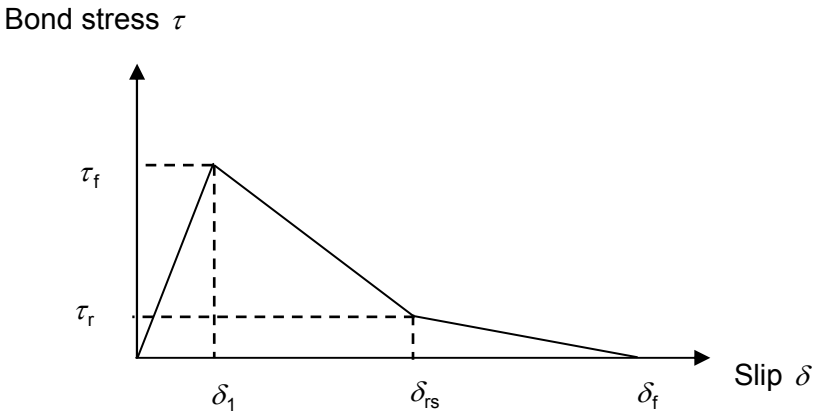

Model I

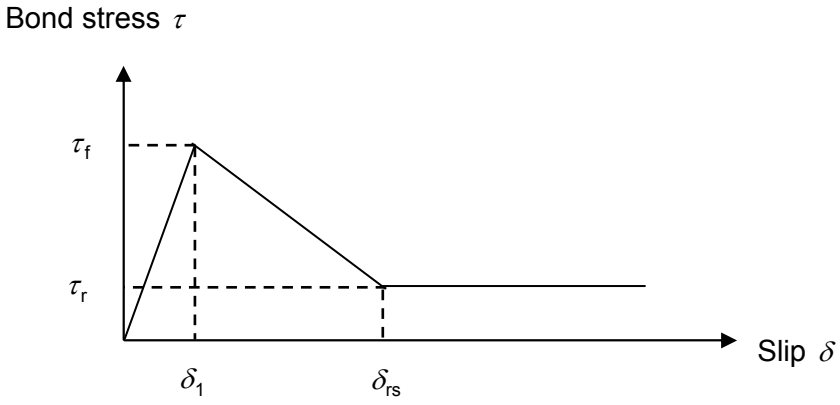

Model II

Figure 6.14 - Practical bond stress-slip models

These two bond models are simplified versions of realistic local bond-slip relationships which have already been reported in the literature (De Lorenzis and Teng, 2007) where the non-linear ascending branch and the post-peak branch up to the frictional bond stress level of those conventional models are replaced by linear branches. Further, in

Model I, it is assumed that bond stress decreases linearly from the frictional bond stress to zero, whereas in Model II, a third branch remains at the value of frictional bond stress as slip approaches infinity, in line with some of bond models for NSM FRP bars where interfacial fracture energy is allowed to become infinite (De Lorenzis and Teng, 2007).

6.5.1 Model I

Figure 6.15 shows the various stages of the debonding process. The solutions of each stage can be obtained by substitution of $\delta_{re} = \delta_{rs}$ in the solutions of the basic bond model. Consequently, the debonding process has only six stages out of the original eight in the basic model because *b* = 0. Now,

$$G_f = \frac{1}{2}\left[\tau_f \delta_{rs} + \tau_r \left(\delta_f - \delta_1\right)\right] \tag{6.92}$$

$$\lambda_4{}^2 = \frac{\lambda^2 2 G_f \tau_r}{\tau_f{}^2 \left(\delta_f - \delta_{rs}\right)} = \frac{\tau_r L_{peri}}{\left(\delta_f - \delta_{rs}\right)}\left[\frac{1}{\left(E_f A_f\right)} + \frac{1}{\left(E_c A_c\right)}\right] \tag{6.93}$$

Figure 6.16 illustrates the full range load-displacement curve for an NSM bonded joint modelled using Model I.

6.5.1.1 Elastic stage

Equations (6.8)-(6.19) are still valid for this stage with the substitutions.

6.5.1.2 Elastic - softening stage

Equations (6.20a)-(6.29) are applicable with the substitutions.

6.5.1.3 Elastic – softening - frictional softening stage

Equations (6.40)-(6.52) are applicable with the substitutions.

6.5.1.4 Elastic – softening - frictional softening - debonding stage

Equations (6.53a)-(6.59) are still valid with the substitutions.

6.5.1.5 Softening - frictional softening - debonding stage

Equations (6.60a)-(6.74) are applicable during this stage with the substitutions.

6.5.1.6 Frictional softening - debonding stage

Equations (6.85)-(6.91) are applicable with the substitutions.

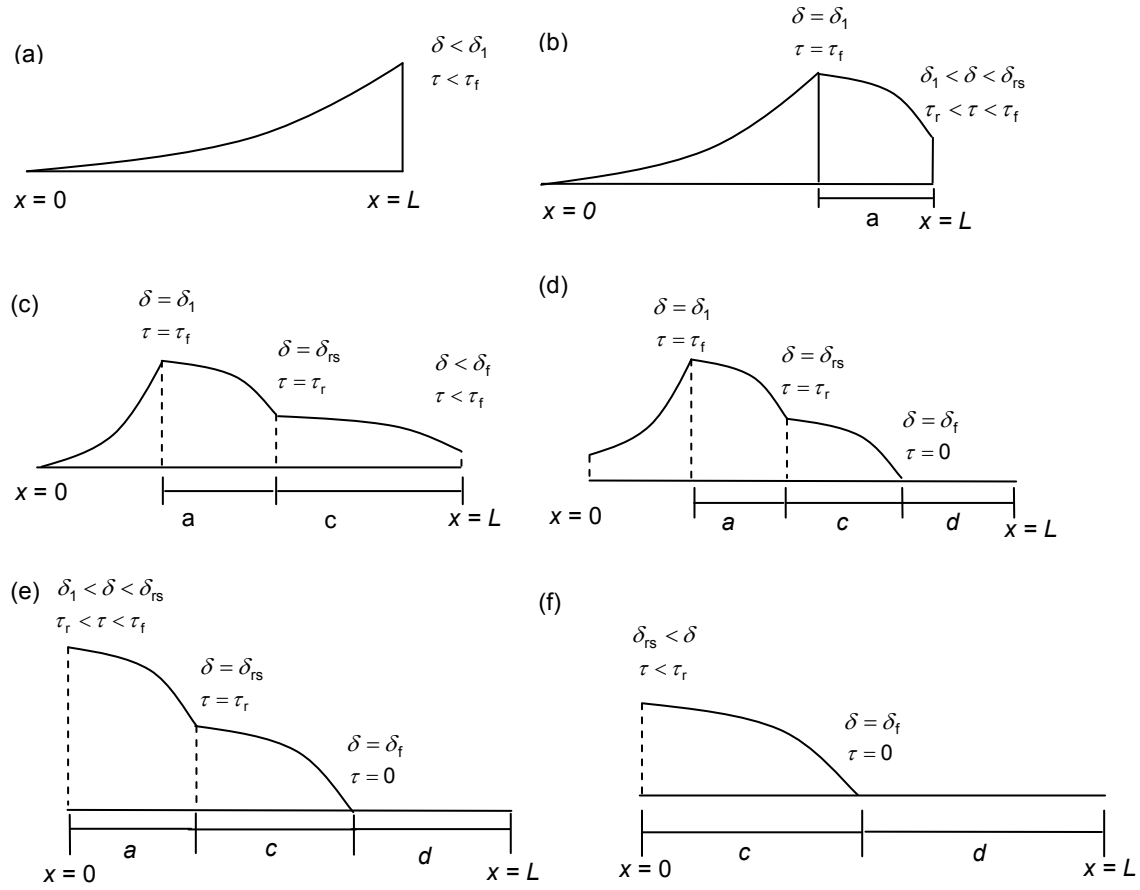

Figure 6.15 - Interfacial shear stress distribution during (a) elastic stage, (b) elastic - softening stage, (c) elastic - softening - frictional softening stage, (d) elastic - softening - frictional softening - debonding stage, (e) softening - frictional softening - debonding stage, and (f) frictional softening - debonding stage

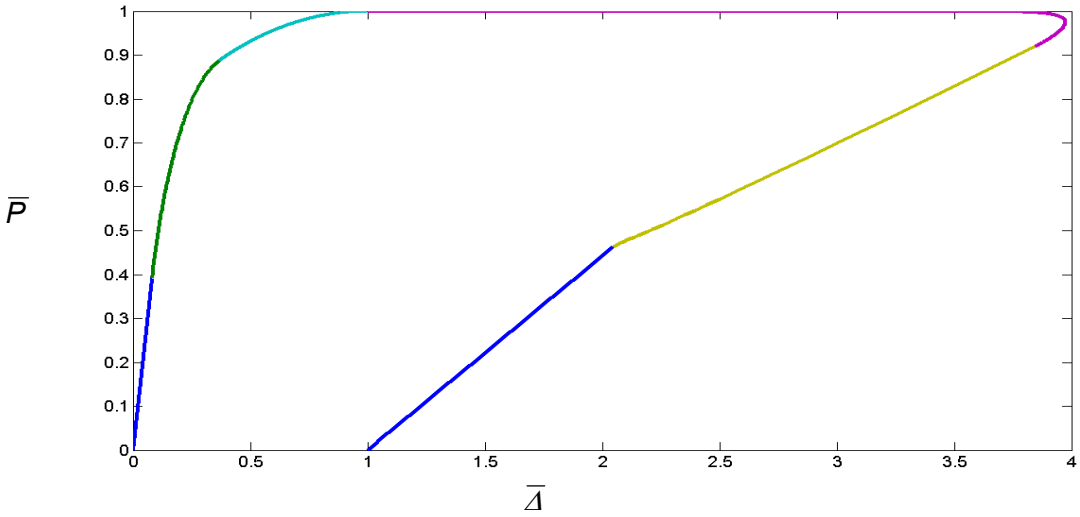

Figure 6.16 - Typical full range load-displacement curve for Model I

Compared to the basic model (Figure 6.5), Figure 6.16 represents the same shape consisting a linear branch, non-linear behaviour up to the peak load, a constant plateau and snap-back behaviour in the softening region. However, the ascending region in Figure 6.5 represents four stages of the debonding process whereas that in Figure 6.16 corresponds to three stages only as the frictional resistance stage does not exist. Similarly, the softening region in Figure 6.5 represents three stages of the debonding process while that in Figure 6.16 represents only two stages because the frictional softening stage does not exist.

6.5.2 Model II

Figure 6.17 shows the various stages of the debonding process. Now, G_f and δ_{re} approach infinity. The solutions of all the stages cannot be obtained by direct substitution in the basic model, unlike in Model I. However, the equations are the same during the first three stages.

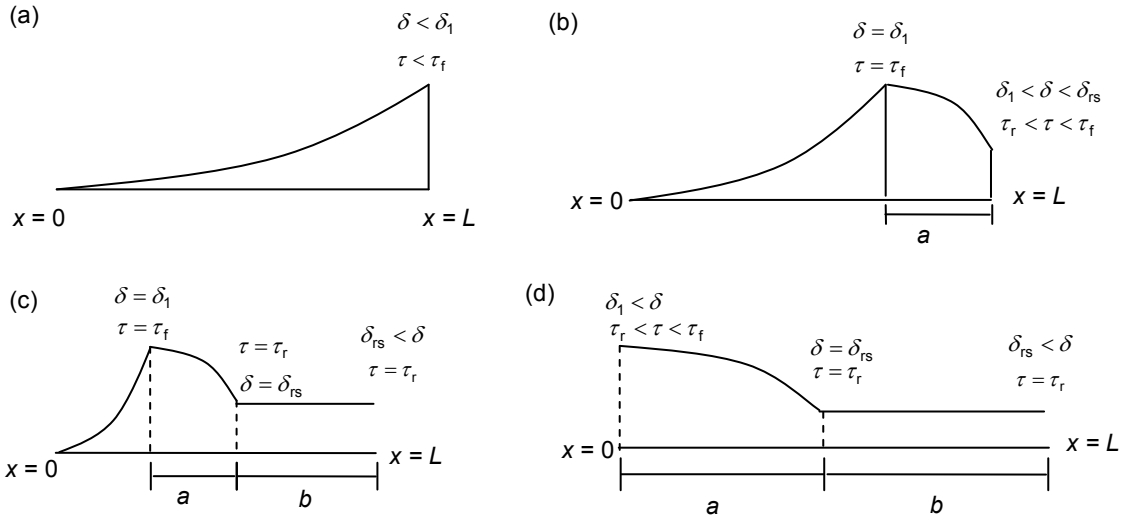

Figure 6.17 - Interfacial shear stress distribution during (a) elastic stage, (b) elastic - softening stage, (c) elastic - softening - frictional resistance stage and (d) softening - frictional resistance stage

6.5.2.1 Elastic stage

Equations (6.8)-(6.13) are still valid. The relationship between the applied load and the displacement at the loaded end is still given by Equation (6.15). The effective bond length during this stage is still given by Equation (6.19).

6.5.2.2 Elastic - softening stage

Equations (6.20a)-(6.21f) are still applicable. The applied load and the displacement at the loaded end are still given by Equations (6.24) and (6.22), respectively. The effective bond length at the end of this stage is still given by Equation (6. 29).

6.5.2.3 Elastic – softening - frictional resistance stage

Equations (6.30)-(6.32f) are still applicable. The applied load and the displacement at the loaded end are still given by Equations (6.33c) and (6.33a), respectively. This stage ends when the elastic zone disappears, i.e. *L-a-b* = 0, yielding the values of '*a*', '*b*' and the applied load, at the end of the stage, as follows.

$$a = \frac{1}{\lambda_2} cos^{-1}\left(\frac{\tau_r}{\tau_f}\right) \tag{6.94}$$

$$b = L - a = L - \frac{1}{\lambda_2} cos^{-1}\left(\frac{\tau_r}{\tau_f}\right) \tag{6.95}$$

$$P = L_{peri}\left\{\tau_r\left[L - \frac{1}{\lambda_2} cos^{-1}\left(\frac{\tau_r}{\tau_f}\right)\right] + \frac{\tau_f}{\lambda_2} sin\left[cos^{-1}\left(\frac{\tau_r}{\tau_f}\right)\right]\right\} \tag{6.96}$$

It can be seen that the load at which the stage ends, is dependent on the bond length.

6.5.2.4 Softening - frictional resistance stage

For the softening region, $0 \le x \le L - b$, Equations (6.60a) to (6.60f) are still valid. For the frictional resistance state, $L - b \le x \le L$, Equations (6.61a) to (6.61f) are still valid.

By applying the condition, $\sigma_f = \frac{P}{A_p}$ at $x = L$, in Equation (6.61f),

$$P = \frac{L_{peri}\,\tau_r}{\lambda_2}\left[\lambda_2 b + tan(\lambda_2 a)\right] \tag{6.97}$$

By applying the condition, $\delta = \Delta$ at $x = L$, in Equation (6.61d),

$$\Delta = \frac{\lambda_1^2 \delta_1 \tau_r}{\tau_f}\left\{\frac{\left(L^2 + a^2\right)}{2} + \frac{(L-a)}{\lambda_2} tan(\lambda_2 a) - La\right\} + \delta_{rs} \tag{6.98}$$

At the end of this stage, the softening zone disappears, i.e., $a = 0$ and $b = L$. The corresponding load and the displacement at the loaded end are,

$$P = L_{peri}\tau_r L \tag{6.99}$$

$$\Delta = \frac{\lambda_1^2 \delta_1 \tau_r L^2}{2\tau_f} + \delta_{rs} \tag{6.100}$$

It can be seen that the load at which the stage ends, is dependent on the bond length.

6.5.2.5 Frictional resistance stage

Now $b = L$ so that the shear stress along the whole bond length is equal to τ_r. It can be shown that the differential equation can be solved for $\tau = \tau_f$ with the boundary conditions of $\sigma_f = 0$ at $x = 0$ and $\sigma_f = \frac{P}{A_p}$ at $x = L$, yielding,

$$P = L_{peri}\tau_r L \tag{6.101}$$

In other words, the applied load remains constant as the displacement at the loaded end increases, even though the applied load reduces when the elastic and the softening zones vanish (Figure 6.18).

Figure 6.18 illustrates the full range load-displacement curve for an NSM bonded joint modelled using Model II, where P and Δ are dimensionless with respect to Equations (6.99) and (6.100), respectively. Compared to the basic load-slip curve (Figure 6.5) and the load-slip curve corresponding to Model I (Figure 6.16), Figure 6.18 shows a significantly different behaviour attributing to the major difference in the bond stress-slip models. That is Model II possesses infinite fracture energy whereas both the basic bond stress-slip model and Model I have finite fracture energy. Figure 6.18 does not possess a maximum load and a constant plateau unlike Figure 6.5. Even though both models display snap-back behaviour, Figure 6.18 consists of another branch after the snap-back region which has a constant load level with increasing slip, representing the frictional resistance at the interface.

If the frictional bond stress level of Model II has a finite value of δ to define a termination, where the bond stress falls to zero at that value of δ, the corresponding debonding process can be obtained by applying the condition $\delta_{re} = \delta_f$ in the equations derived from the basic model.

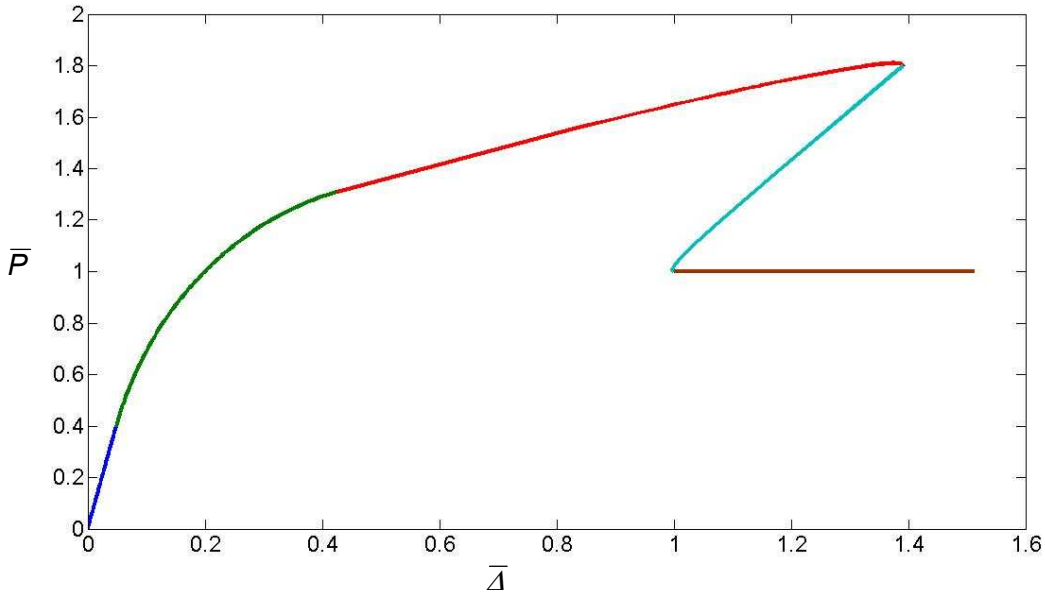

Figure 6.18 - Typical full range load-displacement curve for Model II

6.5.2.6 Development length

Equation (6.96) yields the highest capacity for the bonded joint for a given bond length at the end of the elastic-softening-frictional resistance stage (the slight decrease in load at the end of the stage is disregarded). If the bond parameters of the Model II are known, the ultimate capacity can be predicted for a given bond length provided that the bond length is longer than the effective bond length at the end of the elastic-softening stage. It is seen that the applied load is proportional to the bond length, and by increasing the bond length beyond the effective bond length at the end of elastic-softening stage, the ultimate capacity of the bonded joint can be increased. Figure 6.19 illustrates the effect of different bond lengths on the capacity of a bonded joint with the bond properties described in Section 6.6 (specimen *9-35[S/60/S/Sika/6.4p]*). Therefore, unlike the other models, Model II possesses a development length as opposed to an effective bond length. It is generally accepted that NSM joints with infinite values of interfacial fracture energy can develop the full capacity of the reinforcement bar, and the corresponding value of bond length is termed the development length (De Lorenzis and Teng, 2007).

From Equation (6.96) the development length, l_{dev}, can be obtained as follows,

$$I_{dev} = \frac{P}{L_{peri}\,\tau_r} - \frac{\tau_m}{\tau_r \lambda_2} sin\left[cos^{-1}\left(\frac{\tau_r}{\tau_f}\right)\right] + \frac{1}{\lambda_2} cos^{-1}\left(\frac{\tau_r}{\tau_f}\right) \quad (6.102)$$

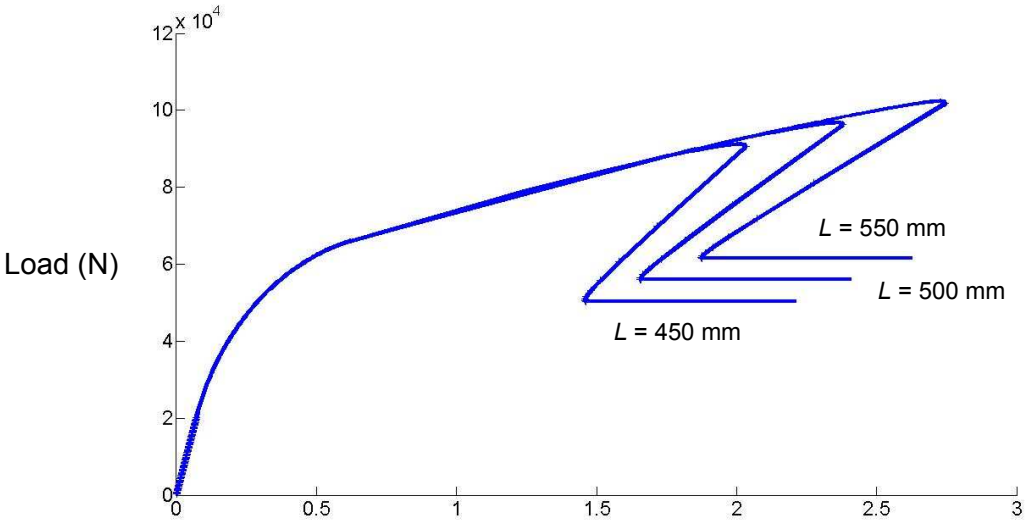

Figure 6.19 - Effect of bond length

6.6 Comparison of analytical solutions with test results

The analytical solutions can be used to predict the experimental load-displacement relationship if the interfacial parameters of the bond stress-slip model are available. There have been two methods developed so far for the derivation of the interfacial parameters. The first is to identify some characteristic points in the experimental load-displacement curve itself (Yuan *et al.*, 2004), for example the coordinates of the end of the elastic branch. The second method involves use of generic equations (which are generic only within the bounds of the variables involved in the particular tests) to predict the bond parameters, without the need for an experimental load-displacement relationship (Mohamed Ali *et al.*, 2008). The latter seems to be more appropriate because it allows prediction of load-slip behaviour without being as specific as the former. The predicted load-displacement behaviour of NSM FRP bonded joints which used the second method to find bond parameters, employing both uni-linear and bi-linear bond stress-slip models, match the experimental behaviour with reasonable accuracy (Mohamed Ali *et al.*, 2008). However, none of the above methods can be considered as generic.

Even though there is no method developed yet to find bond parameters generically, bond parameters of some of the experimental tests found using best fitting of experimental curves are used to verify the analytical solutions as described below. Some of the tested bond specimens showed a frictional bond stress plateau as assumed in Model II (specimens failed in SOOL and specimens in Series 9 and 10). The bond parameters of the corresponding specimens are available in Table 5.1, and here they are relisted in Table 6.1 and used to verify the analytical solutions of Model II. It is assumed that the peak bond stress value and the corresponding slip value, which have been determined using the BEP model, are the same as would have been modelled by a linear branch. By applying the developed analytical solution of Model II, the ultimate load capacity of these specimens is predicted (Equation 6.96), provided that the bond length is longer than the effective bond length at the end of the elastic-softening stage (Equation 6.29). This load is compared with the actual capacity in Table 6.1. It should be emphasised that the loading arrangement of these bond tests (beam-type bond tests) is different to that assumed for the analytical derivation (simple pull-push). However, the primary assumption made for the analytical method, that concrete stresses are uniformly distributed over concrete gross area, is assumed to be valid.

The results show that the analytical solution provides a good estimate of the actual capacity. The analytical solution is also applied to predict the actual capacities of some of the specimens of De Lorenzis (2002) showing the same bond behaviour. The correlation is good for all the specimens (Figure 6.20). The theoretical full range load-slip behaviour of these specimens predicts the experimental behaviour with good accuracy. As an example, the theoretical and experimental behaviour is shown for specimen *9-35[S/60/S/Sika/6.4p]* (Figure 6.21). The material and geometrical properties are as follows: f_{cu} = 60.7N/mm^2, L = 255mm, L_{peri} = 40mm, E_f = 137300N/mm^2, A_f = 100mm, E_c = 32000N/mm^2 (BSI, 1985), and A_c = 24200mm^2. The bond parameters from Table 5.1 are δ_1 = 0.071mm, δ_{rs} = 0.622mm, τ_f = 10.5N/mm^2 and τ_r = 2.8N/mm^2.

Figure 6.22 shows the load-slip predictions for the other specimens showing the same bond behaviour. For all these specimens, the value of L_{peri} (perimeter of the failure interface) is taken as the perimeter of the bar irrespective of the failure interface because if the model is to be used for prediction purposes, it is not possible to know

the failure interface beforehand. For most of the specimens in the figure, the analytical load-slip behaviour approximates the actual behaviour with a reasonable accuracy. However, for specimens *1-3[C12/60/S/6.4p]repeat*, *1-4[C12/60/S/12.7p]* and *1-4[C12/60/S/12.7p]repeat*, the analytical behaviour deviates quite noticeably from the actual behaviour compared to the other specimens due to the following reason. These specimens failed in SOOL so that the actual value of L_{peri} should be slightly less than the bar perimeter. By taking a slightly smaller value than the bar perimeter, a better prediction would have been obtained. For the other specimens, the value of L_{peri} fits well because they failed in pull-out dominant modes where the failure interface is bar-resin interface itself. Consequently, predictions for the other specimens are more consistent.

Specimen	τ_f (N/mm^2)	δ_1 (mm)	τ_r (N/mm^2)	δ_{rs} (mm)	P_{actual}	$P_{predicted}$	$P_{predicted}/P_{actual}$
9-35[S/60/S/Sika/6.4p]	10.5	0.071	2.80	0.622	73.4	68.9	0.938
9-36[S/60/S/Sika/12.7p]	10.5	0.071	2.80	0.622	94.2	97.4	1.030
10-39[S/60/L/Sika/6.4p]	6.90	0.047	2.63	0.124	40.7	37.1	0.911
10-40[S/60/L/Sika/12.7p]	8.33	0.381	3.32	1.171	109	103	0.940
1-3[C12/60/S/6.4p]repeat	29.0	0.060	3.11	0.101	51.5	51.6	1.000
1-4[C12/60/S/12.7p]	29.0	0.060	3.11	0.101	70.8	79.7	1.130
1-4[C12/60/S/12.7p]repeat	29.0	0.060	3.11	0.101	73.1	79.7	1.090
CS3/k1.34/l8 (De Lorenzis, 2002)	8.61	0.069	2.20	0.125	24.9	20.6	0.827
CS3/k1.34/24 (De Lorenzis, 2002)	8.61	0.069	2.20	0.125	22.4	24.3	1.085

Table 6.1 - Comparison of ultimate capacity predicted using Model II with experimental values

It should be noted that the bond parameters of Model II can not at present be generically found for any given bar type. However, if it is identified that a particular bar type shows the bond behaviour of Model II, by conducting some preliminary bond tests, it would be possible to use the corresponding bond parameters to predict the load capacity of a bonded joint with any given bond length provided that the bond length is longer than the effective bond length at the end of the elastic-softening stage.

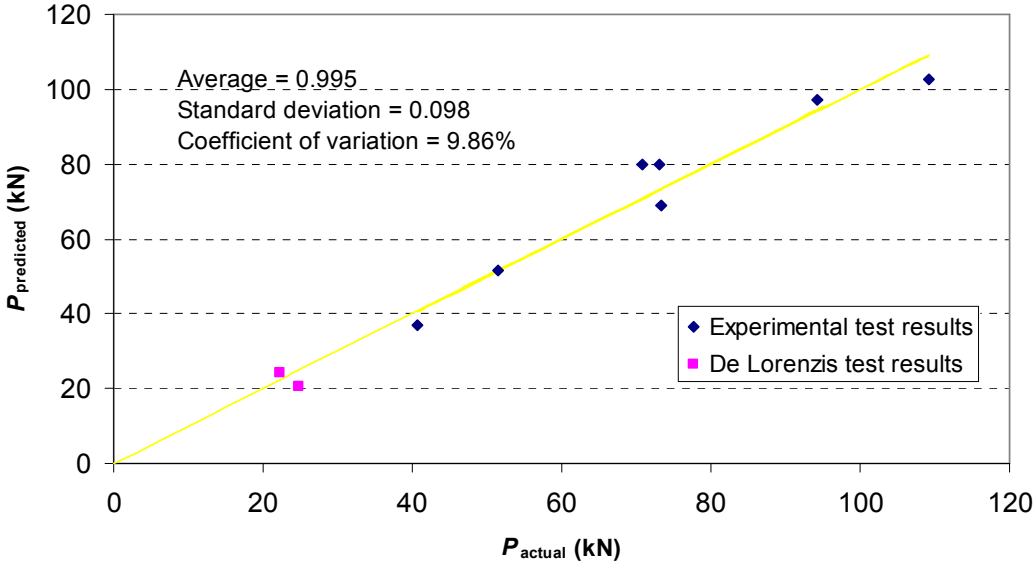

Figure 6.20 - Ultimate capacity predicted using Model II

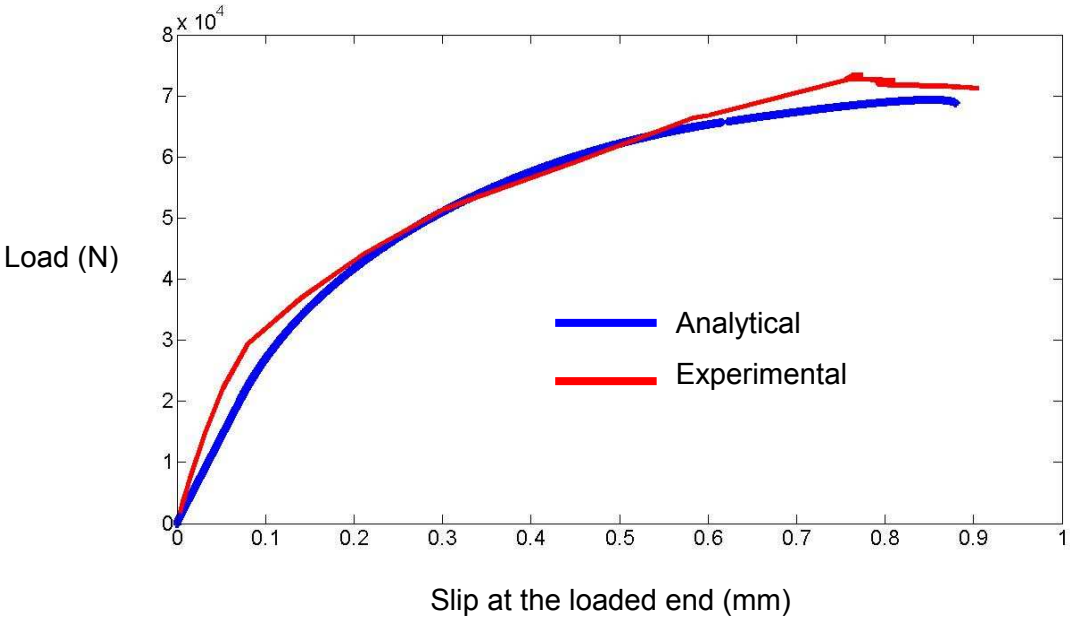

Figure 6.21 - Comparison of experimental data and analytical solution of Model II (Specimen *9-35[S/60/S/Sika/6.4p]*)

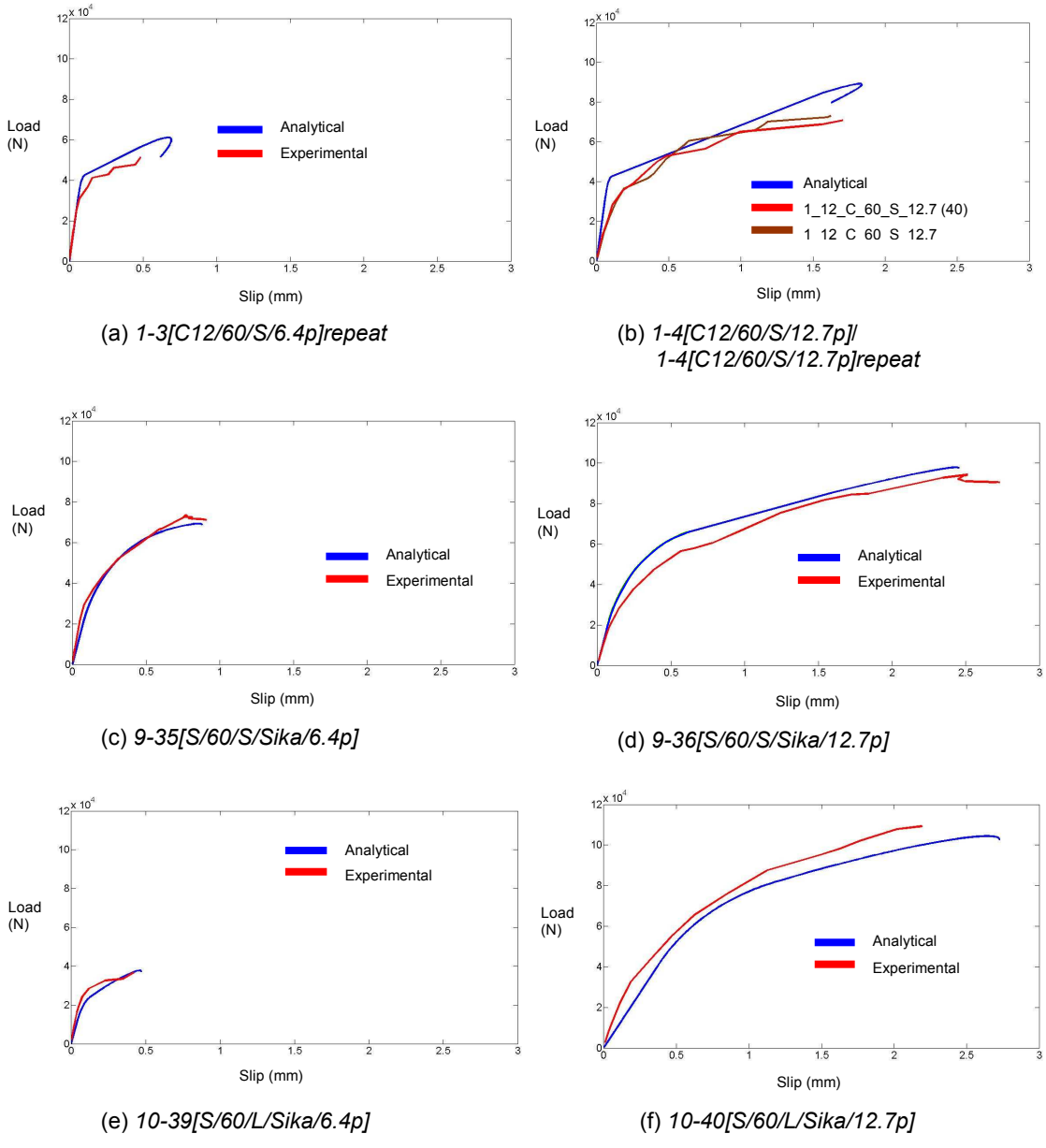

(a) *1-3[C12/60/S/6.4p]repeat*

(b) *1-4[C12/60/S/12.7p]/ 1-4[C12/60/S/12.7p]repeat*

(c) *9-35[S/60/S/Sika/6.4p]*

(d) *9-36[S/60/S/Sika/12.7p]*

(e) *10-39[S/60/L/Sika/6.4p]*

(f) *10-40[S/60/L/Sika/12.7p]*

Figure 6.22 - Comparison of experimental results and analytical solution of Model II

6.7 Conclusions

The complete debonding process of an NSM FRP bonded joint corresponding to different bond stress-slip relationships has been modelled. The fundamental equations for the shear stress, the local slip and the reinforcement stress have been developed corresponding to each stage of the debonding process. Simplified versions of practical

bond stress-slip relationships have been considered. Even though the emphasis is on NSM FRP to concrete joints, the solutions are equally applicable to similar joints with different materials.

Compared to the basic load-slip curve and the load-slip curve corresponding to Model I, the load-slip curve representing Model II shows a considerably different behaviour attributing to the major difference in the bond stress-slip models. That is Model II possesses infinite fracture energy whereas both the basic bond stress-slip model and Model I have finite fracture energy. Due to this major difference in bond stress-slip model, it is seen that the applied load is proportional to the bond length, and by increasing the bond length beyond the effective bond length at the end of elastic-softening stage, the ultimate capacity of the bonded joint can be increased. Therefore, unlike the other models, Model II possesses a development length as opposed to an effective bond length.

For bond specimens that exhibit a bond behaviour shown by Model II there exists a development length, and the value of this development length can be found analytically provided that the bond parameters are known. Furthermore, for a given bond length, longer than the effective bond length at the end of the elastic-softening stage, the highest load capacity can also be found analytically if the bond parameters are available. The analytical predictions using model II were compared with the results of the bond specimens failed in SOOL and bond specimens in Series 9 and 10, and the predictions are in good agreement with the experimental results.

CHAPTER 7 – CONCLUSIONS AND RECOMMENDATIONS

7.1 Conclusions

The use of the Near Surface Mounted (NSM) Fibre Reinforced Polymer (FRP) strengthening technique for retrofit of existing concrete structures is becoming mainstream, with many examples across the world. However, there are still some areas that need to be fully characterised, for example, anchorage design of NSM FRP bars. The particular objectives of this research project were; to investigate the bond behaviour between the NSM CFRP bars and concrete, to understand the critical failure modes and their underlying mechanics and to develop rational analytical models predicting bond strength and anchorage length requirements for NSM FRP bars.

This research has comprised a thorough experimental investigation on bond behaviour of NSM FRP bars and the development of theoretical analyses. A series of 44 small scale bond tests was carried out on NSM CFRP bars considering variables such as bond length, size, shape and surface texture of bar, type of resin, groove dimension and concrete strength. In particular, attention has been focussed on the effect of the bar shape on bond behaviour. Bond behaviour of round, rectangular and square FRP bars, has been compared for a constant bonded surface area. Furthermore, non-circular cross-sections have been compared in terms of an equivalent bar diameter based on an equivalent circular cross-sectional area. The comparison revealed that the definition of bond length in terms of number of bar perimeters appears to be more sensible than defining it in terms of number of bar diameters when it comes to non-circular sections. Standard laboratory tests were conducted on the materials involved in NSM FRP systems to find their mechanical properties.

The effect of the investigated parameters on bond behaviour between NSM CFRP bars and concrete has been discussed. The utilization of tensile capacity of CFRP bars depends on cross-sectional area/perimeter ratio. Rectangular bars seem to be the most effective shape owing to the fact that they have a beneficial cross-sectional

area/perimeter ratio allowing higher tensile stresses to be generated in the bar for a given bond strength.

Different types of failure modes were observed and the critical failure modes were identified. For both circular and square bars the critical failure mode was brittle concrete cover separation failure (CCSF), whereas for rectangular bars, the critical failure mode was tensile rupture of the bar, the desired mode of failure for any type of bar if they are to be used most efficiently. These critical failure modes demonstrate full bond of the CFRP has been maintained to failure. When these bond parameters are optimised, the bond failure is controlled by CCSF for circular and square bars with fairly high cross-sectional area/ perimeter ratios as the upper-bound failure mode, yielding the highest possible load capacity.

The debonding mechanisms of NSM FRP bond tests that have been observed previously are different to those of actual beams strengthened with NSM FRP systems. For example, CCSF has not been previously observed for NSM FRP bond tests (which is primarily due to limitations imposed on the bond length to avoid flexural cracking) even though CCSF has been observed in flexurally strengthened full scale beam tests (refer to Section 4.1.3 for the references). Therefore, results such as bond stress-slip curves of NSM FRP bond tests carried out in previous investigations have not been able to be directly transferred into predictive models for actual beams. This research has been able to demonstrate that the real behaviour of flexurally strengthened beams with NSM FRP systems can be qualitatively correlated with the results of small scale beam-type bond tests containing internal reinforcement as they fail in similar modes to those of flexurally strengthened large scale beams, where flexural/shear cracking occurs. At this stage, it is not possible to incorporate these bond stress-slip results for predictive models for real beams as these results are specimen size dependent. Therefore, it is required to investigate size effects in relation to bond behaviour of NSM FRP bars and concrete and establish correct quantitative correlations between bond test results and beam test results. Once the size-effect issues are addressed, it will then be possible to apply the results of these small scale beam-type bond tests for predicting debonding failures in real beams.

For relatively short bond lengths, the bond behaviour was not affected by flexural/shear cracking and was similar to that of NSM FRP bond tests of previous studies with no

internal steel reinforcement. Moreover, for relatively long bond lengths, the bond behaviour was found to be significantly affected by flexural/shear cracking and was therefore different to that observed from previous NSM FRP bond tests and was similar to that of flexurally strengthened large scale beams.

For both long and short bond length specimens, displacement ranges are quite similar for circular and square bars owing to their similar failure modes, while the range for rectangular bars reaches almost double the range for circular and square bars. Further, for both long and short bond length specimens, rectangular bars display a quite ductile load-slip behaviour compared to the other shapes due to the slip promoted by the common bond mechanism of rectangular bars, macro-cracking in the resin.

The bond behaviour of CFRP bars has also been analysed analytically. Local bond stress-slip relationships of various bar shapes were analysed from slip and strain data, relating to corresponding failure modes and their underlying mechanics. Effect of flexural/shear cracking on pure bond behaviour has been discussed in detail. Theoretical models were developed to predict the bond strength of specimens failing in dominant splitting failure modes and the critical CCSF mode. An upper-bound plasticity model has been developed to attempt to predict CCSF based on the observed bond mechanisms, but it has not proved to be very accurate in capturing the actual brittle behaviour of CCSF. An analytical model developed by a previous researcher to predict resin cover cracking bond strength has been considered in this research and has seemed to be consistent with the experimental results within the range of groove depth/bar diameter ratios examined. An analytical model was developed to predict the concrete splitting resistance of bond specimens. The model seemed to be reasonably consistent with the experimental results of this research and with those of previous research. An approximate analysis involving ultimate local cracking patterns which estimates upper and lower-bounds to local bond strength of specimens failing in splitting failures, developed by a previous researcher, was considered. The experimental local bond strength values seemed to lie well within the resulting bounds.

An analytical solution to predict the complete debonding process of an NSM FRP-to-concrete bonded joint, corresponding to different bond stress-slip relationships was developed based on a similar method to predict full range behaviour of externally bonded FRP-to-concrete bonded joints, developed by a previous researcher. The

fundamental equations for the shear stress, the local slip and the reinforcement stress have been developed corresponding to each stage of the debonding process. Simplified versions of practical bond stress-slip relationships have also been considered.

Compared to the basic load-slip curve and the load-slip curve corresponding to Model I, the load-slip curve representing Model II shows a considerably different behaviour attributing to the major difference in the bond stress-slip models. That is Model II possesses infinite fracture energy whereas both the basic bond stress-slip model and Model I have finite fracture energy. Due to this major difference in bond stress-slip models, it is seen that in Model II, the applied load is proportional to the bond length, and by increasing the bond length beyond the effective bond length at the end of elastic-softening stage, the ultimate capacity of the bonded joint can be increased. Therefore, unlike the other models, Model II possesses a development length as opposed to an effective bond length. The predicted load capacity using Model II was verified with experimental results and found to be in good agreement. The Model II also yields an equation for the development length provided that the bond parameters are known.

To summarise, the influences of several significant factors affecting bond of NSM FRP bars have been rigorously investigated through testing, the bond behaviour analysed and analytical predictions developed to be useful in anchorage design of NSM FRP bars.

7.2 Recommendations

The following suggestions are recommended for further research:

- It is recommended to further investigate on the most critical failure mode which limits further bond development, CCSF, either by limiting the local bond strength or the ultimate load capacity, in order to be able to develop suitable predictive models to avoid brittle catastrophic failure in practice. It is required to quantify the effects of internal reinforcement (varying the amount, termination

point, etc) since the internal reinforcement arrangement is an important influence on CCSF.

- This research was able to demonstrate that the real behaviour of flexurally strengthened beams with NSM FRP systems can be qualitatively correlated with the results of small scale beam-type bond tests containing internal reinforcement because the bond mechanisms are the same. However, these results are specimen size dependent. The next step should be to correlate bond test results and beam test results quantitatively by performing a set of large scale beam tests investigating size effects. Once the size effects are established experimentally and analytically, it will then be possible to apply the results of these small scale beam-type bond tests for predictive models for real beams. This research also revealed that flexural/shear cracking alters the pure-bond behaviour significantly. Therefore, another research area of interest is to quantify the effects of flexural/shear cracking on bond behaviour by monitoring crack patterns, crack widths, etc.

- More research is needed to be able to produce generalised models based on bond mechanics to predict the bond capacity of strengthened beams. It is useful to try to characterise the bond parameters of the current study generically within the bounds of the variables considered, and to perform a sensitivity analysis on the proposed bond capacity model to see whether the developed generic bond parameters are still valid outside the range of the variables involved.

- At present the top research priority is on the structural behaviour of this emerging technique and once this is established, other aspects such as durability concerns, behaviour under different loading conditions and strengthening of structures made of materials other than concrete, have to be addressed.

REFERENCES

ACHILLIDES, Z., PILAKOUTAS, K. & WALDRON, P., (1997). Modelling of FRP rebar bond behaviour. In *3rd International symposium on non-metallic FRP reinforcement for concrete structures.* Sapporo, Japan.

ACI, (2002). ACI 440.2R: Guide for the design and construction of externally bonded FRP systems for strengthening concrete structures. ACI Committee 440, American Concrete Institute.

ACI, (2003). ACI 440.1R: Guide for the design and construction of concrete reinforced with FRP bars. ACI Committee 440, American Concrete Institute.

ASPLUND, S. O., (1949). Strengthening bridge slabs with grouted reinforcement. *Journal of American Concrete Institute*, 45 (1), 397-406.

BARROS, J. A. O., SENA-CRUZ, J. M., DIAS, S. J. E., FERREIRA, D. & FORTES, A. S., (2004). Near surface mounted CFRP based technique for the strengthening of concrete structures. In *Workshop on R+ D+ I in Technology of Concrete Structures-tribute to Dr. Ravindra Gettu.* Barcelona, Spain.

BLASCHKO, M., (2003). Bond behaviour of CFRP strips glued into slits. In *FRPRCS-6.* Singapore, World Scientific.

BLASCHKO, M. & ZILCH, K., (1999). Rehabilitation of concrete structures with CFRP strips glued into slits. In *12th International conference on composite materials.* Paris, Organization of the International Conference on Composite Materials, Paris.

BSI, (1985). BS 8110 - Part 2: Structural use of concrete-Code of practice for special circumstances. British Standards Institution, London.

BSI, (1997). BS EN ISO 527 - 5: Plastics - Determination of tensile properties (Test conditions for unidirectional fibre reinforced plastic composites). British Standards Institution, London.

BSI, (2005). BS EN ISO 196 -1: Methods of testing cement-Determination of strength. British Standards Institution, London.

CARBOPREE, (2003). *Carbopree rods: Technical data sheet* [Online]. Available from:http://www.sireg.it/geo/files/cfrp%20bars.htm [Accessed on 09/11/2006].

CAROLIN, A., NORDIN, H. & TALJSTEN, B., (2001). Concrete beams strengthened with near surface mounted reinforcement of CFRP. In *International conference on FRP composites in civil engineering.* Hong Kong, Research Centre for

Advanced Technology in Structural Engineering, Department of Civil and Structural Engineering, Hong Kong Polytechnic University.

CHEN, J. F., YUAN, H. & TENG, J. G., (2007). Debonding failure along a softening FRP-to-concrete interface between two adjacent cracks in concrete members. *Engineering Structures*, 29 (2), 259-270.

CONCRETE SOCIETY, (2004). Technical Report No. 55: Design guidance for strengthening concrete structures using fibre composite materials. Concrete Society, Camberley.

CORDEN, G., IBELL, T.J. & DARBY, A.P., (2008). Concrete cover separation failure in near-surface mounted CFRP strengthened concrete structures. *The Structural Engineer*, 86 (4), 19-21.

COSENZA, E., MANFREDI, G. & REALFONZO, R., (1995). Analytical modelling of bond between FRP reinforcing bars and concrete. In *RILEM PROCEEDINGS.* CHAPMAN & HALL.

COSENZA, E., MANFREDI, G. & REALFONZO, R., (1996). Bond characteristics and anchorage length of FRP rebars. In *2nd International conference on Advanced Composite Materials in Bridges and Structures (ACMBS-II),* El-BADRY, M. (Ed.). Montreal, Canada.

COSENZA, E., MANFREDI, G. & REALFONZO, R., (1997). Behaviour and modelling of bond of FRP rebars to concrete. *Journal of Composites for Construction*, 1 (2), 40-51.

COSENZA, E., MANFREDI, G. & REALFONZO, R., (2002). Development length of FRP straight rebars. *Composites Part B: Engineering*, 33 (7), 493-504.

DE LORENZIS, L., (2002). Strengthening of RC structures with near surface mounted FRP rods, PhD Thesis. Department of Innovation Engineering, University of Leece, Italy.

DE LORENZIS, L., (2004). Anchorage length of near surface mounted fibre reinforced polymer rods for concrete strengthening - Analytical modelling. *ACI Structural Journal*, 101 (3), 375-386.

DE LORENZIS, L., MILLER, B. & NANNI, A., (2001). Bond of fibre reinforced polymer laminates to concrete. *ACI Materials Journal*, 98 (3), 256-264.

DE LORENZIS, L. & NANNI, A., (2001a). Characterization of FRP rods as near surface mounted reinforcement. *Journal of Composites for Construction*, 5 (2), 114-121.

DE LORENZIS, L. & NANNI, A., (2001b). Shear strengthening of reinforced concrete beams with near surface mounted fibre reinforced polymer rods. *ACI Structural Journal*, 98 (1), 60-68.

DE LORENZIS, L. & NANNI, A., (2002). Bond between near surface mounted fibre reinforced polymer rods and concrete in structural strengthening. *ACI Structural Journal*, 99 (2), 123-132.

DE LORENZIS, L., RIZZO, A. & LA TEGOLA, A., (2002). A modified pull-out test for bond of near surface mounted FRP rods in concrete. *Composites Part B: Engineering*, 33 (8), 589-603.

DE LORENZIS, L. & TENG, J. G., (2007). Near surface mounted FRP reinforcement: An emerging technique for strengthening structures. *Composites Part B: Engineering*, 38 (2), 119-143.

ELIGEHAUSEN, R., POPOV, E. P. & BERTERO, V. V., (1983). Local bond stress-slip relationships of deformed bars under generalised excitations: Report No. UCB/EERC 83–23. *Earthquake Engineering Research Centre, University of California, Berkeley*, 178.

FIB, (2000). Bond of reinforcement in concrete, Bulletin No. 10: State-of-art report. The International Federation for Structural Concrete (fib - fédération internationale du béton)

FOCACCI, F., NANNI, A. & BAKIS, C. E., (2000). Local bond-slip relationship for FRP reinforcement in concrete. *Journal of Composites for Construction*, 4 (1), 24-31.

GOTO, Y., (1971). Cracks formed in concrete around deformed tension bars. *ACI Journal Proceedings* 68 (4), 244-251.

GRECO, C., MANFREDI, G., PECCE, M. L. & REALFONZO, R., (1998). Experimental analysis of bond between GFRP deformed rebars and concrete. In *European Conference on Composite Materials, Naples, Italy,* VISCONTI, I. C. (Ed.). Woodhead Publishing.

HASSAN, T., MOHAMEDIEN, M., HASSAN, N. & RIZKALLA, S., (2001). Bond performance of different FRP strengthening systems. *Engineering Research Journal*, 5 (2), 15-23.

HASSAN, T. & RIZKALLA, S., (2003). Investigation of bond in concrete structures strengthened with near surface mounted carbon fibre reinforced polymer strips. *Journal of Composites for Construction*, 7 (3), 248-257.

HASSAN, T. K. & RIZKALLA, S., (2004). Bond mechanism of near surface mounted fibre reinforced polymer bars for flexural strengthening of concrete structures. *ACI Structural Journal*, 101 (6), 830-839.

HOGUE, T., CORNFORTH, R. C. & NANNI, A., (1999). Myriad convention centre floor system reinforcement. *ACI Special Publication*, 188, 1145-1162.

HUGHES BROTHERS, (2006a). *Aslan 200:Technical data sheet*, Hughes Brothers [Online]. Available from:http://www.hughesbros.com/Aslan200/Aslan200_CFRP_bar.html [Accessed on 02/11/2006].

HUGHES BROTHERS, (2006b). *Aslan 500:Technical data sheet*, Hughes Brothers [Online]. Available from:http://www.hughesbros.com/Aslan500/Aslan500_CFRP_tape.html [Accessed on 02/11/2006].

HULL, D. & CLYNE, T. W., (1996). *An introduction to composite materials*, Cambridge University Press.

IBELL, T. J., MORLEY, C. T. & MIDDLETON, C. R., (1997). A plasticity approach to the assessment of shear in concrete beam-and-slab bridges. *The Structural Engineer*, 75 (19), 331-338.

ICRI, (2001). Cement silo repair and upgrade, *Concrete Repair Bulletin.* International Concrete Repair Institute.

JSCE, (1997). Recommendations for design and construction of concrete structures using continuous fibre reinforcing materials, *Concrete Engineering Series, No 23.* Research Committee on Continuous Fibre Reinforcing Materials, Japan Society of Civil Engineers, Tokyo.

LU, X. Z., TENG, J. G., YE, L. P. & JIANG, J. J., (2005). Bond-slip models for FRP sheets/plates bonded to concrete. *Engineering Structures*, 27 (6), 920-937.

LUNDGREN, K., (2005). Bond between ribbed bars and concrete-Part 1: Modified model. *Magazine of Concrete Research*, 57 (7), 371-382.

MALVAR, L. J., (1994). Bond stress-slip characteristics of FRP bars: Interim report TR-2013-SHR. Naval Facilities Engineering Centre, Port Hueneme, CA 93043-4328.

MALVAR, L. J., COX, J. V. & COCHRAN, K. B., (2003). Bond between carbon fibre reinforced polymer bars and concrete: Experimental study. *Journal of Composites for Construction*, 7 (2), 154.

MOHAMED ALI, M. S., OEHLERS, D. J., GRIFFITH, M. C. & SERACINO, R., (2008). Interfacial stress transfer of near surface mounted FRP-to-concrete joints. *Engineering Structures*, 30 (7), 1861-1868.

MOHAMED ALI, M. S., OEHLERS, D. J. & SERACINO, R., (2006). Vertical shear interaction model between external FRP transverse plates and internal steel stirrups. *Engineering Structures*, 28 (3), 381-389.

NANNI, A. (Ed.) (1993). *Fibre reinforced plastic for concrete structures: Properties and applications*, Elsevier Science, Amsterdam.

NANNI, A., BAKIS, C. E. & BOOTHBY, T. E., (1995). Test methods for FRP-concrete systems subjected to mechanical loads: State of the art review. *Journal of Reinforced Plastics and Composites*, 14 (6), 524-558.

NANNI, A., DI LUDOVICO, M. & PARRETTI, R., (2004). Shear strengthening of a PC bridge girder with NSM CFRP rectangular bars. *Advances in Structural Engineering*, 7 (4), 297-309.

NEUBAUER, U. & ROSTASY, F. S., (1999). Bond failure of concrete fibre reinforced polymer plates at inclined cracks - Experiments and fracture mechanics model. *ACI Special Publication*, 188, 369-382.

NIELSEN, M. P., (1998). *Limit analysis and concrete plasticity*, Taylor & Francis Ltd.

OEHLERS, D. J., LIU, I. & SERACINO, R., (2004). A generic design approach for EB and NSM longitudinally plated RC beams. In *FRP Composites In Civil Engineering 2004 (CICE 2004),* SERACINO, R., CHEN, J. F. & HOLLAWAY, L. (Eds.). Adelaide, Australia, Elsevier.

PARRETTI, R. & NANNI, A., (2004). Strengthening of RC members using near surface mounted FRP composites: Design overview. *Advances in Structural Engineering*, 7 (6), 469-483.

PICKLES, A., (2004). Near surface mounted strengthening of concrete building structures using fibre reinforced polymer composites. Undergraduate Dissertation. University of Edinburgh, UK.

PROTA, A., PARRETTI, R. & NANNI, A., (2003). Upgrade of RC silos using near surface mounted FRP composites. *L'Industria Italiana del Cemento*, 73 (2), 170-183.

SENA CRUZ, J. M., (2004). Strengthening of concrete structures with near surface mounted CFRP laminate strips, PhD Thesis. Department of Civil Engineering, University of Minho, Portugal.

SENA CRUZ, J. M. & BARROS, J. A. O., (2004). Modelling of bond between near surface mounted CFRP laminate strips and concrete. *Computers and Structures*, 82 (17-19), 1513-1521.

SERACINO, R., SAIFULNAZ, M. R. R. & OEHLERS, D. J., (2007). Generic debonding resistance of EB and NSM plate-to-concrete joints. *Journal of Composites for Construction*, 11 (1), 62-70.

SHAVE, J. D., (2005). Shear assessment of concrete bridges: anchorage effects and use of plasticity, PhD Thesis. Department of Architecture and Civil Engineering, University of Bath, UK.

SHIELD, C., FRENCH, C. & MILDE, E., (2005). The effect of adhesive type on the bond of NSM tape to concrete. In *7th International symposium on Fibre Reinforced Polymer Reinforcement for Concrete Structures (FRPRCS-07),* SHIELD, C. (Ed.). Kansas City, Farmington Hills.

SIKA, (2006). Sikadur 30: Technical data sheet, 05/12/2006 edition, Sika Corporation.

SMITH, S. T. & TENG, J. G., (2002). FRP strengthened RC beams- I: Review of debonding strength models. *Engineering Structures*, 24 (4), 385-395.

SOLIMAN, S. M., EL-SALAKAWY, E., BENMOKRANE, B. & ABDEL BAKY, H., (2008). Experimental and numerical investigation of RC beams strengthened in bending with near surface mounted CFRP. In *5th International conference on Advanced Composite Materials in Bridges and Structures (ACMBS-V).* Winnipeg, Manitoba, Canada.

STO, (2007). StoFRP bar: Technical data sheet, 05.10/1 edition, Sto Scandinavia, AB.

STRATFORD, T. J., (2001). The shear of concrete with elastic FRP reinforcement, PhD Thesis. Jesus College, University of Cambridge, UK.

TENG, J. G., DE LORENZIS, L., WANG, B., RONG, L., WONG, T. N. & LAM, L., (2006). Debonding failures of RC beams strengthened with near surface mounted CFRP strips. *Journal of Composites for Construction*, 10 (2), 92-105.

TEPFERS, R., (1973). A theory of bond applied to overlapped tensile reinforcement splices for deformed bars: Publication 73:2. Division of Concrete Structures, Chalmers University of Technology, Goteborg, Sweden.

TEPFERS, R., (1998). Bond between FRP bars and concrete: Publication No 98.3. Division of Building Technology, Chalmers University of Technology, Goteborg, Sweden.

TIMOSHENKO, S. P. & GOODIER, J. N., (1970). *Theory of elasticity*, McGraw-Hill, New York.

UEDA, T. & DAI, J., (2005). Interface bond between FRP sheets and concrete substrates: Properties, numerical modelling and roles in member behaviour. *Progress in Structural Engineering and Materials* 7(1), 27 - 43.

VALERIO, P., (2005). Realistic shear assessment and novel strengthening of existing concrete bridges. Report on transfer from MPhil to PhD. Department of Architecture & Civil Engineering, University of Bath, UK.

VAN DER VEEN, C., (1990). Cryogenic bond stress-slip relationship. PhD Thesis. Concrete Structures Division, Delft University of Technology, Netherlands.

YAN, X., MILLER, B., NANNI, A. & BAKIS, C. E., (1999). Characterization of CFRP rods used as near surface mounted reinforcement. In *8th International conference on structural faults and repair.* Engineering Technics Press, Edinburgh, Scotland.

YUAN, H., TENG, J. G., SERACINO, R., WU, Z. S. & YAO, J., (2004). Full range behaviour of FRP-to-concrete bonded joints. *Engineering Structures*, 26 (5), 553-565.

APPENDIX A – ALIGNMENT OF STRAIN GAUGES

A.1 Circular bars

A.1.1 12mm diameter bars

- 12.7 x perimeter = 480mm

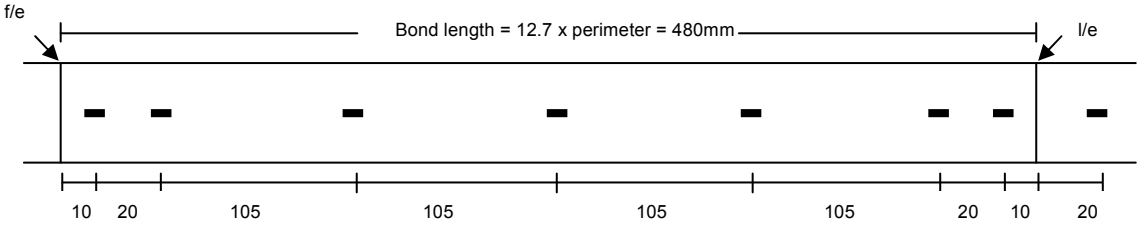

- 6.4 x perimeter = 240mm

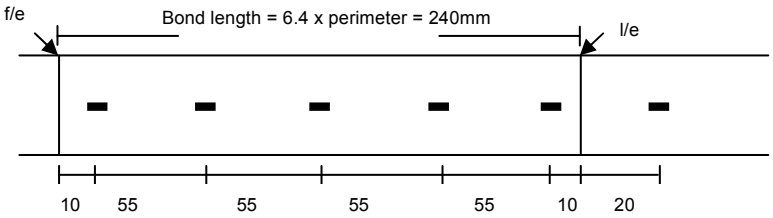

- 3.2 x perimeter = 120mm

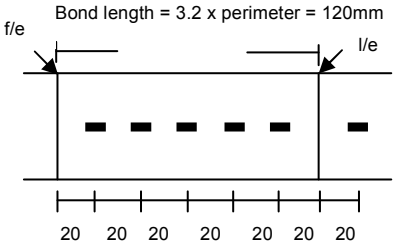

- 1.6 x perimeter = 60mm

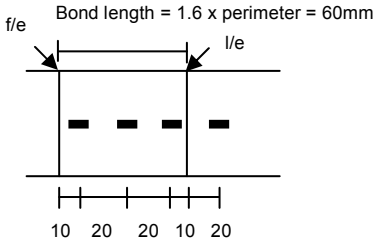

A.1.2 9mm diameter bars

- 12.7 x perimeter = 360mm

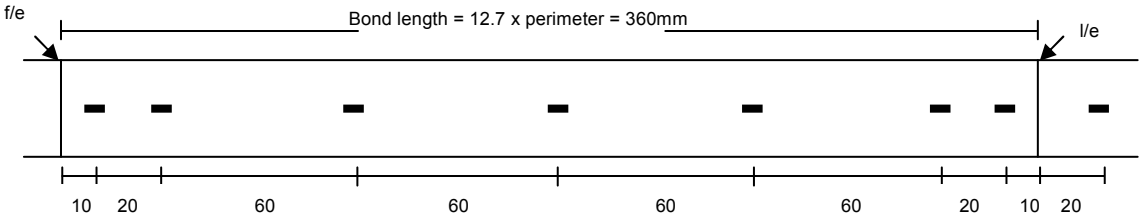

- 6.4 x perimeter = 180mm

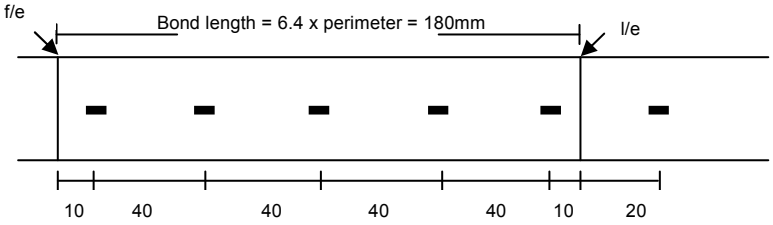

- 3.2 x perimeter = 90mm

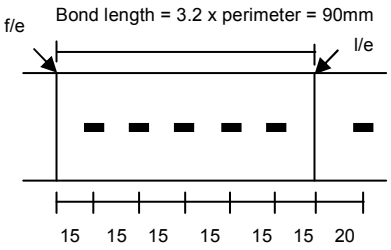

- 1.6 x perimeter = 45mm

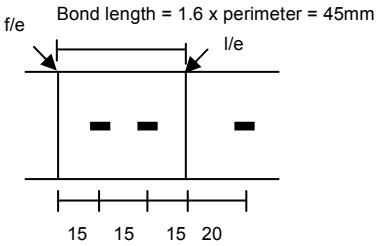

A.2 Rectangular bars

- 12.7 x perimeter = 460mm

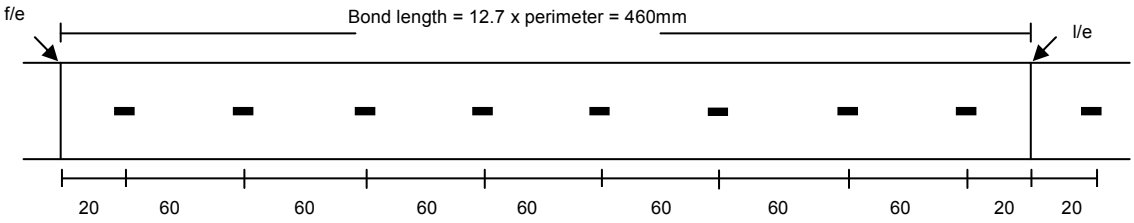

- 6.4 x perimeter = 230mm

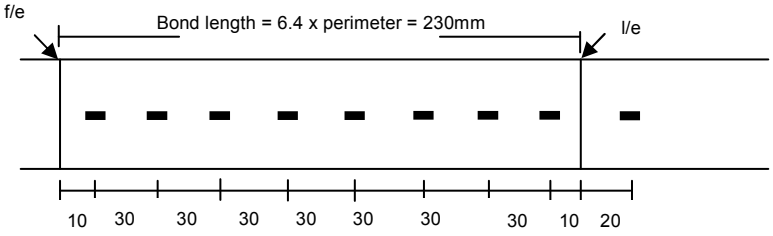

- 3.2 x perimeter = 115mm

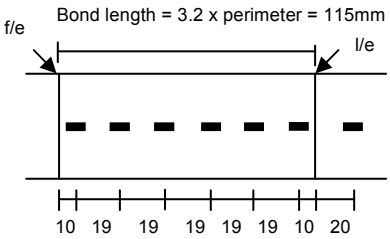

- 1.6 x perimeter = 58mm

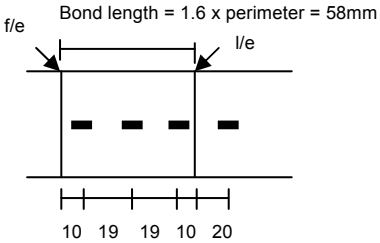

A.3 Square bars

- 12.7 x perimeter = 510mm

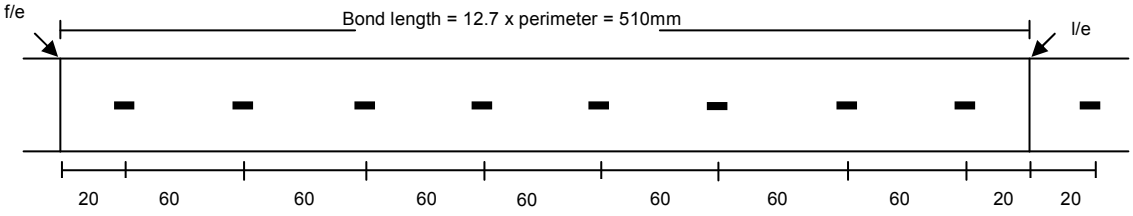

- 6.4 x perimeter = 255mm

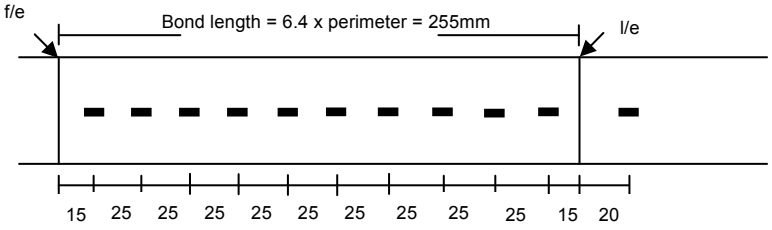

- 3.2 x perimeter = 127.5mm

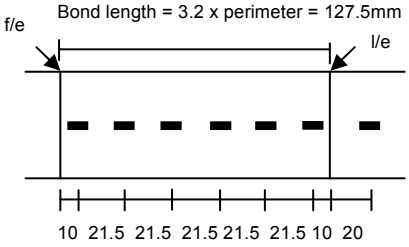

- 1.6 x perimeter = 64mm

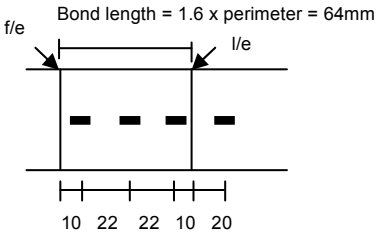

All dimensions are in millimetres, f/e- free end and l/e-loaded end.

APPENDIX B – LOAD VS. SLIP CURVES

B.1 Long bond length specimens

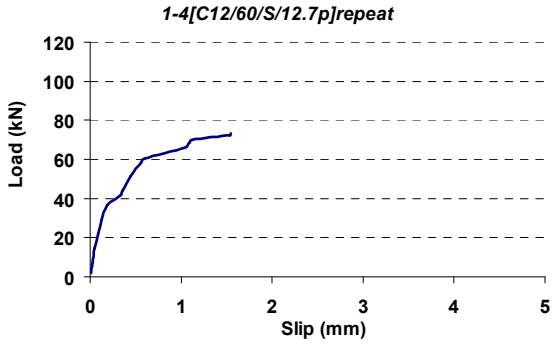

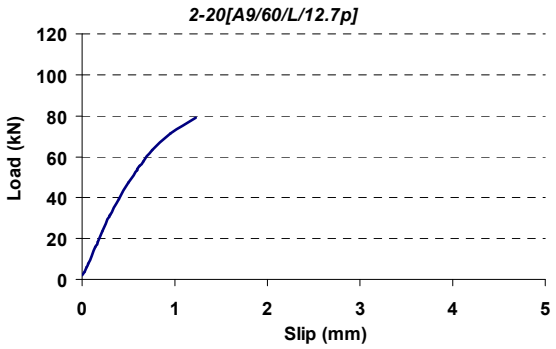

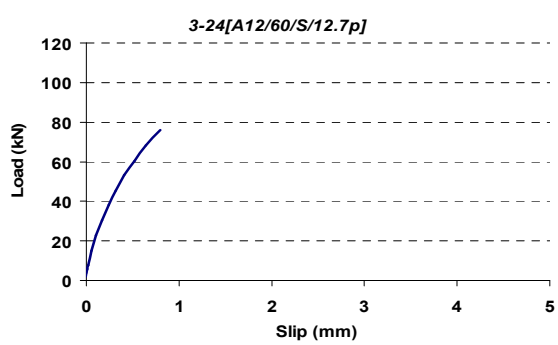

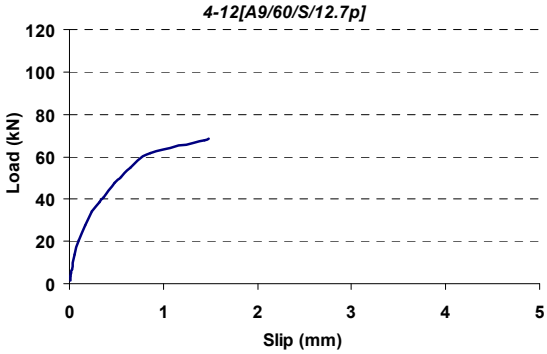

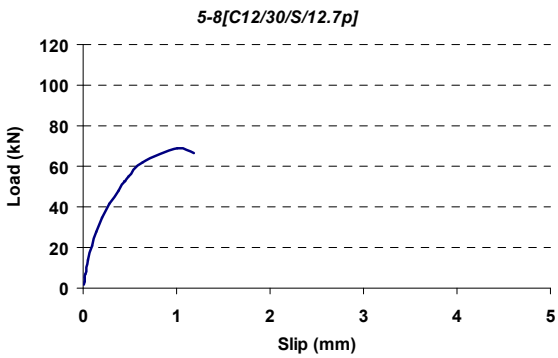

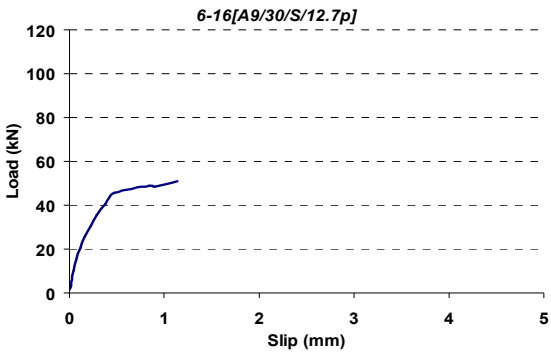

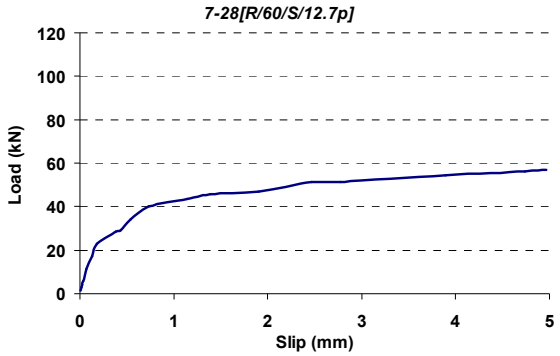
7-28[R/60/S/12.7p]
Load (kN)
Slip (mm)
0
20
40
60
80
100
120
0
1
2
3
4
5

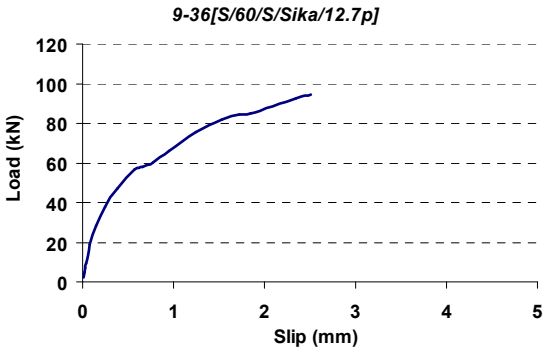
9-36[S/60/S/Sika/12.7p]
Load (kN)
Slip (mm)
0
20
40
60
80
100
120
0
1
2
3
4
5

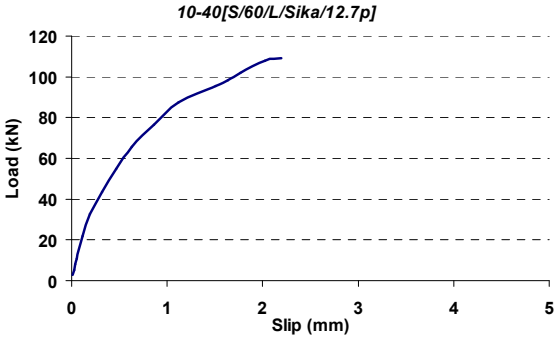
10-40[S/60/L/Sika/12.7p]
Load (kN)
Slip (mm)
0
20
40
60
80
100
120
0
1
2
3
4
5

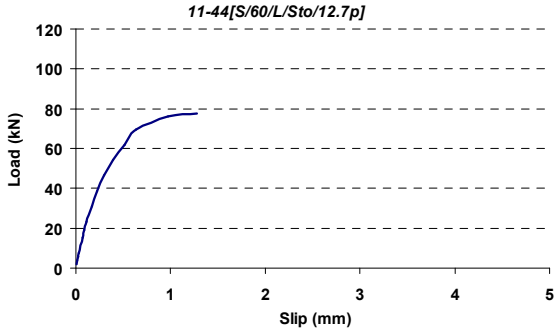
11-44[S/60/L/Sto/12.7p]
Load (kN)
Slip (mm)
0
20
40
60
80
100
120
0
1
2
3
4
5

B.2 Short bond length specimens

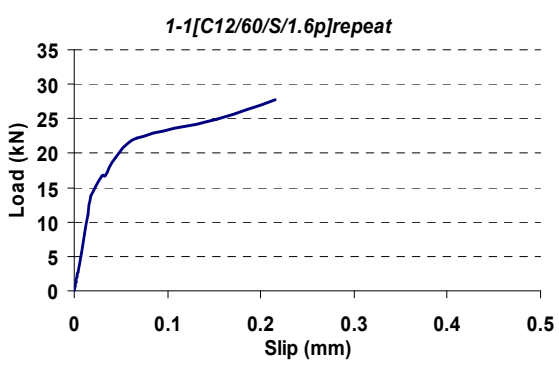

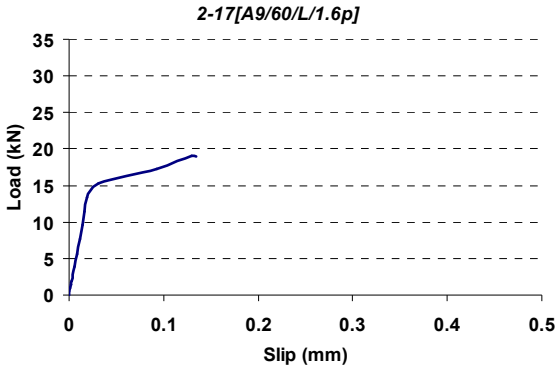

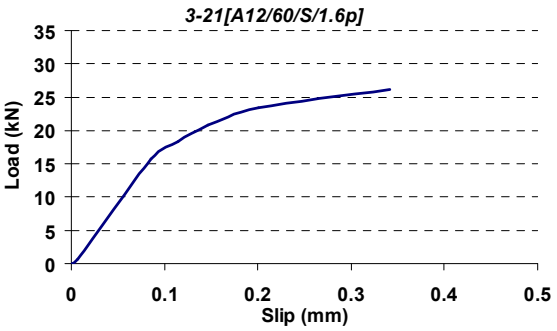

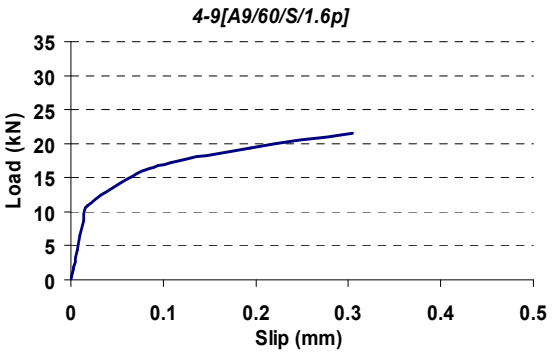

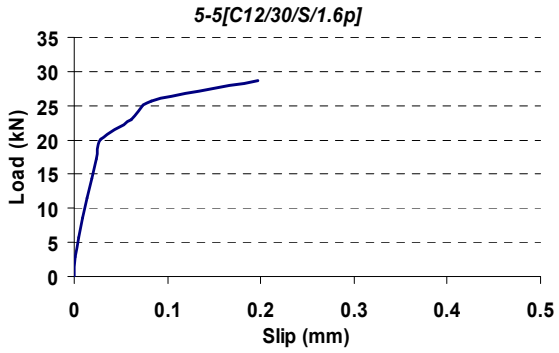

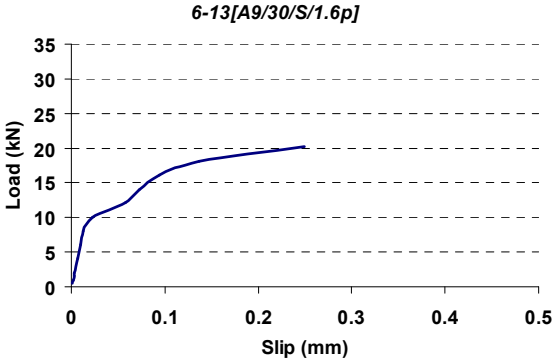

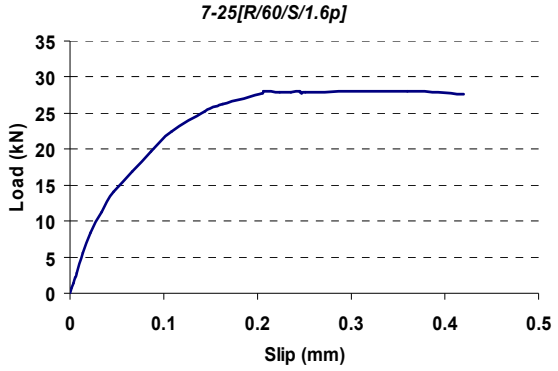
7-25[R/60/S/1.6p]
Load (kN)
Slip (mm)
0
5
10
15
20
25
30
35
0
0.1
0.2
0.3
0.4
0.5

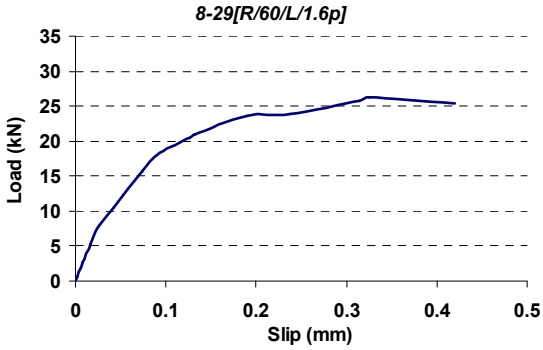
8-29[R/60/L/1.6p]
Load (kN)
Slip (mm)
0
5
10
15
20
25
30
35
0
0.1
0.2
0.3
0.4
0.5

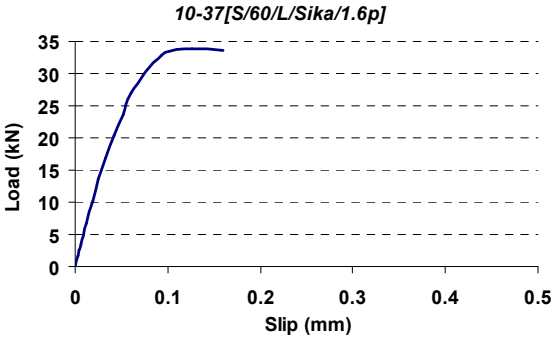
10-37[S/60/L/Sika/1.6p]
Load (kN)
Slip (mm)
0
5
10
15
20
25
30
35
0
0.1
0.2
0.3
0.4
0.5

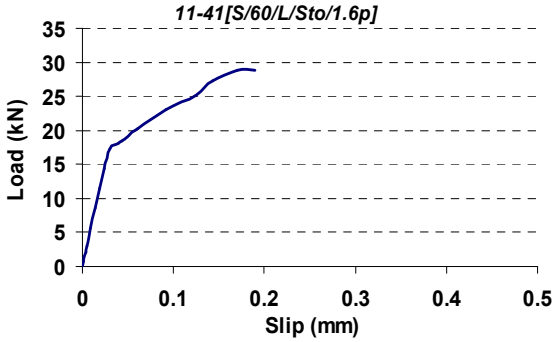
11-41[S/60/L/Sto/1.6p]
Load (kN)
Slip (mm)
0
5
10
15
20
25
30
35
0
0.1
0.2
0.3
0.4
0.5

APPENDIX C – BOND STRESS VS. SLIP CURVES

C.1 Circular bars

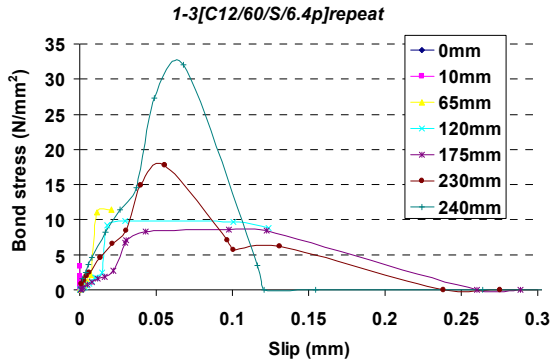

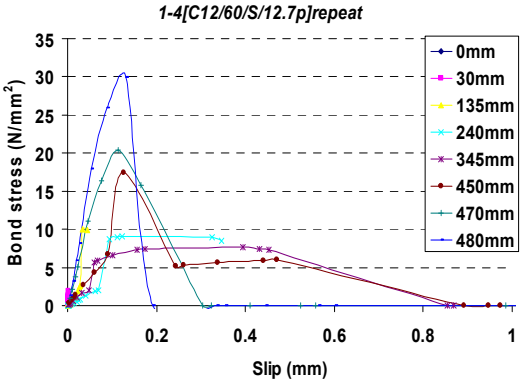

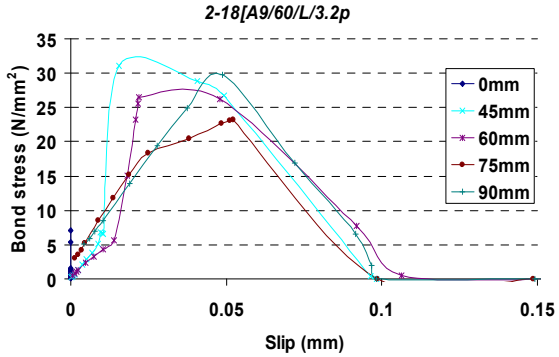

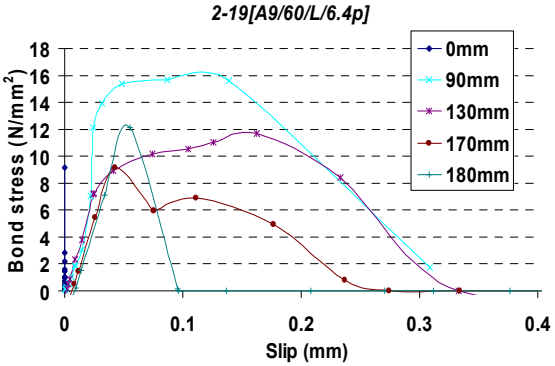

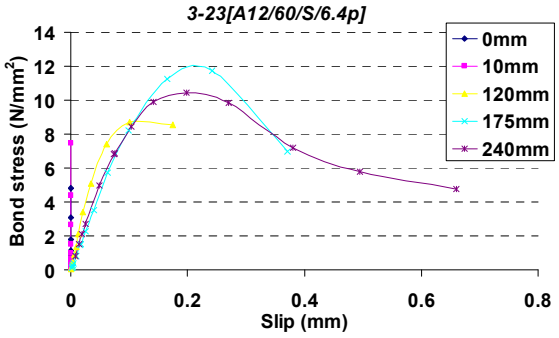

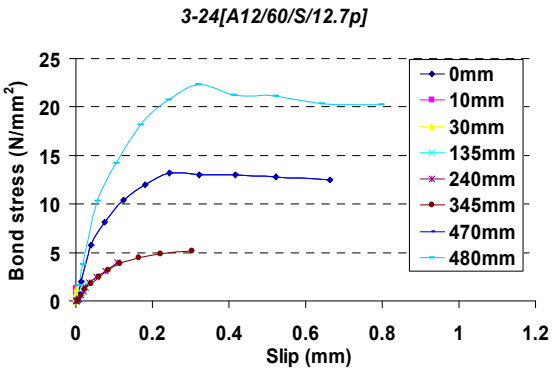

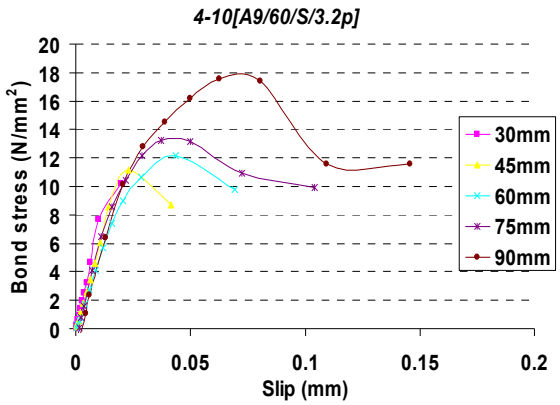
4-10[A9/60/S/3.2p]
Bond stress (N/mm²)
Slip (mm)
30mm
45mm
60mm
75mm
90mm

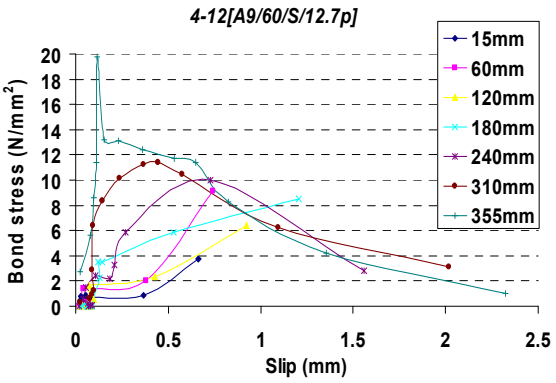
4-12[A9/60/S/12.7p]
Bond stress (N/mm²)
Slip (mm)
15mm
60mm
120mm
180mm
240mm
310mm
355mm

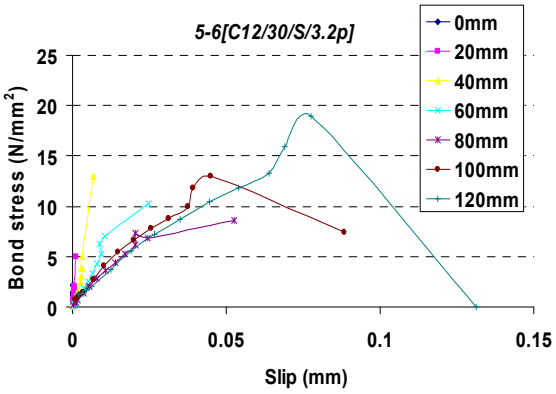
5-6[C12/30/S/3.2p]
Bond stress (N/mm²)
Slip (mm)
0mm
20mm
40mm
60mm
80mm
100mm
120mm

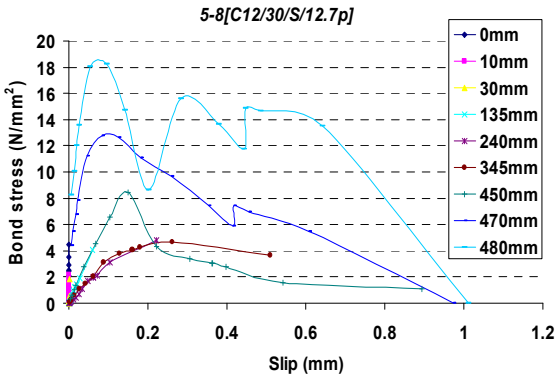
5-8[C12/30/S/12.7p]
Bond stress (N/mm²)
Slip (mm)
0mm
10mm
30mm
135mm
240mm
345mm
450mm
470mm
480mm

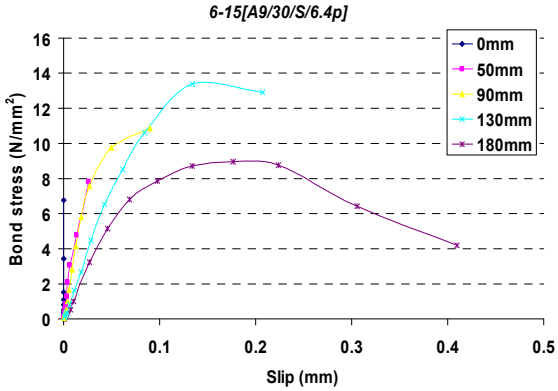
6-15[A9/30/S/6.4p]
Bond stress (N/mm²)
Slip (mm)
0mm
50mm
90mm
130mm
180mm

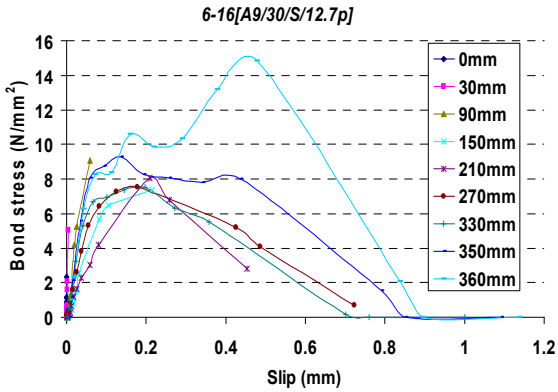
6-16[A9/30/S/12.7p]
Bond stress (N/mm²)
Slip (mm)
0mm
30mm
90mm
150mm
210mm
270mm
330mm
350mm
360mm

C.2 Square bars